

Ductile tearing of AA2198 aluminum-lithium sheets for aeronautic application

Jianqiang Chen

▶ **To cite this version:**

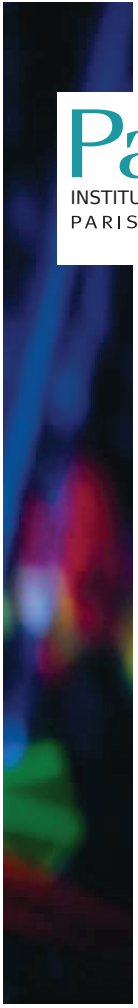
Jianqiang Chen. Ductile tearing of AA2198 aluminum-lithium sheets for aeronautic application. Materials. École Nationale Supérieure des Mines de Paris, 2011. English. NNT : 2011ENMP0040 . pastel-00657028

HAL Id: pastel-00657028
https://pastel.hal.science/pastel-00657028

Submitted on 6 Jan 2012

HAL is a multi-disciplinary open access archive for the deposit and dissemination of scientific research documents, whether they are published or not. The documents may come from teaching and research institutions in France or abroad, or from public or private research centers.

L'archive ouverte pluridisciplinaire **HAL**, est destinée au dépôt et à la diffusion de documents scientifiques de niveau recherche, publiés ou non, émanant des établissements d'enseignement et de recherche français ou étrangers, des laboratoires publics ou privés.



ParisTech
INSTITUT DES SCIENCES ET TECHNOLOGIES
PARIS INSTITUTE OF TECHNOLOGY

MINES ParisTech

École doctorale 432 : Sciences des Métiers de l'Ingénieur

Doctorat ParisTech

T H È S E

pour obtenir le grade de docteur délivré par

l'École nationale supérieure des mines de Paris

Spécialité « Science et Génie des Matériaux »

présentée et soutenue publiquement par

Jianqiang CHEN

le 29 Avril 2011

Déchirure Ductile des Tôles en Alliages d'Aluminium-Lithium 2198 pour Application Aéronautique

Ductile Tearing of AA2198 Aluminum-Lithium Sheets for Aeronautic Application

Directeur de thèse : **Jacques BESSON**
Co-encadrement de thèse : **Yazid MADI**

Jury

M. André PINEAU, Professeur, CdM - Mines ParisTech	Président
M. Ian SINCLAIR, Professeur, University of Southampton	Rapporteur
Mme. Christine SARRAZIN-BAUDOU, Directeur de Recherche, LMPM ENSMA	Rapporteur
M. Serge KRUCH, Ingénieur de Recherche HDR, ONERA Châtillon	Examinateur
M. Jean-Christophe EHRSTRÖM, Ingénieur de Recherche, ALCAN CRV	Examinateur
M. Jacques BESSON, Directeur de Recherche, CdM- MINES ParisTech	Examinateur
M. Yazid MADI, Enseignant-chercheur, Ermess EPF-Ecole d'Ingénieur	Examinateur

MINES ParisTech
Centre des Matériaux - UMR CNRS 7633
B.P. 87 - 91003 EVRY Cedex

THÈSE

Déchirure Ductile des Tôles en Alliages d'Aluminium-Lithium 2198 pour Application Aéronautqiue

Résumé : L'objectif de cette thèse est de progresser dans la compréhension de l'influence de la microstructure sur l'anisotropie plastique et la ténacité de deux nuances d'alliage Al-Cu-Li 2198 sous forme de tôle. L'épaisseur de tôles est 2 mm et 6 mm. Deux traitements thermiques (T351 et T851) ont été étudiés pour chaque nuance. Différentes techniques de caracterisation multi-échelles telles que la microscopie optique, la microscopie électronique en transmission ou encore la tomographie à rayons X ont été utilisées pour identifier les microstructures des matériaux et les micro-mécanismes d'endommagement. L'anisotropie plastique et l'effet d'épaisseur sur la plasticité ont été étudiés via des essais de traction sur les éprouvettes lisses et entaillées selon différentes directions. Les résultats montrent que le comportement plastique est anisotrope dans le plan de tôle. Le comportement en déchirure ductile a été examiné en utilisant des éprouvettes de petite taille de type Kahn ainsi que des plaques larges de type M(T). L'anisotropie de ténacité a été étudiée sur les éprouvettes chargées selon différentes configurations. La fractographie par microscope électronique à balayage (MEB) et la tomographie synchrotron aux rayons X ont clarifié le rôle des structures granulaires et des traitements thermiques sur les mécanismes de la rupture inter-granulaire et trans-granulaire. La croissance de cavités reste limitée dans la zone de propagation de fissure. Enfin, la simulation de la déchirure ductile par élément finis est basée sur l'approche locale de la rupture en utilisant un modèle de zone cohésive (CZM). Les paramètres cohésifs ont été ajustés sur les éprouvettes Kahn. Les paramètres identifiés ont été employés pour prédire la déchirure ductile des essais M(T). Les résultats montrent que la simulation des essais M(T) est plus sensible aux valeurs des paramètres ajustés que la simulation des essais Kahn. L'effet d'épaisseur a été évalué à l'aide de la technqiue de relâchement des noeuds en analysant la variation de la contrainte et de la déformation dans la direction de l'épaisseur.

Mots clés : alliage d'Al-Li, rupture ductile, endommagement, mécanismes de rupture, anisotropie plastique, effet d'épaisseur, simulation par éléments finis, CZM, tomographie à rayons X

Ductile Tearing of AA2198 Aluminum-Lithium Sheets for Aeronautic Application

Abstract : The purpose of this thesis consists in understanding the influence of microstructure on plastic anisotropy and fracture toughness for two grade 2198 Al-Cu-Li alloys. The sheet thicknesses are 2 mm and 6 mm. Two heat treatment conditions (T351 and T851) were studied for each grade. Multiscale characterization techniques including optical micrography, transmission electron microscopy and X-ray computed tomography have been used to identify materials microstructure and damage micromechanisms. Plastic anisotropy and thickness effect on plasticity have been investigated via tensile tests on smooth flat and notched flat specimens showing an anisotropic plastic behaviour along different loading directions. Ductile tearing behaviour was examined using small sized Kahn specimens and large panels M(T) tests. Fracture toughness anisotropy was investigated on different loading configuration tests. Fractography via scanning electron microscopy (SEM) and synchrotron radiation computed tomography (SRCT) have clarified the intergranular and transgranular mechanisms of fracture with respect to grain structure and heat treatment. Void growth is limited in the crack propagation regions. Finally, the finite element simulation of ductile tearing is based on the local approach to fracture using cohesive zone model (CZM). The cohesive parameters were adjusted on small sized Kahn specimens. Fitted parameters were employed to predict the ductile tearing behaviour of M(T) tests. Simulation results show that the fitted cohesive parameters are more sensitive for M(T) tests than for Kahn tests. The thickness effect was assessed using node release technique by analysing variation of stress and strain along thickness direction.

Keywords : Al-Li alloys, ductile fracture, damage, fracture mechanisms, plastic anisotropy, thickness effect, finite element simulation, CZM, X-ray tomography

A mes parents

Remerciements

Ce travail de thèse a été réalisé dans le cadre du projet ALICANTDE, soutenu par l'ANR. J'ai été amené à travailler avec de nombreuses personnes d'Alcan CRV, d'EADS, de l'INPG, de l'ENSMA Poitiers et du Centre des Matériaux Mines ParisTech. Ainsi je tenais à tous les remercier pour ces trois ans de réunions et de discussions.

Je remercie tout d'abord Ian Sinclair et Christine Sarrazin-Baudou d'avoir accepté la lourde tâche d'être rapporteur de mémoire. Merci pour vos rapports complets et enrichissants, pour vos questions pertinentes qui m'ont permis de prendre encore plus de recul sur mes travaux. Je remercie particulièrement Jean-Christophe Ehrström d'avoir accepté de participer à mon jury de thèse et de s'être déplacé spécialement à Paris à cette occasion. Je remercie également Serge Kruch pour sa participation à mon jury de thèse et à l'intérêt qu'il a porté à ce travail.

Je voudrais remercier spécifiquement André Pineau, qui a accepté de présider mon jury de soutenance. C'est un grand honneur pour moi. J'ai fait votre connaissance grâce à votre livre jaune qui est la bible des ingénieurs d'Airbus.

Je voudrais adresser mes plus sincères remerciements à Jacques Besson pour ses précieux conseils tant au point de vue scientifique que sur l'orientation générale de la thèse. Aussi, ce que je retiendrai de ces trois ans de thèse va bien au-delà de la mécanique de la rupture. Je remercie Yazid Madi pour sa précieuse aide sur la partie expérimentale. Sa passion pour les essais est contagieuse et très stimulante. C'est donc avec un réel plaisir que j'ai pu réaliser toutes ces belles expériences et ce, toujours dans la bonne humeur. Je remercie Thilo Morgeneyer pour ses conseils donnés de-ci delà au cours de ma thèse. J'ai toujours considéré ses conseils très avisés.

Merci à Benjamin Decreus et Sébastien Richard, les deux autres thésards de ce projet, respectivement à Grenoble et à Poitier. Les différentes réunions et échanges que nous avons pu avoir ont permis de maintenir toujours le lien métallurgie-mécanique au bon avancement de ce projet.

Je ne pourrais pas oublier de remercier toutes les personnes qui, de près ou de loin, m'ont encouragé, aidé tout au long de cette thèse.

Je remercie mes collègues de bureau, Florian, Clara, Auréliane, Mélanie et Huaidong avec qui j'ai pu partager de nombreux fous rires couplés à des discussions plus sérieuses. Il y a aussi les thésards : Julien, Tung, Matthieu, Yang, Yasuhiro, Abderrahmen, Joào, Yoann, Bahram, Edouard, Vladislav, Thomas, Nicolas, Julie, Delphine, Clémence, Sophie, Florence, Faten, Xu, Kokleang, Duy Khanh, Yang, Laure-Line, Noemi, Minghao et tous les autres pour les moments passés ensemble au bocal, salle de calcul ou ailleurs. Merci à Djamel et Nikolay pour avoir répondu à mes multiples requêtes sur Zébulon.

Je pense à remercier toute l'équipe administrative qui m'a apporté son aide lorsque j'en ai eu besoin : Liliane Locicero, Konaly Sar, Catherine Rouil, Véronique Matos, Véronique Diamantino, Dolorès Daquin, Sarojinee Bonneville et Odile Adam.

Je souhaite aussi remercier, pour leur soutien technique au Centre des Matériaux, Maria Betbeder, Fabrice Gaslain, François Grillon, Anne Laurent, Brigitte Raviard, Michel Rousselot, Régis Clement, Julie Heurtel, Françoise Di Rienzo, Yves Favry, Joseph Valy, Franck Nguyen et Jean-Christophe Teissedre. Je souhaite également remercier Grégory Saint-Luce et Olivier Delhomme pour leur disponibilité et pour avoir répondu à mes multiples questions ainsi qu'à mes soucis informatiques.

Je voudrais exprimer toute ma gratitude à Georges Cassas pour avoir usiné de nombreuses éprouvettes avec sa patience ainsi qu'à Abdennour Meddour pour son soutien exceptionnel pendant les différents essais mécaniques.

Je remercie aussi Elodie Boller et Wolfang Ludwig de la ligne ID19 de Synchrotron de Grenoble, pour leur aide pendant les observations tomographiques. Je remercie également Thilo Morgeneyer et Henry Proudhon pour leurs appuis et leurs conseils sur les analyses en tomographie.

J'aimerais enfin avoir une pensée particulière pour mes parents et pour Yaru Jiang qui m'ont toujours donné leur soutien et pour leur patience au long de ces trois années de thèse. Ces mots ne sont pas suffisants pour exprimer toute ma gratitude.

Je remercie, enfin, tous ceux qui ont contribué de prés ou de loin à la réussite de ce travail.

Jianqiang CHEN

Contents

Remerciements **2**
Table of Contents . . . 3
List of Figures . . . 6
List of Tables . . . 14

1 Introduction **15**
1.1 Industrial background and motivations . . . 15
1.2 Research objectives . . . 16
1.3 Structure of this thesis . . . 17
1.4 Résumé . . . 18

2 Materials and Microstructure **22**
2.1 Introduction . . . 22
2.1.1 Al-Cu-Li alloys . . . 22
2.1.2 Metallurgical considerations . . . 24
2.1.3 Dispersoids and Precipitate free zones . . . 25
2.1.4 Constituent phases . . . 27
2.2 Materials studied . . . 29
2.3 Material microstructure . . . 30
2.3.1 Definition of processing directions . . . 30
2.3.2 Optical micrographs . . . 31
2.3.3 Transmission Electron Microscopy (TEM) . . . 33
2.3.4 X-ray tomography . . . 39
2.4 Conclusions . . . 40
2.5 Résumé . . . 42

3 Plastic Anisotropic Behaviour **44**
3.1 Mechanical tests . . . 45
3.1.1 Specimens for mechanical tests . . . 45
3.1.2 Experimental setup and testing conditions . . . 45
3.2 Experimental results . . . 48
3.2.1 Smooth tensile tests . . . 48
3.2.2 Notched flat tensile tests . . . 52

3.3 Strain rate sensitivity . . . 54
3.3.1 Experimental results at room temperature (293 K) . . . 54
3.3.2 Experimental results at 120°C (393 K) . . . 56
3.3.3 Analysis of DSA effect on necking . . . 57
3.4 Thickness effect on smooth and notched specimens . . . 58
3.5 Failure mechanisms and strain localisation . . . 61
3.5.1 Macroscopic failure . . . 61
3.5.2 Fracture mechanisms at the microscopic level . . . 63
3.6 Modeling of plastic anisotropy . . . 66
3.6.1 Constitute equations . . . 66
3.6.2 Identification of material parameters . . . 67
3.6.3 Results of the optimisation . . . 70
3.7 Analysis of strain localisation . . . 74
3.7.1 Rice's localisation indicator . . . 74
3.7.2 Plastic model with damage . . . 75
3.7.3 Results . . . 75
3.8 Conclusions . . . 77
3.9 Résumé . . . 79

4 Ductile Tearing **81**
4.1 Introduction . . . 81
4.2 Mechanical testing conditions and testing specimens . . . 82
4.3 Experimental results and analysis . . . 86
4.3.1 Kahn tear tests . . . 86
4.3.2 Arcan testing . . . 89
4.3.3 M(T) testing . . . 92
4.4 Thickness effect on fracture toughness . . . 93
4.5 Analysis of R-curve . . . 99
4.6 Fracture mechanisms . . . 102
4.6.1 Macroscopic fracture surface . . . 102
4.6.2 Fractography via SEM . . . 106
4.6.3 X-ray tomography . . . 112
4.7 Discussion . . . 124
4.7.1 Crack bifurcation behaviour . . . 124
4.7.2 Grain boundary fracture and delamination . . . 125
4.7.3 Thickness effect . . . 125
4.8 Conclusion . . . 126
4.9 Résumé . . . 129

5 Modeling of Ductile Tearing **131**
5.1 Introduction . . . 131
5.2 Traction-separation constitutive models . . . 136
5.2.1 Mode I – Traction-separation law . . . 136
5.2.2 Mixed-mode cohesive law . . . 137
5.3 Finite element models . . . 140

5.3.1 Flat crack path model . . . 140
5.3.2 Slant fracture model . . . 143
5.4 Calibration of cohesive zone parameters via Kahn tear tests . . . 145
5.4.1 Material parameters . . . 145
5.4.2 Determination of the cohesive zone parameters . . . 145
5.4.3 Calibration results . . . 146
5.5 Predictions of M(T) tests . . . 151
5.6 Transferability of Kahn to M(T) . . . 153
5.7 Transferability of thickness effect . . . 154
5.8 Simulation and analysis of thickness effect . . . 156
5.8.1 Modeling of slant fracture with node release technique . . . 156
5.8.2 Variation of stress triaxiality along specimen's thickness . . . 157
5.8.3 Variation of out-of-plane stress with accumulated plastic strain . . . 161
5.8.4 Variation of out-of-plane stress with loading time . . . 161
5.8.5 Variation of stress triaxiality stress with CMOD . . . 164
5.9 Conclusions . . . 166
5.10 Résumé . . . 167

6 Conclusions and Prospects **169**
6.1 General conclusions . . . 169
6.2 Main results . . . 170
6.3 Prospects . . . 174

Conclusions et perspectives **176**

Bibliography **183**

A Plan of specimens **192**

B Mechanical Tests **199**

List of Figures

2.1 Content of Cu and Li in the new generation Al-Cu-Li alloys (2098, 2198 and 2050), compared to second generation Al-Cu-Li alloys 2091 (Al-Li-Cu-Mg-Zr) and 2090 (Al-Cu-Li-Zr). The second generation alloy are presented as dashed boxes, the third generation as solid boxes (after Warner.,[118]). 23

2.2 Schematic illustration of some key property variations as a function of Cu and Li concentration in Al-Cu-Li alloys (after Warner., [118]). 24

2.3 Observed precipitates in different Al-Cu-Li systems according Cu and Li contents. (after Silcock., J.M., [102]) 26

2.4 Schematic of precipitates and dispersoids that contribute to strength and toughness in 2099 and 2199 Al-Cu-Li alloys (after Giummarra et al., [39]). 27

2.5 TEM micrograph of Zr containing dispersoid particles (a) and Mn containing dispersoid particles (b). The figure (a) refers to an Al-4.8Cu-0.45Mg-0.39Ag-0.14Zr alloy and the figure (b) refers to an Al-4.9Cu-0.46Mg-0.38Ag-0.32Mn alloy (after Cho et Bès, [26]). 28

2.6 TEM micrograph of Al-2.3Li-1.8Mg-0.15Zr-0.1Cu alloy associated with a clear PFZ. (after Özbilen., [79]). 28

2.7 Two different heat treatment sequences applied to each grade (recrystallized sheet and fibrous sheet). 30

2.8 Definition of L (rolling direction), T (long–transverse direction), S (short–transverse direction) and D (diagonal direction) of the sheet material in this study. 32

2.9 Optical micrographs of the AA2198-T3 2 mm-thick recrystallized material in TS, LS, LT planes and pseudo-3D grain structure. (L: rolling direction, T: long transverse direction and S: short transverse direction). 33

2.10 Optical micrographs of the AA2198-T3 6 mm-thick fibrous material in TS, LS, LT planes and pseudo-3D grain structure. (L: rolling direction, T: long transverse direction and S: short transverse direction). 34

2.11 TEM investigation of naturally aged fibrous material ($T3F_6$), grain boundary and subgrain boundary (a, b), dispersoids (c) can be seen. Note that there is no precipitates decoration of the observed grain boundaries and subgrain boundaries. 36

2.12 TEM investigation of artificially aged fibrous material ($T8F_6$). (a) plate-shaped precipitates of T_1 (Al_2CuLi) in $\{1\ 1\ 1\}$ plane and θ' (Al_2Cu) in $\{1\ 0\ 0\}$ palne, (b) precipitates decoration at grain boundary (horizontal) and subgrain boundary (vertical), (c) dispersoids and inter-granular large precipitates. 37
2.13 TEM investigation of artificially aged fibrous material ($T8F_6$). (a) precipitates decoration at grain boundary, (b) precipitates decoration at subgrain boundary, (c) precipitate free zone (PFZ) and inter-granular large precipitates. 38
2.14 2D images of as-received undeformed materials from high resolution X-ray tomography: (a) Recrystallized material ($T8R_2$) in the L-S plane, (b) Fibrous material ($T8F_6$) in the L-S plane. Constituent particles are composed of Fe and Si (white). . 40
2.15 3D images of as-received T8 recrystallized material by high resolution X-ray tomography. The constituents and pores are in white. The size of the box is 256 pixels = 179.2 μm in each direction. 41

3.1 Geometry of test specimens (all dimensions in mm): smooth flat tensile specimen ST_{12}, notched flat tensile specimen NT_r with radii of 0.5, 1 and 2 mm. 45
3.2 Smooth flat tensile specimen ST_{12} setup with longitudinal and transverse gages during test. 47
3.3 Notched flat tensile specimen NT_r setup with left and right gages during test. . . . 47
3.4 Tensile tests on smooth specimens ST_{12} along L, T and D directions for recrystallized materials ($T3R_2$ and $T8R_2$). Engineering stress (F/S_0) as a function of the normalized plastic load line displacement $\Delta LL_p/L_0$. Width reduction ($\Delta W/W_0$) as a function of the axial strain $\Delta l/l_0$. The testing strain rate is $5.2 \times 10^{-4}\ s^{-1}$. ($F$: force, S_0 initial cross section, ΔLL_p: load line displacement corrected for elastic deformation, L_0: specimen gage length, ΔW: width variation, W_0: initial width, Δl displacement measured by the longitudinal extensometer, l_0 extensometer gage length.) 50
3.5 Tensile tests on smooth specimens ST_{12} along L, T and D directions for fibrous materials ($T3F_6$ and $T8F_6$). Engineering stress (F/S_0) as a function of the normalized plastic load line displacement $\Delta LL_p/L_0$. Width reduction ($\Delta W/W_0$) as a function of the axial strain $\Delta l/l_0$. The testing strain rate is $5.2 \times 10^{-4}\ s^{-1}$. ($F$: force, S_0 initial cross section, ΔLL_p: load line displacement corrected for elastic deformation, L_0: specimen gage length, ΔW: width variation, W_0: initial width, Δl displacement measured by the longitudinal extensometer, l_0 extensometer gage length.) 51
3.6 Tensile tests on notched flat specimens (NT_2) along L-, T- and D-loadings. F stands for the load, S_0 stands for initial minimum cross section, NOD stands for notch opening displacement. 53
3.7 Tensile tests on notched flat specimens with different radii 0.5, 1 and 2 mm for T3 fibrous material loading in T direction. F stands for the load, S_0 stands for initial minimum cross section, NOD stands for notch opening displacement. 54

3.8 Tensile stress–strain curves of fibrous materials $T3F_6$ and $T8F_6$ along different loading directions. True strain $\ln(\Delta l/l_0)$ measured by the longitudinal extensometer (initial gage is 22 mm), curves are cut at maximum loads. (L, T and D directions for $T3F_6$ material, T direction for $T8F_6$ material) under three testing strain rates varying from $5.2 \times 10^{-5}\ s^{-1}$ to $5.2 \times 10^{-3}\ s^{-1}$ at room temperature (293 K). 55
3.9 Tensile stress–strain curves of fibrous material $T3F_6$ in L loading at 393 K for two testing strain rates $5.2 \times 10^{-5}\ s^{-1}$ and $5.2 \times 10^{-4}\ s^{-1}$. 56
3.10 Experimental tensile stress–strain curve and fitted one at 293 K and 393 K in fibrous material ($T3F_6$) of L-loading. The testing strain rate is $5.2 \times 10^{-4}\ s^{-1}$. 57
3.11 Comparison of 2 mm- and 6 mm-thick samples in the case of smooth tensile tests (a) and notched tensile tests (b) for T3 fibrous material. 59
3.12 Comparison of 2 mm- and 6 mm-thick samples in the case of smooth tensile tests (a) and notched tensile tests (b) for T8 fibrous material. 60
3.13 Post-test specimens of smooth flat tensile tests along L-, T- and D-loading for 2 mm thick recrystallized materials. 61
3.14 Post-test specimens of smooth flat tensile tests along L-, T- and D-loading for 6 mm thick fibrous materials. 62
3.15 (a) Schematic view of the fracture plane angles ϕ and θ. (b) Observed fracture plane angles ($T8F_a$) and comparison with the theoretical value for ϕ (eq. 3.5). 63
3.16 L-loading (a, c) and D-loading (b, d) smooth tensile specimen fracture surface for $T3F_6$ material via SEM observations. 64
3.17 Smooth tensile specimen fracture surface of $T8F_{62}$ material in D-loading. 65
3.18 Comparison of experiments (lines) and simulations (symbols) for recrystallized materials in the case of smooth tensile tests (a) and notched tensile tests (b). 70
3.19 Comparison of experiments (lines) and simulations (symbols) for T3 fibrous materials in the case of smooth tensile tests (a) and notched tensile tests (b). For clarity curves corresponding to the $T3F_{62}$ -NT_1 case have been shifted 100 MPa along the vertical axis. 71
3.20 Comparison of experiments (lines) and simulations (symbols) for T8 fibrous materials in the case of smooth tensile tests (a) and notched tensile tests (b) [25]. For clarity curves corresponding to the $T8F_{62}$ -NT_1 case have been shifted 100 MPa along the vertical axis. 72
3.21 Normalised Bron-Besson yield surface (dashed line) compared with von Mises criterion (solid line). BB-T8F: Bron-Besson yield surface for fibrous material T8F. R_0 is set to the yield stress in L-direction (σ_L^0). NT_1_L: path of L–loading notched flat sample NT_1, NT_1_T: path of T–loading notched flat sample NT_1, yielding in NT_1 sample correspond to each loading direction (L and T). 73
3.22 Experimental and simulated fracture path for L loading. 76
3.23 Experimental and simulated fracture path for T loading. 76
3.24 Experimental and simulated fracture path for D loading. 77

4.1 Specimen geometries of Kahn samples [5], Arcan samples [89] and M(T) samples [4] (all dimensions in mm). 83
4.2 (a) Setup of Kahn tear test (b) setup of mode I loading Arcan tear test, the crack growth is recorded by digital camera. 84

4.3 Kahn tear testing configurations (a) L-T loading (b) T-L loading and (c) D-D loading (L: rolling direction, T: long–transverse direction and D: diagonal direction in sheet plane). 85
4.4 Arcan tear tests loading angles Arcan-90° (a) Arcan-60° (b) Arcan-30° (c). 86
4.5 Setup of an Arcan mixed-mode loading specimen with Digital Image Correlation (DIC) device. 87
4.6 Experiments on Kahn tear tests in the case of $T3R_2$ material (a) and $T8R_2$ (b), nominal stress (F/S_0) as a function of the crack mouth opening displacement (CMOD). 88
4.7 Experiments on Kahn tear tests in the case of $T3F_6$ material (a) and $T8F_6$ (b), nominal stress (F/S_0) as a function of the crack mouth opening displacement (CMOD). 89
4.8 Arcan tests for 90° loading (a), and 60° loading samples (b), nominal stress (F/S_0) as a function of the crack mouth opening displacement (CMOD). 92
4.9 Arcan test for 90° loading (mode I) after 8 mm fatigue precracking, nominal stress (F/S_0) as a function of the crack mouth opening displacement (CMOD). 93
4.10 Schematic view of crack extension path for Kahn tear as function of material, loading configuration and thickness (dashed line represents the crack path profile in another side surface). 94
4.11 Schematic view of crack extension path for Arcan-90° tear tests (dashed line represents the crack path profile in another side surface). 95
4.12 Schematic view of crack extension path for Arcan-60° tear tests (dashed line represents the crack path profile in another side surface). 96
4.13 M(T) test results for two artificially aged materials $T8R_2$ (a), and T8F (b), nominal stress (F/S_0) as a function of the crack mouth opening displacement (CMOD). . . 97
4.14 Experiments on Kahn tear tests in the case of $T3F_t$ material (a) and $T8F_t$ material (b), nominal stress (F/S_0) as a function of the crack mouth opening displacement (CMOD). 98
4.15 Experiments on Kahn tear tests in the case of T8F material L-T loading with different specimen thicknesses, nominal stress (F/S_0) as a function of the crack mouth opening displacement (CMOD). 100
4.16 Variation of slant angle θ with specimen thickness 101
4.17 R-curve for AA2198 $T8R_2$ material (a), and AA2198 $T8F_{65}$ material (b). 102
4.18 Through-thickness cross sections in propagation regions of Kahn specimens tested along T-L orientation for all materials studied (*: θ taken at mid-thickness of cut section). Crack-growth direction is given by the outward normal to the plane of the paper. 104
4.19 Through-thickness cross sections in propagation regions of different thickness Kahn specimens tested along L-T orientation for T8 fibrous material (*: θ is the average value of angle taken over thickness). Crack-growth direction is given by the outward normal to the plane of the paper. 105
4.20 Macroscopic fracture surface of T8 fibrous ($T8F_6$) Kahn specimens tested along L-T orientation. 105
4.21 Typical fracture surface of Kahn and M(T) tear test samples. 106

4.22 SEM micrography of T3 recrystallized material ($T3R_2$) of Kahn specimens at flat and slanted regions. The left column refers to L–T loaded samples and the right one to T–L loaded samples. 107
4.23 SEM micrography of T8 recrystallized material ($T8R_2$) of Kahn and M(T) specimens tested in T-L orientation at flat and slanted regions. The left column refers to Kahn sample and the right one to M(T) sample. 109
4.24 SEM micrography of T8 fibrous material of Kahn and M(T) specimens tested in T-L orientation at flat and slanted regions. The left column refers to Kahn sample and the right one to M(T) sample (* sample thickness is 5 mm for M(T) specimens). . 110
4.25 SEM micrography of T3 fibrous material 2 mm and 6 mm thick Kahn specimens at flat and slanted regions. The left column refers to 2 mm thick Kahn sample and the right one to 6 mm thick Kahn sample. 111
4.26 Schematic depiction of arrested crack Kahn sample preparation for X-ray tomography assessment. 113
4.27 Reconstructed of 2D slice showing the entire 1x1 mm^2 section after gallium wetting. Crack growth direction is normal the image plane. 114
4.28 Two-dimensional section of tomography data showing the crack in T-L orientation for the T3 condition 2 mm-thick recrystallized material: (a) without gallium wetting; and (b) after gallium wetting. Crack-growth direction is given by the outward normal to the plane of the section 117
4.29 Two-dimensional section of tomography data showing the crack tip in T-L orientation for the T3 condition 2 mm-thick recrystallized material: (a) without gallium wetting; and (b) after gallium wetting. Crack-growth direction is given by the outward normal to the plane of the section 118
4.30 Two-dimensional section of tomography data showing the crack in T-L orientation for the T8 condition 2 mm-thick recrystallized material: (a) without gallium wetting; and (b) after gallium wetting. Crack-growth direction is given by the outward normal to the plane of the section 119
4.31 Two-dimensional section of tomography data showing the crack in L-T orientation for the T8 condition 6 mm-thick fibrous material: (a) without gallium wetting; and (b) after gallium wetting. Crack-growth direction is given by the outward normal to the plane of the section 120
4.32 Two-dimensional section of tomography data showing the crack in T-L orientation for the T8 condition 6 mm-thick fibrous material: (a) without gallium wetting; and (b) after gallium wetting. Crack-growth direction is given by the outward normal to the plane of the section 121
4.33 Two-dimensional section of tomography data showing the crack in L-T and T-L orientations for the T3 condition 6 mm-thick fibrous material: (a) L-T loading orientation; and (b) T-L loading orientation. Crack-growth direction is given by the outward normal to the plane of the section 122
4.34 Two-dimensional section of tomography data showing the crack in T-L orientation for the T8 condition 2 mm-thick sheet: (a) without gallium wetting; and (b) after gallium wetting. Crack-growth direction is given by the outward normal to the plane of the section 123

4.35 Fracture mode: inter-granular cracks vs. trans-granular cracking. 126

5.1 Representation of the physical fracture process by separation function within interface cohesive elements (after Schwalbe *et al.* [98]). 134
5.2 Various separation laws [124], (a) Dugdale [33]; (b) Barenblatt [10]; Hillerborg *et al.* [48] and other authors, brittle materials; (c) Needleman [75]; Tvergaard [111]; Chaboche *et al.* [24], ductile materials, polynomial equation; (d) Rose *et al.* (1981); Needleman [77, 78], exponential equation; (e) Tvergaard and Hutchinson [113]; Roy *et al.* [92], trapezoidal law; (f) Scheider [95]; 135
5.3 Traction-separation law used in the case of global Mode-I cohesive elements (flat fracture surface). 137
5.4 Scheider cohesive law [95] (a), and modified Scheider cohesive law for mixed-mode cohesive separation (b). 139
5.5 FE-mesh of Kahn specimen with straight flat fracture surface (a), magnification of the initial crack tip region and crack plane (b, c). 141
5.6 Typical mesh for analyses of M(T) specimen (2W=760 mm): (a) specimen geometry, (b) one-eighth symmetric mesh for FE-analyses, (c) local view of crack plane region with interface-cohesive elements. 142
5.7 Flat-to-slant fracture in thin aluminum sheet material. 143
5.8 FE-mesh for a Kahn specimen with flat-to-slant crack plane: (a) the global full mesh, (b) a local view focusing on the crack path region, and (c) a local view showing the transition flat-to-slant crack growth path. 144
5.9 Simulation results of elastic-plastic behaviour for Kahn tear test by fitted parameters on smooth tensile and notched tensile tests, dashed line represents simulation result by von Mises criterion. 146
5.10 Determination of the cohesive stress T_0 on a notched tensile specimen NT_2 for $T3R_2$ and $T8R_2$ materials. 147
5.11 Simulation results of Kahn tear tests by identified cohesive stress on notched tensile specimen and experimental Kahn tear test results for $T3R_2$ material in L-T and T-L loadings. 148
5.12 Simulation results of Kahn tear tests using $2.7\sigma_Y$ as cohesive stress T_0, and experimental Kahn tear test result for $T3R_2$ material in L-T loading. 148
5.13 Experimental Kahn tear test results and fitted ones for naturally aged $T3R_2$ material in L-T and T-L loadings. 149
5.14 Experimental Kahn tear test results and fitted ones for artificially aged $T8R_2$ material in L-T and T-L loadings. 149
5.15 Predicted and experimental load vs. opening displacement responses of M(T) tests for 2 mm-thick T8 recrystallized material ($T8R_2$) in L-T loading (a), and in T-L loading (b). 152
5.16 Buckling effect in 760 mm wide M(T) specimens after Bron [20] for an AA2024 thin sheet (sheet thickness is 1.74 mm). 153
5.17 Influence of cohesive strength (T_0^2) on global load vs. CMOD response for M(T) tests (a), and Kahn tests (b). 154
5.18 (a), fitted results of 2 mm-thick fibrous material ($T8F_{62}$) in L-T loading; (b), prediction result of 6 mm thick fibrous material ($T8F_6$) in the same loading. 155

5.19 Configuration of node release in 3D model with a ”constant” crack front, (a) initial mesh state, and (b) after nodes released (adapted after [42]). 157
5.20 Stress triaxiality ($\sigma_{\mathrm{m}}/\sigma_{\mathrm{flow}}$) in different layers of 2 mm-thick Kahn specimen as a function of the distance from the crack tip at a load just before crack initiation ($\Delta a = 0$). σ_{m} is the hydrostatic stress, σ_{flow} is the flow stress, ΔX is the distance from the crack tip. 159
5.21 Stress triaxiality ($\sigma_{\mathrm{m}}/\sigma_{\mathrm{flow}}$) in different layers of 6 mm-thick Kahn specimen as a function of the distance from the crack tip at a load just before crack initiation ($\Delta a = 0$). σ_{m} is the hydrostatic stress, σ_{flow} is the flow stress, ΔX is the distance from the crack tip. 159
5.22 Variation of stress triaxiality ($\sigma_{\mathrm{m}}/\sigma_{\mathrm{flow}}$) along the thickness at a load before crack initiation for 2 mm-thick Kahn specimen. Δx denotes the distance from the crack tip, Z is the distance from specimen's midsection (Z = 0). 160
5.23 Variation of stress triaxiality ($\sigma_{\mathrm{m}}/\sigma_{\mathrm{flow}}$) along the thickness at a load before crack initiation for 6 mm-thick Kahn specimen. Δx denotes the distance from the crack tip, Z is the distance from specimen's midsection (Z = 0). 160
5.24 Variation of out-of-plane stress (σ_{33}) as a function of accumulated plastic strain for 2-, 3-, 4- and 6 mm-thick Kahn specimens (data taken at 1 mm ahead of the crack tip of midsection). 162
5.25 Variation of out-of-plane stress (σ_{33}) as a function of accumulated plastic strain for 2-, 3-, 4- and 6 mm-thick Kahn specimens (data taken at 5 mm ahead of the crack tip of midsection). 162
5.26 Variation of out-of-plane stress (σ_{33}) as a function of loading time for 2-, 3-, 4- and 6 mm-thick Kahn specimens (data taken at 1 mm ahead of the crack tip of midsection). 163
5.27 Variation of out-of-plane stress (σ_{33}) as a function of loading time for 2-, 3-, 4- and 6 mm-thick Kahn specimens (data taken at 5 mm ahead of the crack tip of midsection). 163
5.28 Variation of stress triaxiality ($\sigma_{\mathrm{m}}/\sigma_{\mathrm{flow}}$) at crack tip (0 mm) and (5 mm away from the crack tip) as a function of the crack mouth opening displacement (CMOD) for 2 mm-thick Kahn specimen (a) and 1.74 mm-thick Kahn specimen (b)([21]) (data taken at midsection of specimen). 165
5.29 Variation of stress triaxiality ($\sigma_{\mathrm{m}}/\sigma_{\mathrm{flow}}$) at crack tip (0 mm) and (5 mm away from the crack tip) as a function of the crack mouth opening displacement (CMOD) for 4 mm-thick (a) and 6 mm-thick (b) Kahn specimens (data taken at midsection of specimen). 165

6.1 New design of Arcan specimen used for mixed-mode loading proposed by Madi *et al.* [64]. 175

A.1 Smooth tensile specimen ST_{12} (dimension in mm). 193
A.2 Notched tensile specimen NT_1 (dimension in mm). 194
A.3 Notched tensile specimen NT_2 (dimension in mm). 195
A.4 Kahn tear test specimen (dimension in mm). 196
A.5 Arcan tear test specimen (dimension in mm). 197

A.6 Center-cracked tension test specimen M(T) (dimension in mm). 198

B.1 . Tensile tests on ST_{12} specimens along L, T and D directions for the $T3R_2$ and $T8R_2$ materials at three different strain rates. 200
B.2 . Tensile tests on ST_{12} specimens along L, T and D directions for the $T3F_6$ and $T8F_6$ materials at three different strain rates. 201
B.3 . Normalized force (F/S_0) as a function of Notch Opening Displacement (NOD) of NT_1 specimens along L and T directions for the $T3R_2$ and $T8R_2$ materials. 202
B.4 . Normalized force (F/S_0) as a function of Notch Opening Displacement (NOD) of NT_2 specimens along L, T and D directions for the $T3R_2$ and $T8R_2$ materials. . . 203
B.5 . Normalized force (F/S_0) as a function of Notch Opening Displacement (NOD) of NT_1 specimens along L and T directions for the $T3F_6$ and $T8F_6$ materials. 204
B.6 . Normalized force (F/S_0) as a function of Notch Opening Displacement (NOD) of NT_2 specimens along L, T and D directions for the $T3F_6$ and $T8F_6$ materials. . . . 205
B.7 . Normalized force (F/S_0) as a function of the Crack tip Mouth Opening Displacement (CMOD) of Kahn tear tests along L–T and T–L loadings for the $T3R_2$ and $T8R_2$ materials. 206
B.8 . Normalized force (F/S_0) as a function of the Crack tip Mouth Opening Displacement (CMOD) of Kahn tear tests along L–T and T–L loadings for the $T3F_6$ and $T8F_6$ materials. 207
B.9 . Normalized force (F/S_0) as a function of the Crack tip Mouth Opening Displacement (CMOD) of Kahn tear tests along L–T and T–L loadings for $T3F_{62}$ and $T8F_{62}$ materials. 208

List of Tables

2.1 Possible precipitates and their forms in Al-Li-Cu system. 25
2.2 Chemical composition limits of AA2198 in weight percent (wt. %) and atomic percent (at. %). 29
2.3 Nomenclature of materials studied. 31

3.1 Room temperature tensile properties of tested materials ($T3R_2$, $T8R_2$, $T3F_6$ and $T8F_6$) along L, T and D directions. (YS: yield strength for 0.2% plastic strain (MPa), UTS: ultimate tensile strength (MPa), UE: uniform elongation (%), $\mathcal{L}_k$: Lankford coefficient for a plastic deformation of 5%. 52
3.2 Strain rate sensitivity SRS (MPa) for different tested materials along different loading direction at room temperature (293 K). The data is calculated at 6 % plastic strain. 56
3.3 Parameters identified for elastic behaviour and work hardening (Young modulus (in GPa) is pre-fixed, R_0 (in MPa) is set to the yield stress in rolling direction (L) for each material). 69
3.4 Parameters describing anisotropic yielding and plastic flow ($c_{i=1,2}^{5,6}$ were set a priori to 1 for thin sheets). 69

4.1 Unit initiation energy (UIE) (N/mm) of Kahn tear tests for recrystallized materials and fibrous materials with different specimen thicknesses and loading orientations (L–T and T–L). 90
4.2 Validity of Kahn tear tests and presence of pop-ins during tests. 91

5.1 Tear specimens investigated by FE-simulations. 140
5.2 Fitted cohesive zone parameters and tear properties for T3 and T8 recrystallized materials ($T3R_2$ and $T8R_2$). 150

Chapter 1

Introduction

1.1 Industrial background and motivations

Aluminum alloys have been widely used for a long time in aerospace industry. Nowadays, increasing payload and fuel efficiency of aircraft has become a major issue for the aerospace industry. This has lead to the development of very high strength 7xxx alloys (e.g. 7075, 7150, 7055 and 7449), very high damage tolerant 2xxx and 6xxx alloys (e.g. 2024 and its variants, 2056, 6013 and 6056) [35, 118]. The latest and upcoming generation of Al-Cu-Li alloy has received much attention for military, space and commercial application because they offer low density, improved specific strength, damage tolerance and high stiffness to weight ratio as compared to the conventional commercial 2xxx and 7xxx series aluminum alloys [39, 57]. The marriage of Li to Al offers the promise of substantially reducing the weight of aeronautic alloys, since each 1 wt. % Li added to Al reduces density by 3 % and increases elastic module by about 6 %. Second generation Al-Li alloys, including 2090, 2091 and 8090, all contain Li in more than 2 % concentrations. Although these alloys have the desired lower density, higher modulus and improved fatigue resistance, they also exhibit lower ductility and fracture toughness in the short-transverse (S-T) direction [51]. Facing the competition of composite materials in the aeronautic industry, recent alloy developments have produced

a new generation of Al-Cu-Li alloys which contain less than 2 % Li and have a higher Cu/Li ratio than the second generation alloys (2090, 2091 and 8090) with a trademark AIRWARE^{TM}. Among these alloys, 2198 Al-Cu-Li alloy, shows a good combination of static tensile properties, damage tolerance and formability. For this reason, they have been considered for the application of fuselage of new generation commercial airplanes.

1.2 Research objectives

This work is part of a project called "ALICANTDE"[1] aiming at investigating damage tolerance of the current Al-Cu-Li alloys for aeronautic application, better understand the relationship between microstructure evolution and damage tolerance properties. This project is divided into three main research subjects.

The first one concerns the study of precipitation in Al-Cu-Li alloys and investigation of the relationship between microstructure and mechanical properties. This work has been accomplished by B. Decreus at SiMAP research center of Insitute Polytechnique de Grenoble.

The second one started at the same time as present work; it deals with the fatigue behaviour of Al-Cu-Li alloys. This work is carried out by S. Richard at LMPM of ENSMA Poitiers.

The third one is the present work and aims at the study of plastic anisotropy , thickness effect and ductile tearing behaviour of Al-Cu-Li alloys. In this study, four different Al-Cu-Li thin sheet materials are investigated experimentally and numerically. The material microstructure was examined by optical micrographs and transmission electron microscopy. Initial void volume fraction and intermetallic particles content are characterized qualitatively via X-ray micro-tomography. Tensile tests are carried out on flat smooth and flat U-notched (with various notch radii) specimens along different direction; tear tests are conducted on small sized Kahn specimens, mixed-mode load-

[1] Aluminium-Lithium pour Constructions Aéronautiques Tolérants aux Dommages

ing Arcan specimens and large M(T) panels. A model describing plastic anisotropy and isotropic hardening is fitted on smooth tensile and notched tensile tests. The macroscopic and microscopic fracture surfaces of the different specimens is observed in detail and fracture micromechansims are analyzed using scanning electron microscopy and high resolution X-ray tomography. Finally cohesive zone model is used to model ductile tearing behaviour of tested materials, transferability from small sized Kahn tests to large M(T) tests is checked by numerical simulations.

1.3 Structure of this thesis

The present thesis consists of five chapters and two appendices. Chapter 1 gives industrial background of development of Al-Cu-Li type alloys, motivations of research project, defines also research objectives and presents an outline of the thesis.

Chapter 2 describes in detail the materials studied, microstructure characterization results by optical microscopy, Transmission Electron Microscopy and X-ray tomography.

Chapter 3 is devoted to the materials' plastic anisotropic behaviour. Mechanical test results and fractography of tested samples are shown and analysed in detail in this chapter for smooth and notched tensile specimens. Thickness effect on plasticity and ductility is shown via experimental test results on different thick specimens. Dynamic strain ageing effect is checked at room temperature and high temperature. The identification of plastic anisotropy and analysis of strain localisation are also addressed in this part.

Chapter 4 deals with materials' ductile tearing behaviour. Three different tear tests including small Kahn specimens, mixed-mode loading Arcan samples and large panel M(T) specimens are used. Thickness effect on fracture toughness was examined via Kahn specimens. The fractography of broken Kahn and M(T) specimens are examined in detail via Scanning Electron Microscopy. X-ray tomography observations are carried out on different arrested Kahn tests including a gallium

wetting treatment.

Chapter 5 presents modeling results of ductile tearing tests by cohesive zone methods on small Kahn tests and large M(T) panels. The transferability between different specimen geometry and specimens thickness is also addressed. Thickness effect are examined by simulation of different thick specimens via a special node release technique on Kahn samples.

Finally, the first appendix gives all specimens dimensions used in this work and the second appendix provides all mechanical test results carried out in this study.

1.4 Résumé

Contexte industriel et motivation de l'étude

Depuis les années 30, les alliages d'aluminium sont largement utilisés pour les structures aéronautiques, grâce notamment à une combinaison entre les propriétés mécaniques élevées et les caractéristiques d'emploi (capacités de mise en œuvre). Aujourd'hui, l'augmentation de la charge utile associée aux économies de carburant est devenue un enjeu industriel majeur dans l'aéronautique. Ceci a abouti aux développements des alliages d'aluminium à haute résistance de série 7xxx (eg. 7075, 7150, 7055 et 7449), des alliages d'aluminium à haute tolérance aux dommages de séries 2xxx et 6xxx (eg. 2024 et ses variantes, 2056, 6013 et 6056) [35, 118]. Les nouveaux alliages d'aluminium-cuivre-lithium ont reçu récemment beaucoup d'attention pour les applications aérospatiales, les principales raisons sont liées à la réduction de la densité et à l'augmentation de la résistance par rapport aux alliages conventionnels 2xxx et 7xxx [39, 57]. En effet, incorporé du lithium dans l'aluminium permet à la fois une baisse de la densité et une augmentation du module d'Young : l'ajout de 1% massique de lithium permet une réduction de la densité de l'alliage de 3% et une augmentation du module élastique de 6%. La deuxième génération d'alliages Al-Li (2090, 2091 et 8090 à titre d'exemple) comporte une teneur en lithium de plus

de 2%. Bien que ces alliages aient une densité plus faible, un module élastique plus élevé et une résistance à la fatigue améliorée, ils présentent une ductilité assez faible, une ténacité réduite dans la direction de travers-court (T-S) [51], et une anisotropie marquée. Aujourd'hui, confrontés à une forte compétitivité avec les matériaux composites dans le domaine aéronautique, les métallurgistes ont développé une nouvelle génération d'alliage Al-Cu-Li comportant moins de 2% de lithium et une teneur en cuivre encore plus élevé que les alliages de deuxième génération (2090, 2091 et 8090) : les alliages à basse densité sont commercialisés chez ALCAN sous le label technologique $AIRWARE^{TM}$. Parmi ces alliages, l'alliage Al-Cu-Li 2198 présente un meilleur compromis entre les propriétés statiques, la tolérance aux dommages et la formabilité que les autres alliages d'aluminium conventionnels. Cet alliage a notamment été choisi pour la réalisation du fuselage des avions commerciaux de la nouvelle génération.

Objectif de la recherche

La présente étude fait partie du projet ANR dénommé ALICANTDE (Aluminium-Lithium pour Constructions Aéronautiques Tolérants aux Dommages) visant à mieux comprendre la relation entre l'évolution de microstructure des matériaux et la tolérance aux dommages. Ce projet de recherche se divise en trois grandes parties. La première partie concerne l'étude de la précipitation dans les alliages Al-Cu-Li et la relation entre microstructures et propriétés mécaniques. Cette étude a été conduite par B. Decreus au centre de recherche SiMAP de l'Institut Polytechnique de Grenoble. La deuxième partie porte sur la résistance à la fatigue d'alliages Al-Cu-Li de la troisième génération. Cette partie a commencé en même temps que l'étude actuelle. Elle est effectuée par S. Richard au LMPM d'ENSMA Poitiers. La troisième partie est l'étude actuelle visant à étudier l'anisotropie plastique, l'effet d'épaisseur et la déchirure ductile dans les alliages Al-Cu-Li. Dans cette étude, quatre différentes tôles d'alliage Al-Cu-Li sont examiné au travers d'essais expérimentaux et de simulations numériques. La microstructure des matériaux est caractérisée par

le microscope optique et le microscope électronique en transmission (MET). La fraction volumique de vides et de particules intermétalliques des matériaux est quantifiée via la tomographie à rayon X. Les essais de traction sont effectués sur les éprouvettes de traction lisse et entaillée selon différentes directions de sollicitation. Les essais de déchirure sont réalisés sur des éprouvettes de petite taille Kahn, des éprouvettes chargées en mode mixte Arcan et des grandes plaques M(T). Un modèle décrivant l'anisotropie plastique et l'écrouissage isotrope est utilisé, identifié sur la base des essais de traction lisse et entaillée. Les faciès de rupture de différentes éprouvettes sont examinés minutieusement au niveau macroscopique et microscopique. Le mécanisme de rupture est analysé via le microscope électronique à balayage (MEB) et la tomographie à rayon X. Enfin, un modèle de zone cohésive est proposé pour modéliser le comportement à la déchirure ductile des matériaux. La transférabilité entre l'éprouvette de petite taille Kahn et de grande taille M(T) est examinée par simulation numérique.

Structure du mémoire

Le mémoire de thèse se compose de six chapitres et deux annexes. Le chapitre 1 fournit brièvement le contexte industriel des développements d'alliages aluminium-cuivre-lithium, les motivations de la recherche et les objectives de cette étude. Le plan du mémoire est aussi présenté dans cette partie. Le chapitre 2 présentera en détail les matériaux de l'étude, la caractérisation multi-échelle de la microstructure par les techniques suivantes : microscopie optique, microscopie électronique en transmission (MET) ou encore la tomographie à rayon X. Le chapitre 3 sera consacré au comportement anisotrope plastique des matériaux. Les essais mécaniques et les faciès de rupture seront analysés et comparés minutieusement dans ce chapitre pour les éprouvettes de traction lisse et entaillée. L'effet d'épaisseur sur la plasticité et la ductilité seront examinés via les résultats expérimentaux sur les éprouvettes de différentes épaisseurs. Le vieillissement dynamique est abordé au travers d'essais de traction à différentes vitesses. L'identification de l'anisotropie

plastique et l'analyse de la localisation de déformation seront aussi présentés dans ce chapitre. Le chapitre 4 se chargera du comportement en déchirure ductile des matériaux. Trois différents types d'éprouvettes (Kahn, Arcan et M(T)) seront utilisés. L'effet d'épaisseur sur la ténacité sera examiné via les éprouvettes Kahn. Les faciès de rupture des éprouvettes Kahn et M(T) seront analysés en détail via la microscopie électronique à balayage (MEB). Les observations de tomographie en haute résolution à rayon X seront effectuées sur les essais Kahn interrompus y compris un traitement de gallium pour mettre en évidence la structure granulaire. Le chapitre 5 décrira l'analyse et les résultats de la modélisation de la déchirure ductile en utilisant un modèle de zone cohésive pour les essais Kahn et M(T). La transférabilité entre les éprouvettes de géométries différentes et d'épaisseurs différentes sera également discutée dans cette partie. L'effet d'épaisseur sera examiné par la simulation éléments finis via une technique de relâchement de nœuds sur les éprouvettes Kahn. Enfin, le chapitre 6 donnera les conclusions et les perspectives de cette étude.

L'annexe 1 donne les dimensions d'éprouvettes utilisées dans ce travail et l'annexe 2 fournira tous les résultats des essais mécaniques effectués dans cette étude.

Chapter 2

Materials and Microstructure

In this chapter we will start by a brief introduction of aluminium-copper-lithium alloys. To facilitate discussion on materials' microstructure, we give a short description of literature survey on metallurgical considerations of Al-Cu-Li alloys and their typical microstructures. Then we will present the materials studied and heat treatments applied in this work. The material microstructure was characterized by various techniques including optical metallographic observation, transmission electron microscopy and X-ray tomography assessment.

2.1 Introduction

2.1.1 Al-Cu-Li alloys

Aluminium-Copper-Lithium alloys are attractive for aerospace applications because they combine strength and damage tolerance along with an increase of the modulus of aluminium and reduction of the density. Each 1 wt % of lithium increases the modulus by about 6% while decreasing the density about 3% [35, 118]. However, the early promise of property improvements with Al-Cu-Li alloys has not been realized. Even the second generation alloys, which contained around 2% lithium, that came out in the 1980s, experienced a number of serious technical prob-

lems: excessive anisotropy in the mechanical properties; lower than desired fracture toughness and ductility; hole cracking and delamination during drilling. The anisotropy found in these alloys is associated with the strong crystallographic textures that develop during processing, with the fracture toughness problem being one of primarily low strength in the short-transverse (S-T) direction [51]. To circumvent some of these problems, a new generation of alloys has been developed with lower lithium contents. As illustrated in Fig. 2.1, these alloys are generally of a higher Cu/Li ratio than the second generation alloys (2090 and 2091 illustrated in this figure). The factors underlying the choice of Cu and Li concentrations in these T_1 (Al_2CuLi) precipitate strengthened alloys are illustrated schematically in Fig. 2.2.

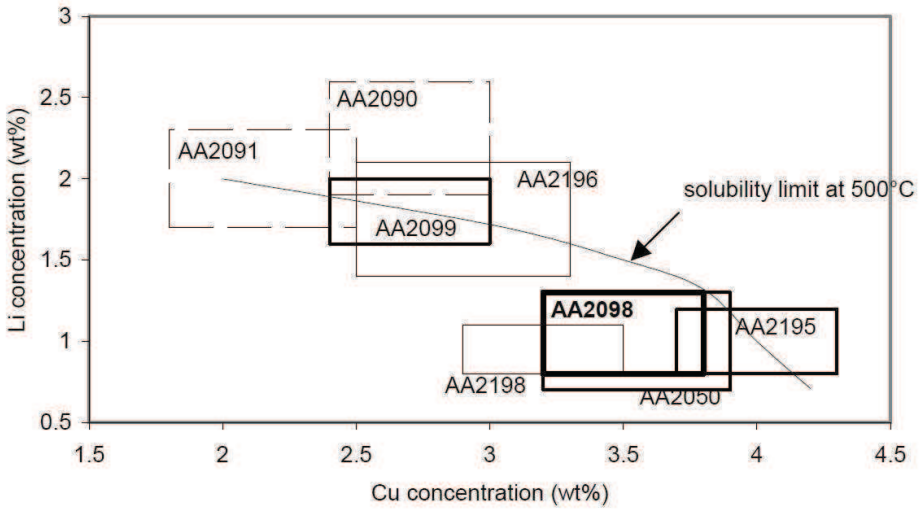


Figure 2.1: Content of Cu and Li in the new generation Al-Cu-Li alloys (2098, 2198 and 2050), compared to second generation Al-Cu-Li alloys 2091 (Al-Li-Cu-Mg-Zr) and 2090 (Al-Cu-Li-Zr). The second generation alloy are presented as dashed boxes, the third generation as solid boxes (after Warner.,[118]).

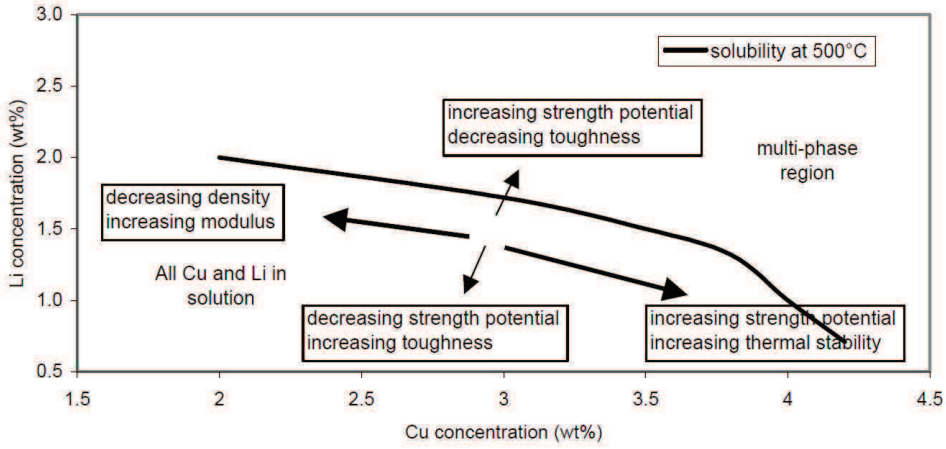


Figure 2.2: Schematic illustration of some key property variations as a function of Cu and Li concentration in Al-Cu-Li alloys (after Warner., [118]).

2.1.2 Metallurgical considerations

According to Cu and Li content, there are a variety precipitation reactions occurring in Al-Cu-Li alloys. For Cu in the range 2 to 5%, three main hardening precipitates can be found.

- For low Li contents ($\leq$ 0.6%) the non-shearable Ω (Al_2Cu) phase is present in the presence of silver [60].

- For medium Li content ($\leq$ 1.0-1.5%) the main hardening phase is T_1 (Al_2CuLi) [38]. The hardening effect of this phase is very large and it is promoted by the addition of Cu. T_1 can heterogeneously nucleate on subgrain boundaries and dislocations. Its nucleation and growth are favored by the limited addition of Mg and Ag and dislocations formed through cold work prior to artificial aging [22].

- For high Li contents ($\geq$ 1.4-1.5%) δ' (Al_3Li) phase also precipitates during artificial aging and contributes to strengthening but to a lesser extent than T_1 [49]; its presence can be detrimental to toughness. Heavy precipitation of this δ' phase is also reported during long thermal

exposure, (e.g., 1000 h at 85°C), and may lead to long-term stability issues, if not properly taken into account in the alloy design.

Fig. 2.3 displays the various precipitates observed by Silcock [102] in Al-Cu-Li alloys according to its Cu and Li contents. Table 2.1 lists the possible precipitates and their form in Al-Li-Cu system. While the Fig. 2.4 gives a schematic view of precipitates and dispersoids that contribute to strength and toughness in AA2099 and AA2199 alloys after Giummarra et al. [39].

Precipitate	Composition	Form
δ'	Al_3Li	plate
θ'	Al_2Cu	plate
S	Al_2CuMg	sticks
Ω	Al_2Cu	plate
T_1	Al_2CuLi	plate

Table 2.1: Possible precipitates and their forms in Al-Li-Cu system.

2.1.3 Dispersoids and Precipitate free zones

In aluminium alloys, Manganese (Mn) is often added to form $Al_{20}Cu_2Mn_3$ incoherent dispersoids as illustrated in Fig. 2.5b. The role of this phase is to help homogenize slip and thereby improve damage tolerance with regards to fracture toughness and fatigue [28]. Mn-bearing dispersoids also help to control grain size and texture evolution during thermo-mechanical processing. Zirconium (Zr) is added to form the coherent β' (Al_3Zr) dispersoid (see Fig. 2.5a). This is the main dispersoid used to control recrystallization. In aluminium-lithium, the strengthening δ' (Al_3Li) phase also precipitates epitaxialy on the surface of Al_3Zr dispersoids [40, 108].

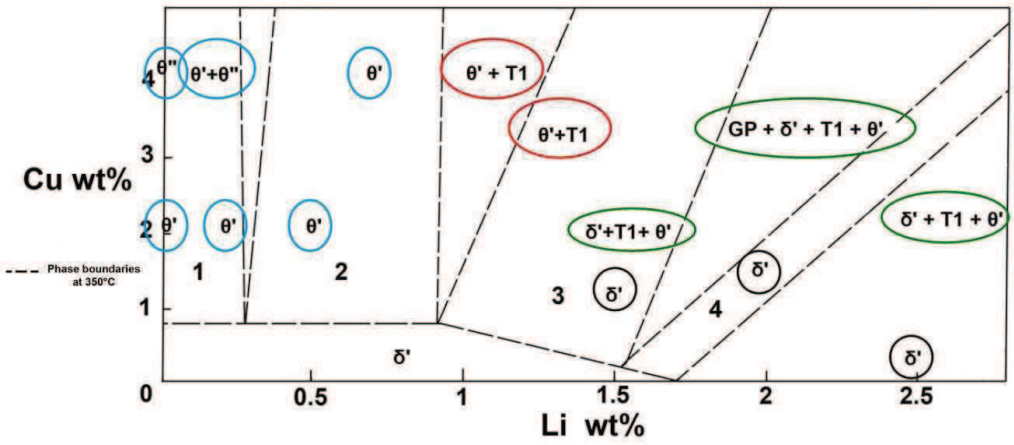


Figure 2.3: Observed precipitates in different Al-Cu-Li systems according Cu and Li contents. (after Silcock., J.M., [102])

Precipitate free zones (PFZ) are commonly situated around grain boundaries as illustrated in Fig. 2.6 observed by Özbilen [79] in an artificially aged Al-Li-Cu-Mg-Zr alloy. The PFZ's may appear in all alloys where precipitation reactions occur. Precipitate free zones (or PFZ's) occur for two reasons [84]: Firstly, the most common reason for the formation of PFZ's is that precipitates nucleate heterogeneously on vacancies. A grain boundary is a sink for vacancies so that regions adjacent to the boundary are unable to nucleate the precipitates, even though the matrix may be supersaturated with solute. The second reason is the grain boundaries themselves are potent heterogeneous nucleation sites. Particles may nucleate first at these boundaries, thereby removing sufficient solute from the adjacent matrix. The solute-depleted region in the proximity of the boundary therefore remains precipitate-free.

PFZs may be detrimental for the mechanical properties of a material as well as for corrosion resistance. The yield strength of the PFZ is significantly lower than that of the main matrix. As such, strain concentrations may then occur in PFZs which may result in premature failure, which will especially influence fracture toughness [116].

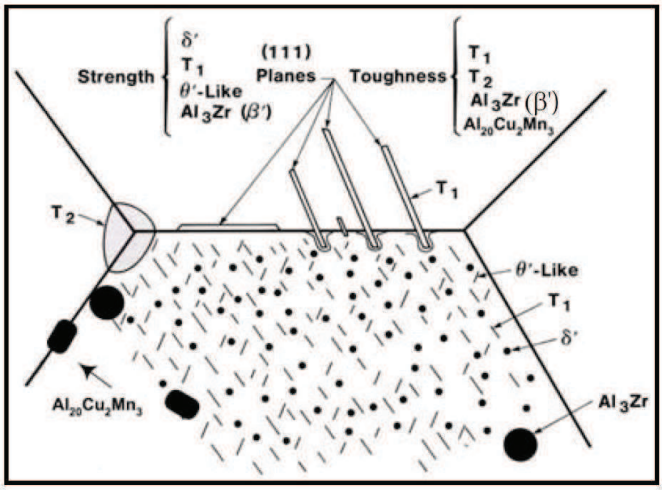


Figure 2.4: Schematic of precipitates and dispersoids that contribute to strength and toughness in 2099 and 2199 Al-Cu-Li alloys (after Giummarra et al., [39]).

2.1.4 Constituent phases

In aluminium alloys for structural applications, the coarse intermetallic particles (Al_7Cu_2Fe and Mg_2Si) form during ingot solidification. These intermetallic particles are detrimental to corrosion, fatigue and fracture toughness. A lower volume fraction of intermetallic compounds improve fracture toughness and fatigue behaviour. For example, the maximum iron content is 0.12% and silicon is 0.10% in 2224 as compared to 0.50% for both impurities in 2024. Due to the high cost of complete removal, these impurities are often limited in a certain range.

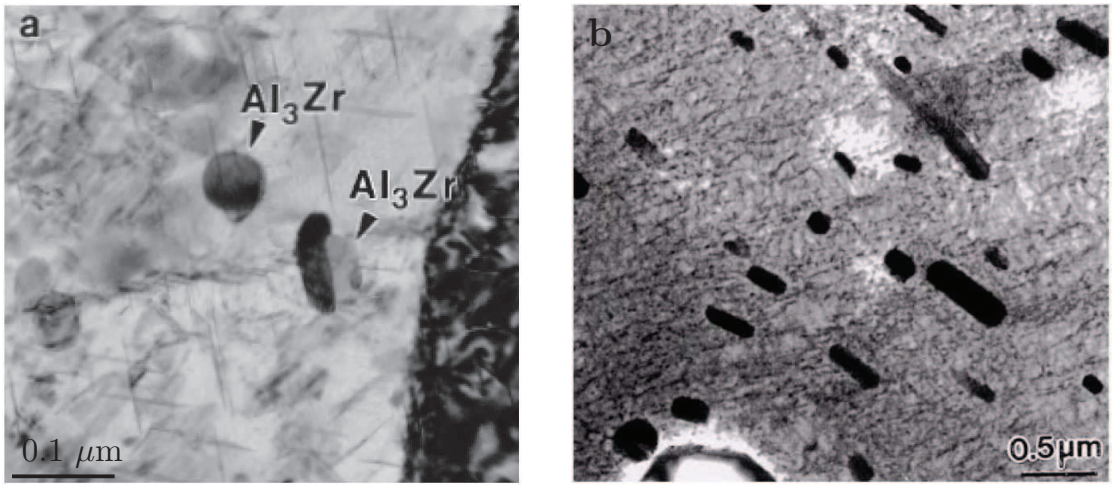


Figure 2.5: TEM micrograph of Zr containing dispersoid particles (a) and Mn containing dispersoid particles (b). The figure (a) refers to an Al-4.8Cu-0.45Mg-0.39Ag-0.14Zr alloy and the figure (b) refers to an Al-4.9Cu-0.46Mg-0.38Ag-0.32Mn alloy (after Cho et Bès, [26]).

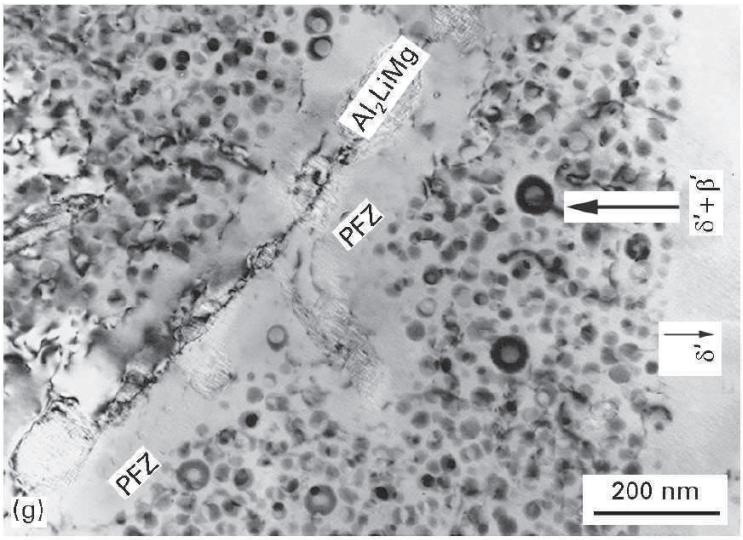


Figure 2.6: TEM micrograph of Al-2.3Li-1.8Mg-0.15Zr-0.1Cu alloy associated with a clear PFZ. (after Özbilen., [79]).

2.2 Materials studied

AA2198 is a new aluminium-copper-lithium alloy which was developed by the aluminium manufacturer Alcan. It is a candidate alloy for fuselage skins and some components of wings for future commercial aircraft. Table 2.2 gives the chemical composition limits of AA2198 alloy in weight percent and in atomic percent. AA2198 has lower Lithium content and higher copper content than the first and the second generation Al-Li alloys. The general trend in the Al-Li alloy development is higher copper and lower lithium content than previous Al-Li alloys [57]. The objective of this composition adjustment is to optimise the toughness and strength. It is important to note that the Lithium content of AA2198 in atomic percent is much higher than it's weight percent. Lithium is the major alloying element when considering atomic percentage.

	Cu	Li	Zn	Mn	Mg	Zr	Si	Ag	Fe
wt. %	2.9-3.5	0.8-1.1	$\leq$0.35	$\leq$ 0.5	0.25-0.8	0.04-0.18	$\leq$ 0.08	0.1-0.5	$\leq$ 0.01
at. %	1.23-1.48	3.11-4.26	$\leq$0.14	$\leq$ 0.25	0.28-0.88	0.01-0.05	$\leq$ 0.08	0.02-0.06	$\leq$ 0.05

Table 2.2: Chemical composition limits of AA2198 in weight percent (wt. %) and atomic percent (at. %).

For this work, two grades of 2198 aluminium-lithium alloy sheets with a nominal thickness of 2 mm (recrystallized sheet materials) and 6 mm (fibrous sheet materials) were supplied by Alcan Centre de Recherches de Voreppe (Alcan CRV). They are referred respectively to as R (Recrystallized sheet materials) and F (Fibrous sheet materials) (see Table 2.3). For each grade, two different heat treatment conditions T351 and T851 were studied. Fig. 2.7 shows the heat treatment sequence applied to materials studied. All sheets are first solution heat treated, stretched by between 2-4% and naturally aged to obtain T351 condition materials, then an artificial ageing step was applied to achieve T851 temper materials.

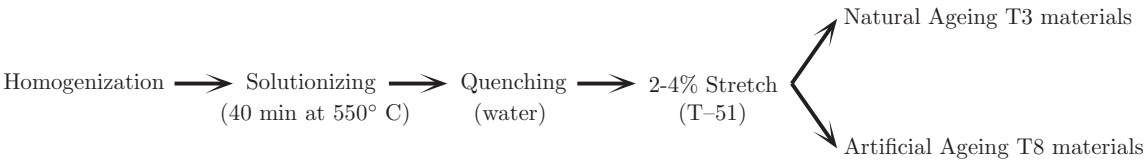


Figure 2.7: Two different heat treatment sequences applied to each grade (recrystallized sheet and fibrous sheet).

For both 6 mm-thick fibrous materials, sheets having a thickness of 2 mm were prepared by slicing the 6 mm sheet into two halves using electrical discharge machining. Each slice was then machined down on both sides to reduce the thickness to 2 mm as proposed in [81, 3] to study thickness effect on plasticity and fracture behaviour. Combining heat treatments and thicknesses results in six different sheets for which a nomenclature is proposed in Table 2.3. For brevity, heat treatment T351 will be identified as T3 and T851 identified as T8 in the following, T–51 corresponds to a mechanical treatment (stress relieved by stretching) which was applied after quenching in our case. The difference between recrystallized sheets and fibrous sheets is not only in it's sheet thickness but also in grain structure which can be seen in the following (cf. section 2.3.2). Thin recrystallized sheets are formed by cold rolling while thick fibrous sheets are by hot rolling. Cold rolling is conducted at temperature below the recrystallization temperature, while hot rolling is above the recrystallization temperature to create a finer grain size and less grain directionality.

2.3 Material microstructure

2.3.1 Definition of processing directions

The materials under study are rolled sheets, due to process of rolling which may create an anisotropic microstructure for sheet metal, it is important to define different processing directions

Material	Heat treatment	Grain structure	Thickness (mm)
$T3R_2$	T351	recrystallized	2
$T8R_2$	T851	recrystallized	2
$T3F_6$	T351	fibrous	6
$T3F_{62*}$	T351	fibrous	2
$T8F_6$	T851	fibrous	6
$T8F_{62*}$	T851	fibrous	2

* 6 mm sheet machined down to 2 mm in thickness

Table 2.3: Nomenclature of materials studied.

for the following studies. The Fig. 2.8 shows the definition of the different directions of our sheet material:

- L: rolling direction,
- T: long–transverse direction,
- S: short–transverse direction (thickness direction),
- D: diagonal direction (45° between L direction and T direction in the sheet plane).

2.3.2 Optical micrographs

Micrographs of grain structure were obtained by optical microscopy. Specimens were prepared following a standard metallographic procedure used for rolled-sheet materials: i.e., three samples were taken from L–T, L–S and T–S planes for each material, grinding with SiC papers, polishing with 3 and 1 μm diamond paste. The etching was carried out using a Keller's solution of

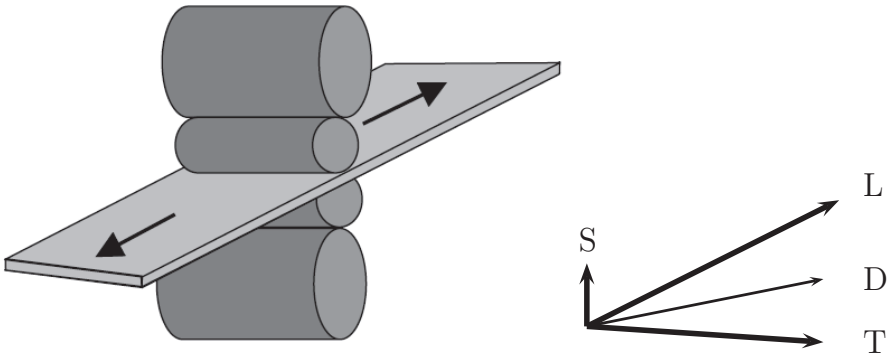


Figure 2.8: Definition of L (rolling direction), T (long–transverse direction), S (short–transverse direction) and D (diagonal direction) of the sheet material in this study.

5% hydrofluoric acid (HF), 10% sulfuric acid (H_2SO_4) and 85% water for 30 seconds. Specimens were examined using a PME Olympos, Tokyo optical microscope.

Representative grain structures are shown in Fig. 2.9 for the 2 mm-thick recrystallized material and in Fig. 2.10 for the 6 mm-thick fibrous material. Large pan-cake shaped grains can be found in L–T plane which is typical for a as-rolled sheet metal (see Fig. 2.9 in L-T plane), it is also shown that the pan-cakes are more equiaxed in recrystallized than that in fibrous materials (see Fig. 2.10 in L-T plane). In L–S and T–S planes grains are elongated along L and T direction respectively, constituent particles (Fe, Si) can be seen aligned along rolling direction. The grain size was measured by using a mean linear intercept method as 200-300 μm along rolling direction (L), 60 μm in long transverse–direction (T) and 25-30 μm in short–transverse direction (S) for recrystallized sheet, 10-15 μm for fibrous sheet. Note that fibrous material exhibits more elongated and thinner grains than recrystallized material. Grains of the fibrous material can reach more than 1000 μm along the L direction and only 10-15 μm along the S-direction. For both materials, images taken from different positions along thickness direction (S) show that there is no grain size gradient, the material can be considered as homogeneous across the thickness. Observation results also show that there are no significant differences in grain structure between T3 condition and T8 condition

for each grade (R and F sheets), so the microstructures were showed for T3 condition materials only.

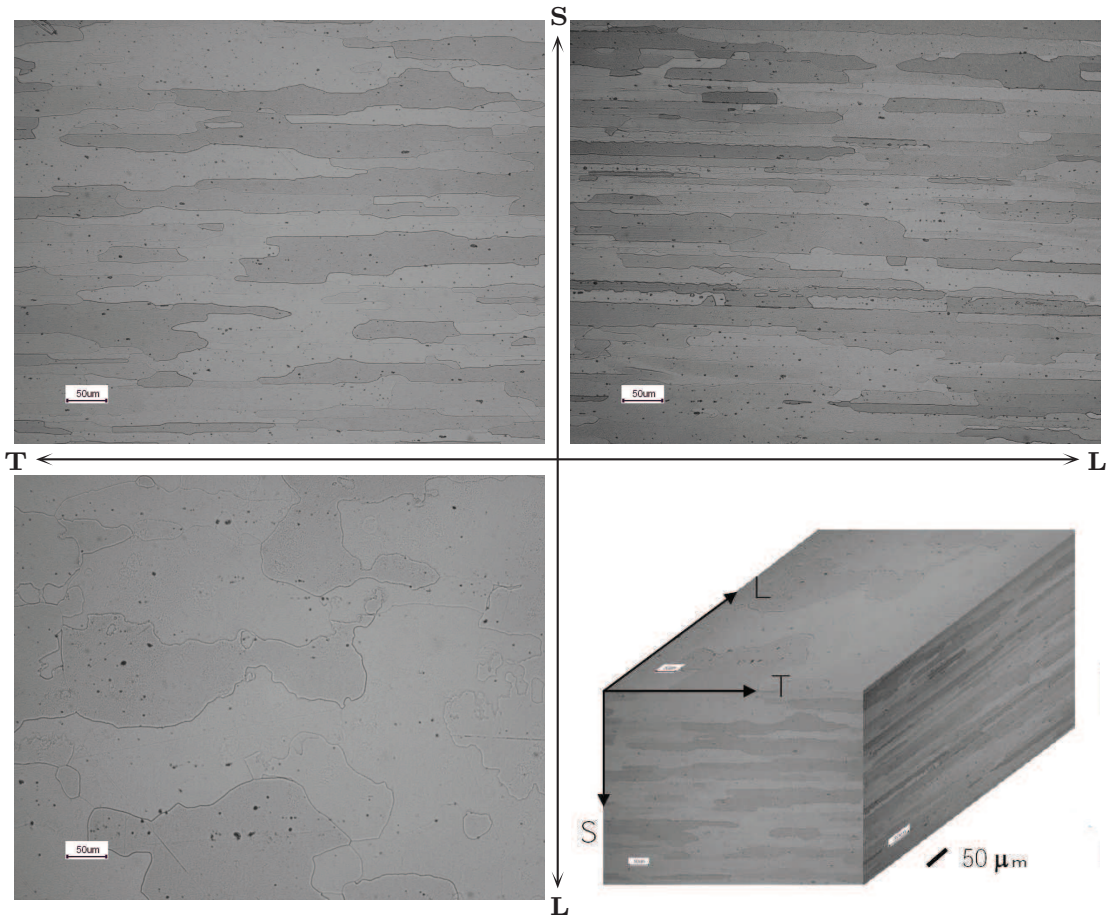


Figure 2.9: Optical micrographs of the AA2198-T3 2 mm-thick recrystallized material in TS, LS, LT planes and pseudo-3D grain structure. (L: rolling direction, T: long transverse direction and S: short transverse direction).

2.3.3 Transmission Electron Microscopy (TEM)

Transmission electron microscopy was used to characterize the inter-granular and trans-granular precipitates. The observations were performed at 200 kV using a TECNAI F20-ST Microscope on both fibrous materials ($T3F_6$ and $T8F_6$). For each material, a 3 mm diameter cylinder

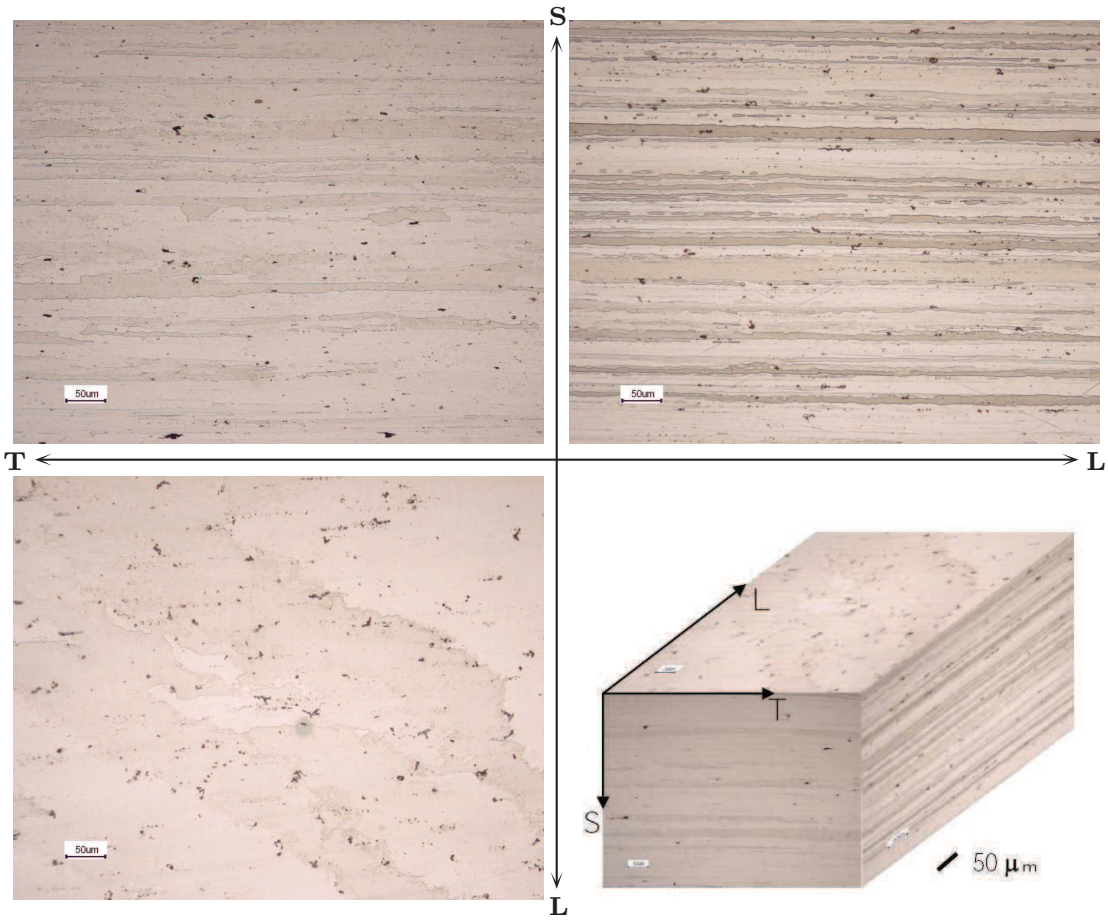


Figure 2.10: Optical micrographs of the AA2198-T3 6 mm-thick fibrous material in TS, LS, LT planes and pseudo-3D grain structure. (L: rolling direction, T: long transverse direction and S: short transverse direction).

was prepared by electrical discharge machining and then cut to thin slices (∼0.3 mm). To ensure the success of investigation, six samples were prepared for each material. Then the slices were manually polished down to a thickness of 120 μm and finally reduced by electro-polishing using a solution of 30% HNO_3 and 70% methanol maintained at -20°C under 15 V.

Fig. 2.11 shows the investigation results of naturally aged fibrous material ($T3F_6$). In this condition, grain boundaries, subgrain boundaries and dispersoids can clearly be seen. Most of dispersoids are composed of $Al_{20}Cu_2Mn_3$ or Al_3Zr. The average diameter of Al_3Zr dispersoids is

about 45 nm and their volume fraction lies between 1.2 and 1.8 %. In Fig. 2.11b, it can be seen that there is no presence of hardening precipitates (T_1 and θ') in this condition. Spectrum analysis shows that the near homogeneous distribution of smaller dark particles are rich in silver and their diameter is about 10-15 nm. There is no precipitate decoration on the observed grain boundaries or subgrain boundaries.

Fig. 2.12 and Fig. 2.13 show the case of artificially aged fibrous material ($T8F_6$). In Fig. 2.12, hardening T_1 (Al_2CuLi) and θ' (Al_2Cu) type plate-shaped precipitates can clearly be seen (Fig. 2.12a). The morphology characteristic of these intra-granular plates was measured by Small-Angle X-ray Scattering carried out by Decreus [32]. T_1 precipitates were shown to present a thickness around 1 nm and a mean length of 40 nm in T8 condition. T_1 precipitates are seen to decorate the grain boundary (horizontal) and subgrain boundary (vertical) (see Fig. 2.12b). In this condition, the dispersoids and inter-granular large precipitates can also be seen (Fig. 2.12c). Precipitate decorations on grain boundary and subgrain boundary are also shown in detail in Fig. 2.13a and Fig. 2.13b respectively. Precipitate free zone (PFZ) can be seen at some part of grain boundary areas as exemplified in Fig. 2.13c. However the PFZ was found only in one of numerous images observed, in general the PFZ of T_1 is absent. It is consistent with the results obtained in the work of Decreus [31] on the same material.

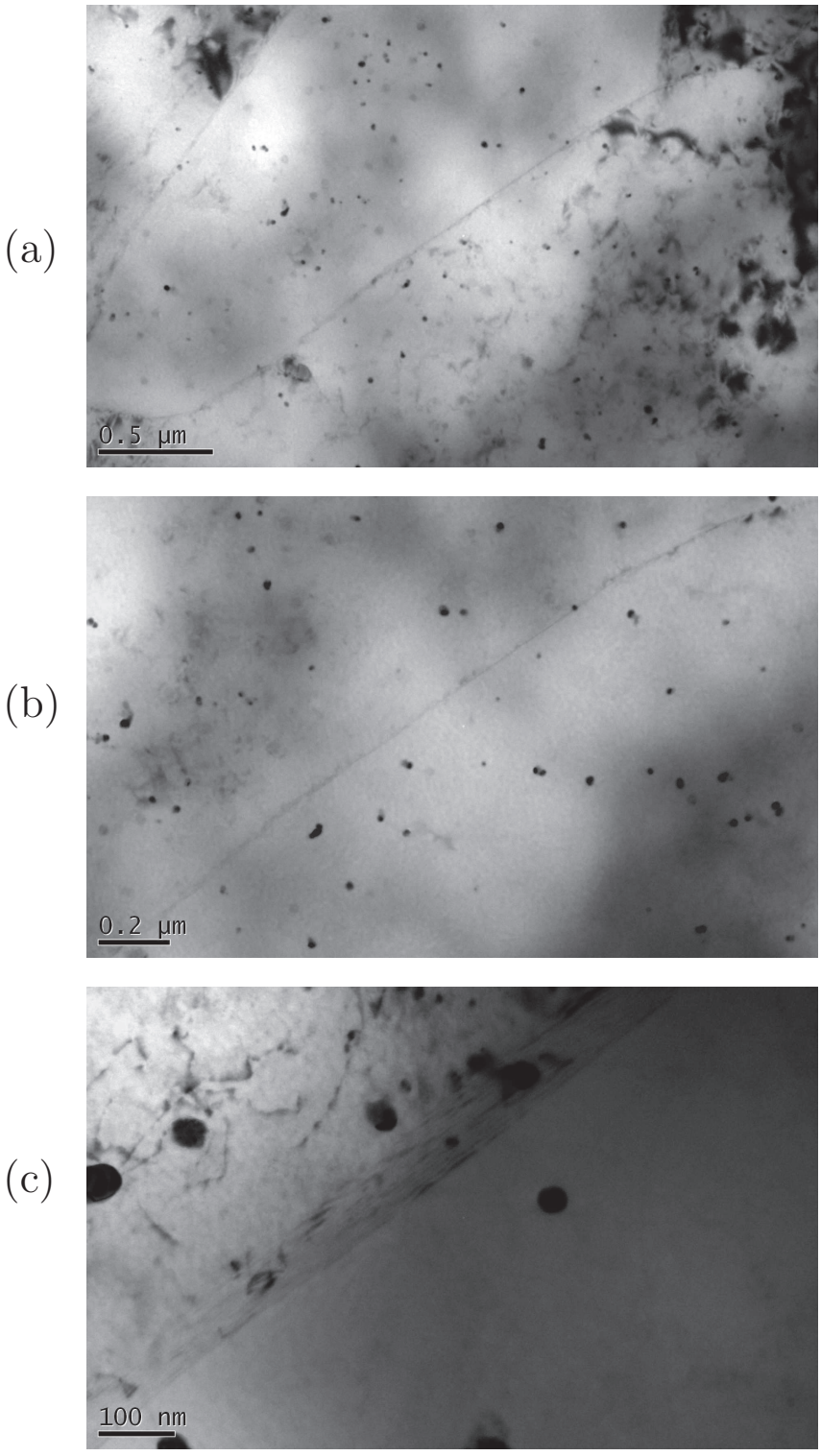


Figure 2.11: TEM investigation of naturally aged fibrous material ($T3F_6$), grain boundary and subgrain boundary (a, b), dispersoids (c) can be seen. Note that there is no precipitates decoration of the observed grain boundaries and subgrain boundaries.

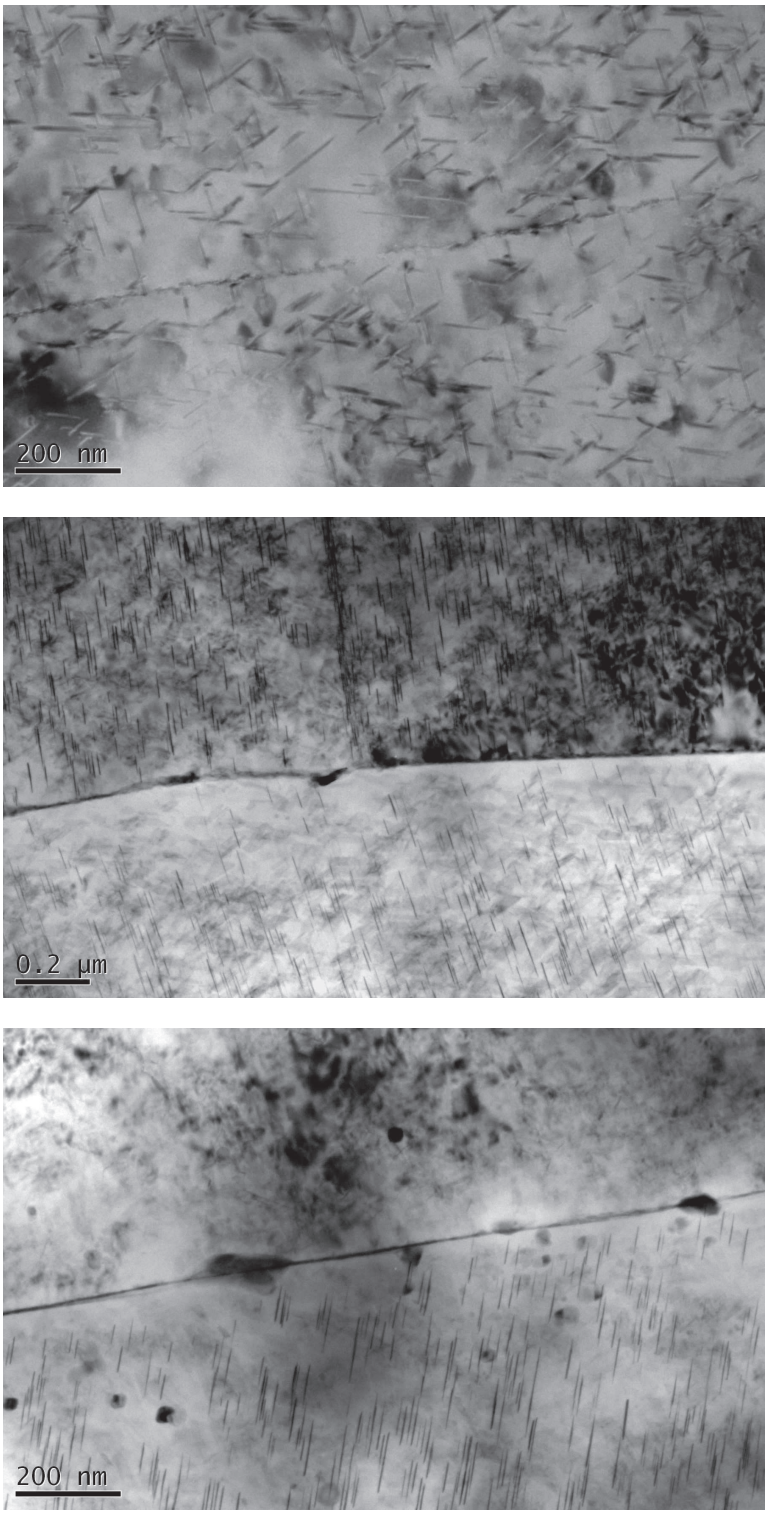


Figure 2.12: TEM investigation of artificially aged fibrous material ($T8F_6$). (a) plate-shaped precipitates of T_1 (Al_2CuLi) in {1 1 1} plane and θ' (Al_2Cu) in {1 0 0} palne, (b) precipitates decoration at grain boundary (horizontal) and subgrain boundary (vertical), (c) dispersoids and inter-granular large precipitates.

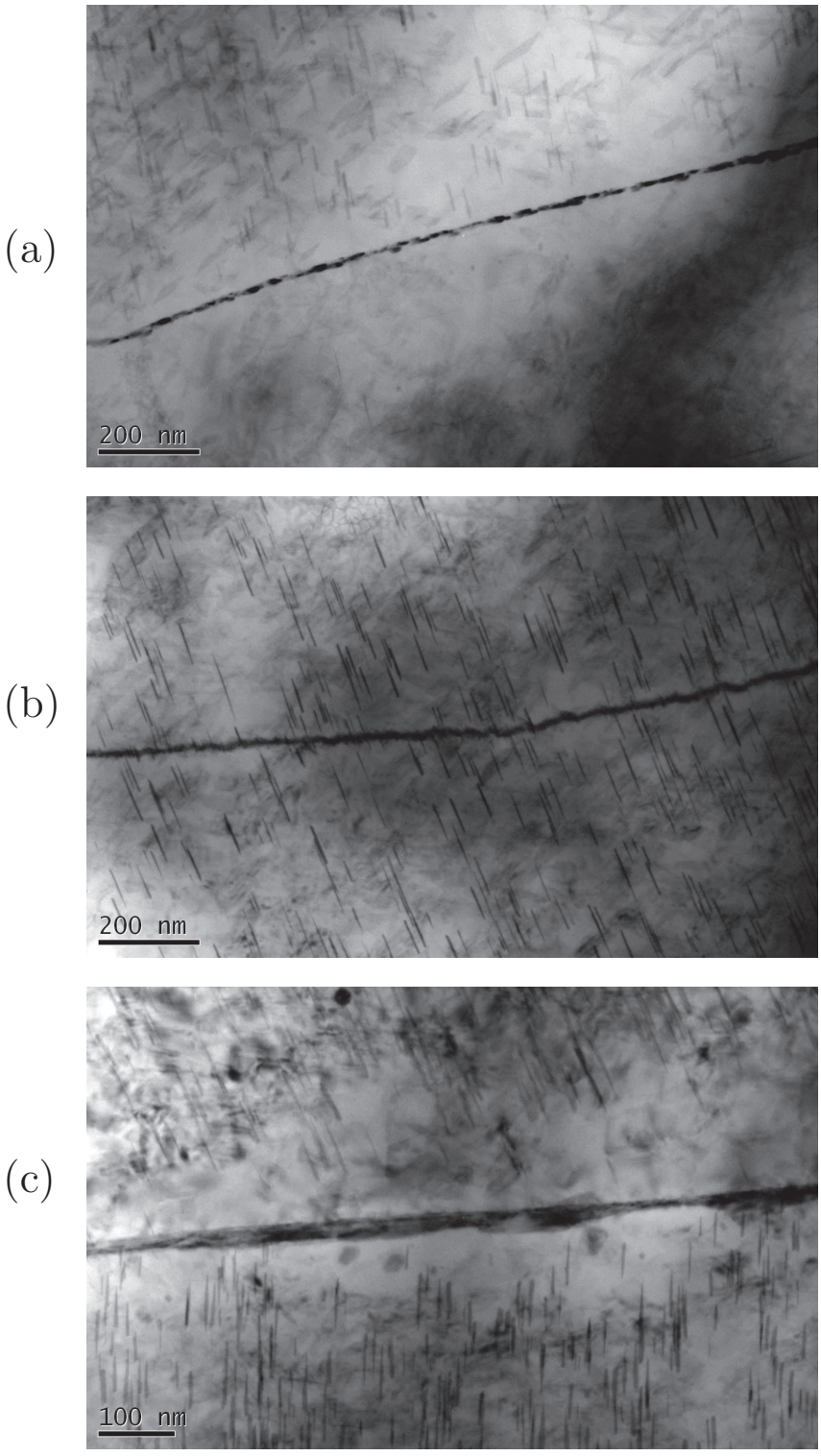


Figure 2.13: TEM investigation of artificially aged fibrous material ($T8F_6$). (a) precipitates decoration at grain boundary, (b) precipitates decoration at subgrain boundary, (c) precipitate free zone (PFZ) and inter-granular large precipitates.

2.3.4 X-ray tomography

The intermetallic particles and initial pores, which act as nucleation sites for voids causing ductile damage, influence the toughness of the material. The volume fraction of these particles and their spatial distribution are important microstructural parameters affecting damage evolution and fracture toughness. The volume fraction of intermetallic particles and pores can be determined by synchrotron radiation computed tomography (SRCT).

X-ray tomography observations were carried out using procedures already described in [74]. A number of pieces of materials were prepared by slicing as-received sheets to small block (dimensions 1 x 1 x 10 mm^3) using electrical discharge machining. Subsequent tomographic scanning of as-received materials could be carried out. X-ray tomography was performed at 20 keV at beamline ID19 of the European Synchrotron Radiation Facility (ESRF), Grenoble, France. The facility provides a highly coherent, spatially and spectrally homogeneous beam with a high photon flux. The typical imaging time was 0.7 sec. For one volume 1500 radiographs were taken using a high performance CCD camera and simultaneously the sample was turned 180° in steps of 0.12°. Flat-field and dark current corrections were performed and reconstruction was carried out using a conventional filtered back projection algorithm [67]. In the reconstructed slices an isotropic voxel size of 0.7 μm was obtained. Phase contrast imaging has been performed allowing to enhance the detection of edges. At the beamline ID19 this is a straightforward technique as advantage is taken of the radiation coherence by adjusting the sample detector distance to obtain near-field Fresnel diffraction effects.

Fig. 2.14 shows typical 2D sections from X-ray tomography data taken for as-received undeformed 2 mm-thick recrystallized material (Fig. 2.14a) and 6 mm-thick fibrous material (Fig. 2.14b) both in T8 temper condition in LS plane. Intermetallic particles composed of iron and silicon (white) can be seen to be elongated and aligned along the rolling direction. Hardly any initial porosity can be found for both recrystallized and fibrous materials. The constituents and void content was measured

via grey value thresholding, the mean value was taken. The mean constituents content is 0.34% for recrystallized material and 0.4% for fibrous material. The initial porosity is very limited ($\leq 0.04\%$) compared to other aerospace aluminium alloys (e.g. AA2024, AA2139) [21, 73]. Fig. 2.15 provides a 3D rendering of the constituents and pores distribution for T8 recrystallized material. Notice that the intrinsic constituent particles and void content of the parent material are exaggerated [74] by the 3D nature of Fig. 2.15, representing the intermetallic particles and void content of a thick cube of material (180 μm $\times$ 180 μm $\times$ 180 μm) rather than a 2D section in traditional metallographic imaging.

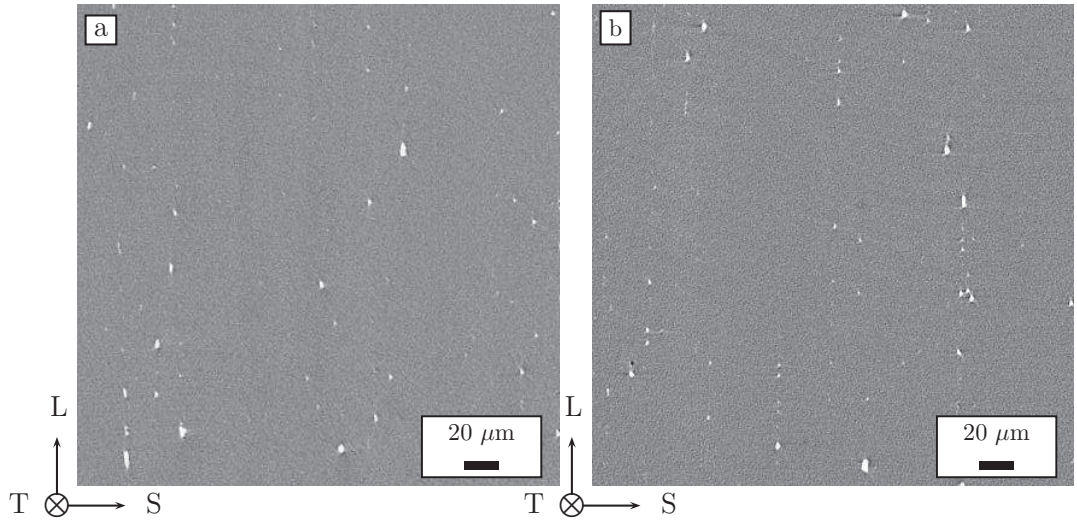


Figure 2.14: 2D images of as-received undeformed materials from high resolution X-ray tomography: (a) Recrystallized material ($T8R_2$) in the L-S plane, (b) Fibrous material ($T8F_6$) in the L-S plane. Constituent particles are composed of Fe and Si (white).

2.4 Conclusions

In this part the materials' microstructure was characterized by various techniques in a multiscale. Metallographic observations conducted by optical microscopy indicated that the materials

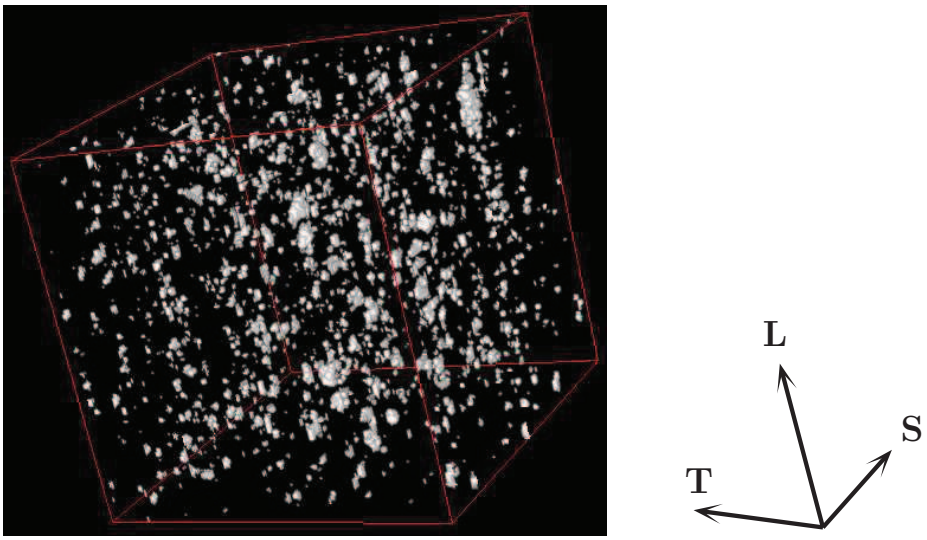


Figure 2.15: 3D images of as-received T8 recrystallized material by high resolution X-ray tomography. The constituents and pores are in white. The size of the box is 256 pixels = 179.2 μm in each direction.

under study have a strongly anisotropic grain structure. For both recrystallized and fibrous materials, large pan-cake shaped grains were observed in the L–T plane. The pan-cakes are more equiaxed in recrystallized than that in fibrous materials. The constituent particles can be seen aligned along rolling direction. Elongated thin form grains can be seen in L-S and T-S planes, there are no grain size gradient across sheet thickness. It is important to note that the 6 mm-thick fibrous materials have much thinner grains and more grain directionality than 2 mm-thick recrystallized materials, grains in the fibrous material can be larger than 1000 μm along the L-direction.

TEM investigation results show that there is a large difference between artificially aged T8 material and naturally aged T3 material. For T8 material, inter-granular precipitates can be found along almost all grain boundary or subgrain boundary areas. Hardening T_1 and θ' type precipitates are formed in this condition. Precipitate free zone can be found in one of images observed while in general the PFZ is absent. For naturally aged T3 material, hardening precipitates T_1 and θ' were not found; there is no precipitate decoration at grain boundaries or subgrain boundaries. In this

condition dispersoids can be seen more clear than in T8 condition due to on presence of precipitates, most of dispersoids composed of Al-Cu-Mn and Al-Zr. Their average diameter is about 45 nm and their volume fraction lies between 1.2 and 1.8 %.

The initial pore and inter-metallic particle content was examined by high resolution X-ray tomography on as-received undeformed materials. It is shown that in AA2198 alloy, hardly any initial pore can be seen. The volume fraction of inter-metallic particles and voids content is only 0.34% for recrystallized material and 0.4% for fibrous material. These values are very limited in comparison to other aluminium alloys (e.g. AA2024, AA2139 etc.).

2.5 Résumé

Nous présentons dans ce chapitre les matériaux et en particulier la caractérisation des différentes microstructures des matériaux étudiées. Deux nuances de l'alliage d'aluminium-lithium 2198 ont été étudiées sous la forme de tôles. La première nuance est une tôle de texture recristallisée d'épaisseur 2 mm qui a été obtenue par un laminage à froid (nuance notée R2). La deuxième nuance est une tôle de texture fibrée d'épaisseur 6 mm qui a été obtenue par un laminage à chaud (nuance notée F6). Pour chaque nuance, deux traitements thermiques ont été étudiés : T351 et T851. Les microstructures fines des matériaux ont été caractérisées par différentes techniques d'observations muti-échelles. L'observation métallographique menée à l'aide du microscope optique montre que les matériaux de l'étude présentent une structure granulaire anisotrope. Les observations au microscope électronique en transmission (MET) ont permis de mettre en évidence des différences importantes entre les matériaux en état T3 et les matériaux en état T8 : la texture T8 se démarque par la présence de précipités durcissant (T1 et θ') dans la matrice et des précipités inter-granulaires plus grossiers aux joints de grains. Enfin, la porosité initiale et le volume des particules intermétalliques, examinés via tomographie haute résolution à rayon X. sont en proportion très limitée (0,34% pour

le recristallisé et 0,4% pour la structure fibrée) comparativement aux autres alliages d‘aluminium.

Chapter 3

Plastic Anisotropic Behaviour

Anisotropy of mechanical properties in sheet materials originates from rolling process. Characterization of the anisotropy and its amplitude is essential for a study of sheet metal. In this part, we will present the specimens used for mechanical tests, experimental procedure, testing conditions and test results. The strain rate sensitivity has been investigated on smooth tensile tests at room temperature and high temperature. The influence of thickness on plasticity and damage has also been examined. In the second part, the macroscopic fracture mechanisms were studied by metallographic observations on cut section of broken specimens. The scanning electron microscopy was used for the microscopic fractography studies. The third part deals with the identification of plastic anisotropic behaviour by an anisotropic yield criterion proposed by Bron and Besson for sheet materials. Finally a localization indicator based on Rice's analysis of bifurcation is used to analyse finite element simulations and predict observed fracture plane orientations.

3.1 Mechanical tests

3.1.1 Specimens for mechanical tests

In this part, mechanical tests are conducted on two different kinds of flat specimens (see Fig. 3.1 for geometries). The ST_{12} specimen is a conventional smooth tensile sample used to determine the elastic-plastic behaviour under uniaxial loading condition. The differently U-notched tensile samples NT_{05}, NT_1 and NT_2 are used to investigate notch strengthening and stress triaxiality ratio effects on damage.

In order to characterize the anisotropy of sheet materials, specimens for mechanical tests are prepared along different directions in the sheet plane (L–T plane). Because all materials studied are thin sheets (2 mm and 6 mm thick), it is difficult to take equivalent tensile specimens along the short-transverse direction (S). The plastic anisotropy is therefore investigated in the sheet plane.

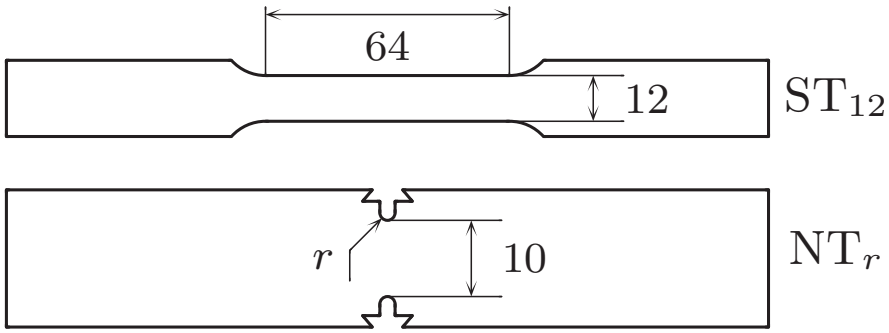


Figure 3.1: Geometry of test specimens (all dimensions in mm): smooth flat tensile specimen ST_{12}, notched flat tensile specimen NT_r with radii of 0.5, 1 and 2 mm.

3.1.2 Experimental setup and testing conditions

All tests are carried out at room temperature under displacement control on a servo-hydraulic testing machine. Tests conducted on smooth tensile specimens ST_{12} are conducted along

three different directions (L, T and D) in the sheet plane. ST_{12} specimens are tested with two displacement gages to record both longitudinal and transverse strain (see Fig. 3.2). This allows for a determination of the R-value (Lankford coefficient see eq. 3.1) defined as the ratio of the true deformation along the width of the specimen to the true deformation along the thickness (S direction). The latter is computed assuming plastic incompressibility.

$$\mathcal{L}_k = \frac{\varepsilon_w}{\varepsilon_s} \tag{3.1}$$

In the following, the smooth tensile experimental curves are plotted using the plastic load line displacement $\Delta \mathrm{LL}_p/L_0$ (corrected for elastic deformation, L_0: specimen gage length (64 mm)) measured by the testing machine. It represents a global measure of material's ductility. In contrast, the extensometer recorded displacement can give a precise measurement of longitudinal and transverse deformation used to compute Lankford coefficient (eq. 3.1). Fig. 3.2 shows a ST_{12} specimen setup during mechanical test. For each material, smooth tensile tests are conducted at different strain rates varying from 10^{-5} to 10^{-3} s^{-1} along each direction (L, T and D) to examine the strain rate sensitivity which will be discussed in detail in the section 3.3. For this part, the experimental results of smooth tensile tests are shown for the strain rate of 10^{-4} s^{-1}.

For notched specimens, opening displacement is measured on both left and right sides and the mean value is used. The difference between both measurements is always less than 3 %. The setup of notched NT tensile test can be seen in Fig. 3.3. For notched samples, tests are performed along two directions (L and T) for NT_1 samples and along three directions (L, T and D) for NT_2 samples. While $NT_{0.5}$ are tested along L and T directions on one fibrous material ($T3F_6$); The cross head speed is 0.2 mm/min for all notched tensile tests.

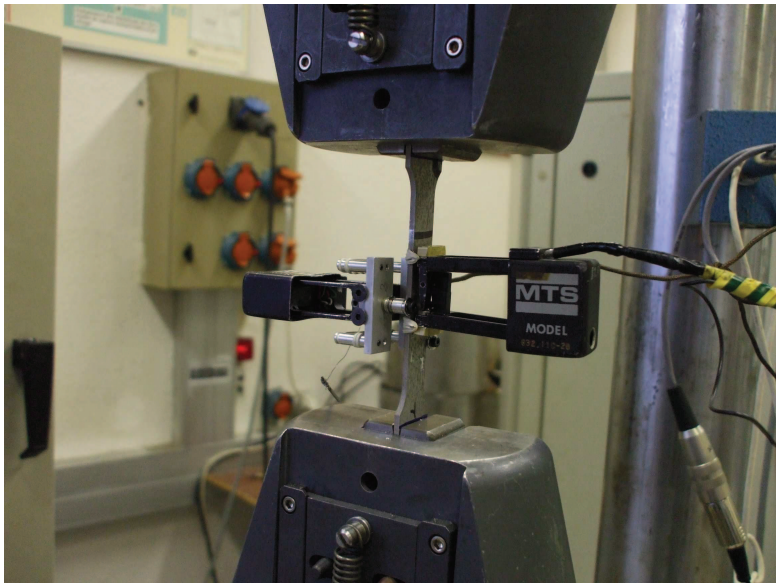


Figure 3.2: Smooth flat tensile specimen ST_{12} setup with longitudinal and transverse gages during test.

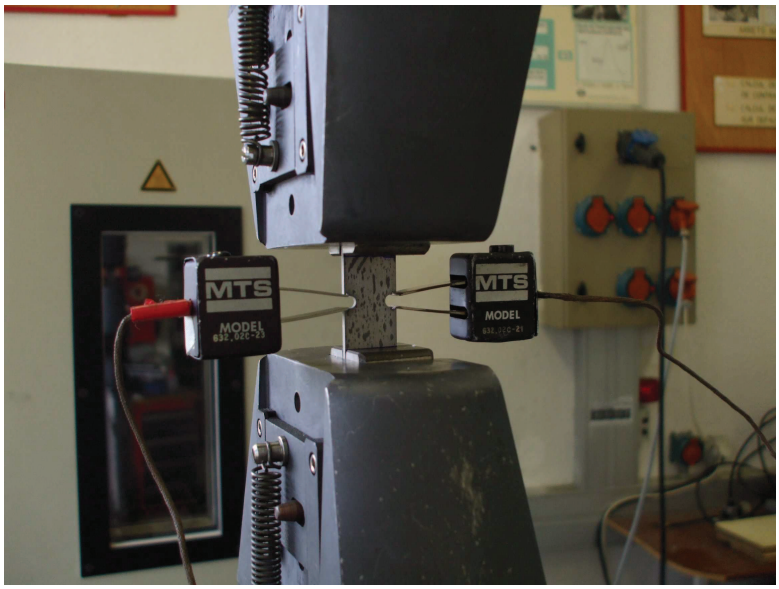


Figure 3.3: Notched flat tensile specimen NT_r setup with left and right gages during test.

3.2 Experimental results

3.2.1 Smooth tensile tests

Fig. 3.4 shows the nominal stress (F/S_0) as a function of the plastic elongation for both 2 mm-thick recrystallized materials ($T3R_2$ and $T8R_2$); where, F is the load and S_0 is the initial cross section. In Fig. 3.4 left, it can be seen that the artificially aged material ($T8R_2$) presents indeed higher yield and ultimate strengths, i.e., in longitudinal (L) direction, the yield stress is 64 % higher than that of naturally aged material ($T3R_2$) whereas the hardening capability and ductility of T8 material are lower than for the T3 material. For each condition (T3 and T8), differences in engineering stress between L, T and D directions are not significant probably owing to process of recrystallisation introduced by cold rolling. Due to pre-strain effect (mechanical treatment of stretching conducted in rolling direction), the longitudinal (L) direction is slightly harder than long-transverse (T) and diagonal (D) directions. Fig. 3.4 right, shows the reduction of the specimen width as a function of the tensile strain. $T3R_2$ and $T8R_2$ materials have very similar results. L, T and D directions follow almost the same line. Results (dots) are compared with the isotropic case (line) showing a large deviation although the plastic behaviour can be considered as ”isotropic” in the sheet plane. The computed Lankford coefficient $\mathcal{L}_k$ and the principal mechanical characteristics of recrystallized materials are gathered in Table 3.1.

Fig. 3.5 provides the results for both 6 mm-thick fibrous materials ($T3F_6$ and $T8F_6$). From Fig. 3.5 left, it can be seen that both fibrous materials show a strong plastic yielding anisotropy which is much higher than corresponding anisotropy observed on both recrystallized materials (see Fig. 3.4). i.e. the yielding stress of L loading test is 20% higher than D loading for T8 fibrous material (only 9% for T8 recrystallized material). For both recrystallized and fibrous materials, L direction is the strongest; the D direction exhibits a much lower yielding limit which is typical of Al-Cu-Li alloys [30, 45, 71, 103]. As observed in both recrystallized materials, fibrous materials

follow the same trends: the T8 material presents higher yield and ultimate strengths but a lower hardening capability. Notice that the T3 material tested along the L direction fails while the load is still increasing and consequently exhibits no necking. This result was reproduced on several test specimens and is not an artifact. For this case, complementary tests were carried out at a higher temperature (cf. section 3.3.2) to investigate this unusual behaviour. The reduction of the specimen width as a function of the tensile strain for both fibrous materials is shown in Fig. 3.5 right. Results (dots) are also compared with the isotropic case (line). For T3 material, it is shown that a large deviation for L and T direction whereas D-direction is close to the isotropic case. In the case of T8 material, similar results were obtained except for T direction which is also close to the isotropic case as the D direction. Results clearly indicate that for tests along the L direction thickness reduction is higher than width reduction. The computed Lankford coefficient $\mathcal{L}_k$ and the principal mechanical characteristics of fibrous materials are also gathered in Table 3.1.

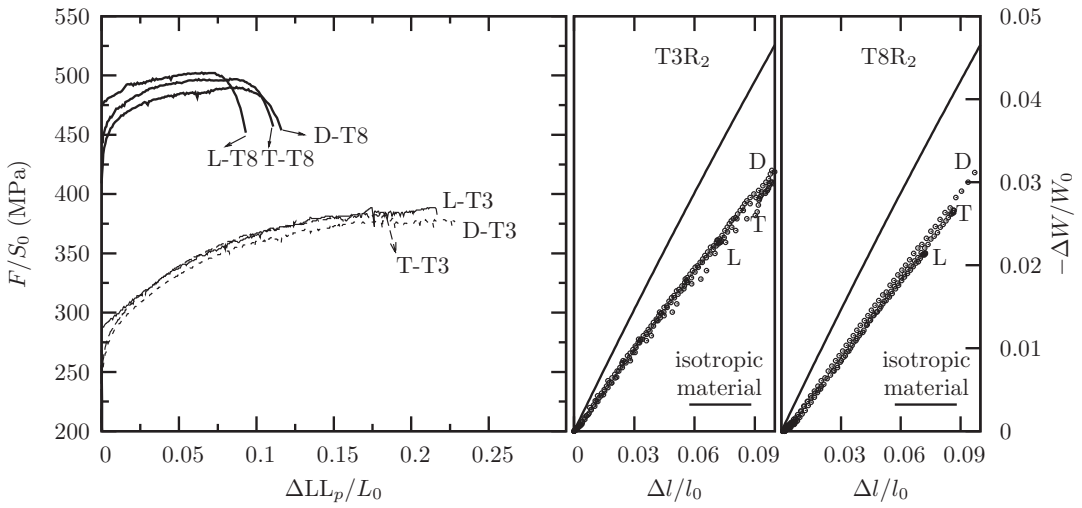


Figure 3.4: Tensile tests on smooth specimens ST_{12} along L, T and D directions for recrystallized materials ($T3R_2$ and $T8R_2$). Engineering stress (F/S_0) as a function of the normalized plastic load line displacement $\Delta LL_p/L_0$. Width reduction ($\Delta W/W_0$) as a function of the axial strain $\Delta l/l_0$. The testing strain rate is $5.2 \times 10^{-4}\ s^{-1}$. ($F$: force, S_0 initial cross section, ΔLL_p: load line displacement corrected for elastic deformation, L_0: specimen gage length, ΔW: width variation, W_0: initial width, Δl displacement measured by the longitudinal extensometer, l_0 extensometer gage length.)

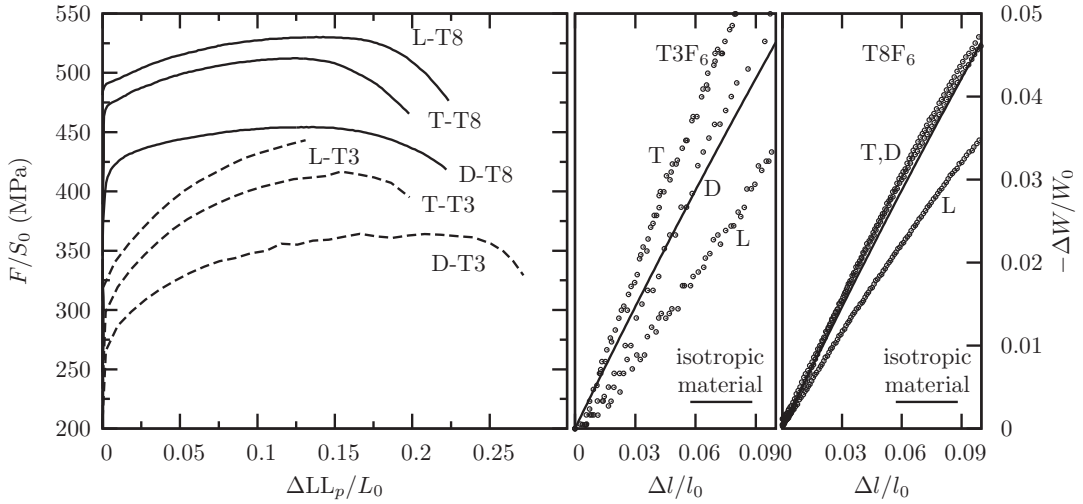


Figure 3.5: Tensile tests on smooth specimens ST_{12} along L, T and D directions for fibrous materials ($T3F_6$ and $T8F_6$). Engineering stress (F/S_0) as a function of the normalized plastic load line displacement $\Delta LL_p/L_0$. Width reduction ($\Delta W/W_0$) as a function of the axial strain $\Delta l/l_0$. The testing strain rate is $5.2 \times 10^{-4}\ s^{-1}$. ($F$: force, S_0 initial cross section, ΔLL_p: load line displacement corrected for elastic deformation, L_0: specimen gage length, ΔW: width variation, W_0: initial width, Δl displacement measured by the longitudinal extensometer, l_0 extensometer gage length.)

	$T3R_2$					$T8R_2$				
	YS	UTS	YS/UTS	UE	$\mathcal{L}_k$	YS	UTS	YS/UTS	UE	$\mathcal{L}_k$
L	290	389	0.745	18.0	0.49	476	504	0.944	7.3	0.48
T	258	386	0.668	18.3	0.50	441	497	0.887	8.7	0.50
D	257	380	0.676	22.1	0.52	435	490	0.888	9.0	0.52
	$T3F_6$					$T8F_6$				
	YS	UTS	YS/UTS	UE	$\mathcal{L}_k$	YS	UTS	YS/UTS	UE	$\mathcal{L}_k$
L	325	440	0.739	13.0	0.52	496	531	0.934	14.0	0.64
T	296	414	0.715	15.4	1.63	473	514	0.920	12.3	1.03
D	262	362	0.724	21.1	1.0	414	454	0.912	13.0	1.06

Table 3.1: Room temperature tensile properties of tested materials ($T3R_2$, $T8R_2$, $T3F_6$ and $T8F_6$) along L, T and D directions. (YS: yield strength for 0.2% plastic strain (MPa), UTS: ultimate tensile strength (MPa), UE: uniform elongation (%), $\mathcal{L}_k$: Lankford coefficient for a plastic deformation of 5%.

3.2.2 Notched flat tensile tests

Fig. 3.6 shows results of mechanical tests conducted on notched flat specimens NT_2 the nominal stress (F/S_0) as a function of the notch opening displacement (NOD); where F is the load and S_0 is the initial minimum cross section. As expected the notch leads to an increase of maximum loads compared to smooth tensile specimens. For recrystallized materials ($T3R_2$ and $T8R_2$), plastic anisotropy keeps the same trends as the smooth tensile tests with L direction being strongest and D direction is weakest. The ductility of T3 condition materials is much higher than T8 condition materials which is consistent with smooth flat tensile tests. i.e. the NOD of T3 material in L loading test is 2 times higher than T8 material in the same loading. For both fibrous materials ($T3F_6$ and $T8F_6$), plastic anisotropy is reduced compared to smooth tensile tests especially in the

case of the T8 material. There are no difference between L-loading and T-loading tests. For the ductility, D-loading has always higher NOD than L- and T-loading tests. Test results with different specimen notch radii are shown in Fig. 3.7 in terms of nominal stress (F/S_0) as a function of the notch opening displacement (NOD). Curves are presented here for the case of T3 fibrous material in T-loading for the brevity (other test results can be found in appendix 2). NT_{05} test has a slightly higher load but a lower ductility than NT_1 and NT_2 tests. The reduction in ductility owing to higher stress triaxiality for smaller notch radii is well observed. For other directions and materials, this effect is also obtained. These tests will be used together with ST_{12} tests to adjust coefficients of a set of constitutive equations accounting for plastic anisotropy following [19].

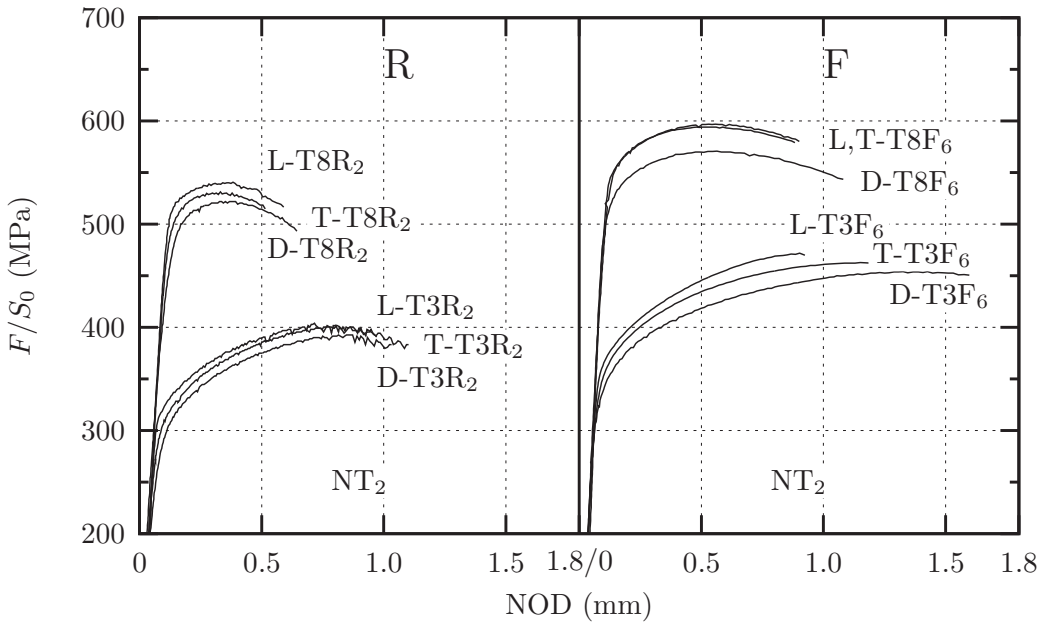


Figure 3.6: Tensile tests on notched flat specimens (NT_2) along L-, T- and D-loadings. F stands for the load, S_0 stands for initial minimum cross section, NOD stands for notch opening displacement.

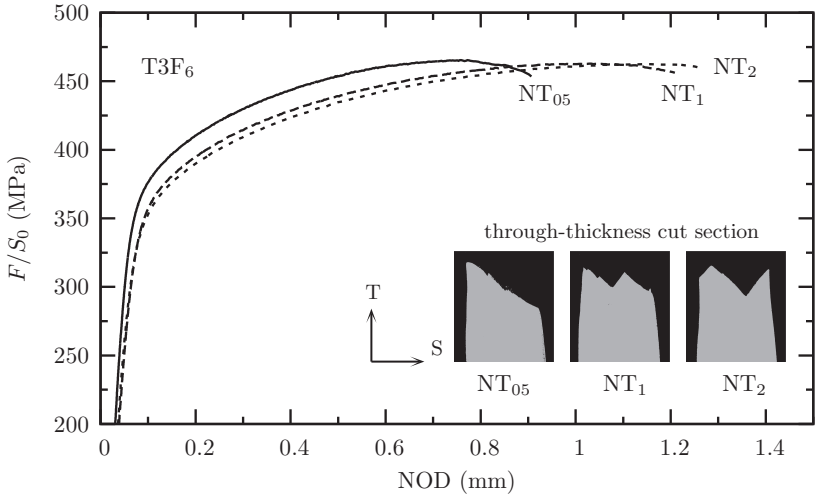


Figure 3.7: Tensile tests on notched flat specimens with different radii 0.5, 1 and 2 mm for T3 fibrous material loading in T direction. F stands for the load, S_0 stands for initial minimum cross section, NOD stands for notch opening displacement.

3.3 Strain rate sensitivity

In order to characterize the strain rate sensitivity of tested materials, smooth tensile tests were first performed at three different strain rates varying from 10^{-5} to 10^{-3} s^{-1} at room temperature for all materials studied. It is well established that strain rate sensitivity is strongly influenced by temperature [12, 41, 46, 121], further complementary tests were carried out at a higher temperature. In our case this temperature is set to 393 K (120°C) which is slightly lower than material's artificial ageing temperature (155°C). The objective is to insure no additional ageing during tests. For brevity, selected curves will be presented here (other test curves can be found in appendix 2).

3.3.1 Experimental results at room temperature (293 K)

Fig. 3.8 shows the results of tests for both fibrous materials in T3 and T8 conditions (T3F$_6$ and T8F$_6$). A slightly negative strain rate sensitivity was observed, this usually corresponds to dynamic strain aging (DSA). The strain rate sensitivity coefficient SRS [2, 13, 46], can be defined

as:

$$SRS = \frac{\sigma_2 - \sigma_1}{log\dot{\varepsilon}_2 - log\dot{\varepsilon}_1} \tag{3.2}$$

where, σ_1 and σ_2 are the flow stresses at 6 % strain at the strain rates $\dot{\varepsilon}_1 = 10^{-5}s^{-1}$ and $\dot{\varepsilon}_2 = 10^{-4}s^{-1}$, respectively. Table 3.2 gathers the measured SRS coefficient of tested materials along L-, T- and D-loading direction at room temperature (293 K). All materials present a negative SRS which is more pronounced for fibrous materials than for recrystallized materials, especially in the case of $T3F_6$ material.

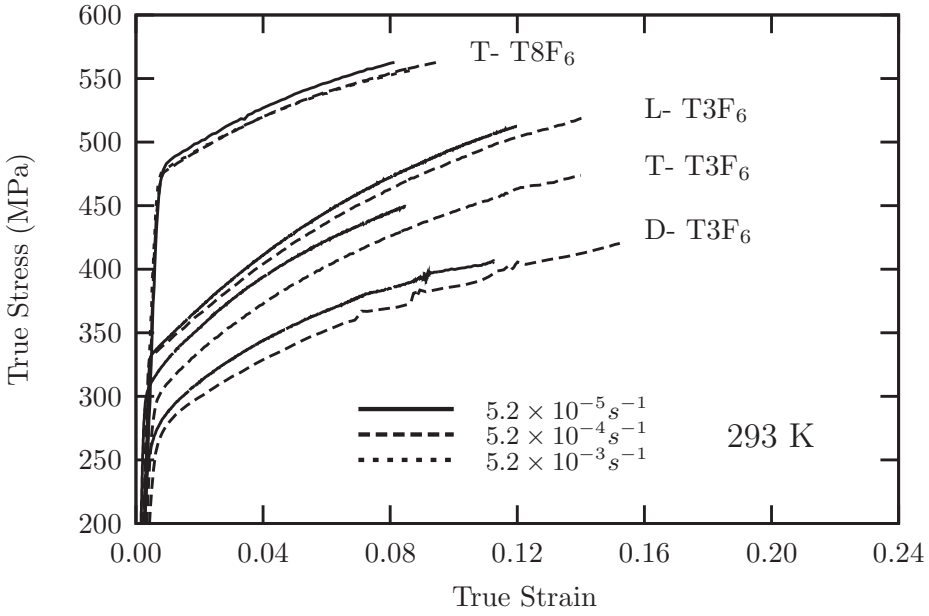


Figure 3.8: Tensile stress–strain curves of fibrous materials $T3F_6$ and $T8F_6$ along different loading directions. True strain $\ln(\Delta l/l_0)$ measured by the longitudinal extensometer (initial gage is 22 mm), curves are cut at maximum loads. (L, T and D directions for $T3F_6$ material, T direction for $T8F_6$ material) under three testing strain rates varying from 5.2×10^{-5} s^{-1} to 5.2×10^{-3} s^{-1} at room temperature (293 K).

3.3.2 Experimental results at 120°C (393 K)

Fig. 3.9 shows the experimental results at 393 K for T3 fibrous material in L loading. In this case, test exhibits a failure without necking and negative strain rate sensitivity at room temperature (see Fig. 3.5 and Fig. 3.8). while at a higher temperature, it is shown that the strain rate sensitivity become positive and failure with necking.

Material	$T3R_2$	$T8R_2$	$T3F_6$	$T8F_6$
L	-10.6	-2.4	-9.4	-9.7
T	-7.0	-2.3	-19.8	-6.9
D	-3.5	—	-15.3	-5.1

Table 3.2: Strain rate sensitivity SRS (MPa) for different tested materials along different loading direction at room temperature (293 K). The data is calculated at 6 % plastic strain.

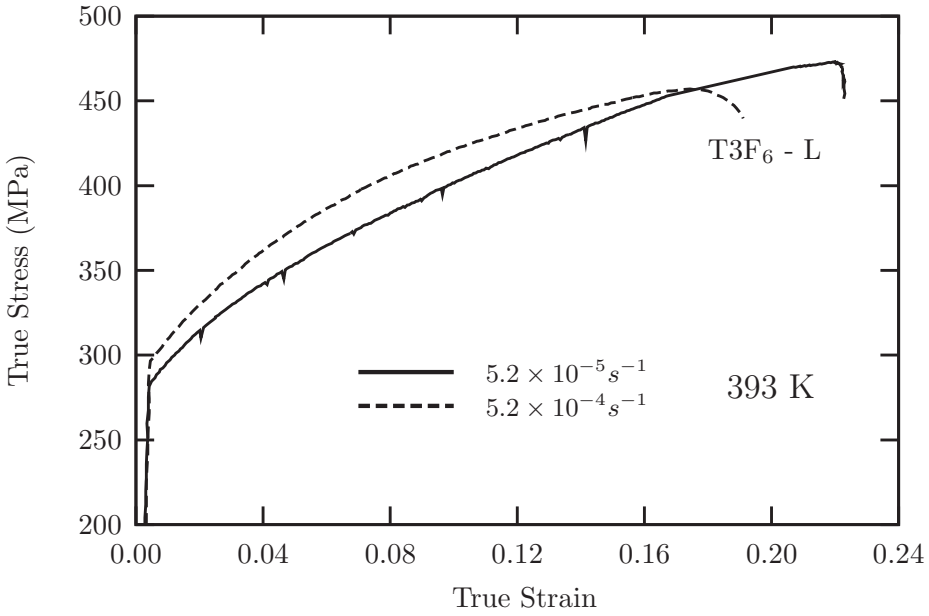


Figure 3.9: Tensile stress–strain curves of fibrous material $T3F_6$ in L loading at 393 K for two testing strain rates $5.2 \times 10^{-5}\ s^{-1}$ and $5.2 \times 10^{-4}\ s^{-1}$.

3.3.3 Analysis of DSA effect on necking

A possible explanation of fracture occurring before necking in the case of T3F$_6$ material L-loading is the presence of a DSA effect together with the strongly anisotropic texture of the material. For an uniaxial tensile test subjected to an axial loading F, necking occurs when F reaches a maximum ($\partial F/\partial l = 0$). The maximum loading, at which necking begins, occurs when the slope of the stress-strain curve satisfies the following condition:

$$\frac{d\sigma}{d\varepsilon} = \sigma \tag{3.3}$$

For a power-law material, which has the relation:

$$\sigma = K\,(1 + \varepsilon_p/\varepsilon_0)^n \tag{3.4}$$

where, K, ε_0 and n are material constants. The corresponding strain at the onset of necking is $\varepsilon = n - \varepsilon_0$ (Considère law).

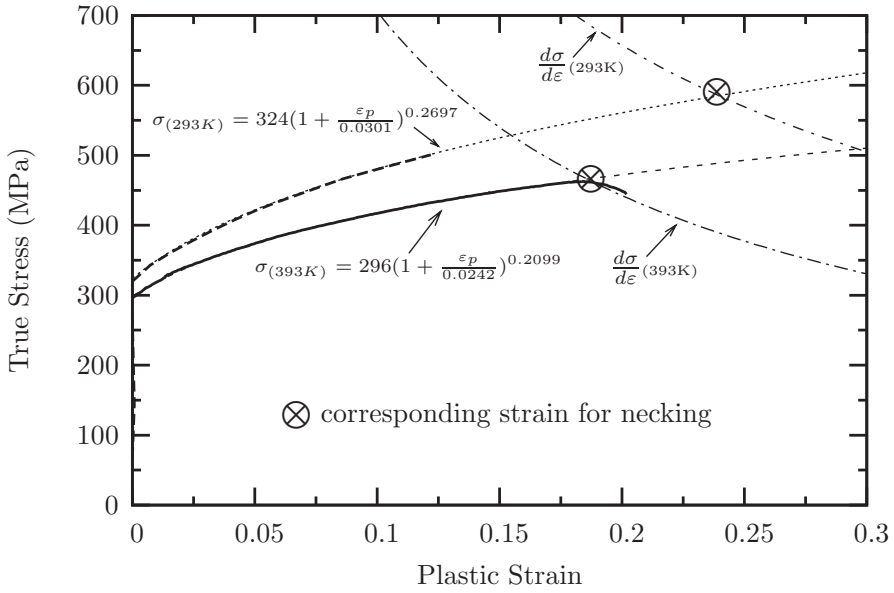


Figure 3.10: Experimental tensile stress–strain curve and fitted one at 293 K and 393 K in fibrous material (T3F$_6$) of L-loading. The testing strain rate is $5.2 \times 10^{-4}\ s^{-1}$.

Fig. 3.10 shows the experimental tensile stress strain curves and the fitted ones at 293 K and at 393 K. It is shown that at room temperature the fracture strain is around 0.13, which is considerably below the theoretical value for the onset of necking 0.24 ($n - \varepsilon_0$). For the same case at 393 K, the strain to fracture is 0.20 which is higher than the corresponding value for the necking 0.186. Similar result in a 5xxx aluminium alloy was observed by Kang *et al.* [53, 52]. However at room temperature, T- and D-loading tests exhibit a normal fracture feature other than the L-loading, probably due to the strongly anisotropic texture of material (see cf. section 3.5). The anisotropy of DSA effect and its interaction with anisotropic texture are, however, beyond the scope of the current investigation. The main objective of the current investigation is to identify materials anisotropic behaviour and the relationship between microstructure and fracture mechanisms.

3.4 Thickness effect on smooth and notched specimens

For both 6 mm-thick fibrous materials ($T3F_6$ and $T8F_6$), specimens having a thickness of 2 mm were prepared by slicing the 6 mm samples into two halves using electrical discharge machining. Each slice was then machined down on both sides to reduced the thickness to 2 mm as proposed in [81, 3] to study thickness effect on plasticity and fracture. Mechanical tests are carried out under the same condition as for 6 mm-thick samples. The testing strain rate is set to 5.2 x 10^{-4} s^{-1}.

Fig. 3.11 and Fig. 3.12 provide the experimental results of 2 mm-thick smooth tensile and notched tensile tests in comparison to 6 mm-thick specimens respectively for T3 material and T8 material. For both case of smooth tensile tests (Fig. 3.11a and Fig. 3.12a), reducing the sample thickness does not modify the plastic behaviour showing that the material does not present a plastic behaviour gradient; however failure occurs for lower elongation due to a more pronounced sensitivity to plastic instability. In the case of notched specimens (Fig. 3.11b and Fig. 3.12b), for both T3

and T8 condition, 2 mm-thick samples have a lower strength and ductility than 6 mm-thick samples due to a lower stress triaxiality. For T3 condition, the strength difference between L- and T-loading tests is smaller than the corresponding anisotropy observed in smooth tensile tests. Ductility is lower for L-loading than for T-loading. In T8 condition, there is no difference between L- and T-loading in terms of strength. As far as ductility is concerned, L-loading specimens fail always earlier than T-loading probably due to pre-strain effect produced in the longitudinal direction (2-4 % stretching).

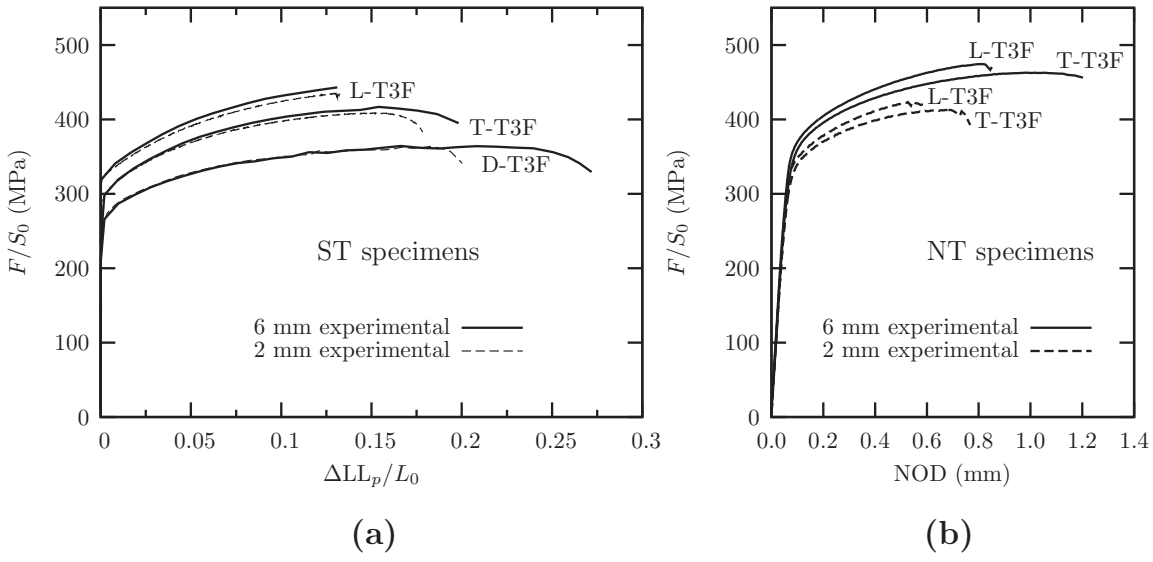


Figure 3.11: Comparison of 2 mm- and 6 mm-thick samples in the case of smooth tensile tests (a) and notched tensile tests (b) for T3 fibrous material.

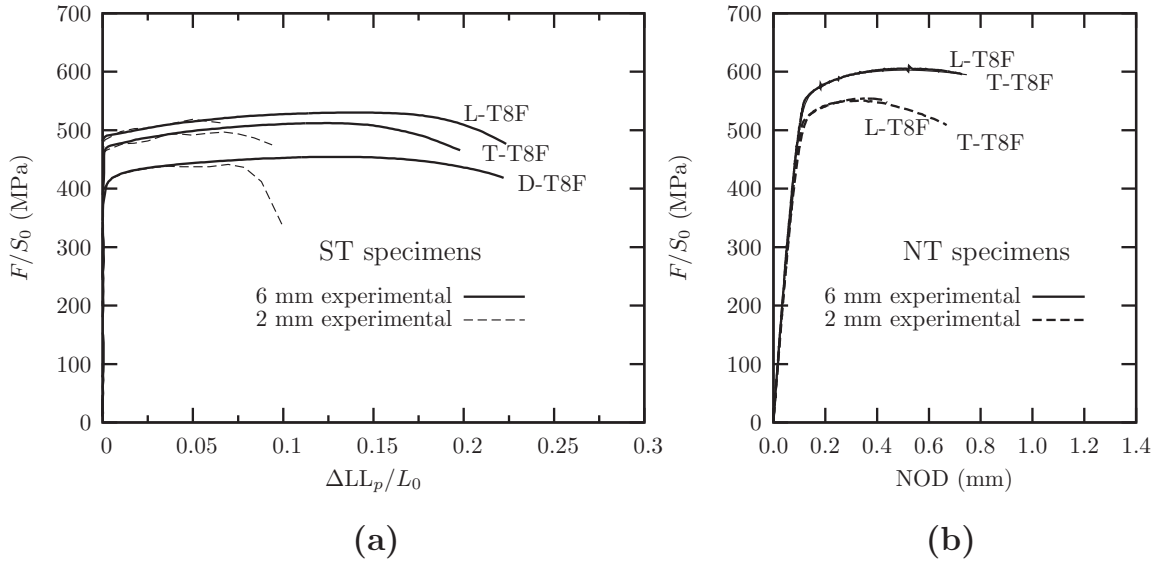


Figure 3.12: Comparison of 2 mm- and 6 mm-thick samples in the case of smooth tensile tests (a) and notched tensile tests (b) for T8 fibrous material.

3.5 Failure mechanisms and strain localisation

3.5.1 Macroscopic failure

Macroscopic fracture surfaces obtained on smooth flat tensile specimens lie in an inclined plane which can be characterized by two angles ϕ and θ as schematically shown on Fig. 3.15-a. Considering a very thin plate under plane stress condition, the theoretical localization angle ϕ is given by:

$$\phi_{\text{th}} = \frac{\pi}{2} - \arctan\sqrt{\frac{\mathcal{L}_k}{1+\mathcal{L}_k}} \tag{3.5}$$

where $\mathcal{L}_k$ is Lankford coefficient.

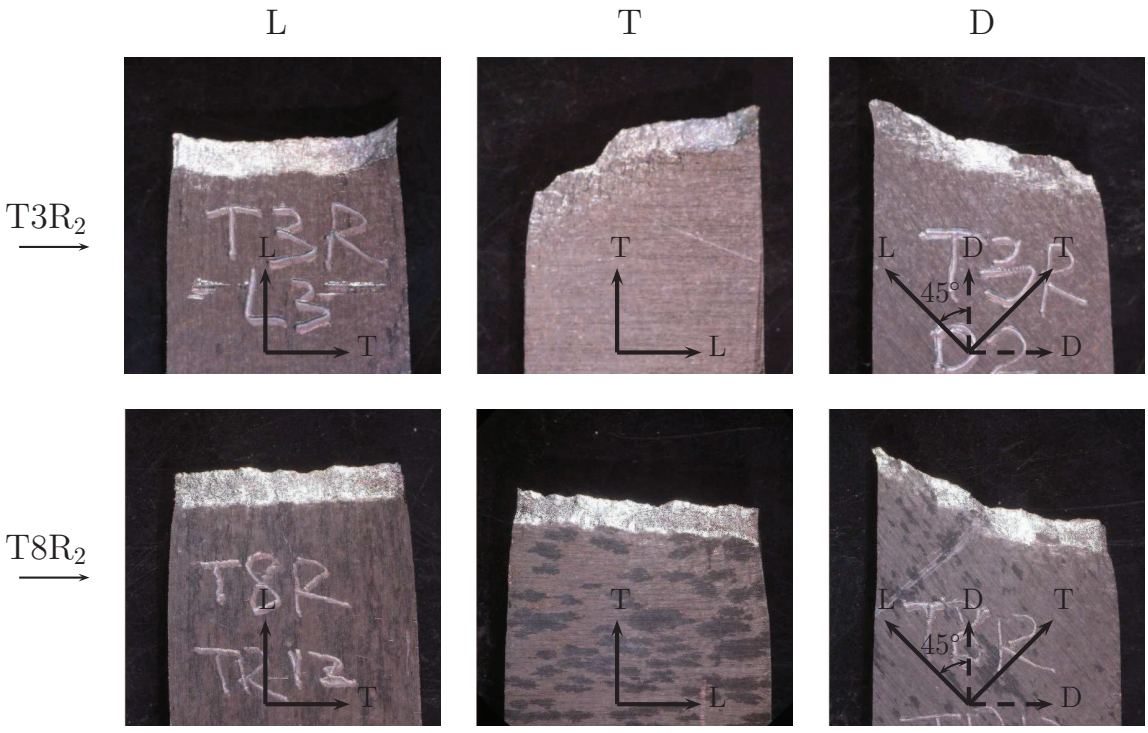


Figure 3.13: Post-test specimens of smooth flat tensile tests along L-, T- and D-loading for 2 mm thick recrystallized materials.

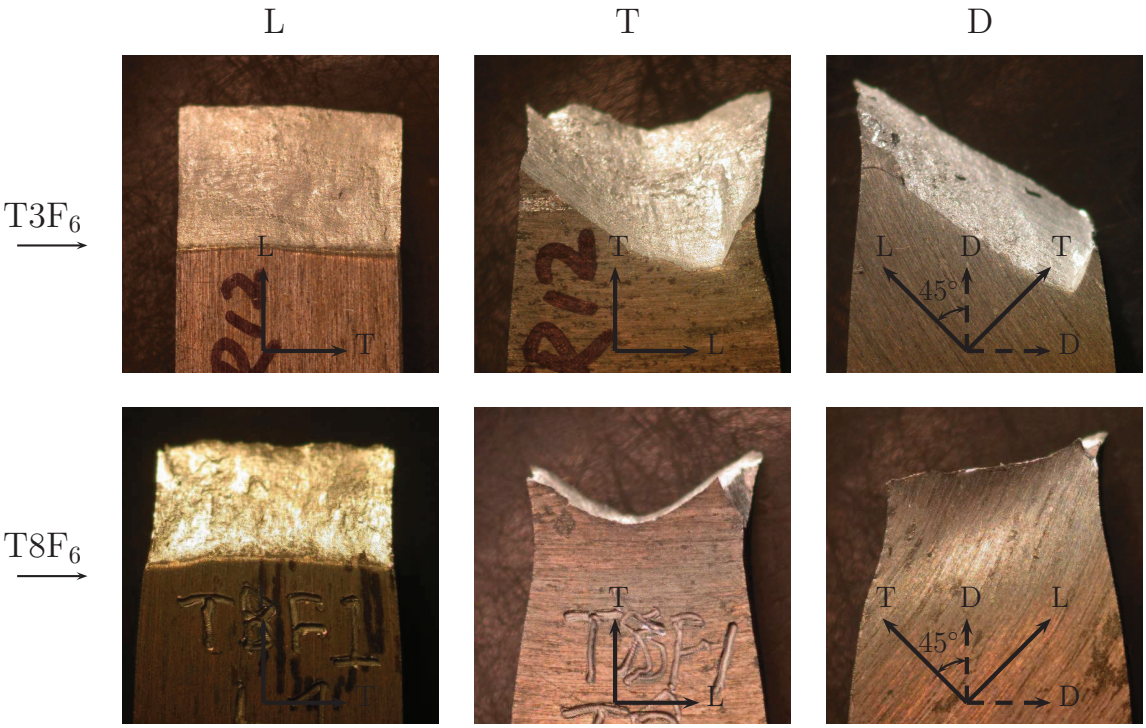
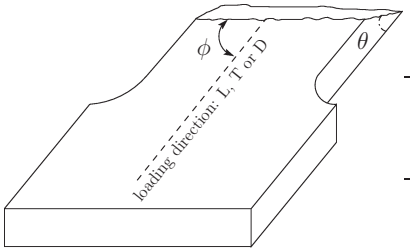


Figure 3.14: Post-test specimens of smooth flat tensile tests along L-, T- and D-loading for 6 mm thick fibrous materials.

Fig. 3.13 and Fig. 3.14 show the macroscopic fracture surface of broken samples along L-, T- and D-loading directions for recrystallized materials and fibrous materials respectively. For L-loading, all materials exhibit very similar fracture surfaces which are perpendicular to loading direction; angle ϕ is near 90°. In T-loading, recrystallized materials have similar fracture surface as corresponding L-loading samples whereas for fibrous materials, more complex fracture surfaces were observed due to stronger necking (see Fig. 3.14 of medium column). For D-loading, fracture surface is inclined both in sheet plane and thickness direction.

Observed fracture angles for T8F condition material (2 and 6 mm) are shown on Fig. 3.15-b. For T and D loading ϕ is close to the theoretical value whereas it is equal to 90° for L loading. Note that θ is not equal to 90°. Similar trends are observed for T3-state except in the case of L load-

ing where θ is significantly lower and equal to 36°. Necking is also an important factor to consider. Large necking is obtained for D loading whereas it is less pronounced for L and T loading. Once again L loading for the T3 state is a special case: necking is not observed. Analysing fracture surface on NT specimens is more difficult. However trends in terms of ductility (i.e. necking) and fracture angles are consistent with observations made on ST specimens.



(a)

	ϕ	θ	ϕ_{th} (T3F$_a$)	ϕ_{th} (T8F$_a$)
L	90°	40–45°	50.9°	52.0°
T	54°	57–65°	58.3°	56.3°
D	57–60°	45–50°	54.7°	55.1°

a: 2 and 6 mm

(b)

Figure 3.15: (a) Schematic view of the fracture plane angles ϕ and θ. (b) Observed fracture plane angles (T8F$_a$) and comparison with the theoretical value for ϕ (eq. 3.5).

3.5.2 Fracture mechanisms at the microscopic level

Two main fracture types were observed using scanning electron microscopy (SEM) as exemplified in Fig. 3.16. The first one (type I) consists in a fibrous fracture surface associated with friction marks and involving failure at grain boundaries (Fig. 3.16-a, c). The second one (type II) consists in a classical dimple fracture surface where voids are initiated at iron containing phases. In the case of the investigated materials this type is always associated with the first one as shown on Fig. 3.16-b, d. Specimens in which a higher stress triaxiality ratio develops are expected to fail by pure dimple fracture. Pure type I fracture surface is observed for ST specimens tested along L and T direction as well as notched flat specimens in the T3 state and tested along the L direction. In all other cases type II is observed in test specimens. In particular it is present in ST specimens

tested along the D direction which exhibit significant necking. Notice that for reduced 2 mm-thick D-loading specimens which exhibit higher strain localisation, both fracture type I and type II can be observed (see Fig. 3.17).

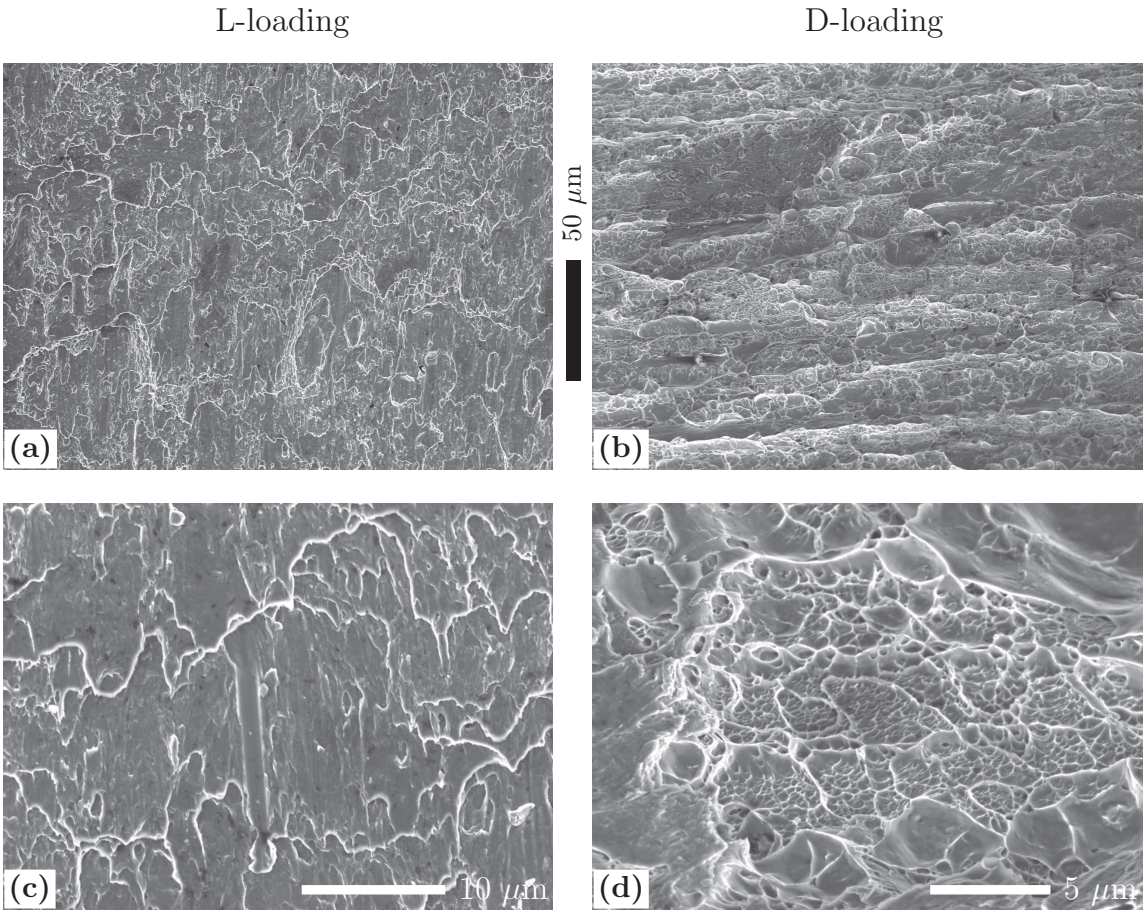


Figure 3.16: L-loading (a, c) and D-loading (b, d) smooth tensile specimen fracture surface for $T3F_6$ material via SEM observations.

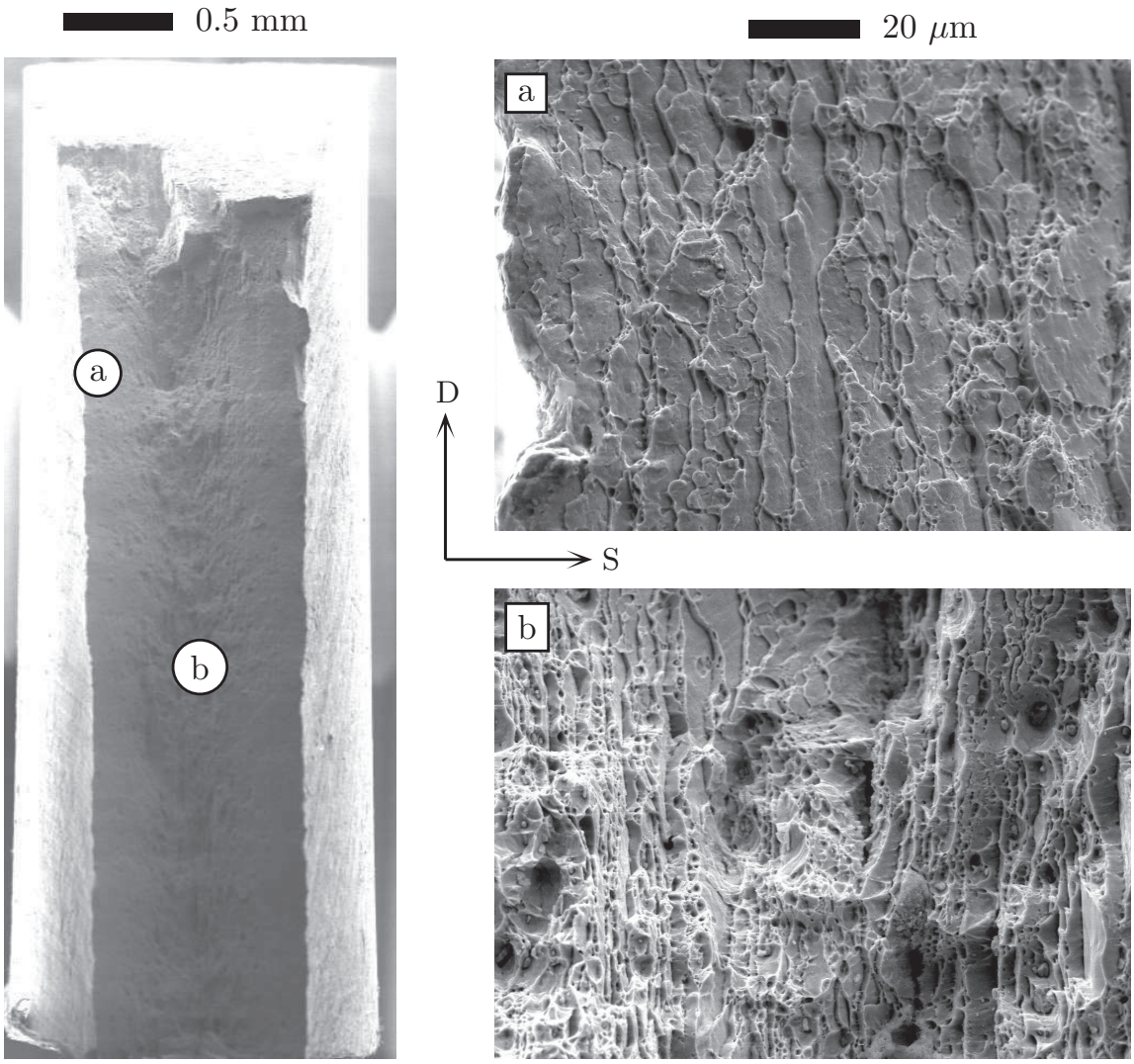


Figure 3.17: Smooth tensile specimen fracture surface of $T8F_{62}$ material in D-loading.

3.6 Modeling of plastic anisotropy

3.6.1 Constitute equations

The material under study presents a complex anisotropic plastic behaviour which cannot be represented by a simple quadratic yield surface such as the one proposed by Hill [47] which is unable to satisfactorily describe simultaneously yield anisotropy and Lankford coefficients in all directions. To overcome this difficulty, the yield condition proposed by Bron and Besson [19] is used in this work. This phenomenological yield function was developed to represent plastic anisotropy of aluminium alloy sheets. It is an extension of the functions given in Barlat *et al.* [11] and Karafillis and Boyce [54]. Plastic anisotropy is represented by 12 parameters in the form of two fourth order symmetric tensors. Four other parameters influence the shape of the yield surface uniformly. The model is based on the definition of an equivalent stress $\overline{\sigma}$ function of the stress tensor $\underline{\sigma}$:

$$\overline{\sigma} = (\alpha_1 \overline{\sigma}_1^a + \alpha_2 \overline{\sigma}_2^a)^{1/a} \tag{3.6}$$

with $\alpha_2 = 1 - \alpha_1$. $\overline{\sigma}_1$ and $\overline{\sigma}_2$ are respectively given by:

$$\overline{\sigma}_1 = \left(\frac{1}{2} \left(|S_1^2 - S_1^3|^a + |S_1^3 - S_1^1|^a + |S_1^1 - S_1^2|^a \right) \right)^{1/a} \tag{3.7}$$

$$\overline{\sigma}_2 = \left(\frac{3^a}{2^a + 2} \left(|S_2^1|^a + |S_2^2|^a + |S_2^3|^a \right) \right)^{1/a} \tag{3.8}$$

where S_1^1, S_1^2 and S_1^3 (resp. S_2^1, S_2^2 and S_2^3) are the eigenvalues of a modified stress deviator $\underline{s}_1$ (resp. $\underline{s}_2$) defined as: $\underline{s}_1 = \underline{\underline{L}}_1 : \underline{\sigma}$ (resp. $\underline{s}_2 = \underline{\underline{L}}_2 : \underline{\sigma}$) where the fourth order tensors $\underline{\underline{L}}_{1,2}$ have the

following form using Voigt notation:

$$\underline{\underline{L}}_k = \begin{pmatrix} (c_k^{\mathrm{LL}} + c_k^{\mathrm{SS}})/3 & -c_k^{\mathrm{SS}}/3 & -c_k^{\mathrm{LL}}/3 & 0 & 0 & 0 \\ -c_k^{\mathrm{SS}}/3 & (c_k^{\mathrm{SS}} + c_k^{\mathrm{TT}})/3 & -c_k^{\mathrm{TT}}/3 & 0 & 0 & 0 \\ -c_k^{\mathrm{LL}}/3 & -c_k^{\mathrm{TT}}/3 & (c_k^{\mathrm{TT}} + c_k^{\mathrm{LL}})/3 & 0 & 0 & 0 \\ 0 & 0 & 0 & c_k^{\mathrm{TL}} & 0 & 0 \\ 0 & 0 & 0 & 0 & c_k^{\mathrm{LS}} & 0 \\ 0 & 0 & 0 & 0 & 0 & c_k^{\mathrm{ST}} \end{pmatrix} \tag{3.9}$$

The yield surface is finally expressed as:

$$\Phi = \overline{\sigma} - R(p) \tag{3.10}$$

where $R(p)$ corresponds to the flow stress expressed as a function of the cumulated plastic strain p. $R(p)$ is expressed as:

$$R(p) = R_0 \left[1 + K_0 p + K_1(1 - e^{-k_1 p}) + K_2(1 - e^{-k_2 p})\right] \tag{3.11}$$

Parameter R_0 is set to the normalised yielding stress in rolling direction (L) for each material, K_0, K_1, k_1, K_2 and k_2 are all adjusted to fit the smooth and notched tensile tests.

3.6.2 Identification of material parameters

The identification of the various material parameters was performed following the procedure similar to the one proposed by Bron and Besson [19]. In order to identify parameters, tests carried out on ST specimens (L, T and D-loading) and NT specimens (L, T and D-loading) were used.

Step I – Optimization of ST tests

The elastic properties Young modulus E is set to 74 GPa and the Poisson's ratio is 0.3. This part of the optimization aims at adjusting the plastic hardening parameters (K_i and k_i) and the

anisotropic parameters c_i^k. As the yield function is optimized for thin sheets, c_i^5 and c_i^6 are taken equal to 1. The identification is carried out on ST_{12} tests along L, T and D direction. Measured Lankford coefficients were also included in the database of adjustment. This optimization step provides all values of parameters fitted to describe the anisotropy of strength and Lankford coefficients.

Step II – Optimization of ST and NT tests

As reported in the section of mechanical tests, NT specimens with different radii are used to identify the yield surface for an anisotropic material. This step is to optimize all parameters using ST and NT tests simulanetously. Added NT specimens are used to adjust the yield surface isotropic parameters a and α under triaxial stress condition. As 3D calculations of NT tests are much more costly, NT_2 tests along L and T direction are first added to smooth tensile ST tests in the database. Finally NT_1 tests are added to the optimisation database. Final optimized material parameters are gathered in Table 3.3 (elasticity and hardening) and in Table 3.4 (anisotropic plastic yield surface) for all materials.

Material	E (GPa)	ν	R_0 (MPa)	K_0	K_1	k_1	K_2	k_2
$T3R_2$	74	0.3	261	3.543	0.087	643	0.293	16.7
$T8R_2$	74	0.3	426	0	0.091	641	0.277	15.9
$T3F_6$	74	0.3	294	0	0.022	187	0.775	10.2
$T8F_6$	74	0.3	475	0	0.093	655	0.292	16.5

Table 3.3: Parameters identified for elastic behaviour and work hardening (Young modulus (in GPa) is pre-fixed, R_0 (in MPa) is set to the yield stress in rolling direction (L) for each material).

Material	a	α	c_1^1 c_2^1	c_1^2 c_2^2	c_1^3 c_2^3	c_1^4 c_2^4	c_1^5 c_2^5	c_1^6 c_2^6
$T3R_2$	16.1	0.680	1.125 0.631	1.149 0.691	0.721 1.386	0.905 1.170	1 1	1 1
$T8R_2$	13.7	0.700	1.097 0.693	1.130 0.752	0.811 1.295	1.006 1.055	1 1	1 1
$T3F_6$	17.8	0.716	1.186 0.467	1.028 0.666	0.461 1.478	1.129 1.252	1 1	1 1
$T8F_6$	16.9	0.700	1.216 0.683	1.195 0.798	0.638 1.512	1.249 1.281	1 1	1 1

Table 3.4: Parameters describing anisotropic yielding and plastic flow ($c_{i=1,2}^{5,6}$ were set a priori to 1 for thin sheets).

3.6.3 Results of the optimisation

Fig. 3.18 a shows a comparison between simulations and experiments in terms of the nominal stress F/S_0, and reduction of width, ΔW, as a function of elongation for smooth tensile along L, T and D direction for both recrystallized materials ($T3R_2$ and $T8R_2$). The nominal stress vs. elongation curves of experiments and simulations agree quite well except for L-loading on the transition between elastic and plastic zone. This can be explained by the presence of kinematic hardening together with pre-strainning along the L-direction [73]. This effect has been taken into account in [73, 101]. As the effect is smaller in our case, simpler isotropic hardening function can also give a satisfactory result. Fig. 3.18 b gives the simulation results for notched tensile tests in terms of the nominal stress F/S_0 as a function of notch opening displacement (NOD). A good agreement between experiments and simulations is also obtained.

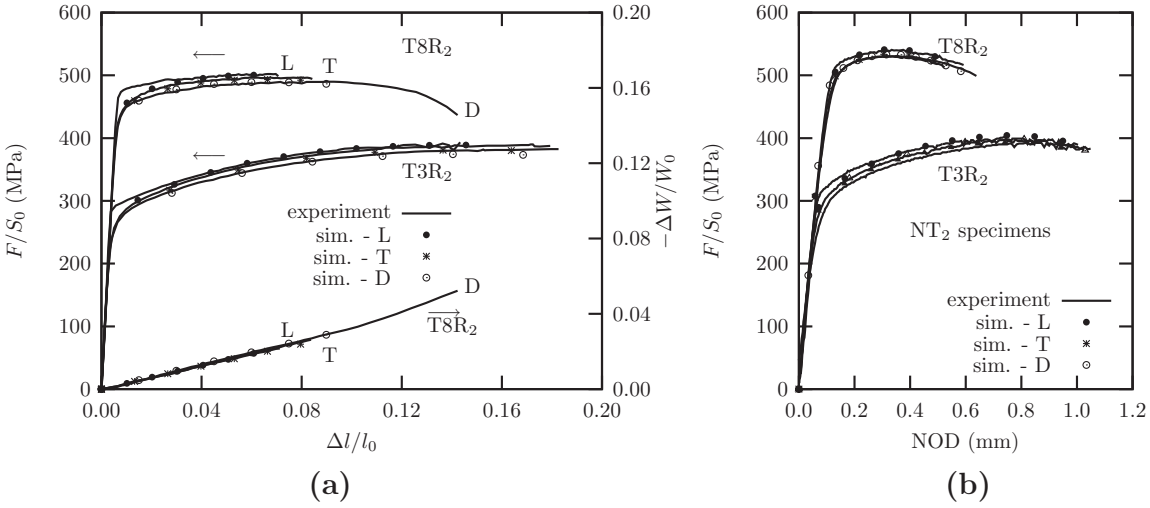


Figure 3.18: Comparison of experiments (lines) and simulations (symbols) for recrystallized materials in the case of smooth tensile tests (a) and notched tensile tests (b).

For strongly anisotropic fibrous materials, the identification results are shown in Fig. 3.19

and Fig. 3.20, respectively for $T3F_6$ material and $T8F_6$ material. The anisotropic behaviour is well reproduced by the Bron-Besson yield function. As reported in section 3.4, the sheet thickness has no influence on the elastic-plastic response for smooth tensile tests, however, has a strong structural effect on notched tensile tests due to a change in stress triaxiality. So in this part, we can use the fitted parameters of 6 mm-thick tests to predict reduced 2 mm-thick tests. The prediction results in comparison with experiments are shown in Fig. 3.19b, and in Fig. 3.20b.

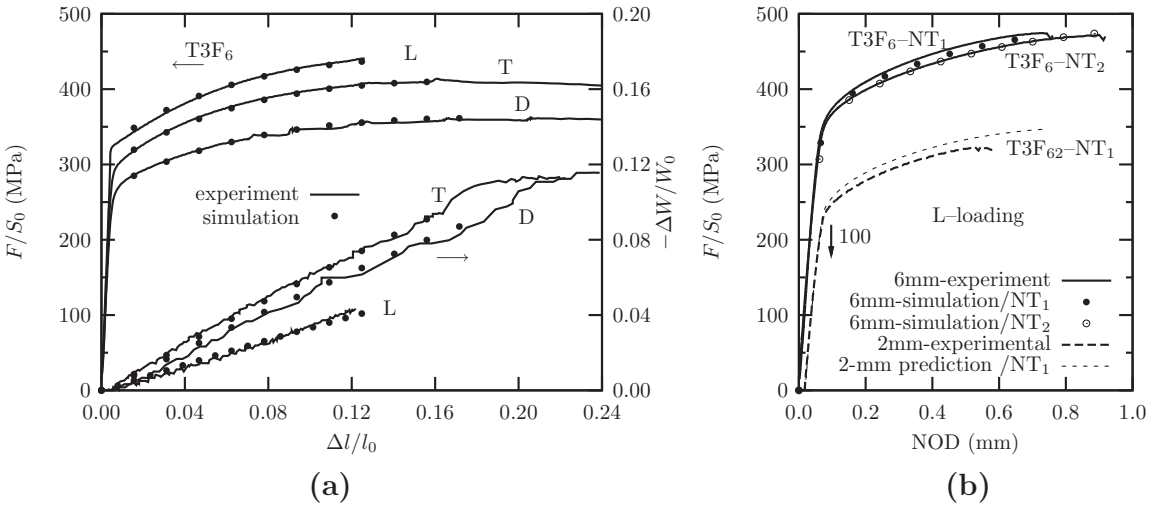


Figure 3.19: Comparison of experiments (lines) and simulations (symbols) for T3 fibrous materials in the case of smooth tensile tests (a) and notched tensile tests (b). For clarity curves corresponding to the $T3F_{62}$ -NT_1 case have been shifted 100 MPa along the vertical axis.

The shape of the yield surface can be represented in a normalised stress plane (σ_{TT}/R_0, σ_{LL}/R_0). Fig. 3.21 gives the difference in yield surface between von Mises criterion and Bron-Besson yield function. It is shown that material behaviour differs radically from the von Mises yield surface (solid line). The stress path corresponding to a material point located at the center of the notch at the free surface (i.e. $\sigma_{TL} = 0$, $\sigma_{SS} = \sigma_{TS} = \sigma_{SL} = 0$) is also plotted in this graph. This shows that NT_1 specimens allow to test biaxial stress states which strongly differ from uniaxial tension. These tests are useful for parameter identification as the yield surface strongly differs from

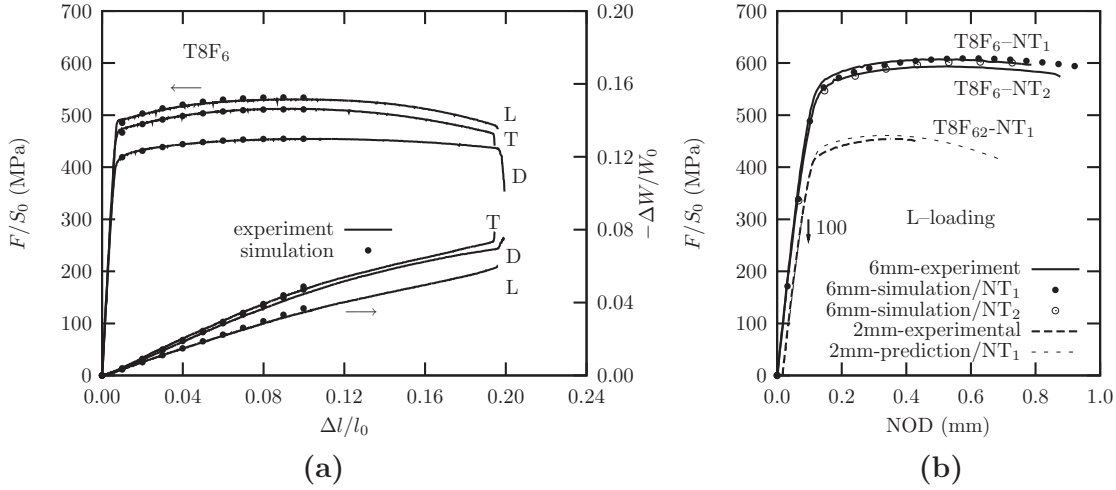


Figure 3.20: Comparison of experiments (lines) and simulations (symbols) for T8 fibrous materials in the case of smooth tensile tests (a) and notched tensile tests (b) [25]. For clarity curves corresponding to the $T8F_{62}$ -NT_1 case have been shifted 100 MPa along the vertical axis.

the von Mises ytield surfaces in this region.

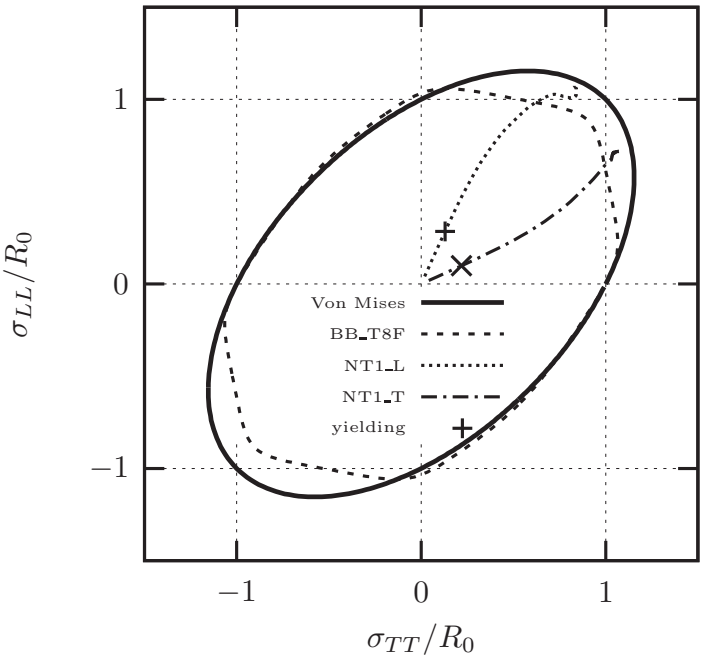


Figure 3.21: Normalised Bron-Besson yield surface (dashed line) compared with von Mises criterion (solid line). BB-T8F: Bron-Besson yield surface for fibrous material T8F. R_0 is set to the yield stress in L-direction (σ_L^0). NT_1_L: path of L–loading notched flat sample NT_1, NT_1_T: path of T–loading notched flat sample NT_1, yielding in NT_1 sample correspond to each loading direction (L and T).

3.7 Analysis of strain localisation

3.7.1 Rice's localisation indicator

In an infinite homogeneous medium, localization is assumed to occur when it becomes possible to form a strain rate discontinuity in a planar band. This band is characterized by its unit normal $\vec{n}$ and the displacement jump across the band whose direction is denoted $\vec{g}$. Note that the magnitude of the jump remains unknown.

In the case of elastoplastic materials, the incremental constitutive equation can be expressed as:

$$\underline{\dot{\sigma}} = \underline{\underline{L}} : \underline{\dot{\varepsilon}} \tag{3.12}$$

where $\underline{\underline{L}}$ is the elastoplastic tangent matrix linking the stress rate $\underline{\dot{\sigma}}$ to the strain rate tensor $\underline{\dot{\varepsilon}}$. Writing the continuity of displacements and the stress equilibrium, it can be shown [86, 87] that the jump of the deformation tensor is expressed as: $\frac{1}{2}(\vec{g} \otimes \vec{n} + \vec{n} \otimes \vec{g})$ and that the condition for bifurcation is written in the case of finite strains (assuming a Jauman stress rate in eq. 3.12) as:

$$\exists \vec{n}, \;\; \det(\underline{A}(\vec{n})) = 0 \tag{3.13}$$

$$\text{with} \quad \underline{A}(\vec{n}) = \vec{n}.\underline{\underline{L}}.\vec{n} + \underline{R}$$

$$\text{and} \quad 2\underline{R} = -\vec{n} \otimes (\vec{n}.\underline{\sigma}) + (\vec{n}.\underline{\sigma}) \otimes \vec{n} + (\vec{n}.\underline{\sigma}.\vec{n})\underline{1} - \underline{\sigma}$$

$\vec{g}$ is then the eigenvector of $\underline{A}(\vec{n}) + \underline{R}$ corresponding to the eigenvalue equal to zero.

Based on the previous localisation condition, a localisation indicator can be defined as:

$$I_l = \min_{\vec{n}} \det(\underline{A}(\vec{n})) \tag{3.14}$$

This indicator can be used to post-process finite element simulations to detect localized zones corresponding to $I_l \leq 0$ where fracture is likely to occur [15, 16]. The actual localization band orientation does not always correspond to the orientation given by the analysis (i.e. $\vec{n}$) which assumes a uniform stress and strain state in an infinite medium whereas gradients exist in practical applications.

3.7.2 Plastic model with damage

Material softening is needed to trigger localization. In this work this is achieved by coupling the anisotropic plasticity model with the Gurson-Tvergaard-Needleman (GTN) model [112] as already done in [20, 104, 73]. The yield surface is now expressed as:

$$\Phi = \frac{\overline{\sigma}^2}{R^2} + 2q_1 f \cosh\left(\frac{q_2}{2}\frac{\sigma_{kk}}{R}\right) - 1 - q_1^2 f^2 = 0 \tag{3.15}$$

where f represents porosity. q_1 and q_2 are model parameters taken equal to 1.5 and 1. respectively. As tomography does not evidence initial cavities, the initial value for f was taken equal to 0. On the other hand, voids can be nucleated on intermetallic phases. It is assumed here that strain controlled nucleation linearly generates 1% porosity for plastic strains p up to 0.2 ; above this limit nucleation stops.

Using these simple assumptions fracture of the various specimens cannot be reproduced. It is therefore assumed that softening by void nucleation and growth will generate zones where strain localization is possible. Inside these localization bands damage nucleation (e.g. by grain boundary decohesion or by nucleation on strengthening particles) will lead to rapid fracture.

3.7.3 Results

Finite element simulation of the various specimens was performed using the *Zset* software [14, 36]. Meshes were constructed using 20 nodes bricks with reduced integration (8 Gauss points). Details about the computation procedure can be found in [15]. Symmetries were used to reduce the problem size. In the following crack paths are predicted by determining zone where I_l is negative (black areas in Fig. 3.22, Fig. 3.23 and Fig. 3.24).

L loading: Fig. 3.22 compares the experimental and simulated macroscopic fracture paths. A good agreement is found for the T8 condition. In particular the fact that $\phi = 90°$ is well reproduced. This is attributed to the low value of the Lankford coefficient (Table 3.1) which

favors necking along the thickness direction thus leading to almost plane strain state along the T direction. In the case of the T3 condition failure occurs before necking as reported above. Before necking I_l always remain positive so that failure cannot be predicted by the present analysis. A possible explanation for this anomalous behaviour is the presence of DSA and PLC effect. In addition PLC effect [72, 100, 99] can be anisotropic thus explaining the difference between L loading and T or D loading.

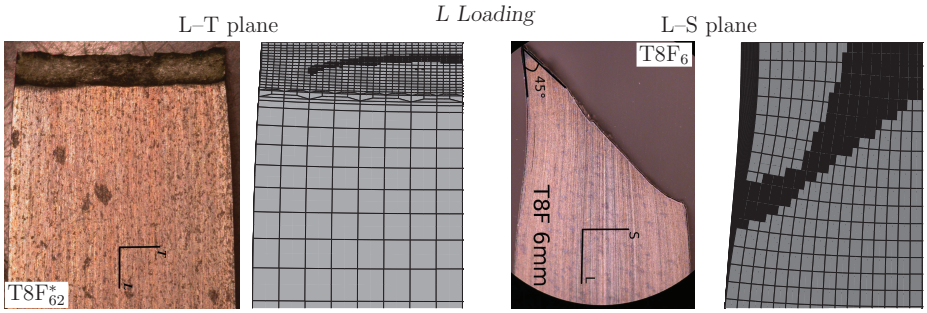


Figure 3.22: Experimental and simulated fracture path for L loading.

T loading: Fracture paths are compared on Fig.3.23 showing general good agreement. The simulation well reproduces the complex crack orientation.

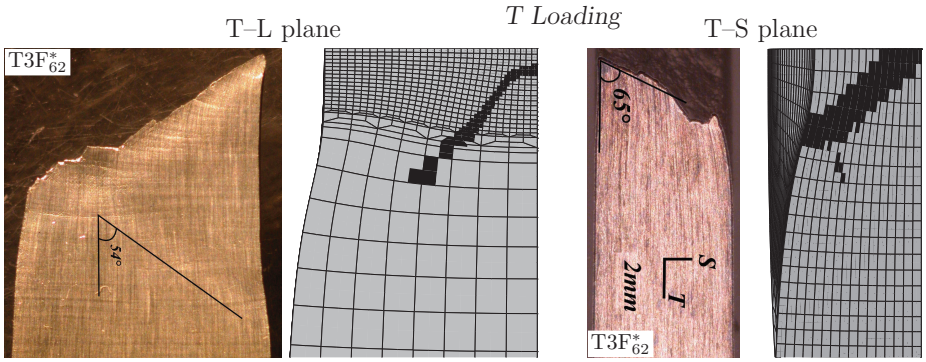


Figure 3.23: Experimental and simulated fracture path for T loading.

D loading: This case is more difficult because the problem has fewer symmetries so that half of the specimen must be meshed. The through thickness crack path is well reproduced whereas two different directions are predicted (white dashed lines on Fig. 3.24). One of these directions corresponds to the fracture orientation.

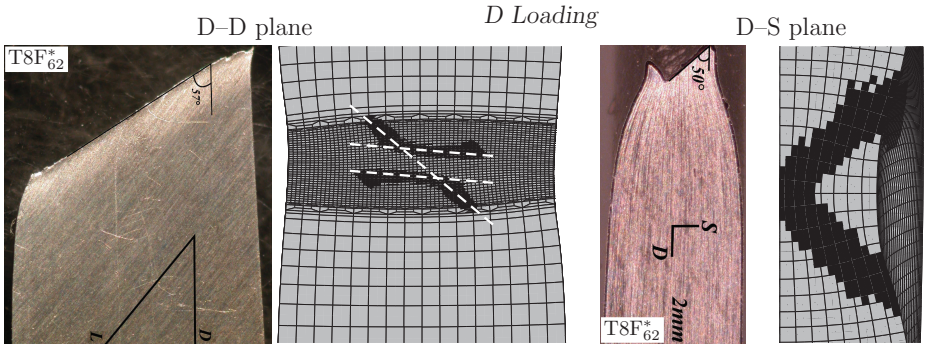


Figure 3.24: Experimental and simulated fracture path for D loading.

The proposed analysis also reproduces the fact that the deformation level required to trigger band localization and fracture is low for L loading, intermediate for T loading and high for D loading.

3.8 Conclusions

In this chapter plastic and fracture behaviour of four AA2198 sheet materials were investigated experimentally and numerically. Smooth and notched flat tensile specimens were used for mechanical tests. For both recrystallized and fibrous materials, T8 state materials have a much higher strength but lower ductility and hardening capacity than T3 materials. All tested materials present an anisotropic behaviour in terms of stress and deformation with L direction being the strongest while D direction is the weakest. In the case of both 6 mm-thick fibrous materials ($T3F_6$ and $T8F_6$), the plastic anisotropy is much stronger than in the case of both 2 mm-thick recrystallized

materials ($T3R_2$ and $T8R_2$).

At the same time, strain rate sensitivity was investigated. At room temperature, a slightly negative strain rate sensitivity (DSA effect) was observed in all tested materials. This effect becomes a normal positive effect at a higher temperature (120° C) in the tested T3 fibrous material. The presence of DSA effect may have an influence on the onset of necking. However, associated with material's strongly anisotropic texture which has also a strong effect on the strain localisation of materials. Such an investigation is too complex and is beyond the scope of the current work.

The sheet thickness effect on smooth and notched tensile tests is examined experimentally. It is shown that reducing sheet thickness does not modify the elastic-plastic behaviour of materials. Thin sheets keep the same level of strength and anisotropy as thick samples. However reducing sheet thickness decreases significantly material's apparent ductility.

The plastic anisotropy of all tested materials can be well represented by the model proposed by Bron and Besson both in terms of strength and Lankford coefficients. The fitted parameters on 6 mm-thick fibrous materials can well predict the elastic-plastic behaviour of thinner tests (2 mm-thick notched samples).

Macroscopic fracture paths as well as microscopic fracture surfaces were investigated. It is shown that fracture path mainly depends on loading direction and to a lower extend on heat treatment and sample thickness. At microscopic level, two different fracture types were identified. One consists in a fibrous fracture surface associated with friction marks and involving failure at grain boundaries and the second one consists in a classical dimple fracture surface where voids are initiated at iron containing phases.

A localization indicator based on Rice's bifurcation analysis is used to predict and interpret experimental fracture paths. The analysis shows that failure of smooth flat specimens is essentially governed by anisotropic plasticity which accounts for the differences observed for L- and T- or D- loading. The analysis also indicates that this failure mechanism does not control failure for

L-loading in the T3 fibrous material where necking is not observed.

The database collected in this part will be used for the analysis of ductile tearing behaviour of materials and the simulation of ductile tearing in the following chapters.

3.9 Résumé

Le chapitre 3 est consacré à l'étude expérimentale du comportement anisotrope plastique des quatre matériaux étudiés (deux nuances R2 et F6, et deux traitements thermiques T3 et T8). Les propriétés mécaniques anisotropes des matériaux sont liées au processus de laminage des tôles minces. La caractérisation de cette anisotropie est essentielle pour l'étude de ces tôles. Dans ce chapitre, nous présentons les éprouvettes utilisées pour les essais mécaniques, la procédure d'expérimental, les conditions d'essais et les résultats expérimentaux. La sensitivité de la vitesse de déformation a également été étudiée. Enfin, l'effet d'épaisseur sur la plasticité et l'endommagement a été aussi examiné dans cette partie. Les essais mécaniques sont effectués sur les éprouvettes lisses (ST) et entaillées (NT) selon différentes directions de prélèvement dans le plan de tôle. Les résultats montrent que la direction longitudinale L est la plus dure et la direction diagonale D est la plus molle. Cette anisotropie est plus marquée pour les tôles fibrées que pour les tôles recristallisées. Pour les éprouvettes entaillées, on constate que plus l'entaille est aiguë, plus la charge augmente, plus la ductilité diminue. Les essais de traction lisse à différentes vitesses, réalisés pour caractériser l'effet de vitesse en température ambiante et à $120°C$, montrent qu'un léger effet de sensibilité négative à la vitesse (manifestation du vieillissement dynamique de l'effet Portevin-LeChatelier (PLC)) est observé dans tous les matériaux à température ambiante. Dans la deuxième partie de ce chapitre, les mécanismes de rupture des éprouvettes ST et NT ont été examinés via des observations métallographiques sur les coupes d'éprouvettes dans la direction d'épaisseur. L'orientation des faciès de rupture dépend non seulement du matériau testé mais également de la direction de trac-

tion. Le microscope électronique à balayage (MEB) a été utilisé pour l'étude fractographique de la rupture. La troisième partie est consacrée à l'identification numérique de l'anisotropie plastique des matériaux. Le critère d'anisotropie, développé par Bron et Besson (2004), permet de représenter de manière remarquable le comportement plastique de tous les matériaux pour les tôles utilisées. Enfin, un indicateur de localisation de déformation d'après l'analyse de Rice (1976, 1980) a été utilisé pour prédire l'orientation des plans de rupture à l'aide de la méthode des éléments finis.

Chapter 4

Ductile Tearing

4.1 Introduction

Airplane designers estimate the fracture resistance of fuselage skin thin sheets using ductile crack growth resistance tests. Large center-crack tension panels M(T) are usually used to obtain a stable crack propagation under Small Scale Yielding (SSY) condition. This is a standard R-curve test used by aircraft manufacturer to qualify aluminium alloys [4]. However, in some conditions this test could possibly be replaced by small sized Kahn tear test specimens proposed by ASTM [5]. It also allows a stable crack propagation but under Large Scale Yielding (LSY) conditions. The transferability from Kahn specimens to M(T) panels has been studied in detail by several authors; Bron *et al.* in [21] on AA2024 materials showing that both small Kahn samples and large M(T) panels have similar failure mechanisms. The transferability was checked using an extension of the Rousselier model [91]. In the study of Morgeneyer *et al.* [73] on an AA2139 aluminium alloys, Gurson-Needleman-Tvergaard type damage model was used to fit model parameters by using microstructural and deformation data and crack extension on small Kahn test samples. Recently Pirondi and Fersini [82] used the crack tip opening angle (CTOA) criterion to simulate large M(T) tests. The transferability from Kahn tests to M(T) panels was examined in both cases. The

use of small Kahn specimens rather than large center-cracked panels M(T) significantly decreases the required amount of material as well as the time cost.

In this part, the results of tests on different kinds of tearing samples, small sized Kahn tear specimens, mixed-mode loading Arcan samples and large panels M(T) , are given. Most ductile tear tests in this work have been carried out using Kahn specimens. The experimental results will be shown and compared on different materials along different loading conditions. Thickness effect on material's fracture toughness are investigated via Kahn tear samples on both fibrous materials ($T3F_6$ and $T8F_6$). The macroscopic fracture surfaces are characterized using polish cross sections of broken samples. Scanning electron microscopy was used to analyse fracture mechanisms at microscopic level. X-ray tomography scanning including gallium wetting of arrested cracks in Kahn tear samples are also conducted.

4.2 Mechanical testing conditions and testing specimens

The ductile tear experiments are performed by using three kinds of tearing specimens, small sized Kahn specimens, mixed-mode loading Arcan specimens and large panels M(T) (see Fig. 4.1 for geometrical parameters).

In this work, the small Kahn tear samples [5] are the main tear tests carried out. The testing conditions are similar as in [19]. Kahn tear samples are made by electrical-discharge machining and not precracked. The radius of the notch root is less than 60 μm. The test consists of tearing the specimen with two pins. The cross head speed is 0.1 mm/min. In order to measure the crack growth rate, two techniques are used in this work. The first one is the classical method as described in the work of Bron [18], straight lines parallel to the loading direction are drawn each millimeter from the notch root to enable crack length measurements on pictures taken with a fixed digital camera. The second is based on Digital Image Correlation (DIC) techniques. In this work, predefined

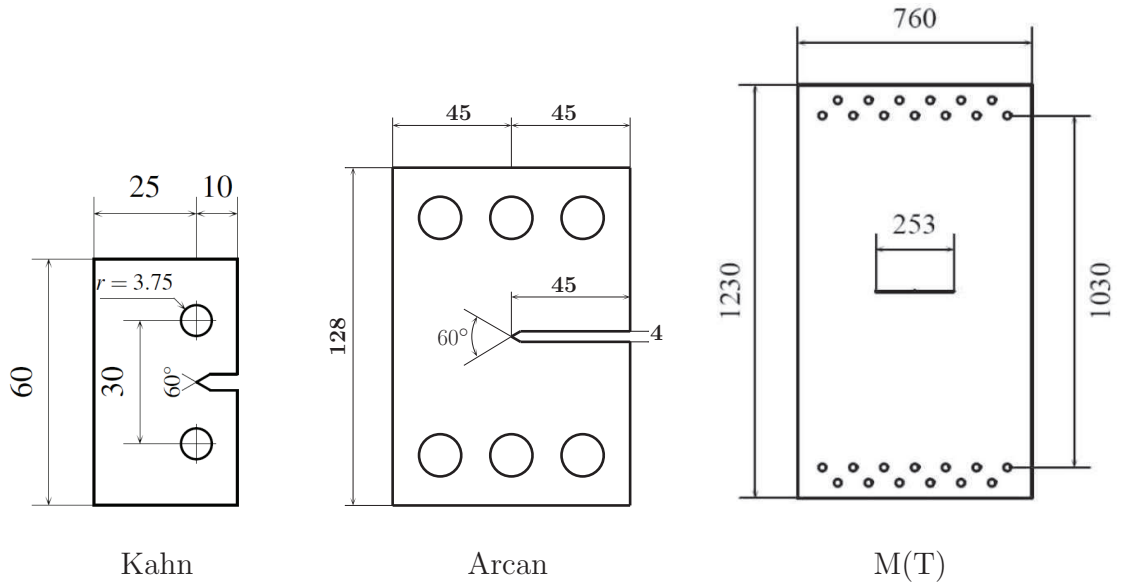
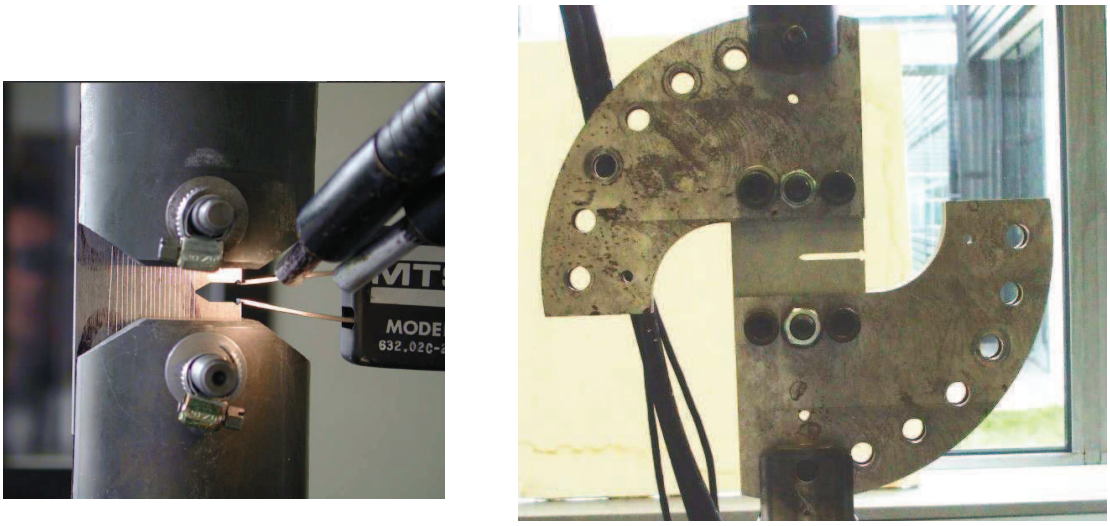


Figure 4.1: Specimen geometries of Kahn samples [5], Arcan samples [89] and M(T) samples [4] (all dimensions in mm).

markers were made to measure crack growth rate and the local displacement in the vicinity of the V-notch using the first method, the measured crack growth rate is relative to the initial geometry. The crack growth rate measured on the initial geometry is very close to the results measured on the deformed geometry [21] as deformation along the crack growth direction is very small. The setup of a Kahn specimen with the classical measurement technique of crack growth is shown in Fig. 4.2 a.

The tear properties of aluminium alloy sheets usually depend on the specimen orientation and the direction in which the force is applied relative to the grain orientation in the specimen. The specimen orientation and loading direction is identified by the following two letter code system: the first letter designates the direction of loading, while the second letter designates the direction of crack propagation. For both 2 mm thick recrystallized materials ($T3R_2$ and $T8R_2$), Kahn tear tests are carried out in L-T (loading in L direction, crack growth in T direction) and T–L (loading in T direction, crack growth in L direction) loading configurations. For both fibrous materials ($T3F_6$ and



(a) (b)

Figure 4.2: (a) Setup of Kahn tear test (b) setup of mode I loading Arcan tear test, the crack growth is recorded by digital camera.

$T8F_6$), additional D–D loading samples are also tested. The definition of different Kahn loading directions can be seen in Fig. 4.3. Notice that D–D loading sample is not symmetric with respect to the crack extension direction.

The Arcan specimens with mixed mode loading device were first developed by Richard [89]. Arcan samples were used to study the material's fracture behaviour under mixed-mode loading. Note that even for pure mode I macroscopic loading, local mixed-mode (I+III modes) can be observed in the case of slant fracture for thin sheet metals. The reason why slant fracture occurs is still not well understood. Several experimental studies [125, 83] introduced an external shear loading (mixed-mode loading) to modify the local state of stress triaxiality to promote one mechanism over another (internal necking and void sheet). The purpose of those tests is to shed some light on the ductile mixed-mode fracture process, its underlying mechanics and influence on crack extension path. Detail investigation of mixed-mode ductile fracture has been done on an AA2024 thin alloy by Madi *et al.* [64]. In the present study, mixed-mode tests were performed only on

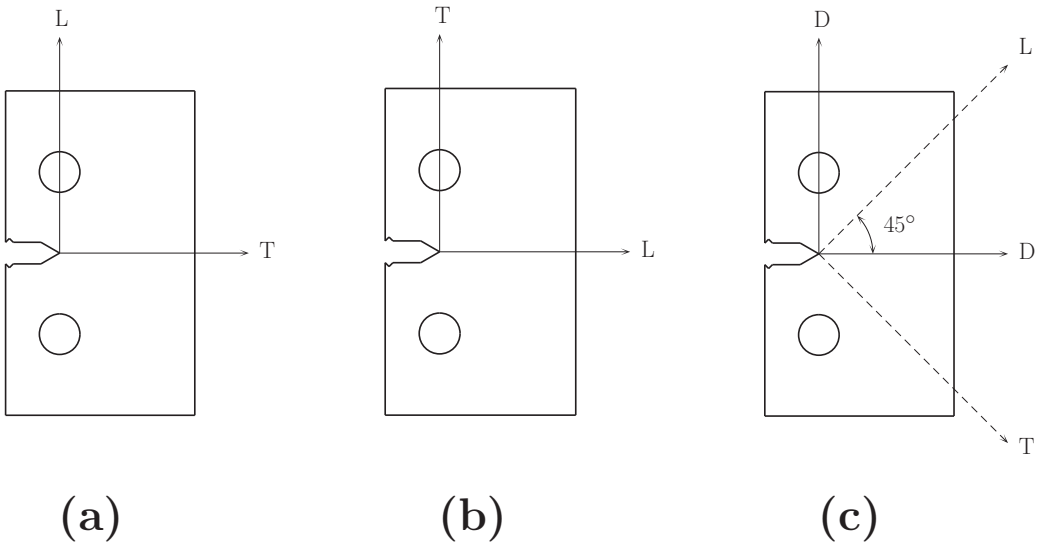


Figure 4.3: Kahn tear testing configurations (a) L-T loading (b) T-L loading and (c) D-D loading (L: rolling direction, T: long–transverse direction and D: diagonal direction in sheet plane).

fibrous material with T8 condition ($T8F_6$) which exhibits unstable crack propagation on small sized Kahn samples. 2 mm thin recrystallized materials were not tested due to problem of buckling on mixed mode loading using the current device (Fig. 4.2 b). Arcan specimens are tested using two loading direction (L-T and T-L, same signification as Kahn sample) and three loading angles 90°, 60° and 30° with respect to the initial crack axis as defined in Fig. 4.4. The case of 90° loading corresponds to the pure mode I test as Kahn tear tests. However their boundary condition is not the same (see Fig. 4.2 b). Kahn tear test specimens are loaded in bending while Arcan tear tests are loaded in tension. As shown in Fig. 4.4, the smaller loading angle is the closer is to pure shear loading (mode II). Fig. 4.5 shows the setup of an Arcan test in 30° loading angle during the tests (with Digital Image Correlation).

M(T) tests (R-curve) are carried out in both L–T and T–L loading configurations on both high strength artificially aged materials ($T8R_2$ and $T8F_6$). M(T) tests were not conducted on two naturally aged materials ($T3R_2$ and $T3F_6$, medium strength), because heat treated materials ($T8R_2$

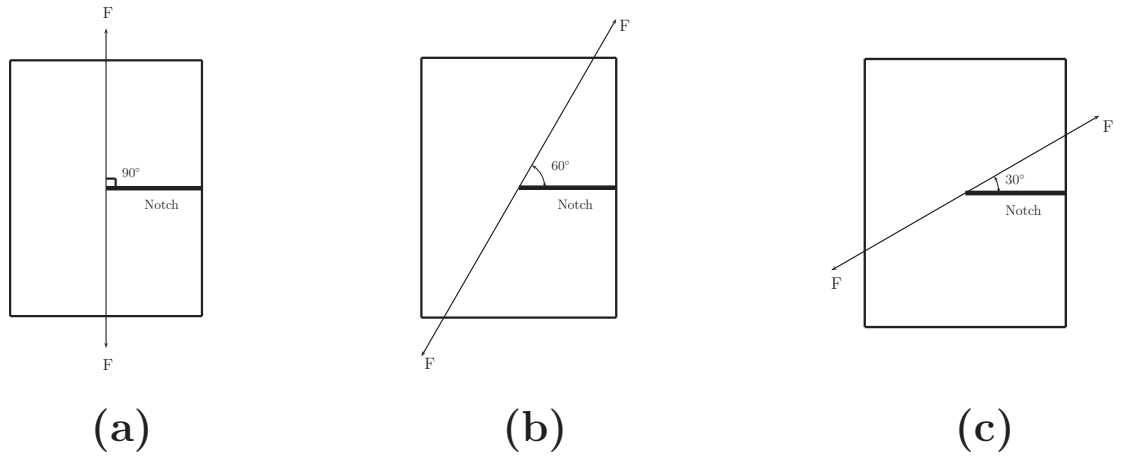


Figure 4.4: Arcan tear tests loading angles Arcan-90° (a) Arcan-60° (b) Arcan-30° (c).

and $T8F_6$) are only ones used for industrial applications due to their high σ_y/E ratio. The mechanical tests were performed at Alcan CRV research center, a displacement gage is used to measure the crack-opening displacement across the crack mouth. The initial gage length is 60 mm. A 1000 kN load cell is used and the cross head speed is 0.1 mm/min. Due to the limited load capacity of the testing machine (maximum load is 1000 kN), the original 6 mm-thick fibrous sheets were machined down to 5 mm thick panels for M(T) tests for both L-T and T-L testing.

4.3 Experimental results and analysis

4.3.1 Kahn tear tests

Recrystallized materials: Fig. 4.6 displays the results of the Kahn tear tests in terms of nominal stress (loading force F divided by the initial ligament area S_0) as a function of the crack mouth opening displacement (CMOD) in L-T and T-L testing orientations for the $T3R_2$ and $T8R_2$ materials. For the $T3R_2$ material (Fig. 4.6a), T-L tests have same level of nominal stress as L-T tests up to maximum loads (indicating similar initiation toughness). However in the propagation

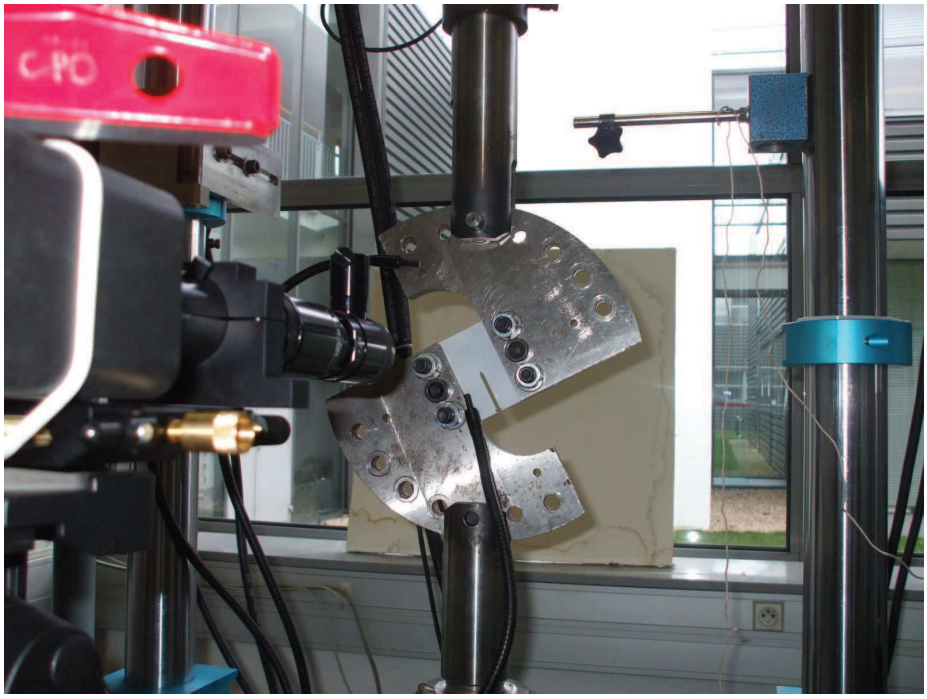


Figure 4.5: Setup of an Arcan mixed-mode loading specimen with Digital Image Correlation (DIC) device.

region L-T sample is tougher than T-L loading sample. The unit initiation energy (UIE, defined as the integral $\int \frac{F}{S_0}\,\mathrm{d}\delta$ [34], where $d\delta$ is the pin displacement, taken from the start of the test to maximum load, see Fig. 4.6a) was measured. The measured UIE for all studied materials is shown in Table 4.1. For $T3R_2$ material the L-T and T-L samples have very similar UIE. In the case of T8R material (Fig. 4.6b), the nominal stress is very similar for both testing orientations up to the maximum load of the T-L sample. The maximum load of the L-T sample is slightly higher than T-L sample, whereas results in the UIE is 40 % higher than for the T-L loading. In the crack propagation region, similar trends are observed as in $T3R_2$ material: L-T loading sample is tougher than T-L loading test. Notice that with Kahn samples both recrystallized materials can obtain a stable crack propagation along both L-T and T-L loading. The crack growth paths and validity of tests are shown in Table 4.2. Stable crack propagation means that the crack is only growing when the applied dis-

placement is increased and crack propagation can be stopped when the displacement is kept constant or decreases. The specimen is in a stable condition. By contrast, unstable crack propagation means that the crack grows without displacement increase. The specimen is in a unstable condition. If it is not arrested after some propagation it will cause the catastrophic failure of the specimen.

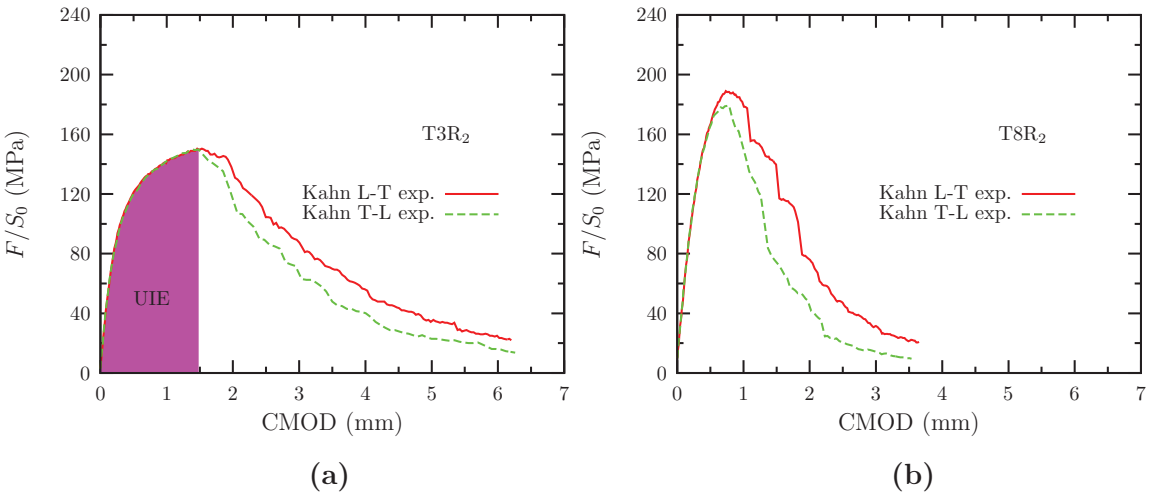


Figure 4.6: Experiments on Kahn tear tests in the case of T3R$_2$ material (a) and T8R$_2$ (b), nominal stress (F/S_0) as a function of the crack mouth opening displacement (CMOD).

Fibrous materials: Fig. 4.7 shows the experimental results of Kahn tear tests in the case of both fibrous materials (T3F$_6$ and T8F$_6$). For the T3 material, before the crack initiation, L-T configuration loads are slightly higher than in T-L configurations which is consistent with the results of smooth tensile tests whereas this difference is clearly lower than the corresponding anisotropy measured for the smooth tensile tests. Stable and straight crack extension is observed in T-L loading test. For L-T loading, the crack extension is stable but presents a strong bifurcation. In the crack propagation region, the difference between L-T and T-L samples is not significant; both loading directions have very similar toughness. T-L sample reached at slightly increased pin displacement ($d\delta$), the UIE is only 5 % higher for T-L loading than for L-T loading. In the case of T8 condition

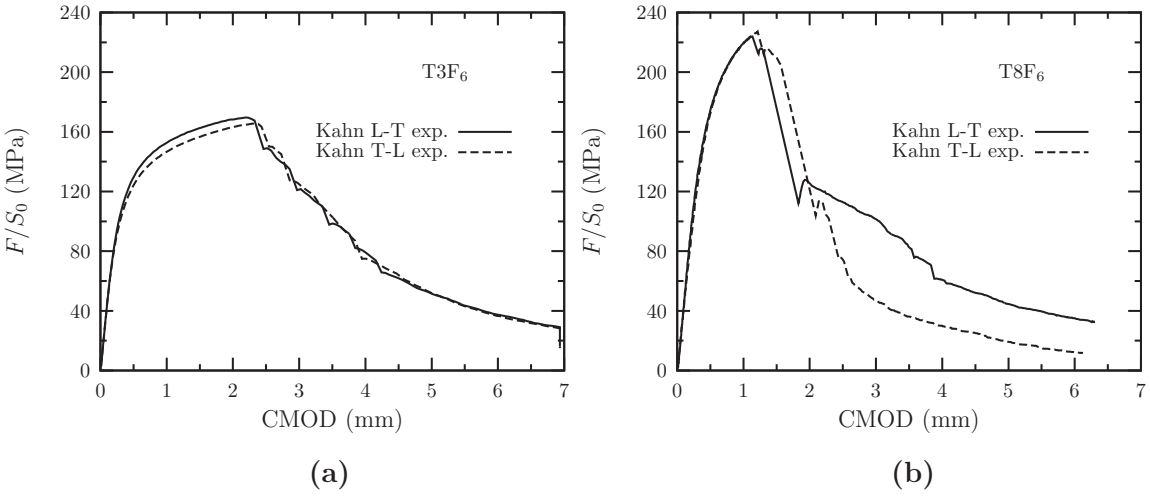


Figure 4.7: Experiments on Kahn tear tests in the case of $T3F_6$ material (a) and $T8F_6$ (b), nominal stress (F/S_0) as a function of the crack mouth opening displacement (CMOD).

fibrous material (Fig. 4.7b), in the crack initiation region, similar trend is observed as in T3 condition material except that the anisotropy is smaller, it is also consistent with the corresponding results of notched tensile tests in terms of loads. However, the crack extension is unstable in both L-T and T-L loading configurations, pop-ins and very strong crack bifurcation were observed during tests. The tests are less reproducible than for $T3F_6$ material; deviation is observed in L-T and T-L tests. According to the ASTM B871 standard [5] tests with strong crack bifurcation are not valid. The validity of tests is shown in Table 4.2. The crack path morphology of all tested materials and loading configurations can be seen in Fig. 4.10. In order to investigate the crack bifurcation and delamination problem, complementary tests are carried out on thinner samples for $T8F_6$ material. The experimental results will be shown and analysed in section 4.4.

4.3.2 Arcan testing

Fig. 4.8 shows the Arcan tear testing results of $T8F_6$ material for 90° loading (Fig. 4.8a) and 60° loading (Fig. 4.8b), respectively. For 90° loading (Mode I), in the crack initiation region,

Material	$T3R_2$	$T8R_2$	$T3F_{62}$	$T3F_6$	$T8F_{62}$	$T8F_{63}$	$T8F_{64}$	$T8F_6$
t (mm)	2	2	2	6	2	3	4	6
L–T (N/mm)	166	116	195	320	124	139	153	175
T–L (N/mm)	165	83	180	337	134	———	———	177

Table 4.1: Unit initiation energy (UIE) (N/mm) of Kahn tear tests for recrystallized materials and fibrous materials with different specimen thicknesses and loading orientations (L–T and T–L).

a similar trend is observed as for corresponding Kahn tear tests: in the propagation region, L–T loading samples are clearly tougher than T–L loading. However, the crack extension is still unstable especially in the case of T–L configuration loading, where an abrupt crack progression of several mm took place. However, the crack bifurcation is less pronounced than for L-T loading. Fig. 4.8b is for 60° loading (mode I+II) tests. The maximum load of both directions (L–T and T–L) is higher than 90° loading samples. There are no significant difference in the initiation region whereas in the crack propagation region, similar results are obtained as in Arcan 90° T-L loading tests. Specimen fails after a small crack extension length. The combination of tensile stress with shear stress which promotes the void sheet formation [37, 7] results in an abrupt failure of specimen. For 30° loading specimens, the crack initiates at the loading holes of specimen, due to a strong shear force, the sample are deformed strongly along loading direction in the head sections. Testing results cannot be used. The experimental results are not presented here.

In order to examine the initial crack tip effect on tear properties of the material, several Arcan specimens were precracked by fatigue (fatigue crack length $a_0 \approx 8$ mm). Tests are performed along T–L configuration for which unstable crack extension was observed during Kahn tests and initially un-precracked Arcan tests. The testing conditions (tension loading) and the radius of initial crack tip is much more similar to M(T) test. For un-precracked Kahn specimens, initial crack tip radius is much larger and exhibits a lower stress triaxiality and larger disturbed plastic zone than

Material	$T3R_2$	$T8R_2$	$T3F_{62}$	$T3F_6$	$T8F_{62}$	$T8F_{63}$	$T8F_{64}$	$T8F_6$
t (mm)	2	2	2	6	2	3	4	6
validity (L–T)	valid	valid	valid	strong deviation	valid	slight deviation	strong deviation	not valid
pop-ins (L–T)	no pop-ins	pop-ins	no pop-ins	no pop-ins	pop-ins	pop-ins	pop-ins	pop-ins
validity (T–L)	valid	valid	valid	slight deviation	zig-zag crack	———-	———	not valid
pop-ins (T–L)	no pop-ins	pop-ins	no pop-ins	no pop-ins	pop-ins	———-	———	pop-ins

Table 4.2: Validity of Kahn tear tests and presence of pop-ins during tests.

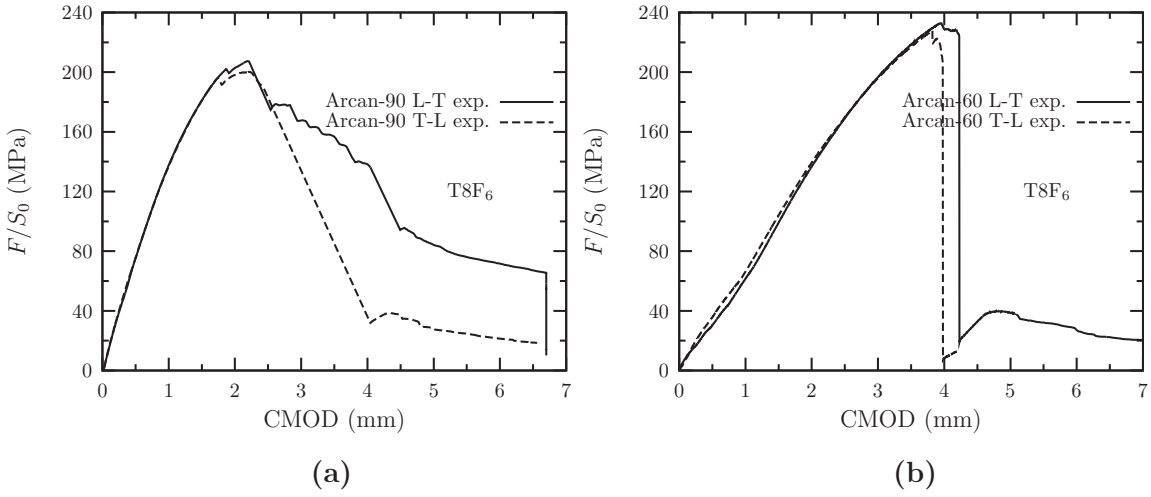


Figure 4.8: Arcan tests for 90° loading (a), and 60° loading samples (b), nominal stress (F/S_0) as a function of the crack mouth opening displacement (CMOD).

precracked M(T) specimens. It is important to note that Kahn tear test is under large scale yielding, M(T) test is under small scale yielding while initially precracked Arcan tear test is between the two cases. Consequently, it can lead to a different ductile tearing behaviour. The experimental results of precracked Arcan tests are shown in Fig. 4.9. A stable near straight crack extension was obtained by this type test. All crack path morphologies of Arcan tests can be found in Fig. 4.11 and Fig. 4.12.

4.3.3 M(T) testing

Fig. 4.13 displays the load-opening curves on M(T) samples for both artificially aged materials (T8R$_2$ and T8F$_{65}$[1]). A slight toughness anisotropy can be identified for the recrystallized material (see Fig. 4.13a) which is consistent with the trends observed in corresponding Kahn tear tests. The maximum load of the L-T sample is ∼15 % higher than for the T-L sample which is higher than the corresponding anisotropy measured for the Kahn tear tests (5 % see Fig. 4.6b). However, for the fibrous material (see Fig. 4.13b), the toughness difference between both loading directions

[1] 6 mm thick sheet reduced to 5 mm due to limited load capacity of the testing machine

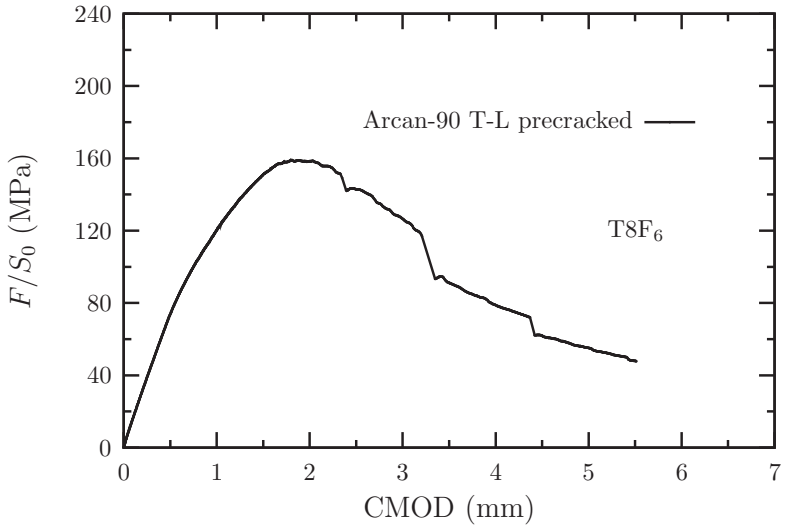


Figure 4.9: Arcan test for 90° loading (mode I) after 8 mm fatigue precracking, nominal stress (F/S_0) as a function of the crack mouth opening displacement (CMOD).

is not significant, which is consistent with the global trends observed on corresponding Kahn tear tests (see Fig. 4.7b). There are no M(T) tests for naturally aged materials (T3R$_2$ and T3F$_6$), because the industrial applications of this alloy require high strength so that artificial aging is needed.

4.4 Thickness effect on fracture toughness

In the case of Kahn tear tests on both fibrous materials (T3F$_6$ and T8F$_6$) which exhibit strong crack bifurcation during mechanical tests, especially in the case of the T8F$_6$ material, unstable crack extension was observed. The recrystallized material (both T3 and T8 conditions) exhibits stable and straight crack propagation. The main difference between both materials is the sheet thickness. In order to investigate the effect of thickness on the stability of crack growth and fracture toughness in the case of the fibrous material, specimens having a thickness of 2 mm were prepared by slicing the 6 mm samples into two 2 mm samples. For artificially aged T8F$_6$ material, several additional specimens with a thickness of 3 and 4 mm are also tested along the L-T direction to ex-

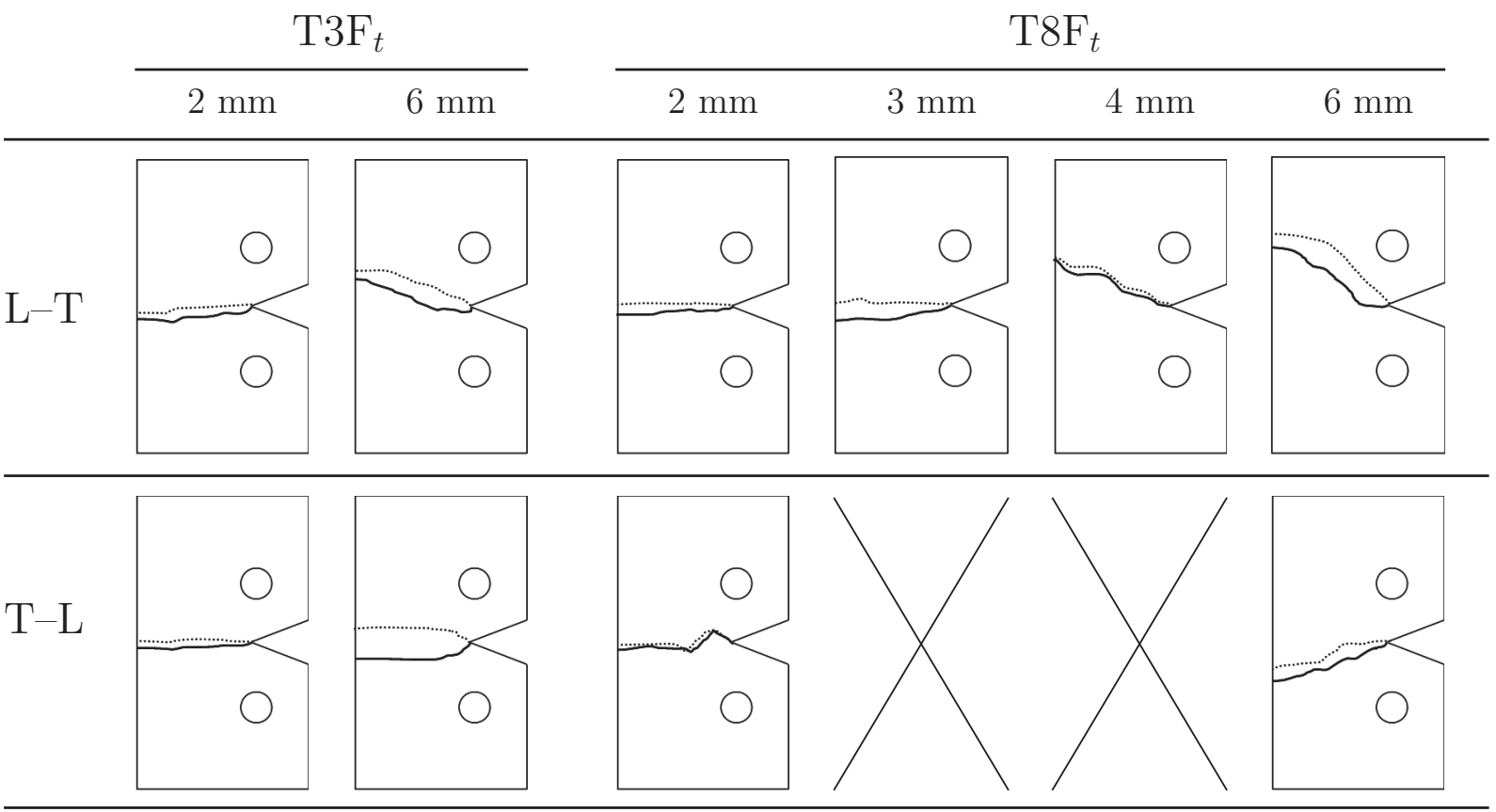


Figure 4.10: Schematic view of crack extension path for Kahn tear as function of material, loading configuration and thickness (dashed line represents the crack path profile in another side surface).

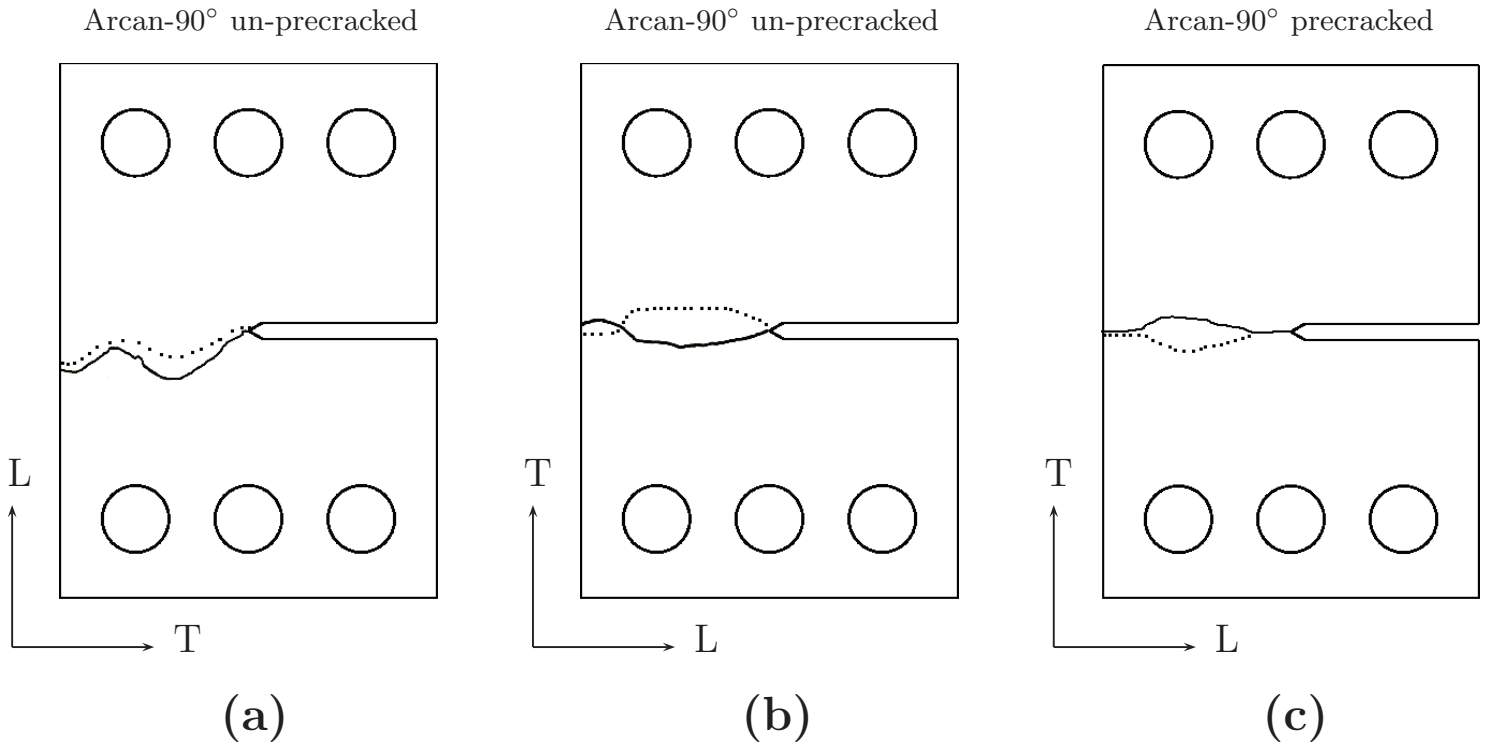


Figure 4.11: Schematic view of crack extension path for Arcan-90° tear tests (dashed line represents the crack path profile in another side surface).

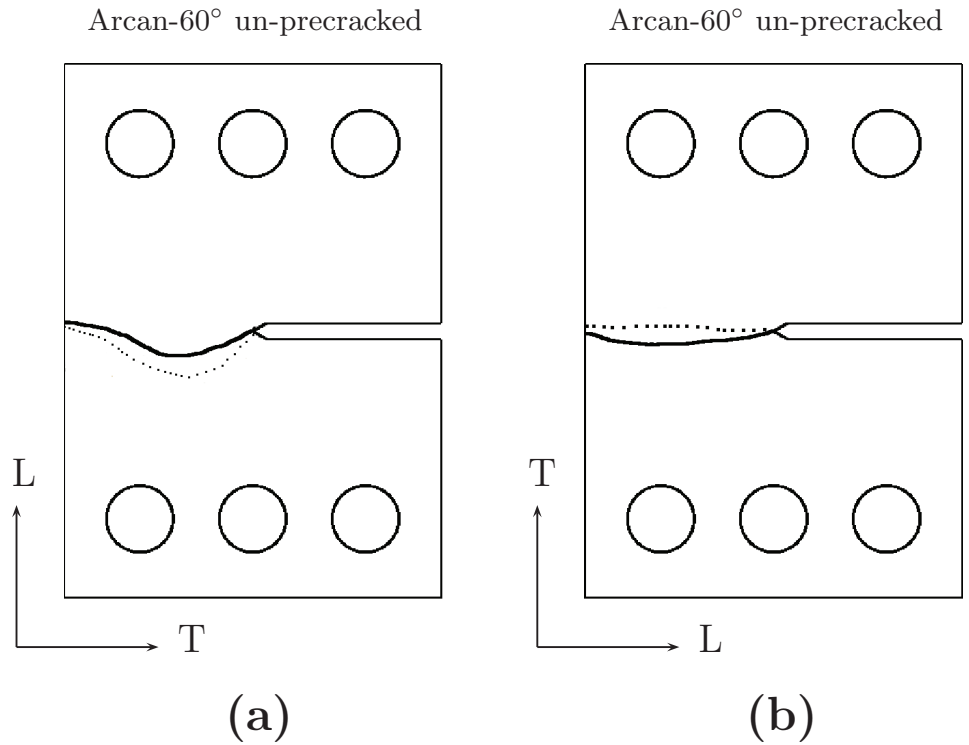


Figure 4.12: Schematic view of crack extension path for Arcan-60° tear tests (dashed line represents the crack path profile in another side surface).

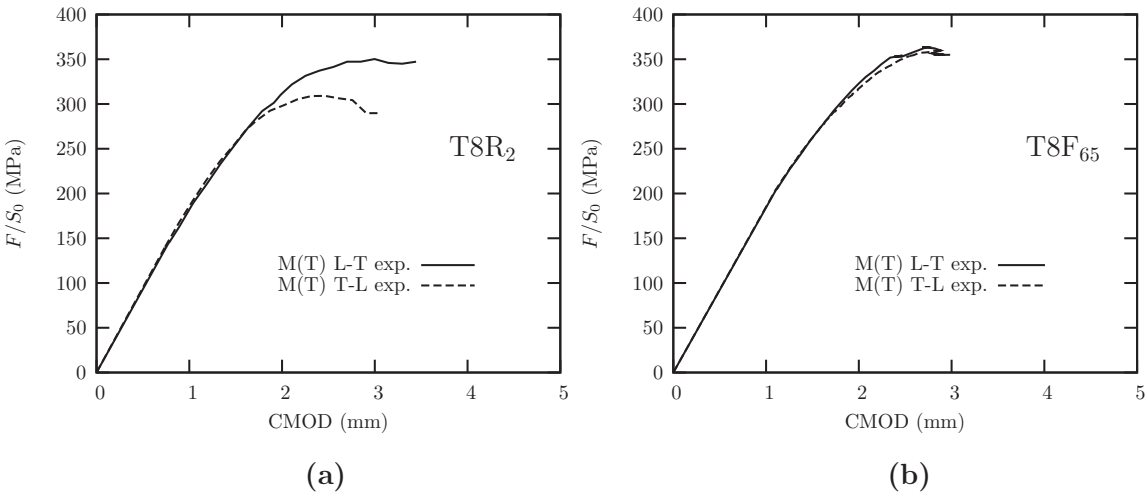


Figure 4.13: M(T) test results for two artificially aged materials T8R$_2$ (a), and T8F (b), nominal stress (F/S_0) as a function of the crack mouth opening displacement (CMOD).

amine the delamination problem. All those mechanical tests are carried out under the same testing condition as original 6 mm thick samples.

Fig. 4.14 shows the nominal stress (F/S_0) as a function of crack tip mouth opening displacement (CMOD) in both L–T and T–L loading directions for T3 and T8 conditions of fibrous materials (T3F$_t$ and T8F$_t$). For both conditions, the peak nominal stresses and the CMOD at peak load of 6 mm thick samples are higher than for 2 mm thick samples. This can be explained by the stress triaxiality which increases with increasing specimen thickness. Thicker specimens can support a higher load. The CMOD at peak load can be viewed as the ”deformation to crack initiation” of Kahn specimens, which increases with increasing specimen thickness. This is consistent with results of notched tensile tests in terms of ductility. However, increasing the sheet thickness over a certain limit can become deleterious, as the stress triaxiality increases causing rapid damage growth. This point has been proven by Rivalin *et al.* [90] in a pipeline-steel and Asserin Lebert *et al.* [3] in 6065 aluminium sheets.

For T3 condition (see Fig. 4.14a), in the crack initiation region, both 2 mm and 6 mm tests

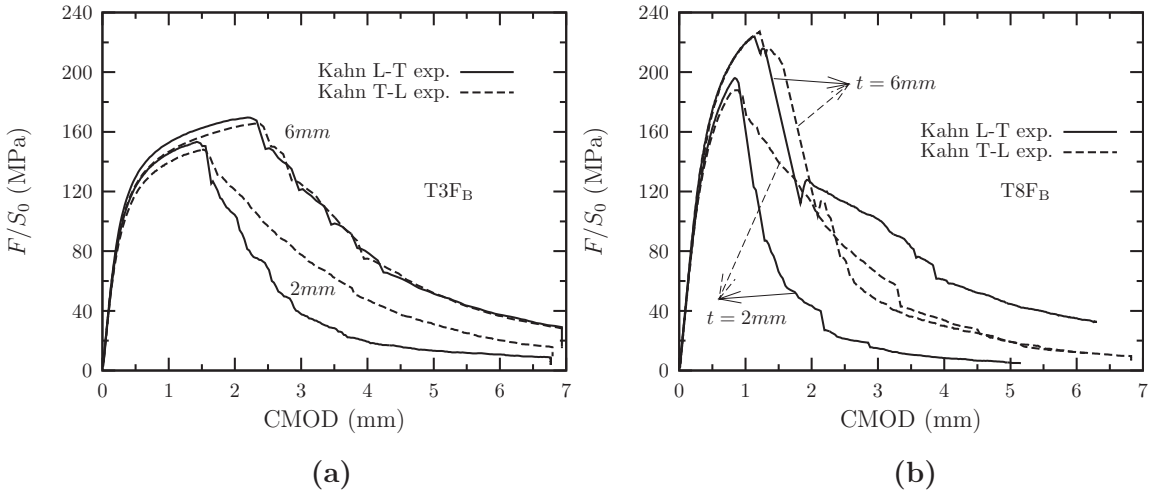


Figure 4.14: Experiments on Kahn tear tests in the case of T3F$_t$ material (a) and T8F$_t$ material (b), nominal stress (F/S_0) as a function of the crack mouth opening displacement (CMOD).

keep similar anisotropy (L-T loading achieves higher loads than T-L loading up to maximum load) as in smooth and notched tensile tests. However, the maximum load of the 6 mm thick L-T sample is $\sim$12 % higher than for 2 mm thick specimens tested along the same loading orientation. The crack initiation CMOD of 6 mm samples can be $\sim$60 % higher than that of 2 mm samples. Consequently, the UIE of 6 mm thick L-T loaded sample is $\sim$64 % higher than for the corresponding loading direction of 2 mm thick samples and $\sim$87 % higher for T-L loaded samples (see Table 4.1 for UIE values). In the propagation region of 2 mm-thick Kahn specimens, T-L loaded specimens have a higher toughness than L-T loaded specimens. This is not consistent with original 6 mm tests (L-T loadings have similar level toughness as T-L loadings). The main reason for this result is the zig-zag crack extension path produced in T-L loading tests (see Fig. 4.10 crack path morphologies). The origin of zig-zag cracking is probably due to the strongly anisotropic texture of fibrous material, and needs further work. In general L-T loaded specimens exhibit a stronger crack deviation than T-L loaded samples (see also in Fig. 4.10 for crack path morphologhies).

In the case of T8 condition materials (see Fig. 4.14b), in the crack initiation region, as

observed in notched tensile tests, there are no significant differences between both loading orientations for each thickness. However, in the crack propagation region, the 2 mm thick L-T loading sample exhibits a more straight crack growth path than the 6 mm thick sample along the same loading configuration. This means that the thickness has a strong influence on crack extension path morphology. In T-L loading of 2 mm thick tests, as illustrated in T3 condition material (Fig. 4.14a), zig-zag crack path was observed during tests which also result in a higher toughness for T-L loaded specimens than L-T loaded specimens.

Complementary tests carried out on 3 and 4 mm thick Kahn samples in L-T loading for the $T8F_6$ material are shown in Fig. 4.15. Test results are compared with 2 and 6 mm thick specimens: the thicker the samples the higher the normalized stress and the larger crack mouth opening displacement (CMOD). This trend is also followed by 3 and 4 mm thick specimen tests. The initiation toughness of UIE also increases with specimen thickness (see Table 4.1). The crack path morphology changes with thickness of specimens. In thick specimens constraint varies through the specimen thickness, and the conditions vary with the magnitude of the thickness. Different thick specimens exhibit different out-of-plane constraint which, in addition, varies along the thickness direction. Variable constraint across the thickness has conseqences for the behaviour of the crack extension and failure mechanisms. Comparison of crack-path morphologies along different loading directions with different materials and thicknesses can be seen in detail in Fig. 4.10.

4.5 Analysis of R-curve

R-curves characterize the resistance to fracture of materials during incremental slow-stable crack extension and results from growth of the plastic zone as the crack extends from initial pre-crack. They provide a record of the toughness development as a crack is driven stably under

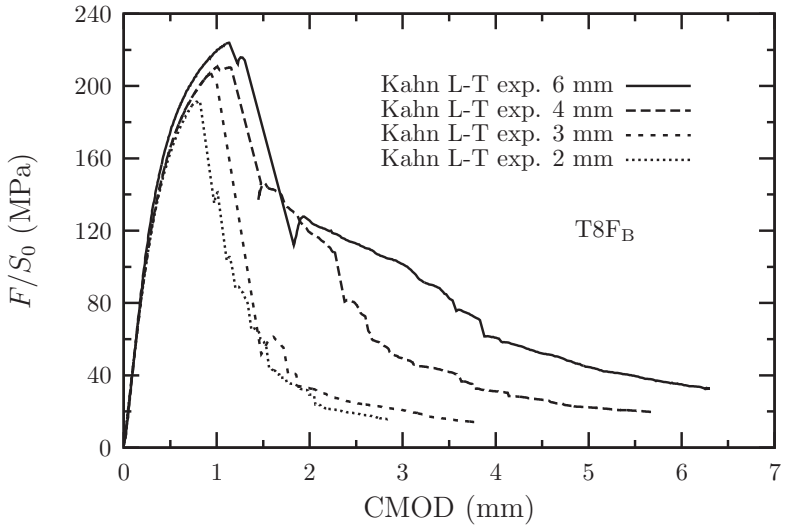


Figure 4.15: Experiments on Kahn tear tests in the case of T8F material L-T loading with different specimen thicknesses, nominal stress (F/S_0) as a function of the crack mouth opening displacement (CMOD).

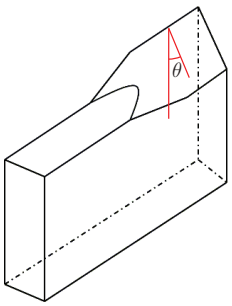
increasing applied K (stress intensity factor). They are dependent upon specimen thickness, temperature, and strain rate [4]. The fracture resistance curve (R-curve) is a function of the crack tip loading in terms of K, K_{eff} or elastic-plastic parameters of stable crack extension Δa_0 (Krafft *et al.* [58]):

$$K_{\text{eff}} = \frac{P}{2WB}\sqrt{\frac{\pi a_{\text{eff}}}{\cos(\pi a_{\text{eff}}/W)}} \tag{4.1}$$

where P is the recorded load, a_{eff} the effective half-crack length, W is the half specimen width and B specimen thickness. The effective crack length a_{eff}, is the total physical crack length plus Irwin's correction [50] of plastic zone, r_{Y}:

$$a_{\text{eff}} = a + \frac{1}{2\pi}\left(\frac{K}{\sigma_Y}\right)^2 \tag{4.2}$$

The physical crack length a is determined by an analytical formula from the measured



(a)

Material	$T8F_{62}$	$T8F_{63}$	$T8F_{64}$	$T8F_{6}$
Specimen Thickness (mm)	2	3	4	6
Slant angle (θ)	41°	36°	41°*	31°

* V slant fracture surface

(b)

Figure 4.16: Variation of slant angle θ with specimen thickness

compliance of the specimen as follows:

$$\frac{v}{P} = \frac{2Y}{EBW}\sqrt{\frac{\pi a/W}{\sin(\pi a/W)}}\left(\frac{2W}{\pi Y}\cosh^{-1}\left(\frac{\cosh(\pi Y/W)}{\cos(\pi a/W)}\right) - \frac{1+\mu}{\sqrt{1+\left(\frac{\sin(\pi a/W)}{\sinh(\pi Y/W}\right)}} + \mu\right) \tag{4.3}$$

(valid for $0.2 < \frac{2a}{W} < 0.8$; $\frac{Y}{W} \leq 0.5$) where v is the center-opening displacement at center hole, P the load, E is the Young's modulus, $2Y$=60 mm is total span of gage, a is the half-crack length and μ is the Poisson's ratio.

Fig. 4.17a shows the R-curve for $T8R_2$ material in terms of effective stress-intensity factor K_{eff}, as a function of effective crack length (Δa_{eff}) in both L-T and T-L loading orientations. It is shown that there are no difference between L-T and T-L loading up to crack initiation. However, in the crack propagation phrase, L-T loaded specimens exhibit a higher toughness than T-L loaded specimens. It is consistent with test results on small sized Kahn specimens. For 6 mm-thick T8 fibrous $T8F_6$, M(T) tests are performed on reduced 5 mm thick panels (due to the limited capacity of the testing machine). The corresponding R-curve is shown in Fig. 4.17b, both L-T and T-L loaded panels fail at a length of effective crack about 60 mm which is shorter than recrystallized material (80–90 mm). Notice that the crack of T-L loaded specimens initiates at the same applied

stress intensity factor (K_{eff}) as L-T loaded panels. In the stable crack propagation regions, there are no significant difference between L-T and T-L loadings.

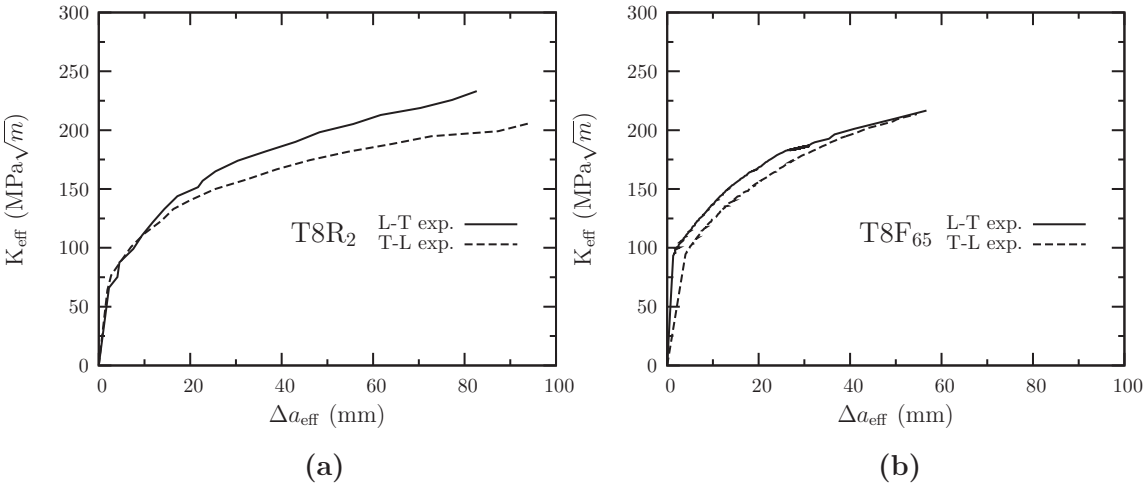


Figure 4.17: R-curve for AA2198 T8R$_2$ material (a), and AA2198 T8F$_{65}$ material (b).

4.6 Fracture mechanisms

4.6.1 Macroscopic fracture surface

Ductile thin sheet metals generally exhibit slant fracture surface as shown by various studies of pipeline-steel and aluminium sheets [70, 69, 65, 59, 106]. However, the slant angle of fracture surface can change with specimen thickness [66, 9] and material microstructure. In this part, macroscopic fracture surface orientation and crack-path morphologies were first examined on cross sections of broken Kahn tear specimens. These cross sections are obtained by cutting through the sample thickness direction in the crack propagation regions of Kahn specimens. Fracture surfaces can be characterized by the angle θ between the normal to the fracture surface and the loading direc-

tion (see Fig. 4.18a for definition of angle θ). Fig. 4.18 gives the images of through-thickness cross sections in various tested materials for T-L loading. It is shown that both 2 mm-thick recrystallized materials have very similar fracture angles, the θ equals to $\sim$49° for T3R_2 material while to $\sim$47° for T8R_2 material which is close to the 45° shear mode fracture for very thin sheet. For the two 6 mm-thick fibrous materials, it is difficult to obtain a precise value representing for θ as θ changes along the thickness direction. In the mid-thickness, θ equals $\sim$30° for T3F_6 material and $\sim$32° for T8F_6 material. Similar observations have been made on specimens of different thicknesses (see Fig. 4.19). It can be seen that θ changes with specimens thickness, here we take the case of the T8 fibrous material tested along L-T loading as an example. From 2 mm to 6 mm the fracture surface keeps in slant form in the propagation regions, with an exception of the 4 mm thick specimen which develops a V-slant fracture surface (see Fig. 4.19 (c)). For 2 mm thick Kahn samples, θ is $\approx$ 41° which is close to low triaxiality fracture ($\theta \approx 45°$) as for 2 mm-thick recrystallized materials. This angle decreases with increasing specimen thickness, except for the case of 4 mm thick specimen which fails via a V-slant fracture mode.

Macroscopic delamination cracking was observed on 6 mm-thick T8 fibrous of Kahn tests loaded in L-T orientation (see Fig. 4.20). The occurrence of delamination cracks in second generation of thick plate Al-Li alloys (2090, 8090, 8091, 2091) has been demonstrated through experimental studies by Rao *et al.* [117] in 1990s and recently by Kalyanam *et al.* [51] on a third generation AA2099-T87 alloy. This phenomenon is well known for thick Al-Li alloy plates and high strength 7xxx Al-Zn alloys. This is a possible explanation for the lower fracture toughness along the short transverse direction (S). In the present case, delamination is not observed when the specimen thickness is reduced to 4 mm and less (3 mm and 2 mm). It can be explained as the stress triaxialiy which is higher for thick components. Consequently, a higher through-thickness stress is produced in thicker specimens. Another important reason is the presence of inter-granular precipitation and inclusions in T8 condition materials (cf. chapter 2, section 2.3.3.). This can result in an embrit-

tlement of grain boundaries causing grain boundary decohesion. Notice that 6 mm-thick naturally aged materials do not appear to suffer from macroscopic delamination.

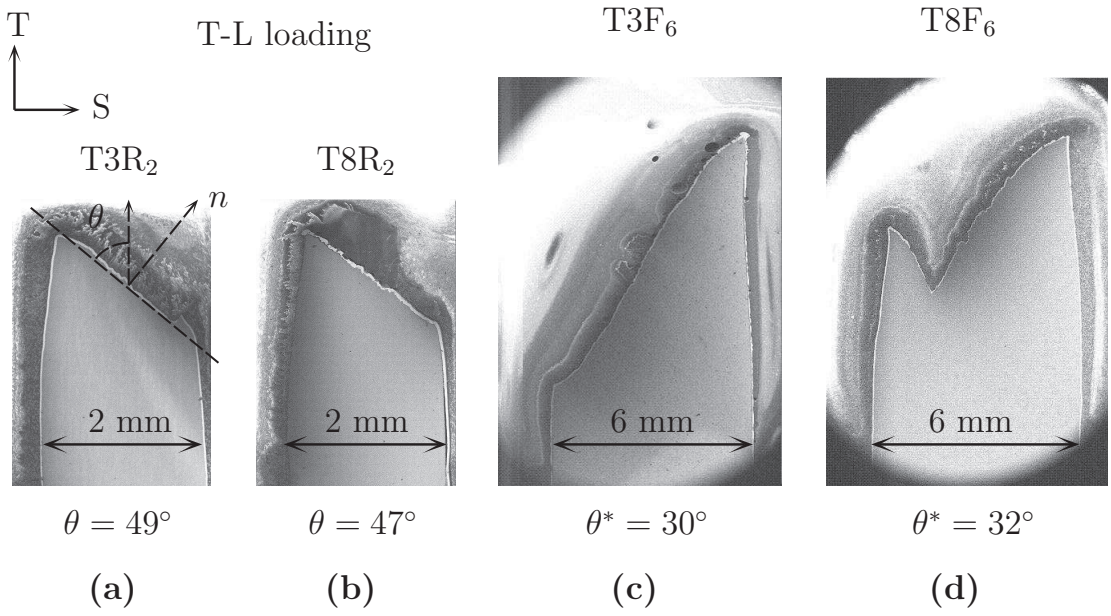


Figure 4.18: Through-thickness cross sections in propagation regions of Kahn specimens tested along T-L orientation for all materials studied (*: θ taken at mid-thickness of cut section). Crack-growth direction is given by the outward normal to the plane of the paper.

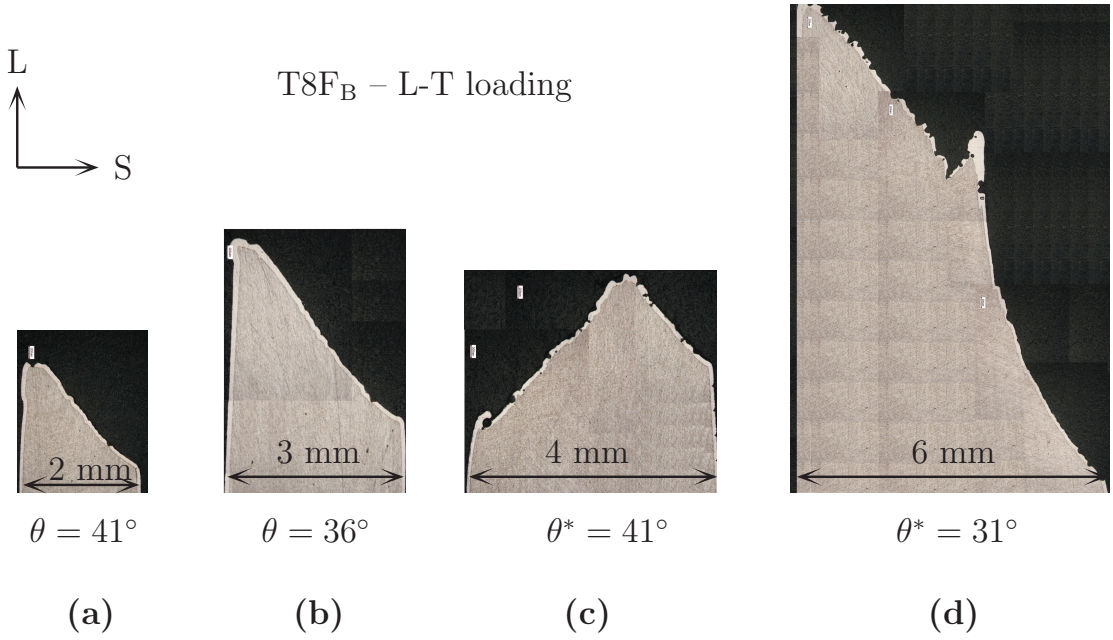


Figure 4.19: Through-thickness cross sections in propagation regions of different thickness Kahn specimens tested along L-T orientation for T8 fibrous material (*: θ is the average value of angle taken over thickness). Crack-growth direction is given by the outward normal to the plane of the paper.

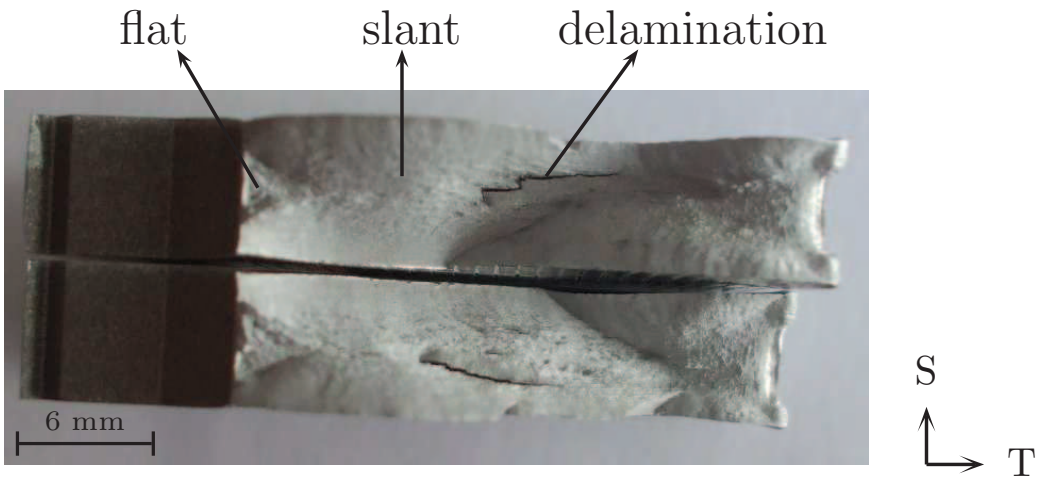


Figure 4.20: Macroscopic fracture surface of T8 fibrous (T8F$_6$) Kahn specimens tested along L-T orientation.

4.6.2 Fractography via SEM

The fractographic examinations at microscopic level are carried out mainly on Kahn and M(T) broken samples using a Zeiss DSM982 microscope. The typical macroscopic fracture surfaces of Kahn and M(T) tear specimens are shown in Fig. 4.21. The crack begins with a small flat triangular zone perpendicular to the loading direction, followed by a transition to a slant fracture surface in crack propagation region. This phenomenon has also been seen in previous studies of other aluminium alloys by Bron on AA2024 alloy [18] and Morgeneyer on AA2139 alloy [73]. It is well established that flat-to-slant transition is consistent with the evolution of the triaxial constraint conditions [56]: in the triangular region, high stress triaxiality is encountered during crack initiation, while increasing plastic zone size as the crack propagates lead to a loss of constraint and hence to a decreased triaxiality (see Ref. [21]). The observation by scanning electron microscopy are conducted at these two different locations on fracture surfaces of different materials, loading directions and specimen thicknesses.

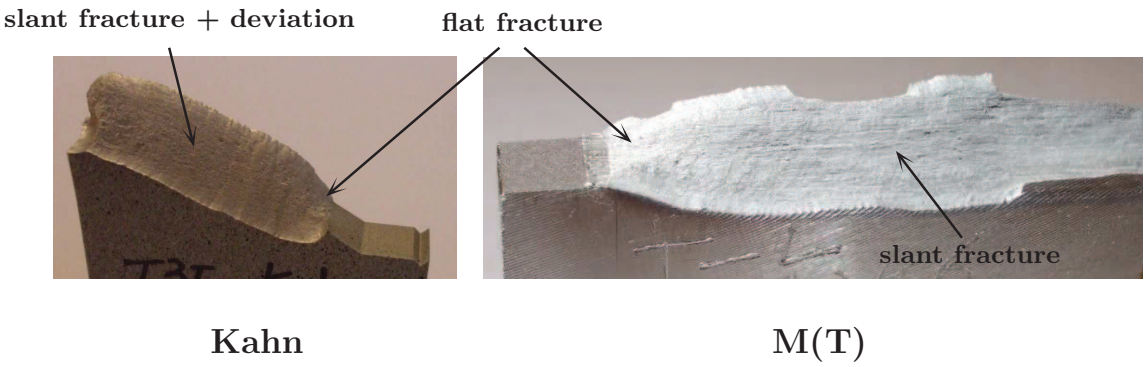


Figure 4.21: Typical fracture surface of Kahn and M(T) tear test samples.

Effect of the loading direction:

Selected fractographs are shown in Fig. 4.22–4.25 to illustrate the trends in fracture modes observed as a function of orientation, material and specimen thickness. Fig. 4.22 shows the case of T3 recrystallized material ($T3R_2$) for Kahn specimens tested along L-T (Fig. 4.22 left) and T-L (Fig. 4.22 right) directions.

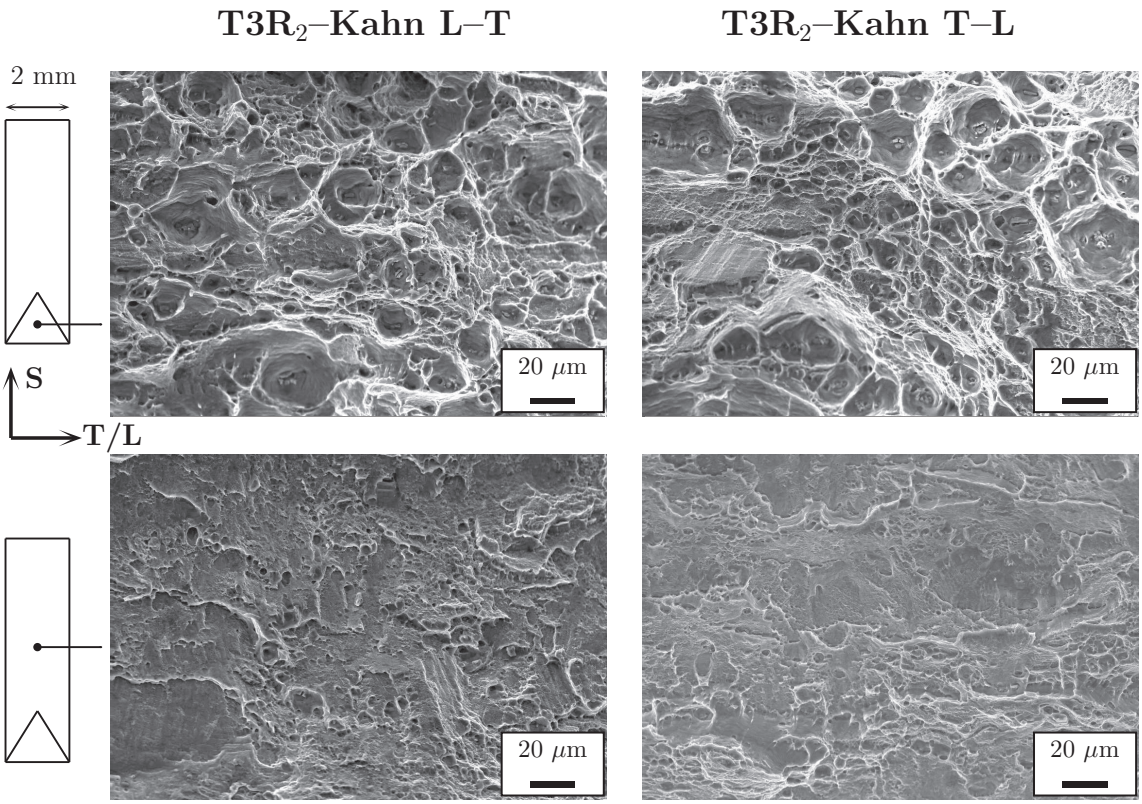


Figure 4.22: SEM micrography of T3 recrystallized material ($T3R_2$) of Kahn specimens at flat and slanted regions. The left column refers to L–T loaded samples and the right one to T–L loaded samples.

No significant difference can be observed between L-T and T-L loading specimens. However, for each loading, two different failure mechanisms can be identified: in the flat triangular

region, coarse voiding can be seen; void growth is the controlling damage mechanism. Ductile failure by internal necking initiated at large intermetallic particles can clearly be observed on the fracture surfaces. In the slant region, a nearly smooth surface can be seen; void growth is very limited and very small secondary dimples are observed at a higher magnification. These observations are similar to those on smooth tensile specimens.

Kahn vs. M(T):

Comparisons of fracture surfaces at microscopic scale between small sized Kahn specimens and large panels M(T) specimens are shown in Fig. 4.23 for the 2 mm-thick T8 recrystallized material ($T8R_2$) and in Fig. 4.24 for the T8 fibrous material ($T8F_t$)[2]. Same microscopic fracture surfaces are observed on both Kahn and M(T) specimens; void growth domiant fracture in flat triangular region. While in the slant region, inter-granular fracture was observed. The predominant fracture mode may be the grain boundary decohesion. For T8 fibrous material in Fig. 4.24, in the flat region, the large dimples are typically associated with void initiation at particle clusters.

Effect of thickness:

Thickness effect on fracture surfaces are examined on the original 6 mm-thick Kahn specimens and the reduced 2 mm-thick Kahn specimens. The comparison of fracture surfaces is shown in Fig. 4.25 in the case of the T3 fibrous material ($T3F_t$). For both thicknesses in the flat triangular regions, dimple fracture surfaces can be identified whereas at a higher magnification, the appearance of the 2 mm-thick specimen and the 6 mm-thick specimens are different. The dimples are much smaller for 2 mm specimens than for 6 mm thick specimens. It is consistent with the evolution of stress triaxiality, which is lower in 2 mm-thick specimen causing a slower void growth than in 6 mm-thick specimens. Rice and Tracey of void growth model [88] has proved this point numeri-

[2] 6 mm-thick for Kahn specimens and 5 mm-thick for M(T) panels

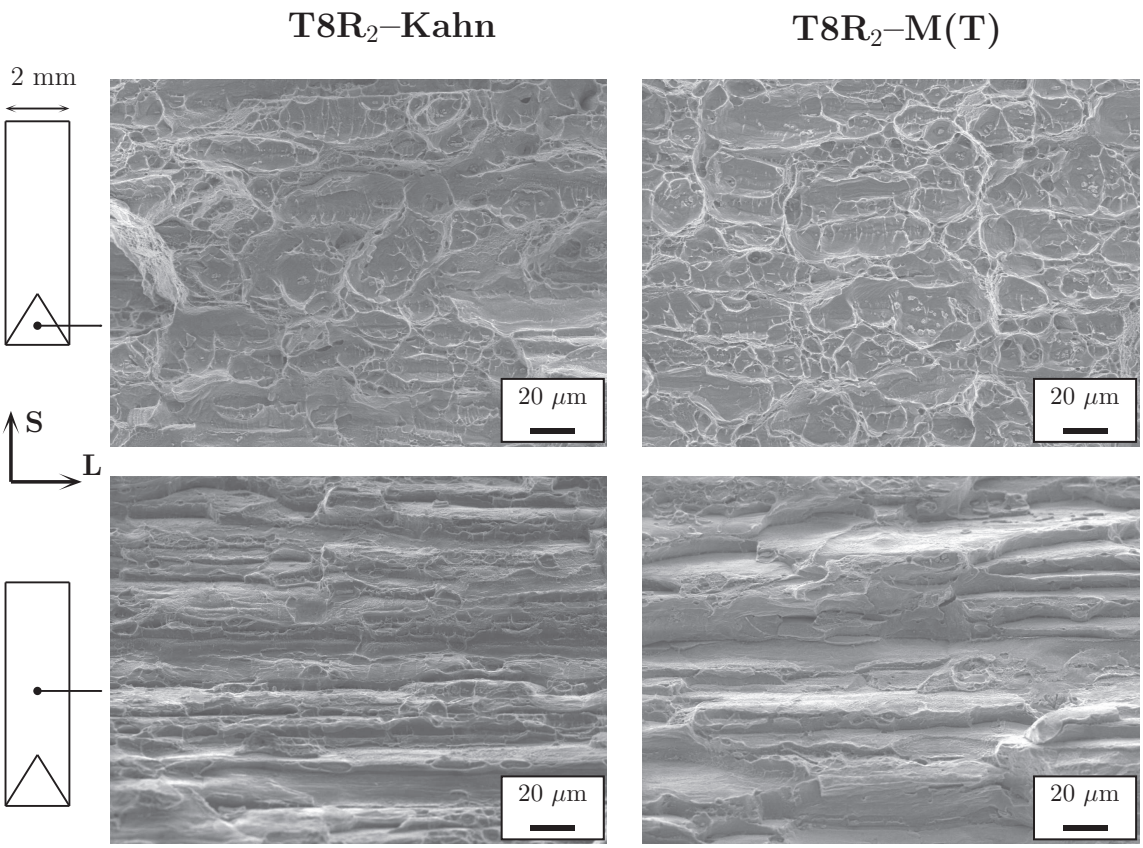


Figure 4.23: SEM micrography of T8 recrystallized material ($T8R_2$) of Kahn and M(T) specimens tested in T-L orientation at flat and slanted regions. The left column refers to Kahn sample and the right one to M(T) sample.

cally and experimentally. In the slant region for both thicknesses, apparent smooth shear areas were observed on all fracture surfaces as shown in Fig. 4.25. Grain boundary decohesion with friction marks is the predominant fracture mode in this region.

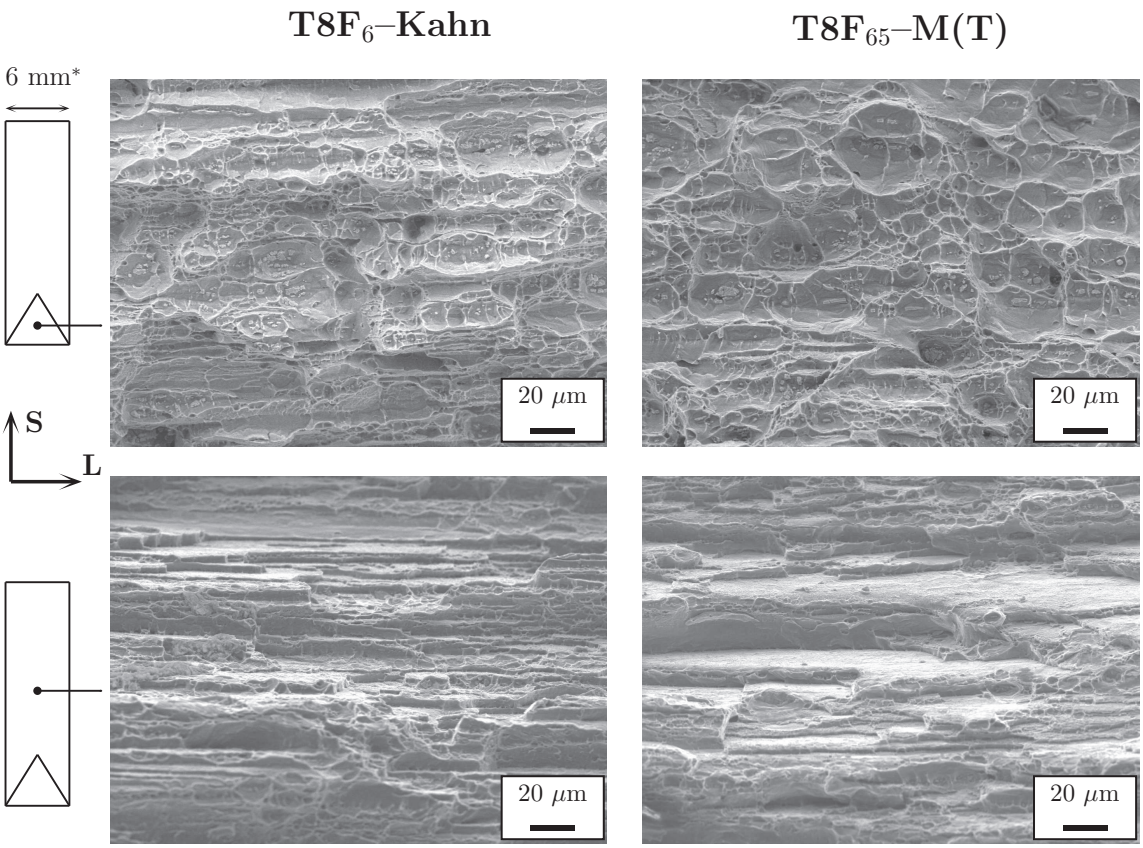


Figure 4.24: SEM micrography of T8 fibrous material of Kahn and M(T) specimens tested in T-L orientation at flat and slanted regions. The left column refers to Kahn sample and the right one to M(T) sample (* sample thickness is 5 mm for M(T) specimens).

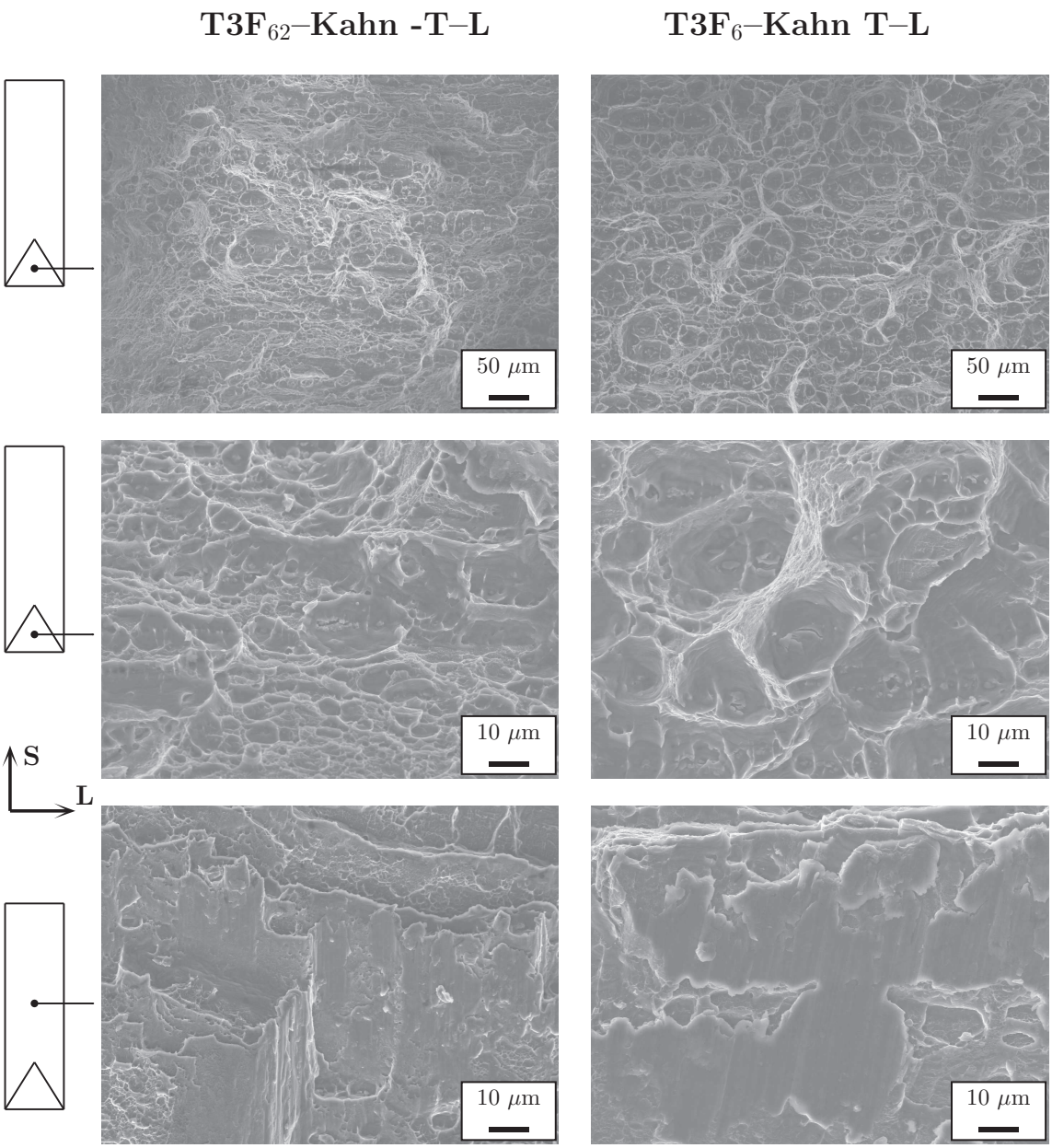


Figure 4.25: SEM micrography of T3 fibrous material 2 mm and 6 mm thick Kahn specimens at flat and slanted regions. The left column refers to 2 mm thick Kahn sample and the right one to 6 mm thick Kahn sample.

4.6.3 X-ray tomography

X-ray micro-tomography is a very attractive technique in materials science to investigate the fracture mode of tested materials and characterize damage development around crack tips. It enables visualisation of internal features in opaque samples. In the field of damage/fracture characterization, it has been used for visualising crack in metallic materials [44, 107, 55]. In our case, high resolution tomographic observations were carried out on arrested Kahn tear samples. Sample preparation was carried out using similar procedures as in [73]. Cracks were grown in Kahn tear specimen [5] to a length of about 10 mm. A small block of material (dimensions $1 \times 1 \times 10$ mm^3) was then extracted at the crack tip region using electrical-discharge machining at mid-thickness: as such, subsequent tomographic scanning of the crack itself could be carried out, as well as the material immediately ahead of the crack tip. Fig. 4.26 illustrates a schematic depiction of arrested Kahn sample preparation for X-ray tomography assessment.

Micro-tomographic observations were performed at European Synchrotron Radiation Facility (ESRF) in Grenoble, on the beamline ID19. The facility provides a highly coherent, spatially and spectrally homogeneous beam with a high photon flux. The energy of the incident beam used in this case is 20 keV (for light metal). For one volume 1500 radiographs were recorded for a rotation between 0° and 180°. Image analysis, segmentation and 3D rendering were carried out using a commercial software package (Volume Graphic GmbH, VGStudio Max).

When liquid gallium is brought in contact with aluminium the gallium can penetrate the grain boundaries. Gallium has a very high X-ray attenuation coefficient compared to Aluminium [62]; this renders gallium layers visible by high resolution absorption micro-tomography. After being in contact with gallium, the sample was annealed for about 1 h at 100° C before imaging in order to improve the wetting of the grain boundaries. In spite of the heat treatment, low angle grain boundaries cannot be wetted by gallium and are not visible on the 3D reconstructed images (approximately 10 % of the grain boundaries) [63, 85]. Fig. 4.27 presents a reconstruction of 2D

slice of sample wetted with gallium (Ga). Grain boundaries, crack front and intermetallic particles can clearly be seen at micrometer scale (voxel size is 0.7 μm^3). The anisotropic shape of the grains is also clearly seen in this figure.

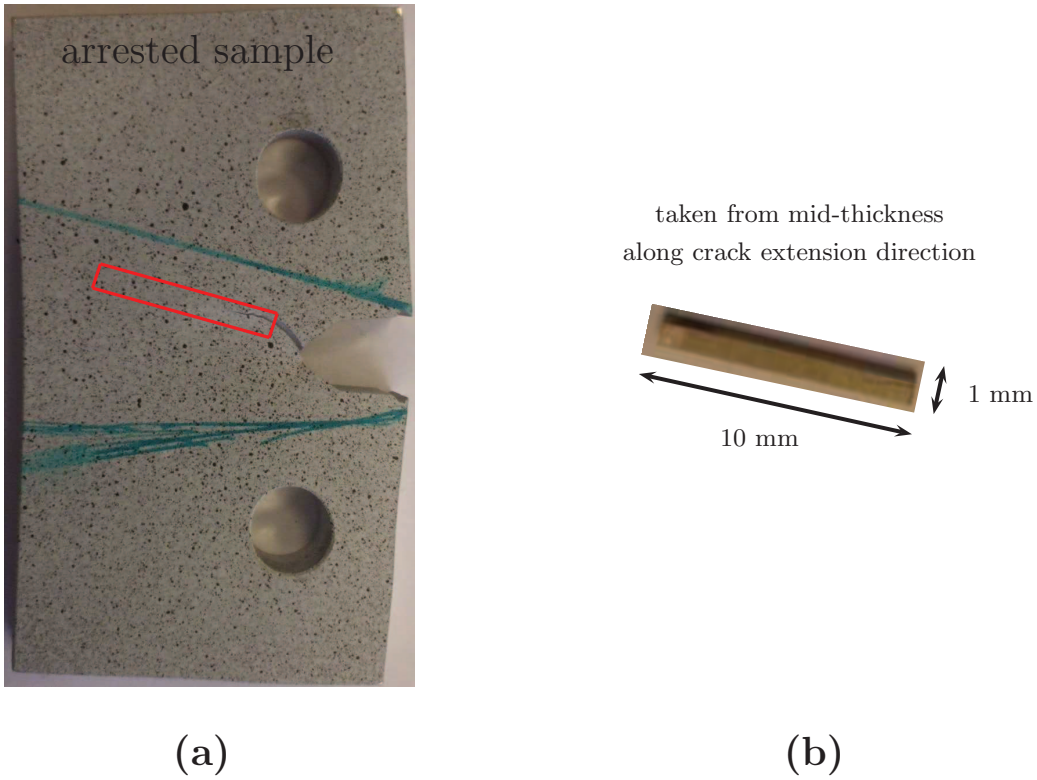


Figure 4.26: Schematic depiction of arrested crack Kahn sample preparation for X-ray tomography assessment.

Fig. 4.28 shows 2D tomography sections of the crack in naturally aged recrystallized material ($T3R_2$) before and after gallium wetting (Fig. 4.28 a and b, respectively) with the crack growth direction normal to the image plane. On the figure before gallium wetting (Fig. 4.28a), the aluminium matrix (grey), intermetallics (white) and pores, as well as the crack (black), are clearly delineated, with the phase contrast fringes highlighting the associated edges/interfaces. It can be seen that in this material void growth is limited in the crack propagation region close to cracks. It is

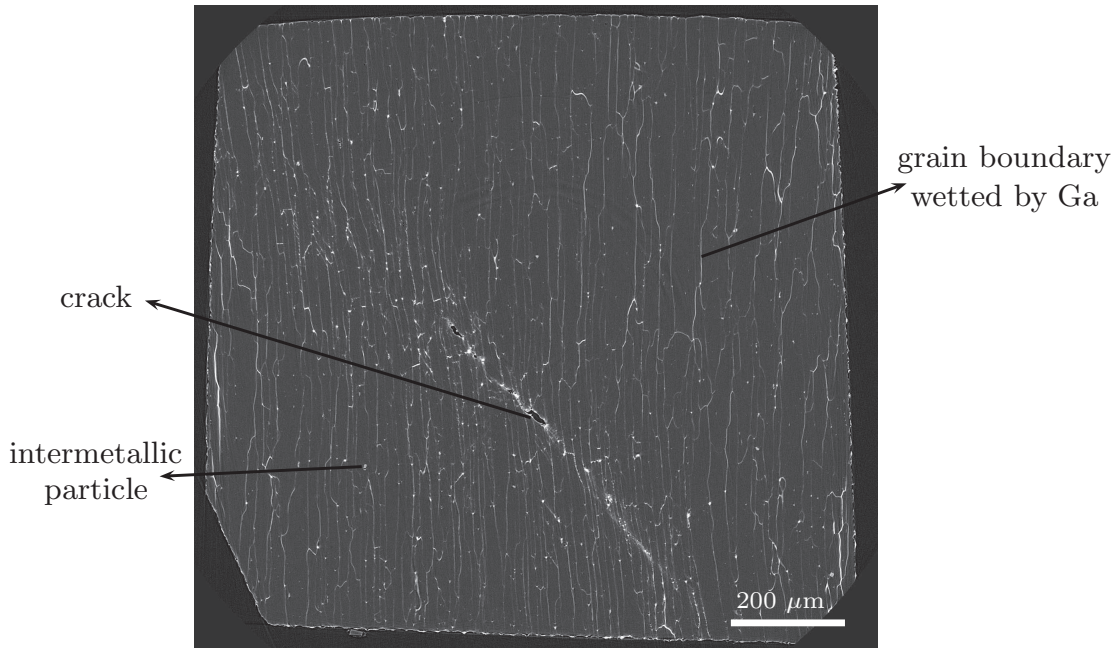


Figure 4.27: Reconstructed of 2D slice showing the entire 1x1 mm^2 section after gallium wetting. Crack growth direction is normal the image plane.

mainly due to a limited initial voids volume (cf. chapter 2, section 2.3.4) and low stress triaxiality in test specimens. In Fig. 4.28b, the grain boundaries can also be seen (running from top-to-bottom and some in horizontal direction on image), owing to the local segregation of gallium. As reported above, not all grain boundaries can be seen in this condition. Fig. 4.28a reveals that the main crack path is inclined with respect to the loading direction. Comparing the crack in the gallium wetted sample with the sample before gallium wetting indicates that much of the crack path crosses the grains, trans-granular crack is predominant fracture mode in $T3R_2$ material.

Fig. 4.29a shows the section near crack tip of naturally aged recrystallized material ($T3R_2$) before gallium wetting, while Fig. 4.29b shows the same location after the gallium wetting. From image before gallium liquid treatment, some broken intermetallic particles can be seen around crack tips, but the void growth rest limited. In Fig. 4.29b, the inclined crack crosses grains which clearly confirms that trans-granular fracture is dominant in thin $T3R_2$ material.

For the case of artificially aged $T8R_2$, experimental results are given in Fig. 4.30. It is shown that around the crack tip hardly any void growth can be seen. The section after gallium treatment shows trans-granular fracture as the main fracture mode in $T8R_2$ material. Compared to $T3R_2$ material, no significant difference of fracture can be observed, very similar fracture mode was identified in $T8R_2$ material as in $T3R_2$ material.

In the case of two fibrous materials ($T3F_6$ and $T8F_6$). The prepared X-ray tomography samples were extracted at the mid-thickness of 6 mm-thick Kahn specimens. So the following images reveal the fracture mode in center of specimen which is different compared to side part (cf. chapter 3, section 3.5.2).

Fig. 4.32 shows 2D tomography sections of a crack in artificially aged 6 mm-thick fibrous material ($T8F_6$) loaded in T-L configuration before and after gallium wetting (Fig. 4.32 a and b, respectively) with the crack growth direction normal to the image plane. Fig. 4.32a reveals crack areas that are oriented in the loading direction and other parts that are inclined with respect to the loading direction. Comparing the crack in the gallium wetted sample with the sample before gallium wetting indicates that much of the crack path follows vertical grain boundaries (direction 2) as illustrated in Fig. 4.32b. However, due to a low visibility of grain boundaries in horizontal direction (direction S), the inter-granular or trans-granular crack path is less clear in horizontal direction (S). Notice that void growth again rests limited around crack in this material whereas the fracture mode is different from both recrystallized materials ($T3R_2$ and $T8R_2$).

Fig. 4.32a reveals crack areas that are oriented in the loading direction and other parts that are inclined with respect to the loading direction. Comparing the crack in the gallium sample with the sample before gallium wetting indicates that much of the crack path follows grain boundaries. This is particularly obvious for the parts of the crack that are oriented in the loading direction, but is also evident for areas that are inclined with respect to the loading direction.

Fig. 4.31 shows the sections in the case L-T loading configuration of artificially aged

fibrous material ($T8F_6$). Similar results were found as in T-L loading tests, inter-granular cracking is the predominant fracture mode. At a higher magnification, as illustrated in Fig. 4.31a (before gallium wetting) some coarse voids can be seen around the crack tip. A more open delamination crack is clearly showed in Fig. 4.31b.

For the case of $T3F_6$ material, observations were done on L-T and T-L loaded samples without gallium treatment. Fig. 4.33 provides slice of tomographic images in L-T loading (Fig. 4.33a) and T-L loading (Fig. 4.33b). For both loadings, some coarse voids can be seen. It is also shown that crack opening is larger for L-T loading than for T-L loading. The fracture mode of T-L loading is very similar as in $T8F_6$ material in the same loading orientation (see Fig. 4.32b).

And finally, Fig. 4.34 shows failure in $T8F_{62}$ material (6 mm-thick sample reduced to 2 mm in thickness). Most of the crack is straight in this case. The strongly deformed grains and the formation of a shear band can be seen. However, no grain boundary delamination can be seen as in 6 mm-thick samples in the same testing condition. It can be explained by the stress triaxiality which is lower in 2 mm than in 6 mm-thick sample. The stress in the thickness direction has a predominant influence on delamination in tested materials (cf. section 4.6.1).

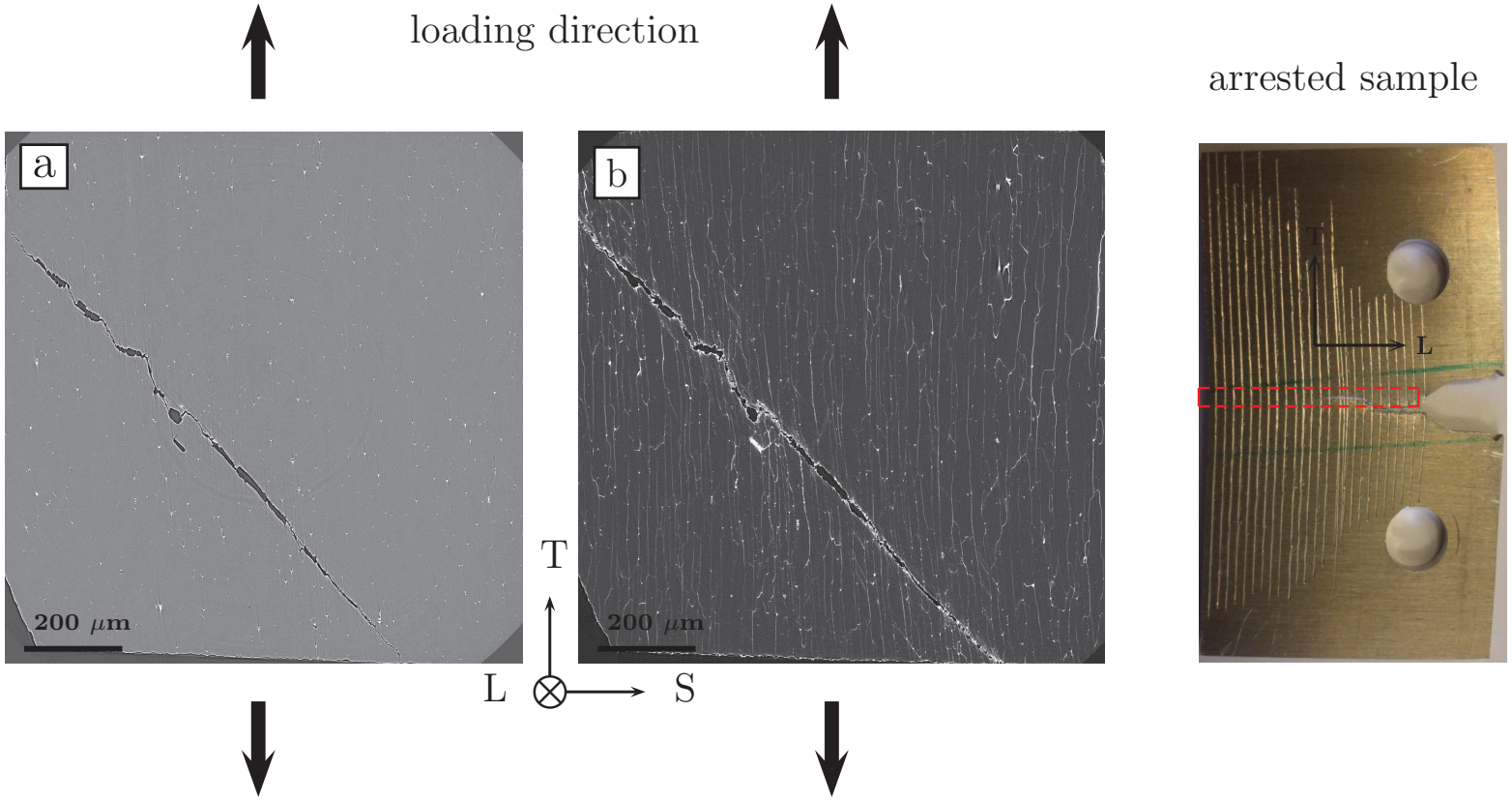


Figure 4.28: Two-dimensional section of tomography data showing the crack in T-L orientation for the T3 condition 2 mm-thick recrystallized material: (a) without gallium wetting; and (b) after gallium wetting. Crack-growth direction is given by the outward normal to the plane of the section

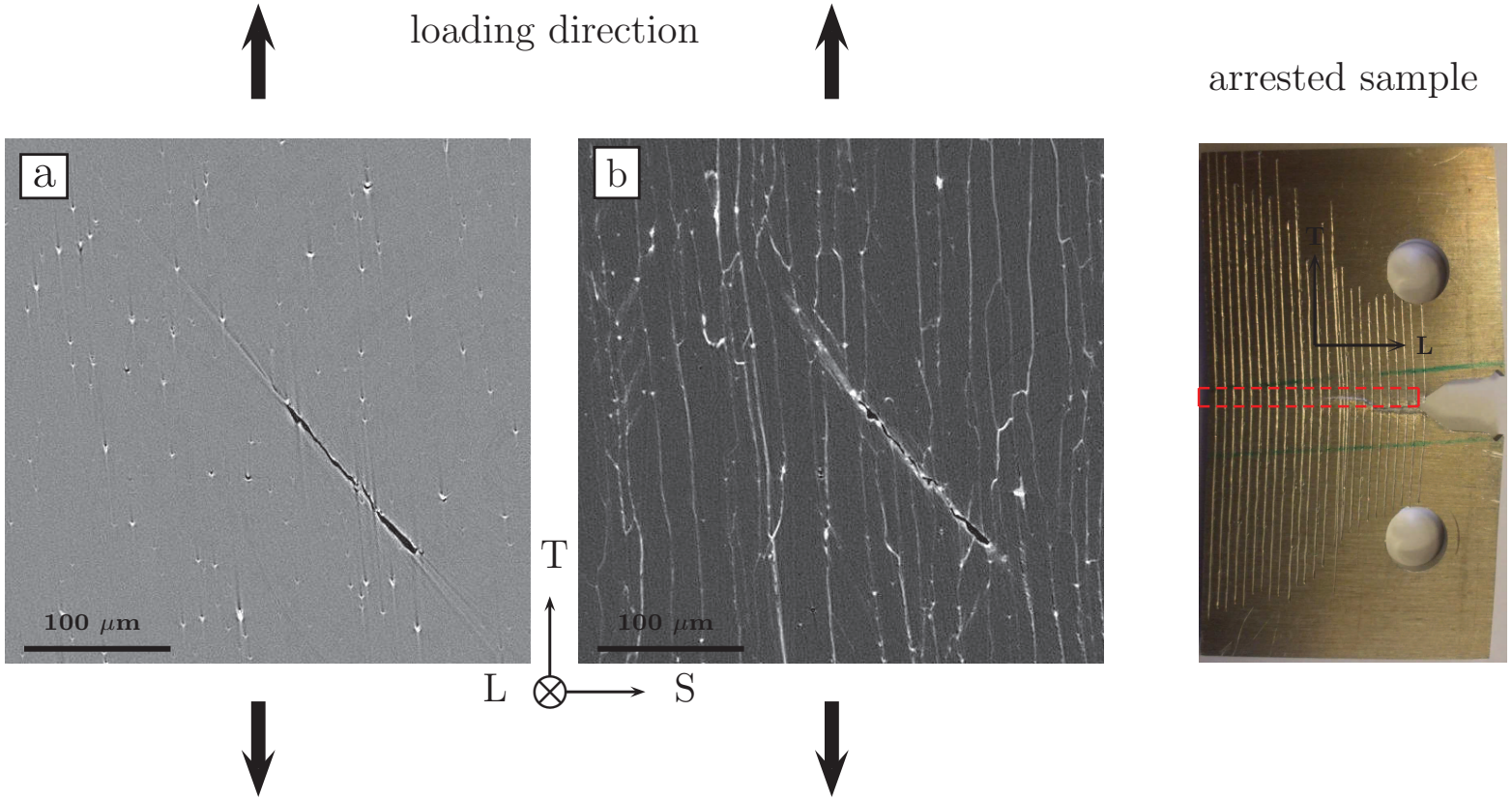


Figure 4.29: Two-dimensional section of tomography data showing the crack tip in T-L orientation for the T3 condition 2 mm-thick recrystallized material: (a) without gallium wetting; and (b) after gallium wetting. Crack-growth direction is given by the outward normal to the plane of the section

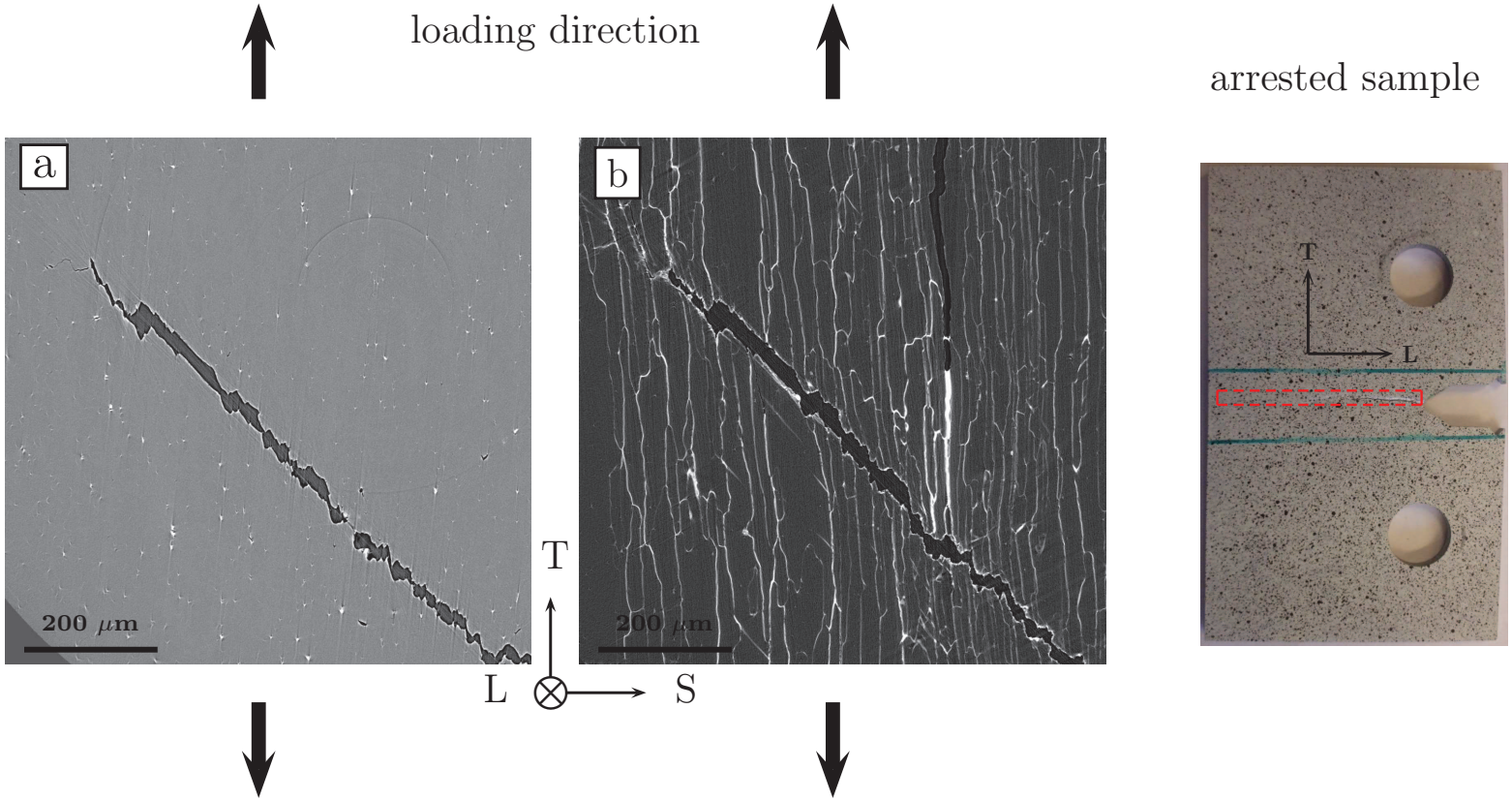


Figure 4.30: Two-dimensional section of tomography data showing the crack in T-L orientation for the T8 condition 2 mm-thick recrystallized material: (a) without gallium wetting; and (b) after gallium wetting. Crack-growth direction is given by the outward normal to the plane of the section

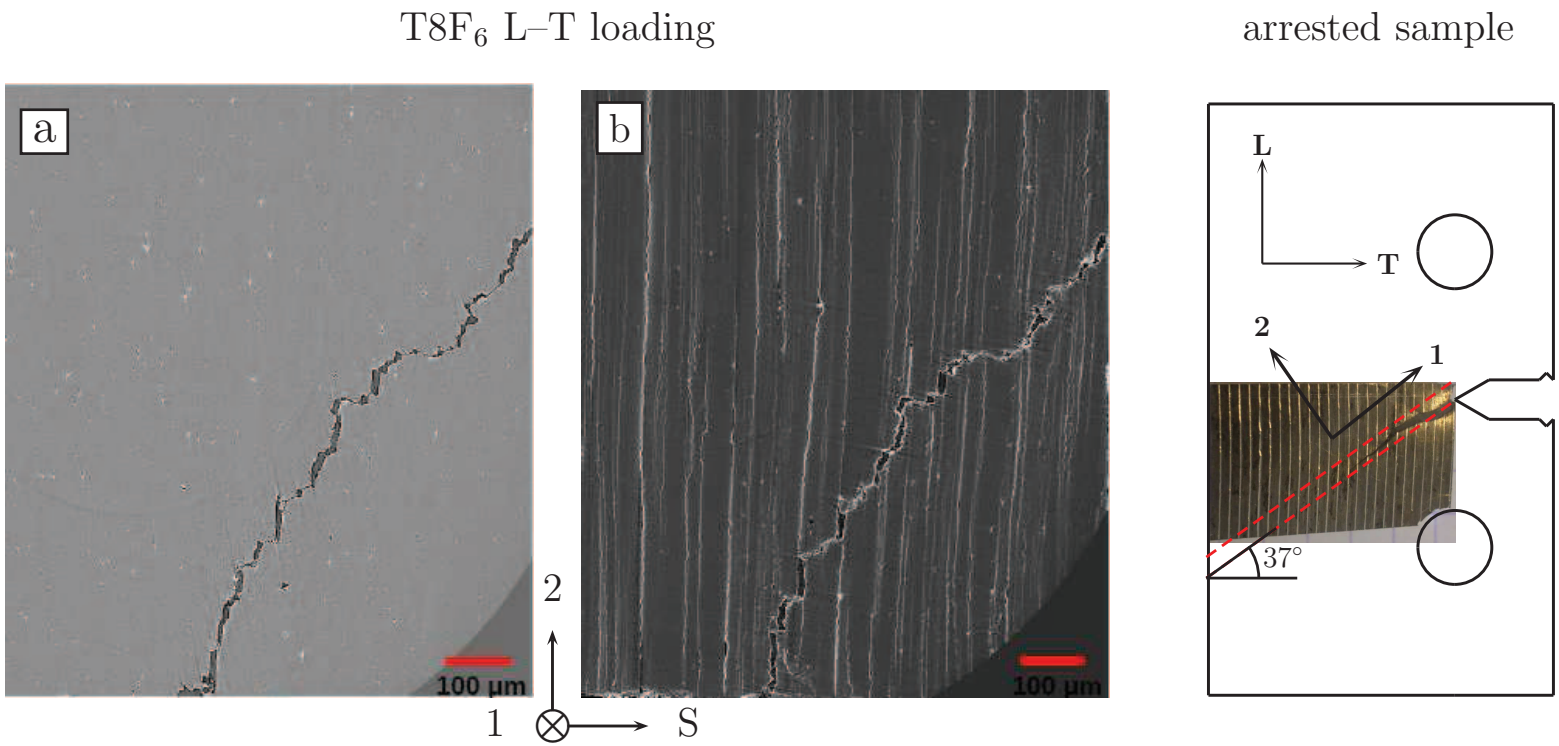


Figure 4.31: Two-dimensional section of tomography data showing the crack in L-T orientation for the T8 condition 6 mm-thick fibrous material: (a) without gallium wetting; and (b) after gallium wetting. Crack-growth direction is given by the outward normal to the plane of the section

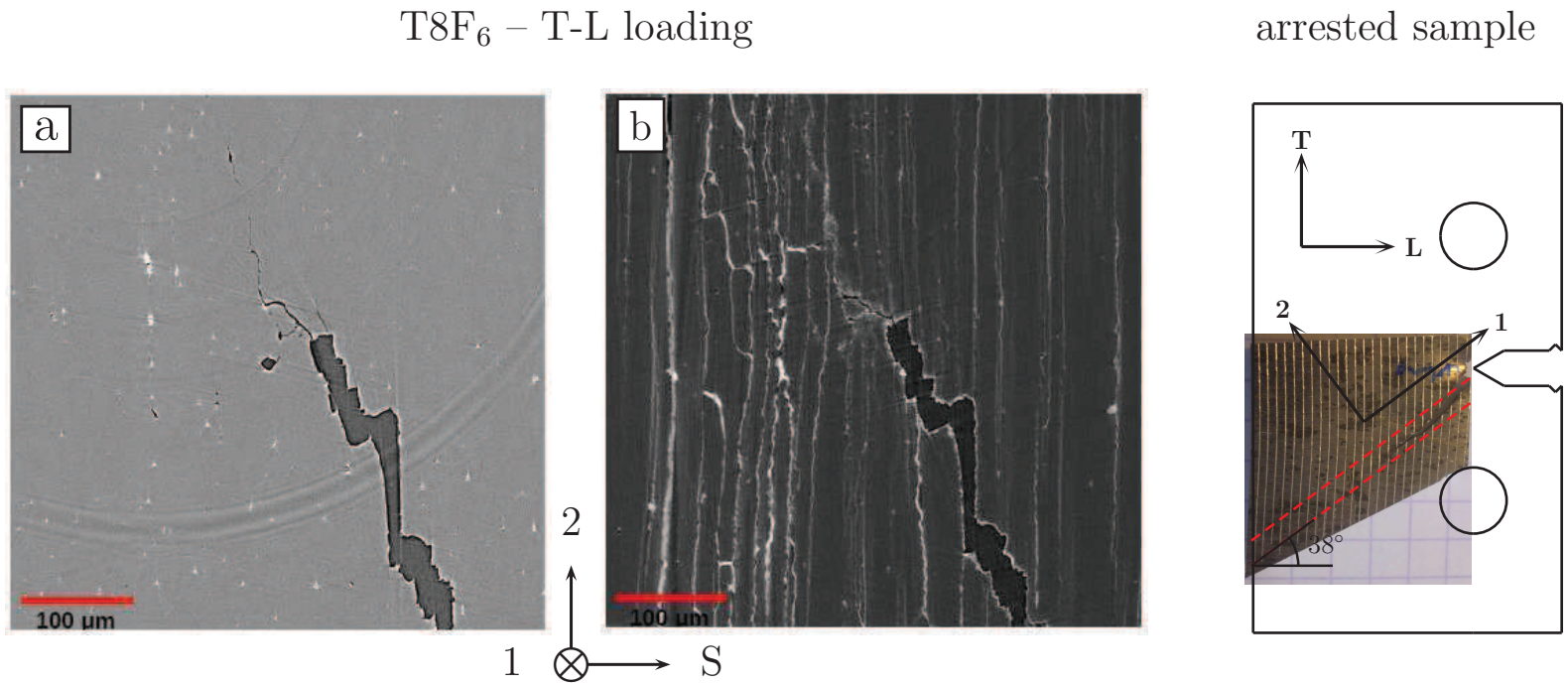


Figure 4.32: Two-dimensional section of tomography data showing the crack in T-L orientation for the T8 condition 6 mm-thick fibrous material: (a) without gallium wetting; and (b) after gallium wetting. Crack-growth direction is given by the outward normal to the plane of the section

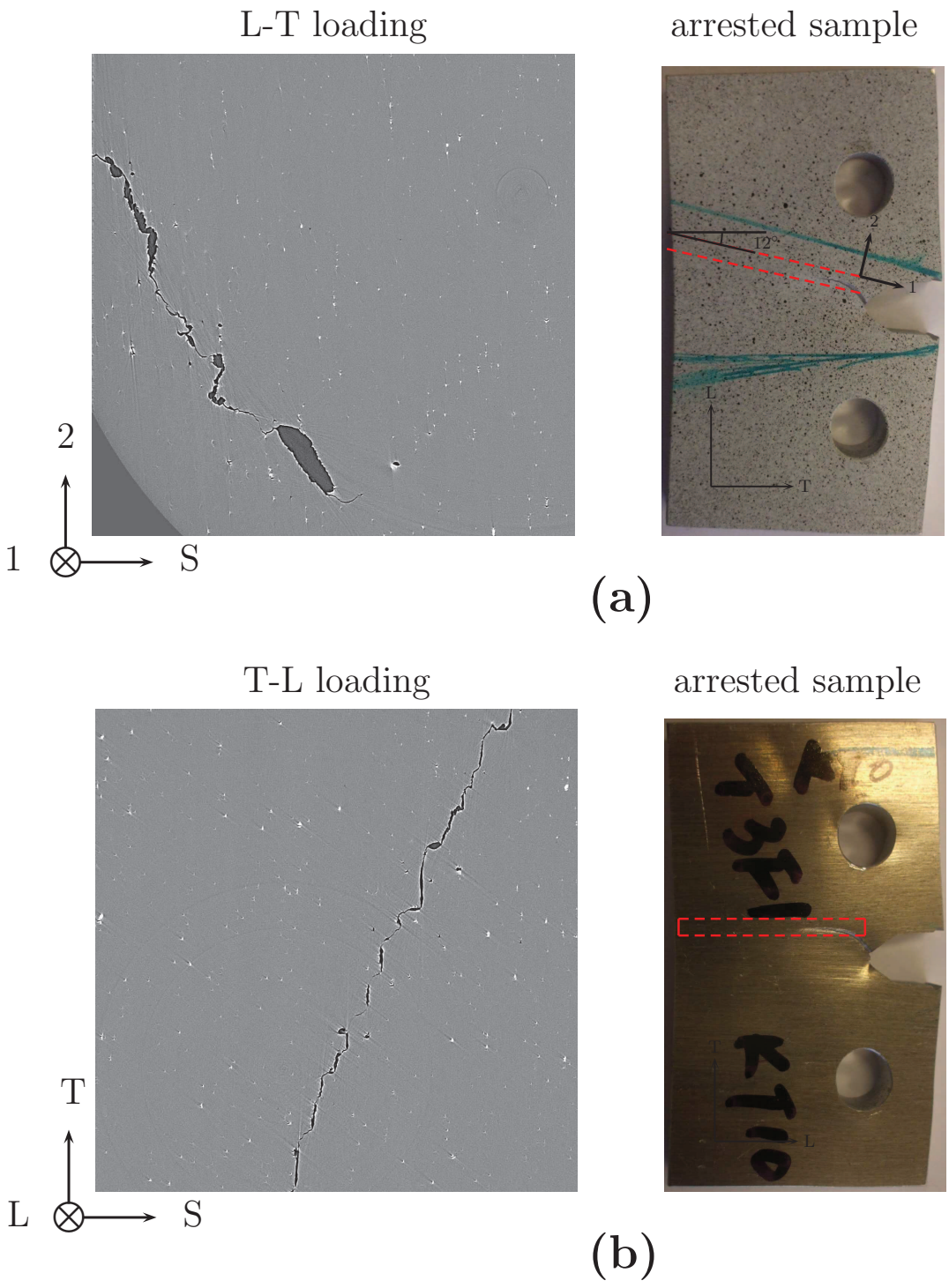


Figure 4.33: Two-dimensional section of tomography data showing the crack in L-T and T-L orientations for the T3 condition 6 mm-thick fibrous material: (a) L-T loading orientation; and (b) T-L loading orientation. Crack-growth direction is given by the outward normal to the plane of the section

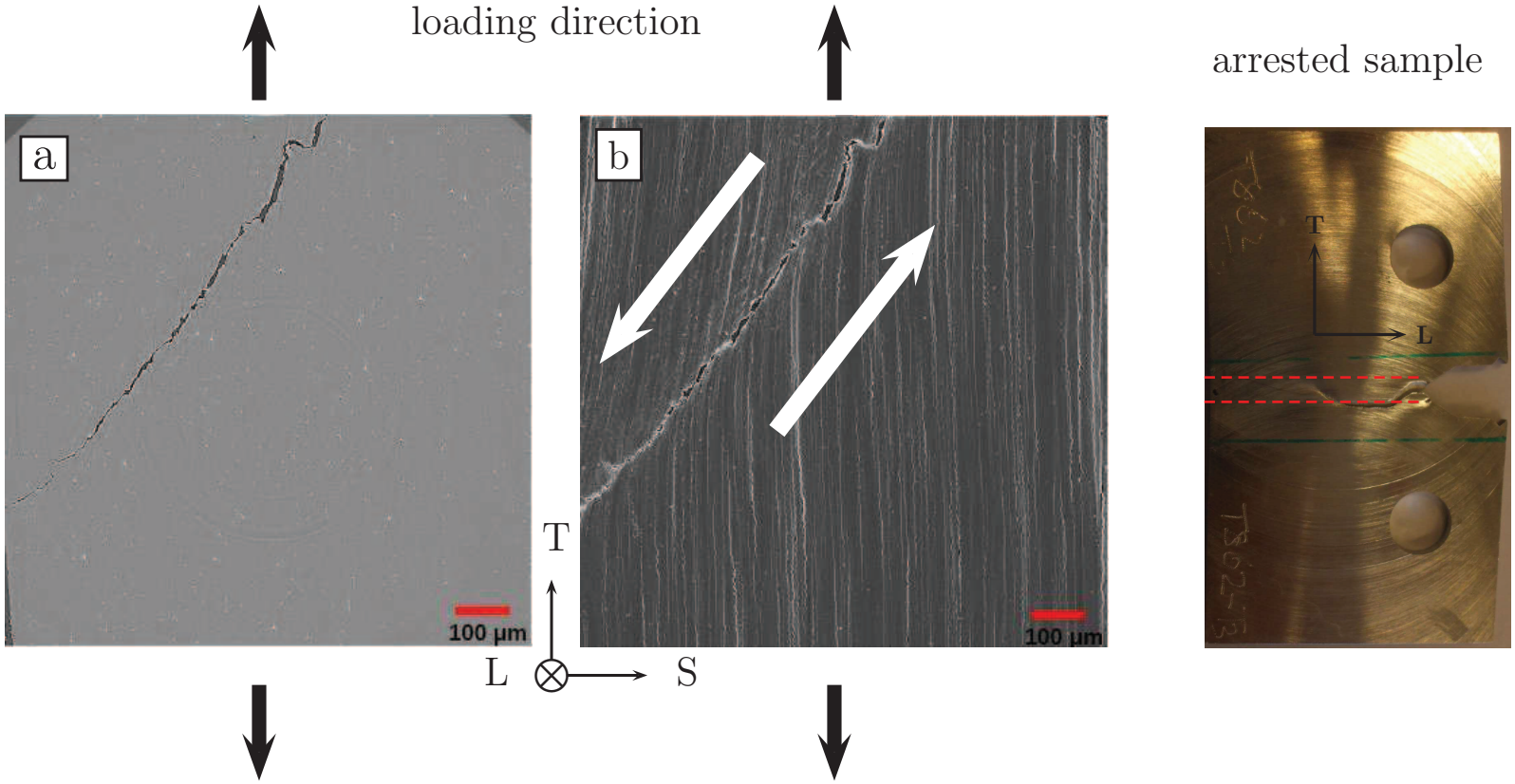


Figure 4.34: Two-dimensional section of tomography data showing the crack in T-L orientation for the T8 condition 2 mm-thick sheet: (a) without gallium wetting; and (b) after gallium wetting. Crack-growth direction is given by the outward normal to the plane of the section

4.7 Discussion

4.7.1 Crack bifurcation behaviour

The tear tests on small sized Kahn specimens show that the 6 mm-thick fibrous materials ($T3F_6$ and $T8F_6$) exhibit a complex fracture surface in 3D view; in the sheet plane (L–T), crack bifurcation was observed, and in the thickness direction (S), slant fracture was obtained. When reducing the specimen thickness to 2 mm ($T3F_{62}$ and $T8F_{62}$), the crack turning problem is less pronounced than thicker ones. It is well established that the sheet thickness has a strong influence on crack extension behaviour in high strength aluminum alloys [51, 105]. Because different sheet thickness exhibit different out-of-plane constraint (σ_{33}) and stress triaxiality. Variable constraint and triaxiality across the thickness has consequences for the behaviour of the crack extension. In addition to this, the plastic zone also changes with sheet thickness for notched specimens (e.g. NT and tear samples in ours case). Before crack initiation, 2 mm-thick Kahn specimen has a smaller plastic zone than 6 mm-thick one. It will be shown in the following chapter with FE-simulations on different thick specimens. Secondly, the structural effect has also influence on crack turing behaviour; M(T) panels exhibit more straight crack path than Kahn specimens with the same material and loading orientation. Between the two case, a near straight crack extension path was observed on medium sized Arcan sample. The problem of crack turning behaviour has been shown by Crill *et al.* [29] on AA2050-T87 Al-Cu-Li thick plate and also on a high strength AA7050-T7451 Al-Zn plate. The results suggest the crack turning behaviour witnessed in AA2050-T87 Aluminium-lithium alloy is associated with the resistance to changing the mode of crack growth from plane strain to plane stress behaviour. In a 3D view, the crack is slanted and has a strong bifurcation in the sheet plane. As a consequence, it will make the modeling of crack extension become more complex (cf. chapter 5, section 5.3).

4.7.2 Grain boundary fracture and delamination

The investigation of arrested Kahn specimens via X-ray micro-tomography techniques shows that void growth is very limited in the propagation regions (slant regions). Grain boundary decolesion is the predominant fracture mode in 6 mm-thick fibrous materials as illustrated here in Fig. 4.35. As a consequence, a lower fracture toughness in the short-transverse direction (S) was observed due to delamination crack. And this has been demonstrated via short-bars tests [6] along S direction carried out by Decreus [31]. Through our work, two essential reasons were identified. The first one is the stress triaxialiy state in specimens. 6 mm-thick Kahn specimens have a higher triaxiality ratio than 2 mm-thick ones. It has been proved via tests by reducing specimen thickness. The fracture mode of 2 mm thick samples is predominantly in shear mode where delamination is not observed. Secondly, from material microstructure characterization, inter-granular precipitates and inclusions were observed in T8 condition fibrous material ($T8F_6$) but not in T3 condition ($T3F_6$). It can explain that why the T3 material does not suffer delamination as the T8 material even with same specimen thickness. The inter-granular ductile fracture is well known in high strength aerospace aluminium plates (usually in T8 state) [34, 51, 105]. The competition between inter-granular and trans-granular fracture has been investigated by Pardoen *et al.* [80] on an AA7050 Al-Zn alloy. It is shown that the main parameters increasing the risk of grain boundary failure are large stress triaxiality and small value of the void spacing. In our case the initial porosity is very limited and as a consequence, void growth is also limited in the crack propagation regions. This is consistent with the conclusion of Pardoen *et al.* study [80].

4.7.3 Thickness effect

Comparing of different thickness Kahn tear tests indicates that thickness affects fracture toughness. This result is consistent with [119, 3, 9, 90]. It provides clear evidence that ductility

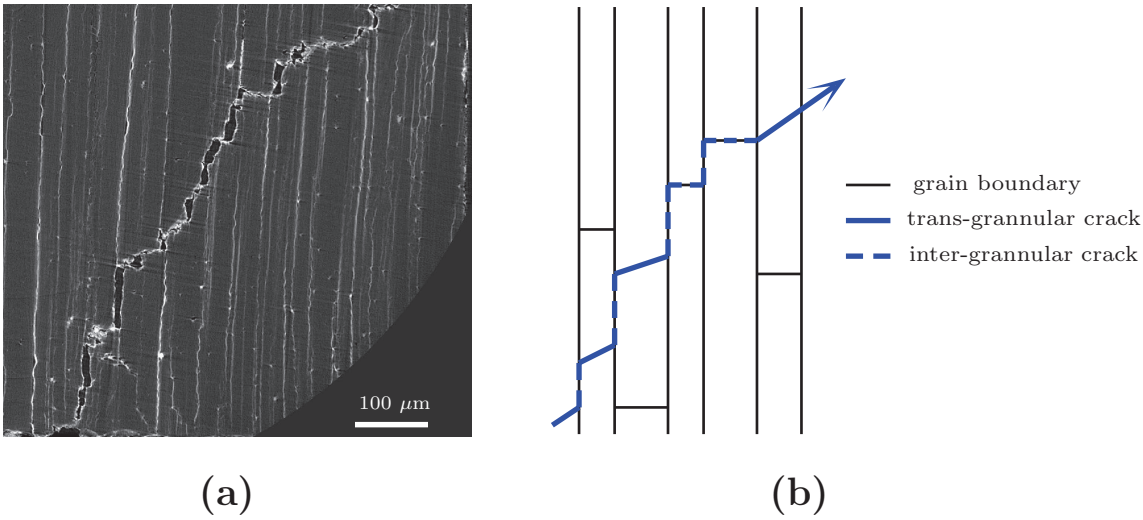


Figure 4.35: Fracture mode: inter-granular cracks vs. trans-granular cracking.

and fracture toughness increase with increasing specimen thickness until a limited thickness. This critical thickness varies with materials [120, 90]. As thickness increases, the deformation condition along the thickness direction progressively changes from plane stress to plane strain. This results in an increase of the stress triaxiality ratio. However, the increase of the stress triaxiality has two antagonist effects: for thin sheets: higher stresses are generated in the loading direction leading to a higher dissipated energy; for thick plates: the void growth rate is increased causing a rapid damage development [1, 17, 90].

4.8 Conclusion

In this chapter, the tear properties were investigated experimentally. Three different types of tearing samples including small sized Kahn tear specimens, mixed-mode loading Arcan specimens and large panels M(T) were used

For Kahn tear tests, stable crack extension can be obtained on the two recrystallized ma-

terials ($T3R_2$ and $T8R_2$) in both T3 and T8 condition. For both conditions, L-T loading tests have a higher toughness than T-L loadings. In the case of both fibrous materials ($T3F_6$ and $T8F_6$), tests carried out on T3 condition material can obtain a stable crack extension but with a strong crack bifurcation especially in the case of L-T loading test. For T8 condition material ($T8F_6$), strong crack turning behaviour was identified with presence of pop-ins during tests. According to ASTM standard, the crack bifurcation has passed the valid limit; tested results cannot be used for the interpretation of fracture toughness.

Arcan tear tests were performed on artificially aged fibrous material ($T8F_6$) which exhibit unstable crack extension like Kahn tests. For pure mode I loading (Arcan $_90$), results were compared to corresponding Kahn tear tests. L-T loading Arcan tests have a slightly higher toughness than T-L loading which is different from Kahn test results. However, due to an abrupt crack propagation in T-L loaded specimens, further investigations need to be done in order to confirm this conclusion. For the mixed-mode loading (Arcan $_60$), the crack extension are also not stable (presence of pop-ins). However, with an initially pre-cracked Arcan specimen, stable crack extension can be obtained in mode I loading. Which means that the initial crack tip condition has an effect on crack extension behaviour.

Experimental results on large panels M(T) tests (performed on $T8R_2$ and $T8F_{65}$ materials) show that both conditions exhibit a straight crack extension path. For $T8R_2$ material, L-T loaded panels have a higher fracture toughness than T-L loaded panels which is consistent with experimental results of small size Kahn tests. In the case of T8 fibrous material ($T8F_{65}$), there are no difference between L-T and T-L loading specimens in terms of toughness.

Examination of broken samples at a macroscopic scale indicates that both small sized Kahn specimens and large panels M(T) specimens have the same fracture surfaces. The crack begins with a small flat triangular region perpendicular to the loading direction followed by a flat-to-slant transition. Outside of this zone, typical slant fracture is observed. Observations of fracture

surface at a microscopic scale indicate that two different fracture mechanisms can be identified on both Kahn samples and M(T) panels. In the flat region, void growth mechanism is dominant due to a higher triaxiality ratio; very large dimples can be seen. In the slant zone, void growth is very limited, the failure at grain boundaries is predominant in T8 fibrous material ($T8F_6$).

Investigation of arrested Kahn tests via high resolution X-ray tomography techniques with gallium wetting treatment gives more accurate results concerning the fracture mode and damage development in tested materials. In all materials studied, void growth is limited in the slant regions. For both 2 mm-thick recrystallized materials ($T3R_2$ and $T8R_2$), trans-granular fracture is the predominant fracture mode in the crack propagation regions; However, for two 6 mm-thick fibrous materials ($T3F_6$ and $T8F_6$), in the mid-thickness of samples, inter-granular crack was observed in both T3 and T8 conditions. In the case of T8 condition material which contains inter-granular precipitates and inclusions (see TEM observations), delamination cracking was observed in the case of L-T loading tests.

Thickness effect on fracture toughness were examined on two 6 mm-thick fibrous materials by reducing sheet thickness to 2 mm in the case of Kahn tear specimens. Experimental results show that fracture toughness decreases with decreasing sheet thickness, 2 mm-thick tests have a lower nominal peak stress and a smaller crack mouth opening displacement at maximum load. Complementary tests on 3 and 4 mm tests in the case of $T8F_6$ material confirm this evolution of fracture toughness with sample thickness. The results also indicate that thickness has a strong influence on crack turning behaviour. With thinner specimens, a more straight crack extension path can be obtained with same kind specimen on the same material.

However, for both fibrous materials, strong crack bifurcation behaviour make the modeling of crack extension by finite element method become too complex. The investigation of arrested tests by X-ray tomography observation also gives a guide for the choice of fracture modeling models. Due to a very limited void growth, the classical Gurson-Tvergaard-Needleman type models

[43, 109, 110, 115] are not suitable for the modeling of fracture.

4.9 Résumé

L'objectif de ce chapitre est de comprendre les mécanismes de la déchirure ductile des matériaux et de construire une base de données expérimentale permettant de modéliser la propagation de fissure (cf. chapitre 5). Trois différents types d'éprouvettes ont été utilisés dans cette partie pour l'expérience. L'éprouvette de petite taille Kahn, l'éprouvette à chargement en mode-mixte Arcan et l'éprouvette structure M(T) (grande plaque fissurée). Pour les essais Kahn, la propagation de fissure est stable pour les deux matériaux recristallisés en état T3 et T8, la configuration L-T étant plus tenace que la configuration T-L. Dans le cas des deux matériaux fibrés, la propagation de fissure est stable pour le matériau en état T3 mais pas pour celui en état T8. Pour le matériau en état T3, la configuration T-L a le młme niveau de ténacité que la configuration L-T alors que pour le matériau en état T8, des pop-ins (décrochement dans la courbe force-déplacement) et des grosses déviations de fissure ont été observés pendant les essais. De ce fait, ces derniers essais ne sont pas valides au sens de la norme ASTM. Les essais Arcan de chargement en mode mixte sont réalisés sur le matériau fibré en état T8F6. Dans le cas de chargement en mode-I pure, les résultats sont cohérents avec les essais Kahn, la propagation de la fissure est plutôt stable. Dans le cas du chargement en mode-mixte, la propagation de la fissure est instable. Néanmoins, une propagation de fissure stable a été obtenue avec une éprouvette pré-fissurée par fatigue. Ces résultats montrent que la condition du fond d'entaille a un effet important sur la propagation de la fissure.

Les résultats de la structure M(T) montrent que la fissure se propage de manière stable et droite dans les deux matériaux en état T8. Pour le matériau recristallisé, la configuration L-T est plus tenace que la configuration T-L, ce qui est cohérent avec l'essai Kahn. Pour le matériau fibré, il n'y a pas de différence entre les configurations L-T et T-L au niveau de la ténacité. Les tôles fibrés

avec épaisseurs réduites ont permis d'étudier l'effet d'épaisseur sur la rupture ductile. Les résultats montrent que la ténacité diminue lorsque l'épaisseur d'éprouvettes entre diminue (de 6 mm à 2 mm). L'analyse fractographique indique que les surfaces de rupture d'éprouvettes Kahn et d'éprouvettes M(T) sont similaires. La fissure commence avec une petite région triangulaire perpendiculaire à la direction de chargement suivie par une zone de transition de plat-à-biseau. Au delà de cette zone, la propagation de la fissure se poursuit en biseau. Les observations microscopiques montrent deux différents mécanismes de rupture. Dans la zone triangulaire, la croissance de cavités est dominante du fait de haute triaxialité de contrainte, des grosses cupules ont été observées. Dans la zone en biseau, la croissance de cavités est limitée due à une faible triaxialité, la rupture par cisaillement est prédominante. Les observations d'éprouvettes Kahn interrompues par tomographie haute résolution à rayon X confirment que la croissance de cavités reste limitée dans la zone de propagation de fissure en biseau. Les traitements au gallium des échantillons ont permis de mettre en évidence une rupture inter-granulaire prédominante pour les matériaux fibrés.

Chapter 5

Modeling of Ductile Tearing

5.1 Introduction

The accurate prediction of ductile crack growth plays a key role in thin-walled structures (e.g. airplane fuselage, space shuttle fuel tank and pipeline). Methodologies to model ductile crack growth by finite element method have evolved primarily along two lines of development [42]: approaches based on damage mechanics that use accumulated damage along the crack front as a growth criterion, and approaches that control crack extension via a macroscopic measure of deformation such as the CTOA (Crack Tip Opening Angle) and the CTOD (Crack Tip Opening Displacement). Current research in the first category often uses the Gurson-Tvergaard-Needleman (GTN) constitutive model [43, 27, 76, 112] to characterize the void nucleation, growth and coalescence process which drive crack growth. Various researchers [94, 122] have shown that such approaches are highly effective in producing geometry- and loading- independent predictions of crack growth in 2-D and 3-D for typically thick sections of ductile steels. However, the GTN constitutive model relies upon high levels of stress triaxiality to drive the damage process. Thin aluminum components cannot develop sufficient through-thickness stress to provide high stress triaxiality at the crack tip; the void growth and coalescence process more typically occurs along bands of large plastic strain.

Therefore, GTN-based approaches appear less applicable for thin specimens [42].

In the previous chapters, it has been shown that the initial void is limited in the present Al-Cu-Li sheet materials, and the void growth is also limited in the crack propagation region of arrested Kahn specimens (cf. 4.6.3). The GTN type damage models based on the phenomena of void growth and coalescence are not adapted to the modeling of fracture behaviour of investigated materials. By contrast, the purely phenomenological cohesive zone models (CZM) which describe the crack extension via a simple traction-separation law (also called cohesive law) can be used to model the ductile tearing behaviour of current studied materials. The fracture process is represented by the specified traction-separation law along the predefined crack plane, and the surrounding material is modelled by its elastic-plastic properties.

Cohesive zone models were first introduced by Dugdale [33] with the idea of a cohesive force preventing a crack from extending, in the early 1960. The magnitude of cohesive force is set to the yield strength σ_{Y} of the material. Later Needleman was the first to use a cohesive zone model for the analysis of micro damage in ductile materials [75]. Pioneering work was performed by Tvergaard and Hutchinson [111, 113] for the macroscopic crack extension in ductile materials. Recently, Scheider *et al.* at GKSS Research Center have contributed to the application of cohesive zone models in various materials and problems [97, 96, 98]. For all cohesive zone models, each separation law is characterized by its specified shape and by two parameters, a maximum tensile stress T_0 and a critical displacement δ_0 after which no additional tensile stress is sustained. The area under the T-δ curves is the separation energy Γ_0. More generally the traction vector has one normal (mode I) and two tangential (modes II and III) components, each of which corresponds to a separation parameter set, T_0 and δ_0. As illustrated on Fig. 5.1, Schwalbe *et al.* give a schematic description of physical fracture process represented by the cohesive zone model. For pure mode I loading the normal tensile stress $\mathrm{T}_{0\mathrm{N}}$ is correlated with a relative displacement d_N. For shear mode (mode II), the cohesive parameters are shear stress $\mathrm{T}_{0\mathrm{S}}$ and relative shear displacement d_S. Fig. 5.2

shows various traction-separation functions having been used for ductile fracture in literature [124].

In this part, two different traction-separation laws are used to model ductile tearing behaviour of studied materials. The first one is the classical Needleman traction-separation law which was used to model global mode-I fracture with a flat crack extension plane. Secondly, a modified Scheider mixed-mode separation law is proposed to model mixed-mode slant fracture. The transferability from small sized Kahn specimens to large panel M(T) tests via finite element simulation by cohesive zone model was assessed. Thickness effect was investigated numerically on Kahn specimens with a specific node release technique. Stress triaxiality and out-of-plane stress were analysed along specimen's thickness and with crack extension length.

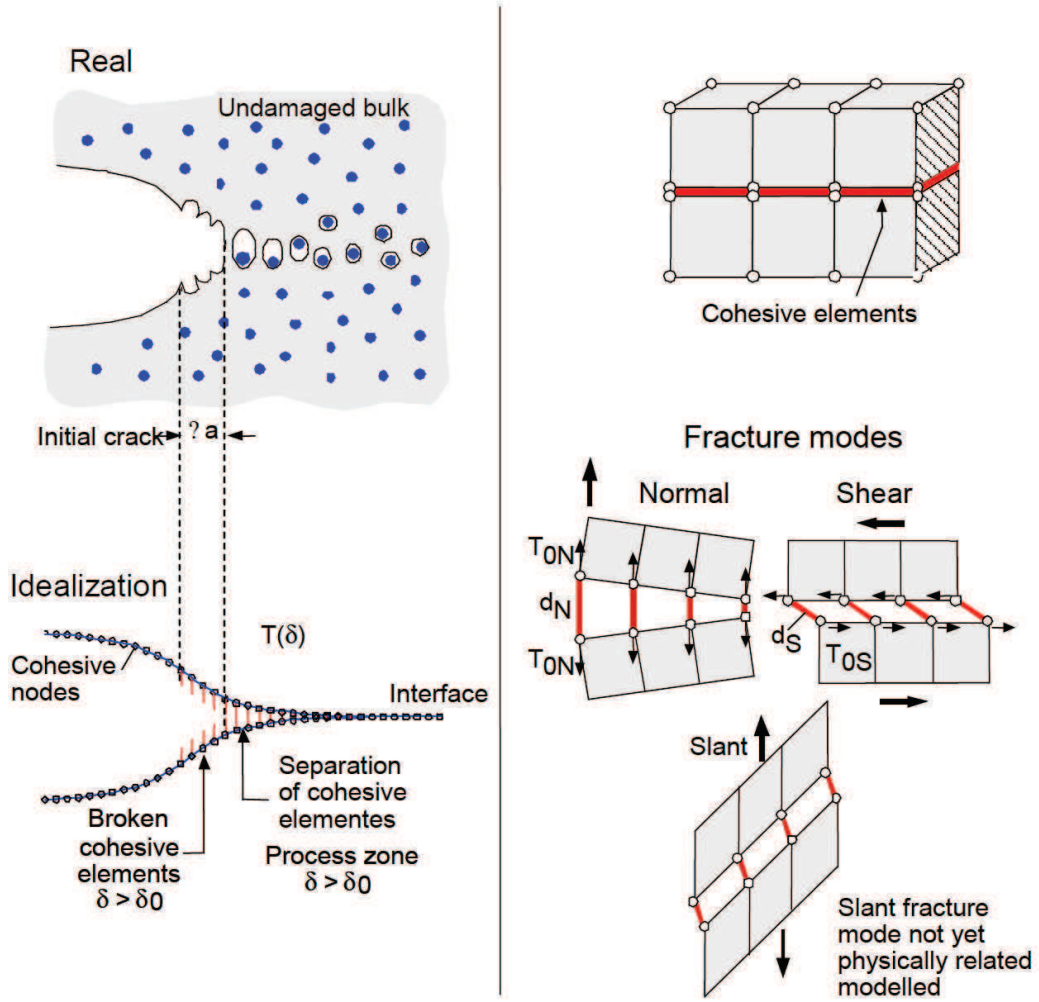


Figure 5.1: Representation of the physical fracture process by separation function within interface cohesive elements (after Schwalbe *et al.* [98]).

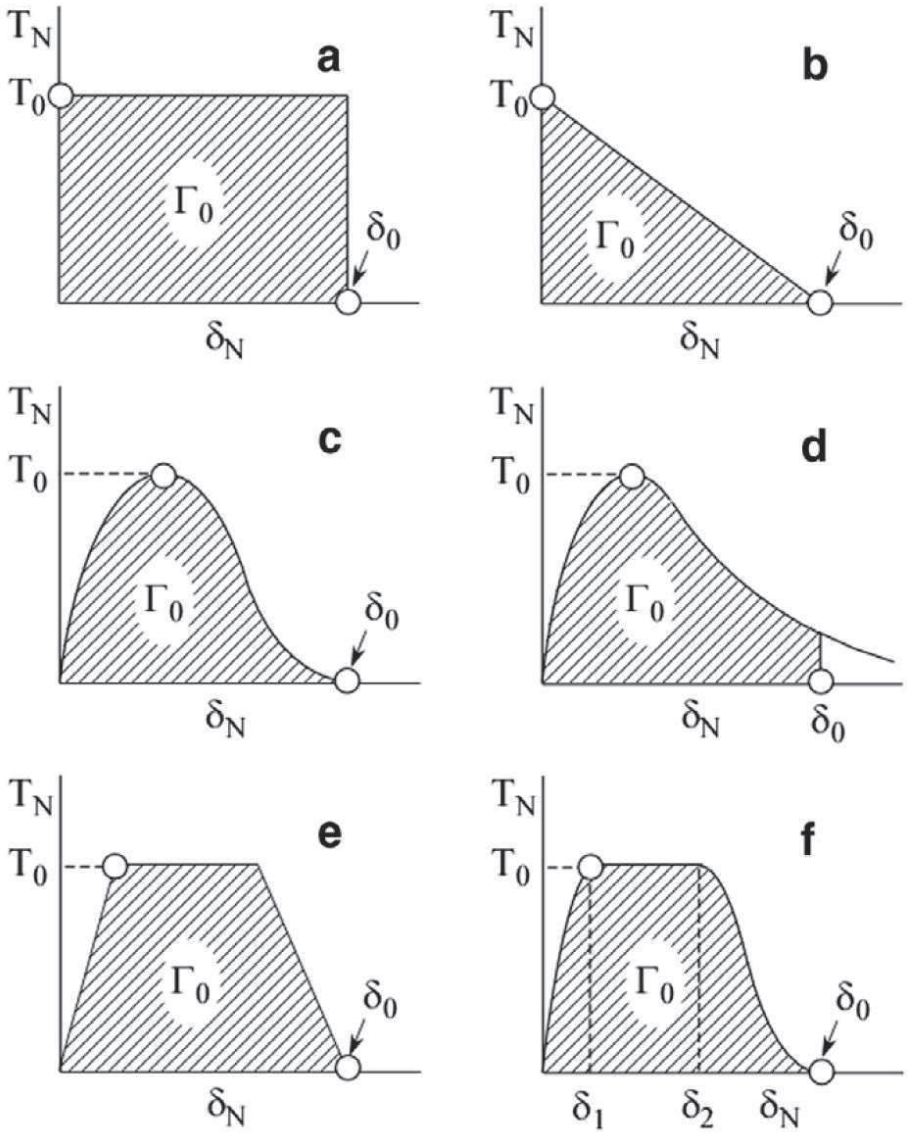


Figure 5.2: Various separation laws [124], (a) Dugdale [33]; (b) Barenblatt [10]; Hillerborg *et al.* [48] and other authors, brittle materials; (c) Needleman [75]; Tvergaard [111]; Chaboche *et al.* [24], ductile materials, polynomial equation; (d) Rose *et al.* (1981); Needleman [77, 78], exponential equation; (e) Tvergaard and Hutchinson [113]; Roy *et al.* [92], trapezoidal law; (f) Scheider [95];

5.2 Traction-separation constitutive models

5.2.1 Mode I – Traction-separation law

As illustrated in the previous chapter (cf. Ductile Tearing), all tear specimens (Kahn, Arcan and M(T)) exhibit slant fracture surfaces after a short flat-to-slant transition. In the case of 2 mm-thick recrystallized materials (T3R$_2$ and T8R$_2$), straight and stable crack extension was obtained with small sized Kahn specimens, whereas strong crack deviation was observed in the case of 6 mm-thick fibrous materials (T3F$_6$ and T8F$_6$). Modeling of such strong crack bifurcation is not meaningful and cannot be used to predict corresponding large M(T) tests which exhibit straight crack extension path. The ductile tearing modeling was carried out on two recrystallized materials (T3R$_2$ and T8R$_2$) in the following. In order to model crack extension of Kahn specimens, straight and flat fracture surface (cf. Fig. 5.5) was first modelled by cohesive zone model (CZM). The cohesive zone model used in the current case (global mode I fracture) is based on the Needleman polynomial function [75]. The relationship between the cohesive normal tensile strength, T_n and the separation distance normal to the crack plane, δ_n, across the crack plane is defined as:

$$T(\delta) = \begin{cases} \frac{27}{4} T_0 \frac{\delta_n}{\delta_0} (1 - \frac{\delta_n}{\delta_0})^2 & \text{if } \delta_n \leq \delta_0 \\ 0 & \text{if } \delta_n > \delta_0 \end{cases} \tag{5.1}$$

The function is plotted on Fig. 5.3 where T_0 is the maximum sustainable tensile stress (cohesive strength), δ_0 the critical normal separation distance at which the traction drops to zero. It also can be calculated that when the δ_n equals $\frac{1}{3}\delta_0$, T_n reaches its maximum T_0. The separation energy Γ_0 spent in the separation process (area under T-δ curve), is defined as:

$$\Gamma_0 = \int_0^{\delta_0} T(\delta)\, \mathrm{d}\delta \tag{5.2}$$

Inserting eq. 5.1 into eq. 5.2, the three parameters Γ_0, T_0 and δ_0 are related by

$$\Gamma_0 = \frac{9}{16} T_0 \delta_0 \tag{5.3}$$

If the cohesive energy Γ_0 is known from experiments, the separation distance can be given by

$$\delta_0 = \frac{16}{9} \frac{\Gamma_0}{T_0} \tag{5.4}$$

The two most important parameters characterizing the fracture process in present model are Γ_0 and T_0 [113].

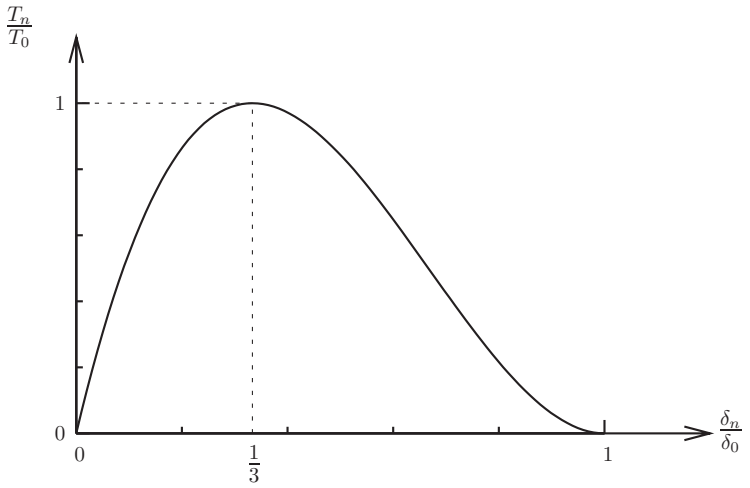


Figure 5.3: Traction-separation law used in the case of global Mode-I cohesive elements (flat fracture surface).

5.2.2 Mixed-mode cohesive law

The separation law used for the investigations of slant fracture modeling is based on an extension of Scheider cohesive law [95]. It is capable of shear separation and can be applied to

three-dimensional problems. The separation components tensile force, T^n and shear force, T^t are defined as:

$$\begin{aligned} T^N &= T^N(\delta^N, \delta^T) = T_0^N f(\delta^N) g(\delta_{max}^T) \\ T^T &= T^T(\delta^T, \delta^N) = T_0^T f(\delta^T) g(\delta_{max}^N) \end{aligned} \tag{5.5}$$

δ_{max}^T, δ_{max}^N denote the maximum tangential and normal separation displacement having occurred so far, $g(\delta)$ is the interaction function. For pure normal (or pure tangential) separation, the function $g(\delta)$ has the value 1.

The separation function proposed here for slant fracture modeling is similar to the function presented by Scheider [95], as shown on Fig. 5.4. In order to avoid an unwanted "elastic" opening of the cohesive element, an infinite stiffness is chosen for the beginning (δ_1 is very small). The function $f(\delta)$ contains one additional parameter, η, to define the start of softening region. The resulting cohesive law for pure normal (or tangential) separation law is plotted on Fig. 5.4b.

The function $f(\delta)$ is written as:

$$f(\delta) = \begin{cases} 1 & \text{if } \delta \leq \eta \\ 2(\frac{\delta-\eta}{\delta_0-\eta})^3 - 3(\frac{\delta-\eta}{\delta_0-\eta})^2 + 1 & \text{if } \delta > \eta \end{cases} \tag{5.6}$$

The cohesive energy for pure normal or tangential separation can be determined using eq. 5.5 and eq. 5.6 by

$$\Gamma_0 = \int_0^{\delta_0} T(\delta)\, \mathrm{d}\delta = T_0 \delta_0 \left(\frac{1}{2} + \frac{1}{2} \frac{\eta}{\delta_0} \right) \tag{5.7}$$

Notice that here the peak stress T_0 denotes the maximum normal or maximum tangential cohesive stress which are different. Consequently, the cohesive energy Γ_0 for pure normal or tangential

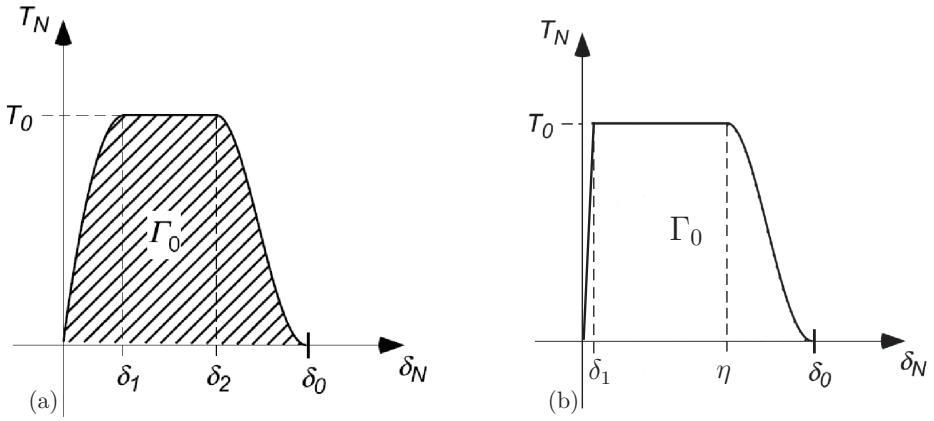


Figure 5.4: Scheider cohesive law [95] (a), and modified Scheider cohesive law for mixed-mode cohesive separation (b).

separation is also different. The function $g(\delta)$ in eq. 5.5 defines the interaction between normal and tangential separation. There is no obvious physical foundation for choosing a specific function. In our case, the same function is chosen as in Scheider and Brocks [97].

$$g(\delta) = 2\left(\frac{\delta}{\delta_0}\right)^3 - 3\left(\frac{\delta}{\delta_0}\right)^2 + 1. \tag{5.8}$$

5.3 Finite element models

5.3.1 Flat crack path model

The simulation of crack growth was realised in the object-oriented finite element code Zébulon [14, 36]. Table 5.1 summarizes the specimens investigated in the present study. One-fourth of Kahn specimen with a straight flat crack plane was modelled due to twofold symmetry. In the 3D FE-model, the plane $z = 0$ represents the mid section of specimen, and the plane $z = 1$ mm represents the side-surface for 2 mm-thick Kahn specimen. There are 4 layers in the thickness direction (z), the layer thickness is 0.25 mm for 2 mm thick specimens. Eight-node solid elements with full integration are used for the bulk elements (surrounding material). As reported in the chapter of "Ductile Tearing" (cf. section 4.6), two different failure mechanisms were identified by scanning electron microscopy (SEM) observations on broken Kahn and M(T) specimens. For the modeling of crack extension, the correct way is to model crack growth with two different process regions and with different cohesive zone parameters (T_0 and δ_0). The crack plane is divided into two zones, "flat triangular" region (zone 1) and "slant" region (zone 2). The size of zone 1 is set to equal the equivalent flat triangular region measured by SEM observation on Kahn fracture surfaces. The length of zone 1 and zone 2 for each material and loading configuration is given in Table 5.2. Typical mesh used for Kahn specimen is shown on Fig. 5.5. The crack extension is in x–direction, the size of the interface-cohesive elements in x–direction is 0.1 mm for the first 10 mm ligament ($0 \leq x \leq 10$).

Specimen	H (mm)	W (mm)	B (mm)	a/W
Kahn (no pre-cracked)	60	35	2, 3, 4, 6	0.29
M(T) (pre-cracked)	1030	760	2, 5	0.33

Table 5.1: Tear specimens investigated by FE-simulations.

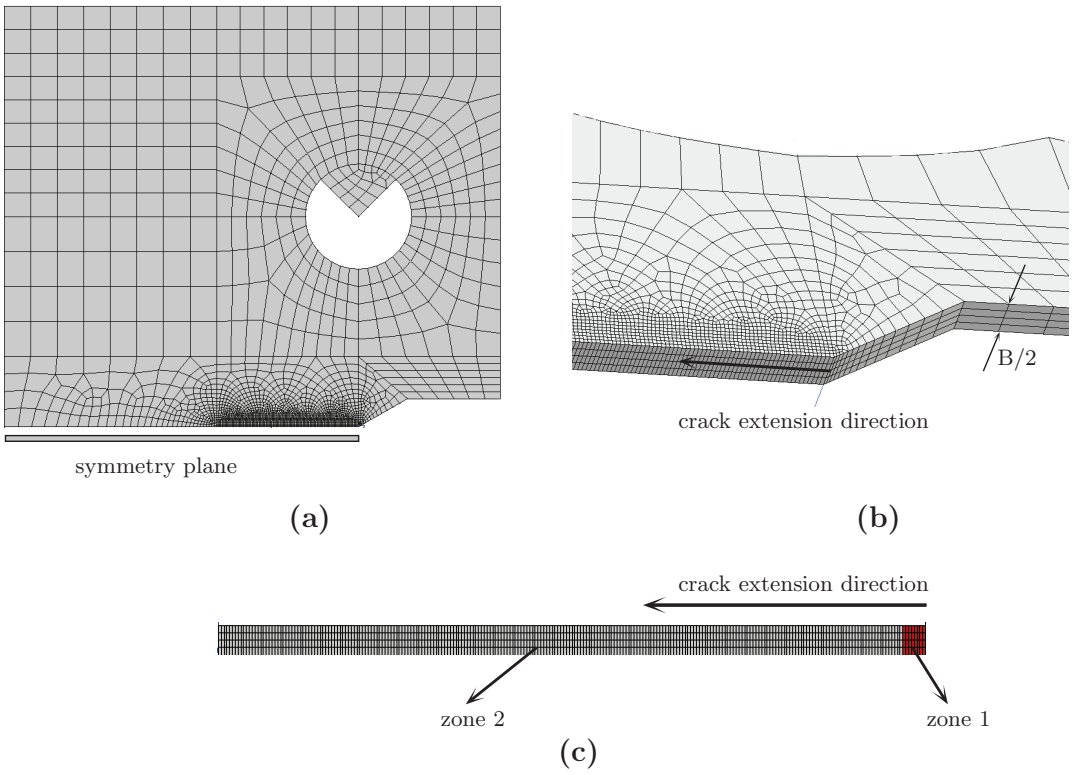


Figure 5.5: FE-mesh of Kahn specimen with straight flat fracture surface (a), magnification of the initial crack tip region and crack plane (b, c).

As for Kahn tear specimens, straight flat crack plane is modelled for M(T) tests. Fig. 5.6 shows full details of the finite element model for large panel M(T) specimens. One-eight of specimen was modelled due to a full symmetry. The crack grows into meshes having element sizes L_e = 0.1 mm for the first 45 mm (126.5$\leq x \leq$171.5) which then increase to 2 mm in the rest of crack plane. Interface-cohesive elements in the direction of crack growth have the same size. The crack plane is divided into two regions as in Kahn samples, the area of "zone 1" for M(T) panel equals experimental flat triangular region area. Study on mesh convergence carried out with different layers of elements over thickness demonstrated that four layers of uniformly sized elements provide sufficient resolution to capture through-thickness variation in constraint. So in our case, four layers of elements were used to save computation time. For such large thin panel tests (1030 $\times$ 760 $\times$ 2 mm),

out-of-plane bending is often observed during tests. To avoid out-of-plane bending, symmetric meshes in the thickness direction are used.

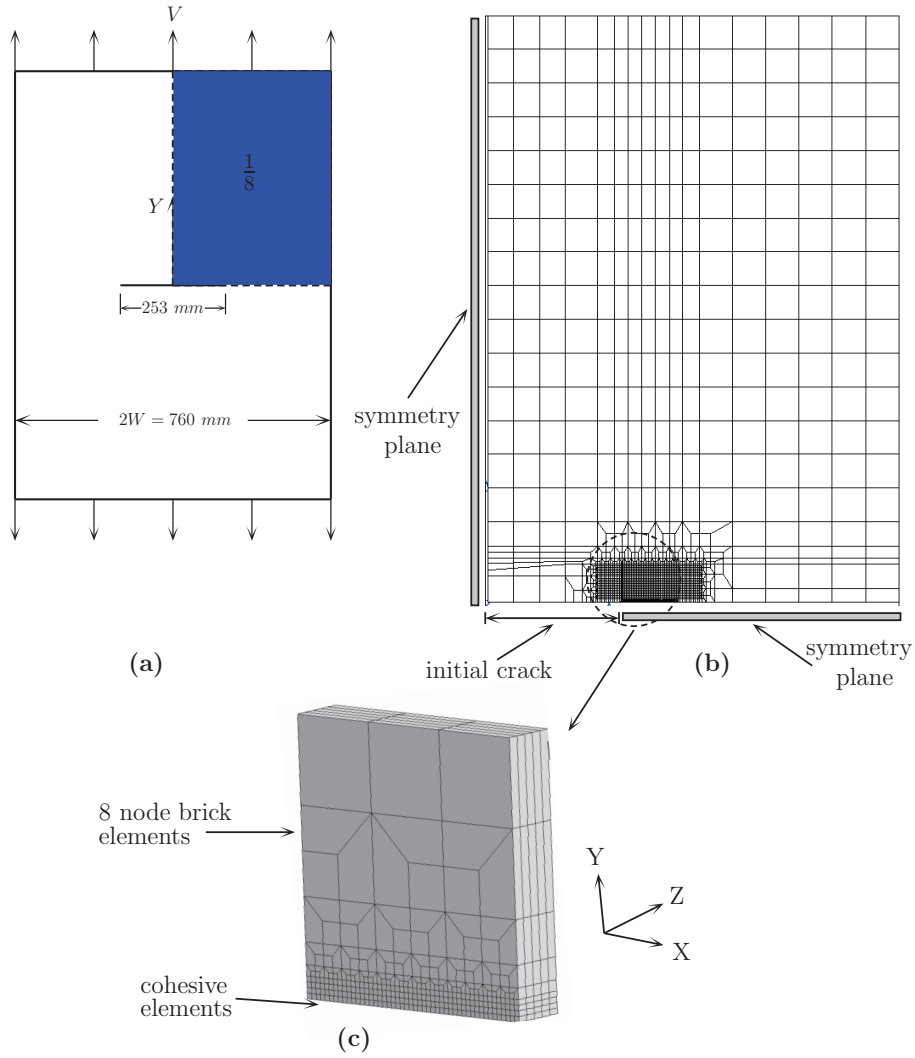


Figure 5.6: Typical mesh for analyses of M(T) specimen (2W=760 mm): (a) specimen geometry, (b) one-eighth symmetric mesh for FE-analyses, (c) local view of crack plane region with interface-cohesive elements.

5.3.2 Slant fracture model

As observed in experimental tear tests, thin sheet materials exhibit a slant fracture surface after a short flat-to-slant transition as illustrated on Fig. 5.7. Since the tested specimens have this feature of flat-to-slant transition fracture, the correct way is to model the fracture process with flat-to-slant fracture surface in finite element models. In this study, we proposed to used the following mesh (see Fig. 5.8) to model crack growth in tearing tests on small Kahn samples and large M(T) panels. The typical mesh of small sized Kahn specimen is shown on Fig. 5.8. This flat-to-slant fracture surface is generated by a node position transition in Y–direction with an initial flat crack plane (e.g. Fig. 5.5). The size of triangular zone is set equal to the measured triangular region. The initial slant angle is slightly smaller than experimental value so that ”final slant angle” (experimental value) can be obtained.

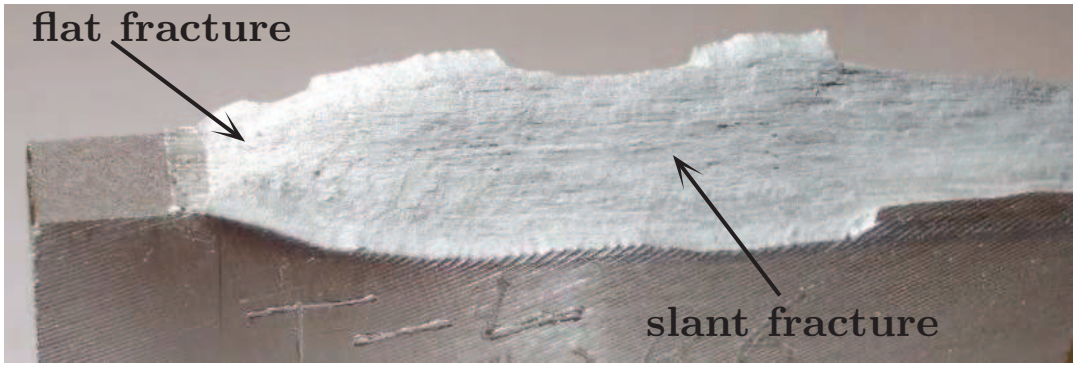


Figure 5.7: Flat-to-slant fracture in thin aluminum sheet material.

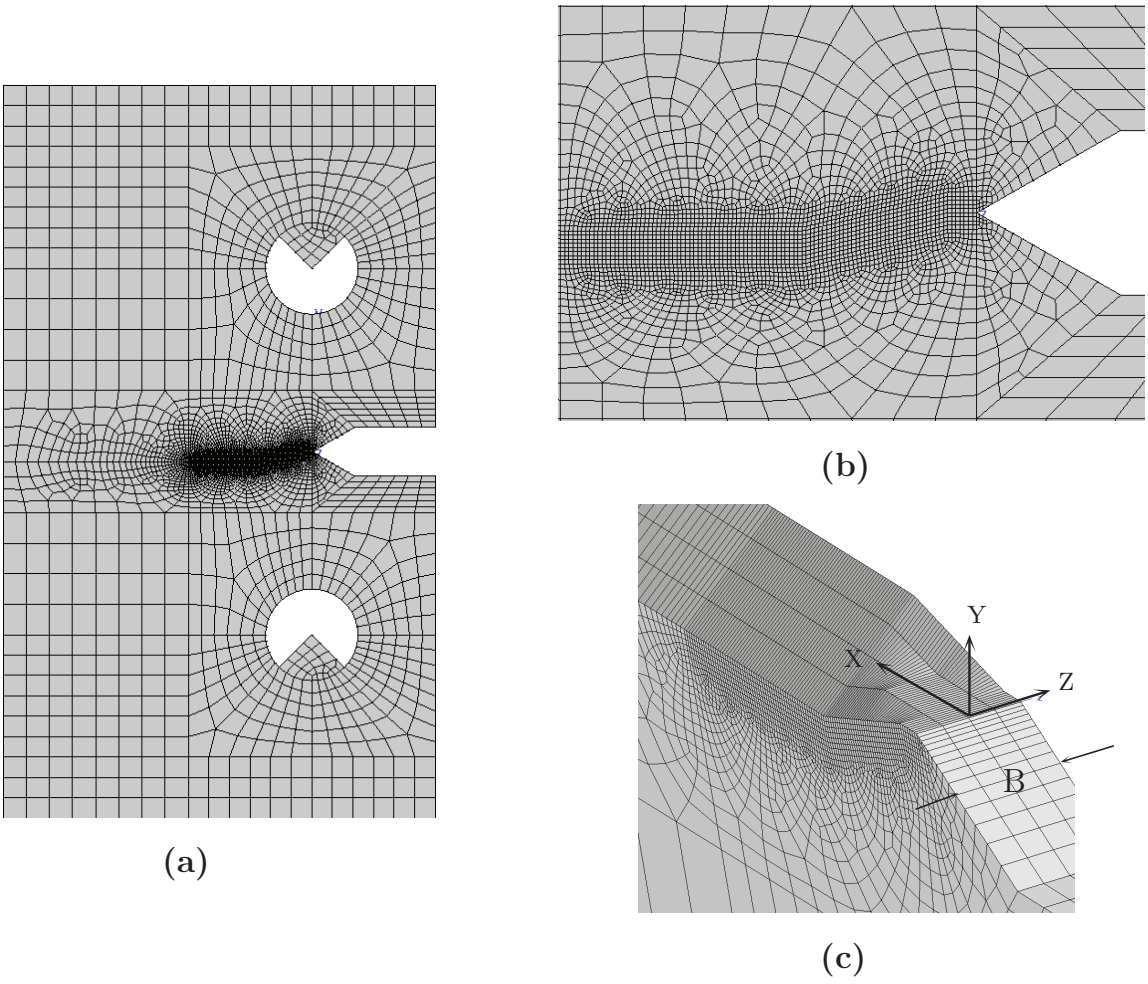


Figure 5.8: FE-mesh for a Kahn specimen with flat-to-slant crack plane: (a) the global full mesh, (b) a local view focusing on the crack path region, and (c) a local view showing the transition flat-to-slant crack growth path.

5.4 Calibration of cohesive zone parameters via Kahn tear tests

5.4.1 Material parameters

It is known that the response of cohesive model is very sensitive to changes in elastic-plastic properties of the surrounding material [113, 114, 96]. An accurate identification of material's elastic-plastic behaviour is important for the following simulations. At first, the identified material's elastic-plastic parameters using smooth tensile and differently notched tensile tests (cf. chapter 3) are used to simulate the Kahn tear specimen's elastic-plastic behaviour. Fig. 5.9 gives the simulation results of Kahn specimen by fitted elastic-plastic parameters and von Mises criterion. Compared to von Mises isotropic criterion, it is clearly shown that the description of plasticity by fitted anisotropic parameters is very accurate except where crack extension starts at the notch root. The identified material elastic-plastic parameters on smooth tensile and notched tensile tests can well represent the background material behaviour of tearing specimens (Kahn and M(T)).

5.4.2 Determination of the cohesive zone parameters

The cohesive zone parameters T_0 and δ_0 or Γ_0 and δ_0 which describe the fracture process by a separation law cannot be measured in a direct way for ductile materials, but have to be identified by fitting finite element results to experimental data. The determined cohesive zone parameters for different separation laws are also different, as a result they should not be regarded as model independent material parameters [124]. They are also different for 2-D and 3-D simulations [96]. In our case, the simulations are all performed in 3-D.

In this work, two different ways have been used for the determination of the cohesive stress, T_0. According to various publications [123, 61, 98], cohesive stress, T_0 can be estimated on a notched tensile specimen. In our case, a NT_2 specimen was simulated by finite element using fitted elastic-plastic parameters, the simulation stopped at the experimental beginning of fracture.

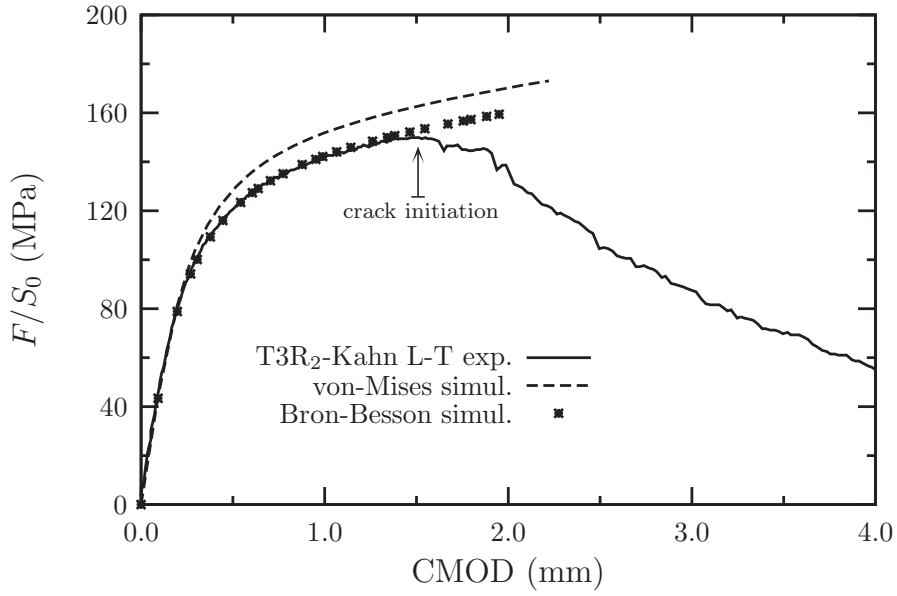


Figure 5.9: Simulation results of elastic-plastic behaviour for Kahn tear test by fitted parameters on smooth tensile and notched tensile tests, dashed line represents simulation result by von Mises criterion.

The tensile stress (axial stress) distribution over the specimen's ligament is shown on Fig. 5.10 for T3R$_2$ and T8R$_2$ materials along L and T loadings. The cohesive strength, T_0 is set to equal the corresponding maximum value of tensile stress. In second way, it has been suggested by Roychowdhury *et al.* . ([93]) that the cohesive stress T_0 can be set to equal 2 – 3 times σ_{Y} for aluminium sheets as the initial value of calibration; where σ_{Y} is the yield stress of material.

5.4.3 Calibration results

The simulation results of Kahn tear tests using identified cohesive stress on notched tensile specimens are shown on Fig. 5.11 as exemplified here only for T3R$_2$ material for brevity. It is seen that the crack initiates much earlier than experimental tests, maximum nominal stresses are $\sim$10% lower than experimental values. Fig. 5.12 gives the simulation results of Kahn tear tests using

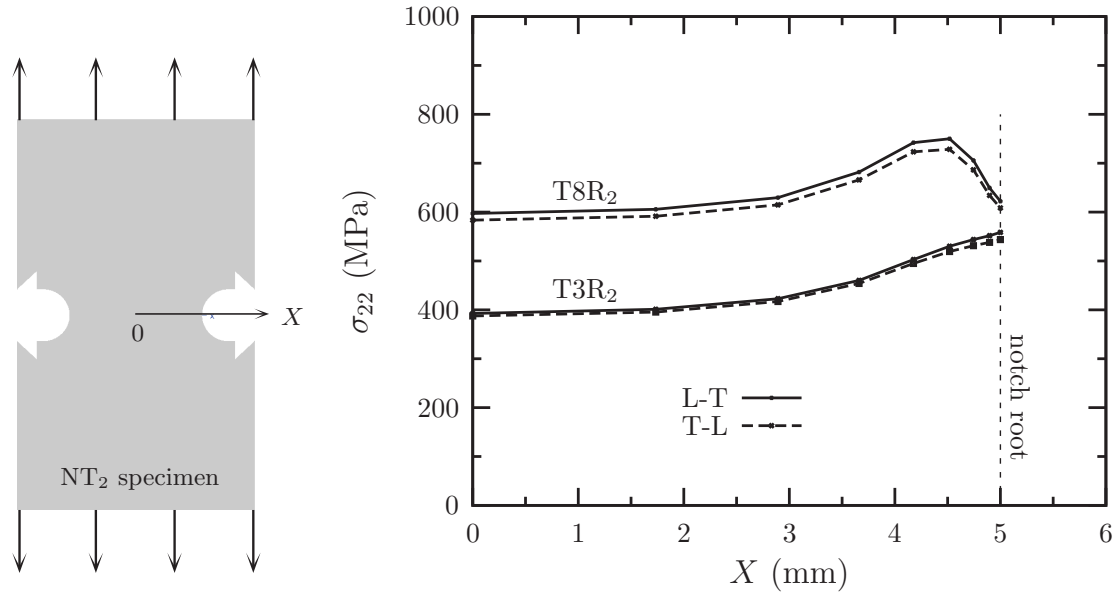


Figure 5.10: Determination of the cohesive stress T_0 on a notched tensile specimen NT_2 for $T3R_2$ and $T8R_2$ materials.

$2.7\sigma_Y$ as cohesive stress T_0 for $T3R_2$ material in L-T loading. It can be seen that T_0 ($2.7\sigma_Y$ = 783 MPa) is also little lower than experimental value. Based on these simulation results, cohesive stress, T_0 and separation distance, δ_0 are adjusted directly on experimental Kahn tear test results.

The final identification results of $T3R_2$ material along L-T and T-L loading are given in Fig. 5.13 via nominal stress (F/S_0) in terms of crack mouth opening displacement (CMOD) responses. While Fig. 5.14 shows the calibrated results for the case of $T8R_2$ material. For both cases, the ductile tearing of small sized Kahn tests can be well represented by mode I fracture using cohesive zone model; the fracture toughness between L-T and T-L loadings can be identified with two different couples of cohesive zone parameters. The fitted cohesive zone parameters for both $T3R_2$ and $T8R_2$ materials along L-T and T-L loadings are gathered in Table 5.2.

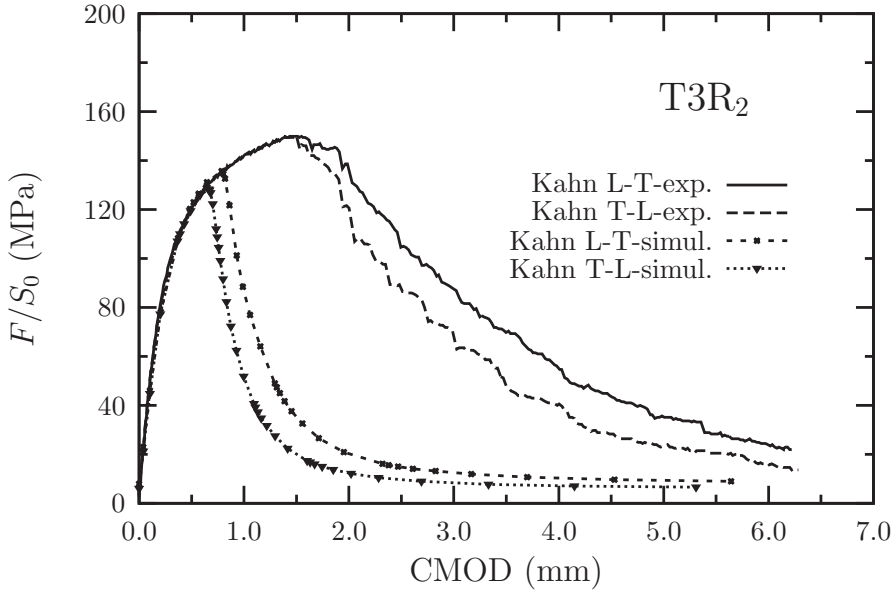


Figure 5.11: Simulation results of Kahn tear tests by identified cohesive stress on notched tensile specimen and experimental Kahn tear test results for $T3R_2$ material in L-T and T-L loadings.

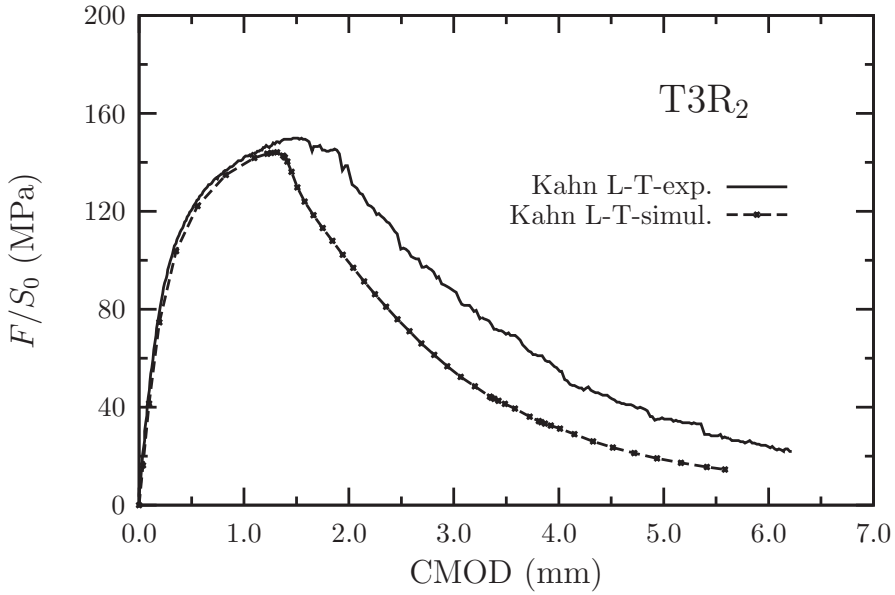


Figure 5.12: Simulation results of Kahn tear tests using $2.7\sigma_Y$ as cohesive stress T_0, and experimental Kahn tear test result for $T3R_2$ material in L-T loading.

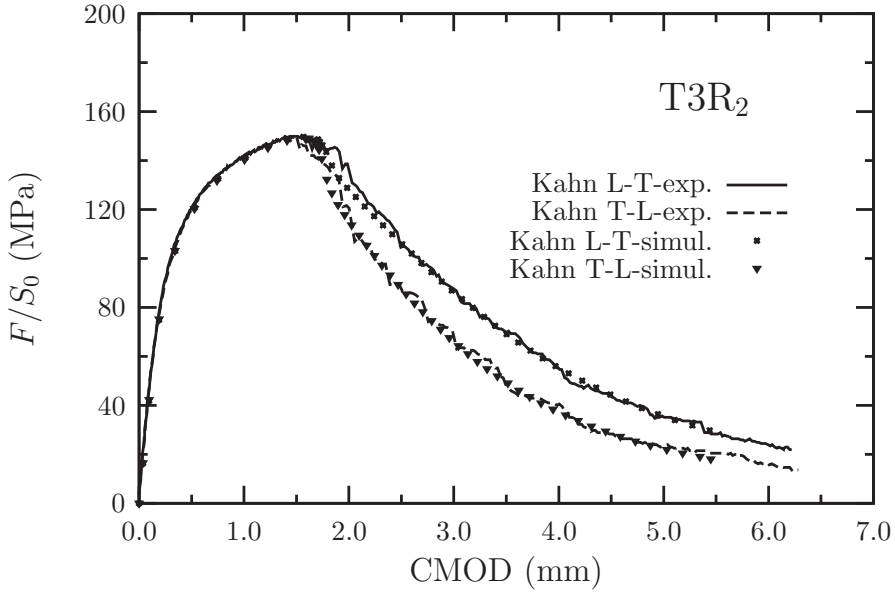


Figure 5.13: Experimental Kahn tear test results and fitted ones for naturally aged $T3R_2$ material in L-T and T-L loadings.

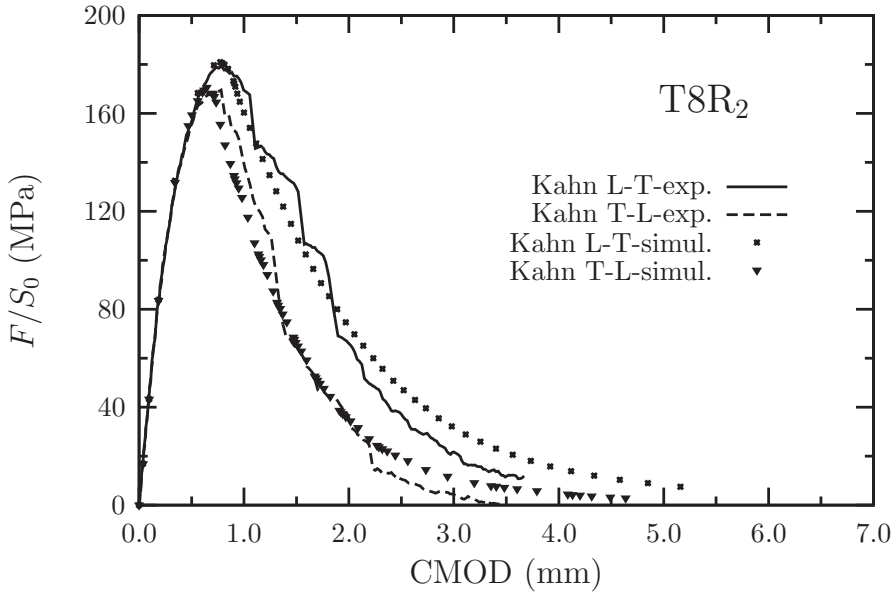


Figure 5.14: Experimental Kahn tear test results and fitted ones for artificially aged $T8R_2$ material in L-T and T-L loadings.

		T3R$_2$		T8R$_2$	
		Zone 1	Zone 2	Zone 1	Zone 2
L–T	Length (mm)	0.9	24.1	0.8	24.2
	T_0 (MPa)	975	820	825	820
	δ_0	0.21	0.09	0.21	0.08
	Γ_0 (N/mm)	115.2	41.5	98.63	36.9
	UIE (N/mm)	166	—	116	—
	σ_{ts} (MPa)	601	—	754	—
T–L	Length (mm)	0.9	24.1	0.8	24.2
	T_0 (MPa)	975	820	765	750
	δ_0	0.21	0.059	0.20	0.08
	Γ_0 (N/mm)	115.2	27.2	86.1	33.7
	UIE (N/mm)	145	—	83	—
	σ_{ts} (MPa)	601	—	716	—

Table 5.2: Fitted cohesive zone parameters and tear properties for T3 and T8 recrystallized materials (T3R$_2$ and T8R$_2$).

For Kahn tear tests, according to [5], the so-called tear strength σ_{ts} can be calculated as follows:

$$\sigma_{\text{ts}} = \frac{\text{P}}{\text{A}} + \frac{\text{MC}}{\text{I}} \text{ (Nominal direct stress + Nominal bending stress)} \tag{5.9}$$

where: $\frac{\text{P}}{\text{A}} = \frac{\text{P}}{\text{bt}}$, $\frac{\text{MC}}{\text{I}} = \frac{3\text{P}}{\text{bt}}$ (P is the maximum force, t represents average specimen thickness, b equals width (distance between notch root and back edge of specimen), M is the bending moment, C is distance from neutral axis to outermost fiber, and I is moment of inertia), tear strength σ_{ts} is given by

$$\sigma_{\mathrm{ts}} = \frac{4\mathrm{P}}{\mathrm{bt}} \tag{5.10}$$

Measured tear strength σ_{ts} for both $T3R_2$ and $T8R_2$ materials are given in Table 5.2. For the T8 condition the measured tear strength for L-T sample is $\sim$9% lower than the fitted zone 1 cohesive strength and only $\sim$6% lower for T-L sample. For the T3 condition, the measured tear strength for both L-T and T-L samples is $\sim$38% lower than the corresponding fitted ones.

5.5 Predictions of M(T) tests

As reported in previous parts, the large scale M(T) tests are expensive and require a large amount of time and material. Methods of analysis based on the linear fracture mechanics using plastic zone corrections can hardly be used since valid tests, according to the standard, would require very large panels (several meters) [20, 4, 23]. Hence, the numerical simulation of ductile tearing of large scale M(T) test is of great value. Simulation of the M(T) (R-curve) test by FE-method allows a fast determination of fracture toughness of materials, it is then possible to give guidelines for material improvement.

M(T) tests (R-curve) are available only for two artificially aged materials ($T8R_2$ and $T8F_{65}$), because industrial applications of aluminium-lithium alloys are based on heat treated material's high strength/stiffness ratio. Due to the limited capacity of the testing machine, 6 mm-thick fibrous sheets ($T8F_6$) were machined on both side down to 5 mm for M(T) tests.

For the validation of cohesive zone model (CZM), the cohesive zone parameters identified on small sized Kahn tests are employed to predict the crack extension of M(T) tests. The validation is checked on $T8R_2$ materials on which straight and stable crack extension was obtained on Kahn tear tests. The prediction results of M(T) tests are shown on Fig. 5.15 in terms of the nominal stress (F/S_0) vs. opening displacement in L-T loading (a), and T-L loading (b), respectively. It is

shown that the crack extension resistance is over-estimated in both L-T and T-L loading. The maximum load of both L-T and T-L samples is ∼14% higher than corresponding experimental results. Two reasons can explain this over-estimated results of M(T) tests. First, in the experimental, testing 2 mm-thick M(T) is difficult because of buckling (the dimension of specimen is $1030 \times 760 \times 2$ mm in current case). During mechanical tests, an anti-buckling device was used but its two rigid plates affixed to the central region of the specimen cannot be squeezed to much because of friction. Consequently buckling cannot be completely avoided and the supported load is reduced [20]. As showed in the study of Bron [20] (see Fig. 5.16), simulation of symmetry condition in the thickness direction (buckling is not allowed) is ∼40% higher than simulation with a very small perturbation in the initial node positions. Second, it is the transferability from Kahn tests to M(T) tests via cohesive zone models. This will be discussed in the following section (cf. 5.6).

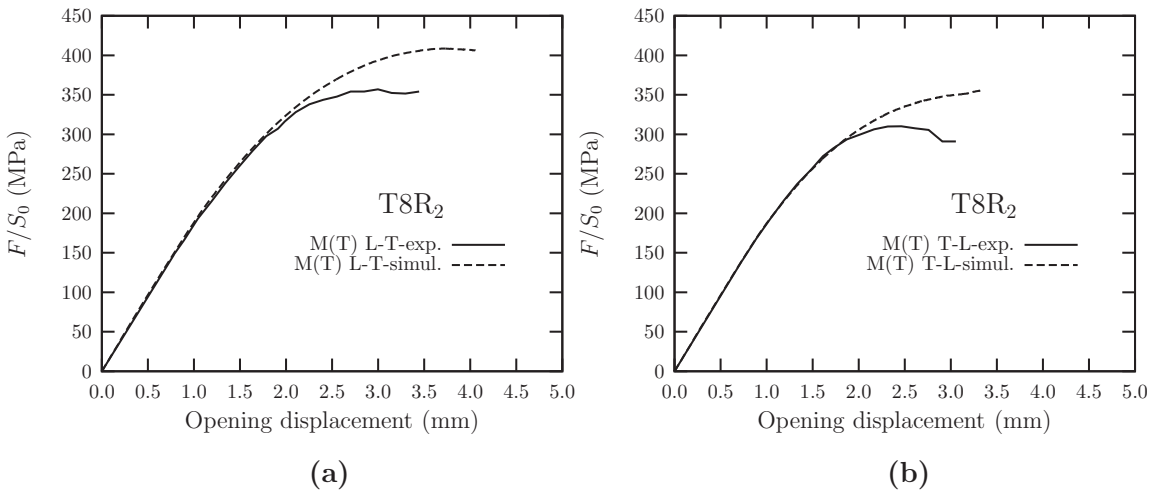


Figure 5.15: Predicted and experimental load vs. opening displacement responses of M(T) tests for 2 mm-thick T8 recrystallized material ($T8R_2$) in L-T loading (a), and in T-L loading (b).

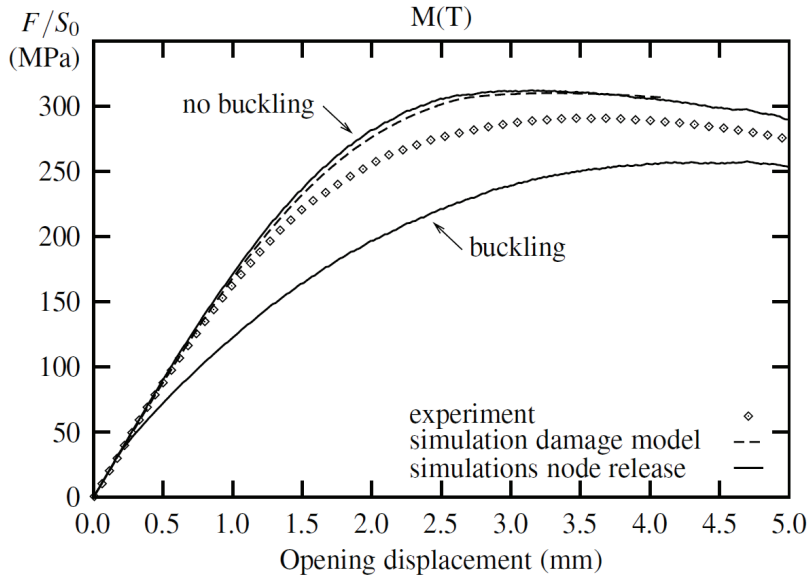


Figure 5.16: Buckling effect in 760 mm wide M(T) specimens after Bron [20] for an AA2024 thin sheet (sheet thickness is 1.74 mm).

5.6 Transferability of Kahn to M(T)

The transferability of tests on small sized specimens to large ones is of great interest for the numerical simulation. In this work, the transferability from small sized Kahn tests to large M(T) panels using cohesive zone model (CZM) was examined. As reported in the section 5.5, the prediction of M(T) tests with fitted cohesive zone parameters on Kahn tests are higher than experimental data. Simulation results using two different process regions (zone 1 and zone 2 cf.5.3.1) show that it is the zone 2 cohesive parameters determine the global response of the M(T) tests, because for M(T) tests, the ”flat triangular region” (zone 1, 0.9 mm long) is too small compared to ”slant region” (zone 2, 252.6 mm long). For the study of cohesive parameter sensitivity, three different cohesive strengths in the slant region are applied on both Kahn and M(T) specimens. Comparisons of nominal stress vs. opening displacement response are given on Fig. 5.17a for M(T) tests, and on Fig. 5.17b for Kahn tests. It can be seen that the magnitude of cohesive strength has a stronger

effect on large scale M(T) tests than on small scale Kahn tests. However, accurate identification of cohesive strength in Kahn specimens is difficult, very small deviation of load-CMOD curves can result in a strong effect on the prediction of M(T) test.

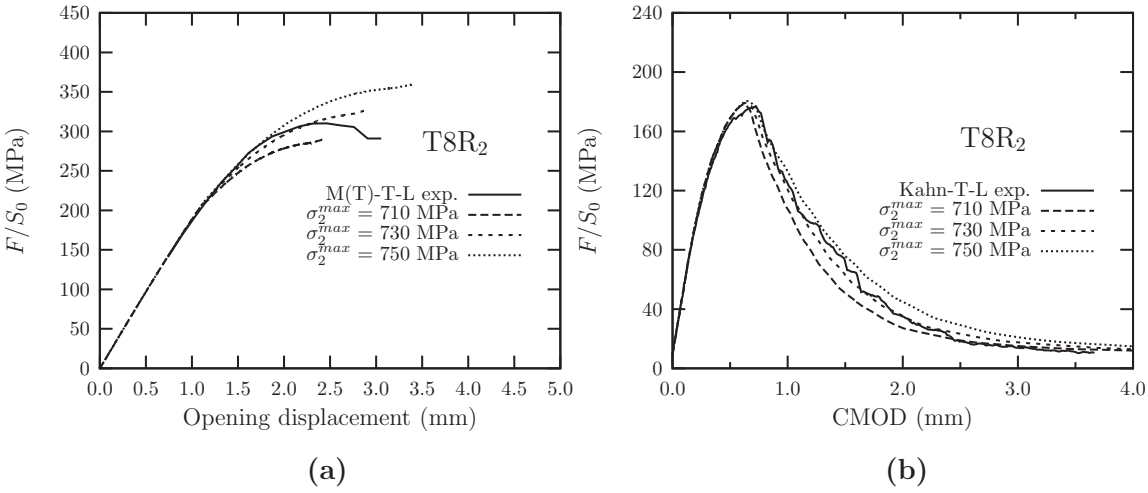


Figure 5.17: Influence of cohesive strength (T_0^2) on global load vs. CMOD response for M(T) tests (a), and Kahn tests (b).

5.7 Transferability of thickness effect

In this work, the transferability between different specimen thicknesses via cohesive zone model was also examined on Kahn specimens. If it could be transferable, we could use thinner specimens which exhibit stable crack growth to simulate thicker ones. It would be of great interest for the simulation of different thickness structures. In our case, the determination of cohesive zone parameters was carried out on 6 mm reduced to 2 mm thick Kahn tests which exhibit a straight and stable crack growth in L-T loading. Fig. 5.18a provides the experimental and fitted results. Fitted cohesive parameters were employed to simulate 6 mm thick Kahn test and compared with its experimental results. Fig. 5.18b gives the prediction results in comparison to experimental response

of 6 mm thick Kahn tests. It is shown that with fitted cohesive zone parameters, tear behaviour of thick component cannot be represented by thin ones even with same specimen geometry. Thin specimens usually exhibit lower triaxiality than thick ones (cf. 5.8.2), the cohesive model used here did not take the stress triaxiality into account. The parameters determined on thin specimens are not suitable for prediction of thick ones, and vice versa.

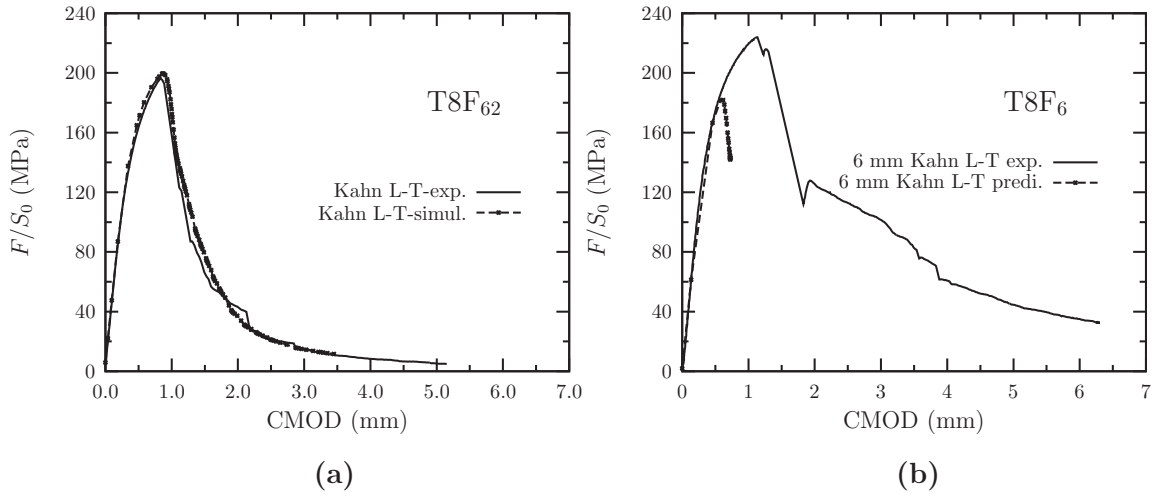


Figure 5.18: (a), fitted results of 2 mm-thick fibrous material (T8F$_{62}$) in L-T loading; (b), prediction result of 6 mm thick fibrous material (T8F$_6$) in the same loading.

5.8 Simulation and analysis of thickness effect

5.8.1 Modeling of slant fracture with node release technique

Experiments on Kahn tear specimens provide a good case for investigating the slant fracture phenomenon. Due to convergence problem of slant fracture modeling by cohesive zone models, a specified node release technique was used here to model crack growth with slant fracture surface. Objective is to obtain an order of specimen thickness effect on the fracture by analysing stress triaxiality and out-of-plane stress, simulations are performed on different Kahn specimen thicknesses (2, 3, 4 and 6 mm). The crack length is set equal to the experimentally measured value. Fig. 5.19 illustrates the nodal release configuration with a constant crack front for the 3D model (adapted after [42]). Constant crack front means that all nodes on the crack front are released simultaneously. As shown in experimental tests, tearing crack growth process (cf. Fig. 5.5) starts from a small flat triangular region and changes into a slant crack growth region. In the FE-model, the initial slant angle is set to smaller value than the experimental value in order to obtain the measured fracture angle. To avoid a brutal crack growth, a special process was developed in this study to release the node smoothly.

The elastic-plastic behavior is optimized to match smooth tensile and U-notched tensile tests as described in chapter 3 (cf. Plastic anisotropic behaviour). Due to a slight curvature of lines initially parallel to the initial crack; the node release technique is applied to each individual node lying on the potential crack path and not to a line of nodes as in [42].

Stress triaxiality and hydrostatic stress are paramount important parameters in the fracture mechanisms. McClintock [68] and Rice and Tracey [88] have shown that fracture of ductile metals are strongly dependent on stress triaxiality χ which is defined as $\sigma_m/\sigma_{\mathrm{eq}}$; where, σ_m is the hydrostatic stress and σ_{eq} is the von Mises equivalent stress. Recent analysis by Bao and Wierzbicki [8, 9] on the dependence of fracture ductility on specimen thickness and stress triaxiality have confirmed

this point via various experimental tests and numerical simulations on different thick specimens.

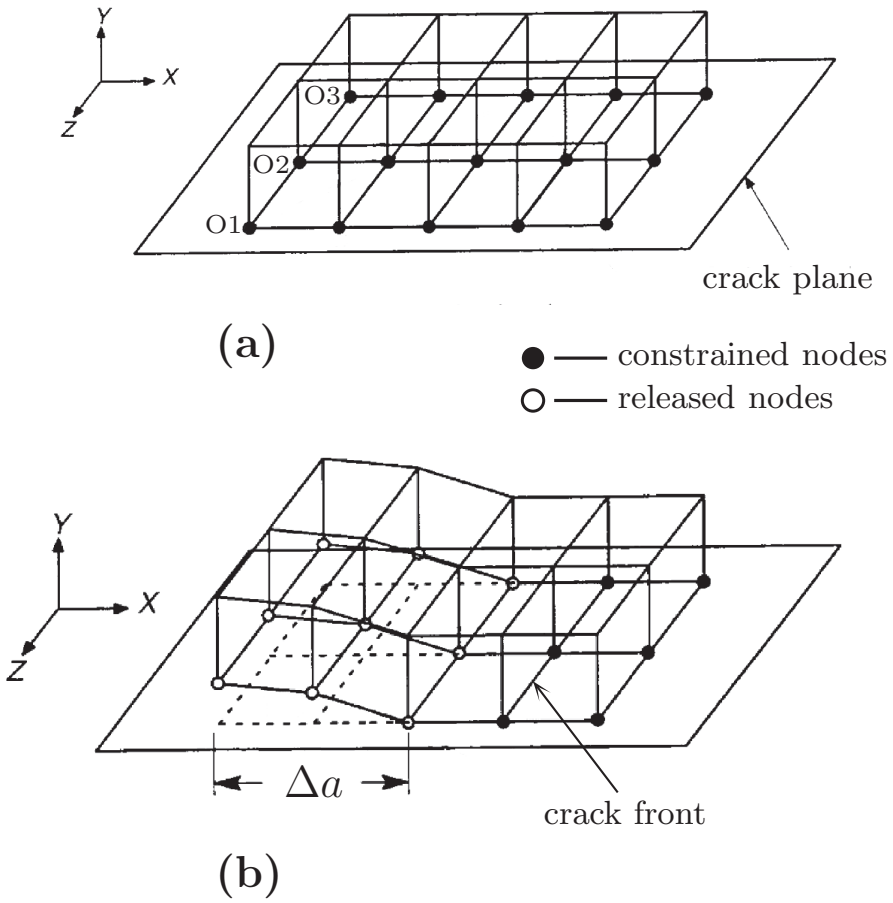


Figure 5.19: Configuration of node release in 3D model with a ”constant” crack front, (a) initial mesh state, and (b) after nodes released (adapted after [42]).

5.8.2 Variation of stress triaxiality along specimen's thickness

Fig. 5.20 and Fig. 5.21 show the stress triaxiality ($\sigma_{\mathrm{m}}/\sigma_{\mathrm{flow}}$) in different layers of 2 mm-thick Kahn specimen (Fig. 5.20), and 6 mm-thick Kahn specimen (Fig. 5.21) as a function of the distance from the crack tip at a load just before crack initiation ($\Delta a = 0$). For 2 mm-thick Kahn specimen, it can be seen that with increasing distance from the crack tip, the triaxiality first

increases drastically, reaches a peak value, and then decreases. The highest triaxiality peak appears in the specimen's midsection ($\chi_{max} \approx 1.4$), it is also shown that midsection has highest triaxiality values after the triaxiality peak, and the triaxiality decreases from midsection to the side-surface. The location of the triaxiality peak in the layers near midsection is about 0.3 mm ahead of the crack tip. This means that near the midsection the micro-fracture processes are initiated about 0.3 mm ahead of the crack tip. At the side-surface no distinct triaxiality peak ($\chi_{max} \approx 0.65$) is observed. In the case of 6 mm-thick Kahn specimen (Fig. 5.21), similar trends are observed as in 2 mm-thick one between different positions. However, in midsection of 6 mm-thick specimen, triaxiality is higher than in corresponding position of 2 mm-thick specimen, the triaxiality peak $\chi_{max} \approx 1.75$; the location of the triaxiality peak is about 0.6 mm ahead of the crack tip in the midsection.

Variation of stress triaxiality along the thickness at crack initiation for 2 mm-thick and 6 mm-thick Kahn specimens are given on Fig. 5.22 and on Fig. 5.23, respectively. In the regions close to crack tip (i.e. Δx is small, correspond to flat region of broken sample), the triaxiality varies smoothly near midsection (keeps a high triaxiality level), but decreases drastically when approaching the side-surface which can be seen clearly in the case of 6 mm-thick specimen (Fig. 5.23). In the regions far away of crack tip (e.g. Δx = 5 mm, correspond to slant region of broken sample), the variation of triaxiality is limited along thickness, the triaxiality keeps at a low level ($\chi_{max} \approx 0.6$).

From the simulation results shown on Fig. 5.20 – Fig. 5.23, it can be concluded that the distribution of the stress triaxiality ahead of the crack tip and the variation of the stress triaxiality along the thickness are consistent with the fractography observations of broken Kahn samples (c.f. 4.6.2). In regions near crack tip (flat regions) where the stress triaxiality is high, void controlling damage is promoted; in regions far away of crack tip (slant regions), due to a lower triaxiality, void growth is limited.

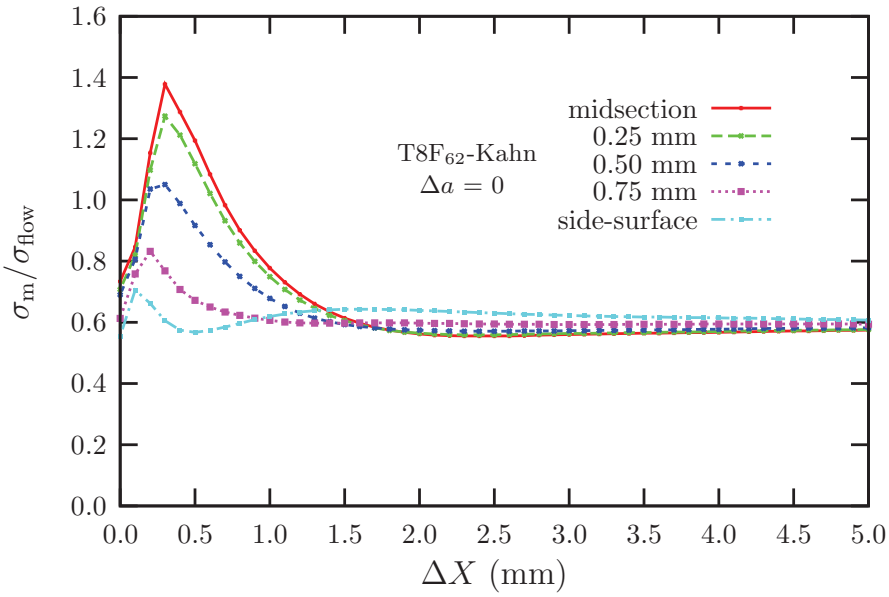


Figure 5.20: Stress triaxiality (σ_m/σ_{flow}) in different layers of 2 mm-thick Kahn specimen as a function of the distance from the crack tip at a load just before crack initiation ($\Delta a = 0$). σ_m is the hydrostatic stress, σ_{flow} is the flow stress, ΔX is the distance from the crack tip.

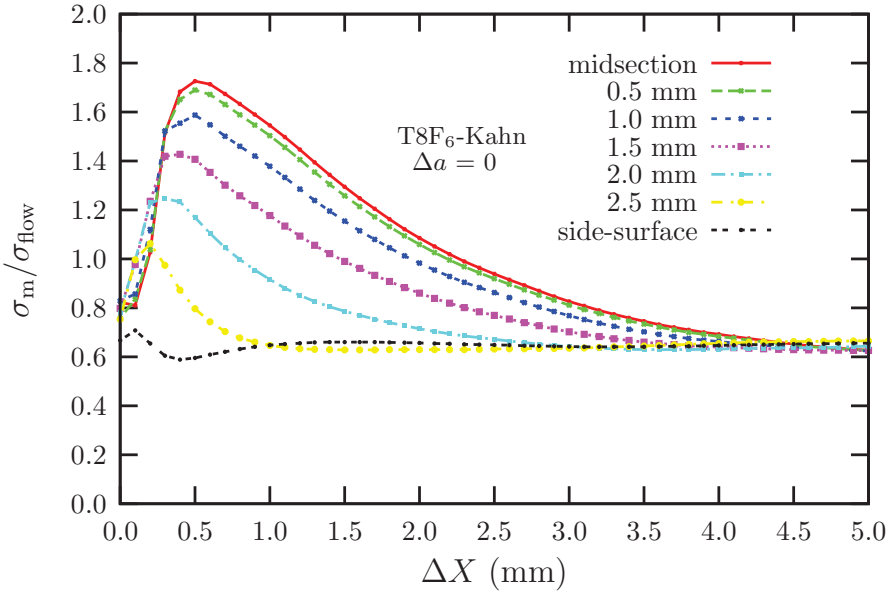


Figure 5.21: Stress triaxiality (σ_m/σ_{flow}) in different layers of 6 mm-thick Kahn specimen as a function of the distance from the crack tip at a load just before crack initiation ($\Delta a = 0$). σ_m is the hydrostatic stress, σ_{flow} is the flow stress, ΔX is the distance from the crack tip.

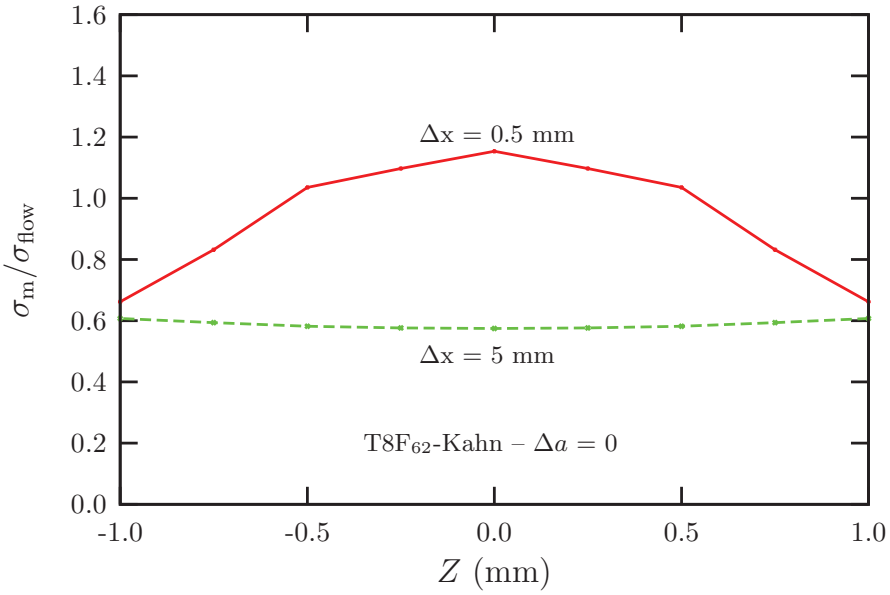


Figure 5.22: Variation of stress triaxiality (σ_m/σ_{flow}) along the thickness at a load before crack initiation for 2 mm-thick Kahn specimen. Δx denotes the distance from the crack tip, Z is the distance from specimen's midsection ($Z = 0$).

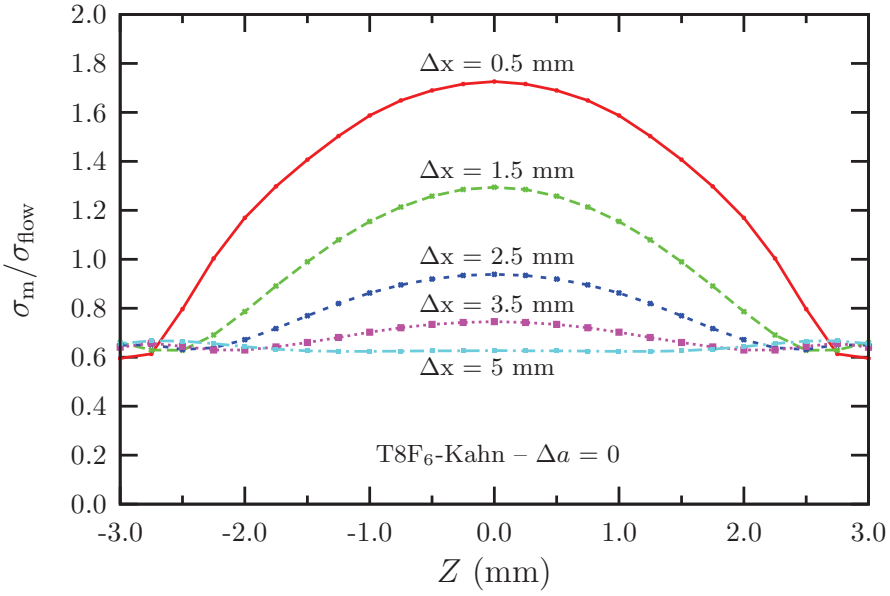


Figure 5.23: Variation of stress triaxiality (σ_m/σ_{flow}) along the thickness at a load before crack initiation for 6 mm-thick Kahn specimen. Δx denotes the distance from the crack tip, Z is the distance from specimen's midsection ($Z = 0$).

5.8.3 Variation of out-of-plane stress with accumulated plastic strain

Fig. 5.24 give the variation of out-of-plane stress σ_{33} as a function of accumulated plastic strain in flat region (data taken at 1 mm ahead of the crack tip of midsection) for 2-, 3-, 4- and 6 mm thick Kahn specimens. The out-of-plane stress increases with increasing specimen thickness. It is seen that when the crack length Δa reaches to 1 mm (i.e. before an abrupt increasing of σ_{33}) 6 mm-thick sample's out-of-plane stress is near 6 times higher than 2 mm-thick sample's at the same position. The variation of out-of-plane stress σ_{33} as a function of accumulated plastic strain in slant region is given on Fig. 5.25, the data was taken at 5 mm ahead of the crack tip of midsection. For all thicknesses, σ_{33} is much smaller than in corresponding flat region. The σ_{33} increases smoothly with accumulated plastic strain, it is hard to detect the position where crack extension Δa equals 5 mm from those σ_{33} vs. accumulated plastic strain curves.

5.8.4 Variation of out-of-plane stress with loading time

The variation of out-of-plane stress σ_{33} as a function of loading time in flat region is given in Fig. 5.26, the data was taken at 1 mm ahead of the crack tip of midsection. It is clearly shown that the out-of-plane stress increases smoothly with loading time before the crack length reaching to 1 mm. When the crack length reaches to 1 mm, an abrupt increasing of out-of-plane stress is observed; after a short loading time, σ_{33} decreases to zero. In slant region (see Fig. 5.27, the data was taken at 5 mm ahead of the crack tip of midsection), as observed on Fig. 5.25, it is also hard to detect the position where crack extension Δa equals 5 mm from σ_{33} vs. loading time curves.

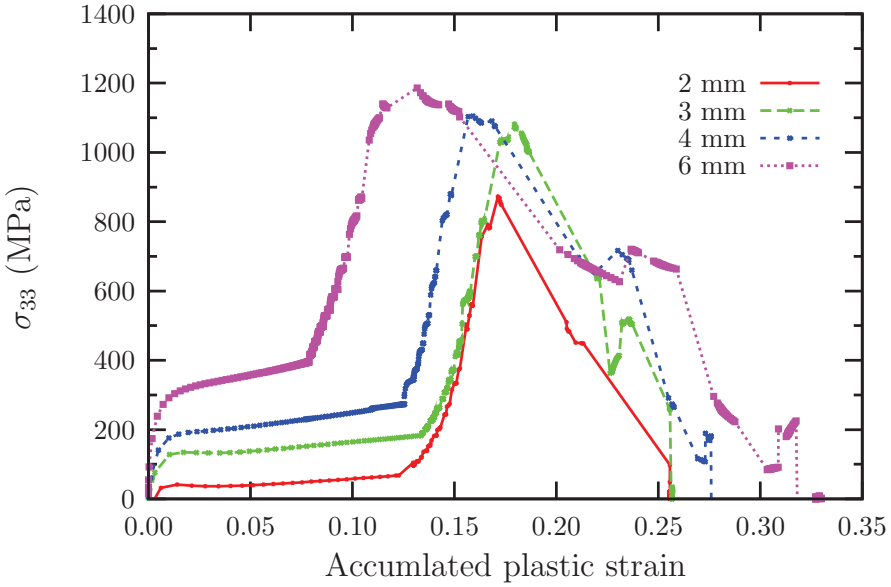


Figure 5.24: Variation of out-of-plane stress (σ_{33}) as a function of accumulated plastic strain for 2-, 3-, 4- and 6 mm-thick Kahn specimens (data taken at 1 mm ahead of the crack tip of midsection).

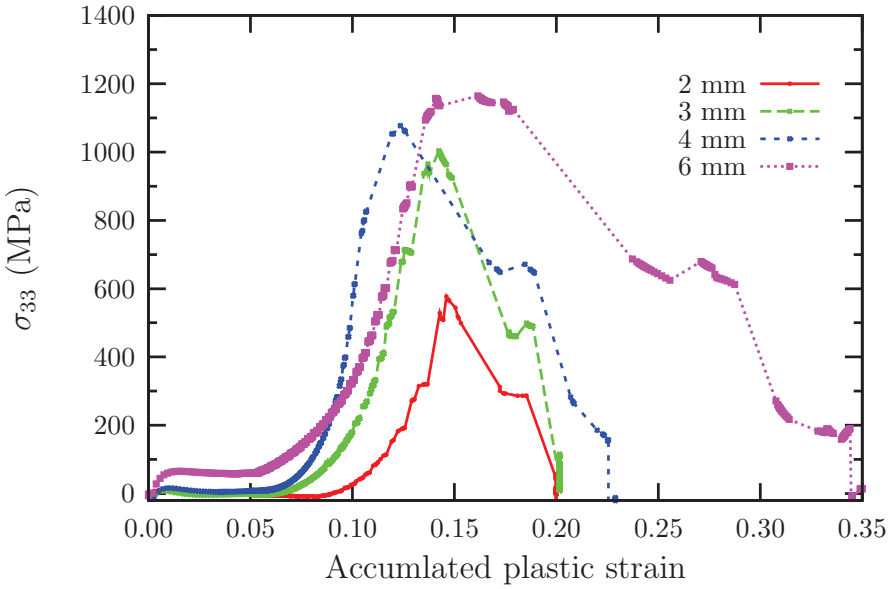


Figure 5.25: Variation of out-of-plane stress (σ_{33}) as a function of accumulated plastic strain for 2-, 3-, 4- and 6 mm-thick Kahn specimens (data taken at 5 mm ahead of the crack tip of midsection).

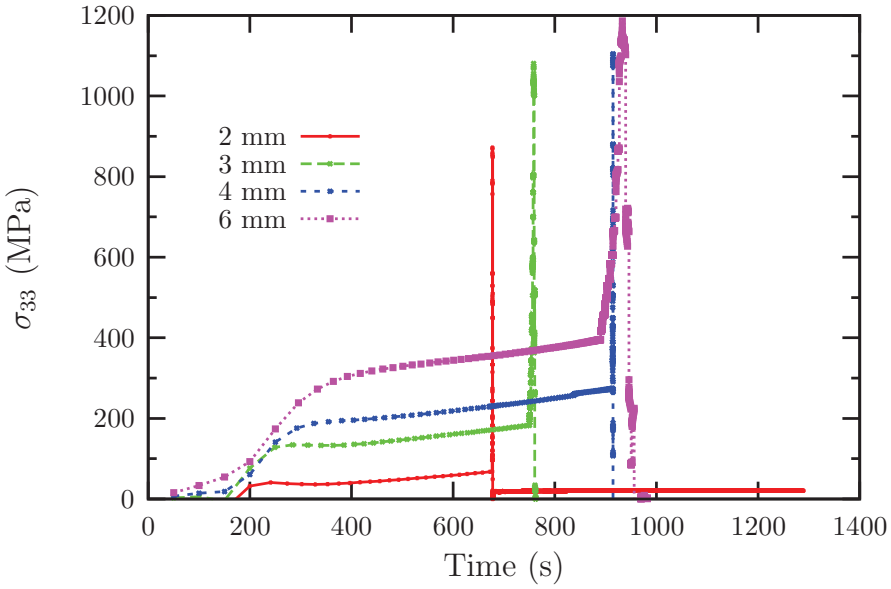


Figure 5.26: Variation of out-of-plane stress (σ_{33}) as a function of loading time for 2-, 3-, 4- and 6 mm-thick Kahn specimens (data taken at 1 mm ahead of the crack tip of midsection).

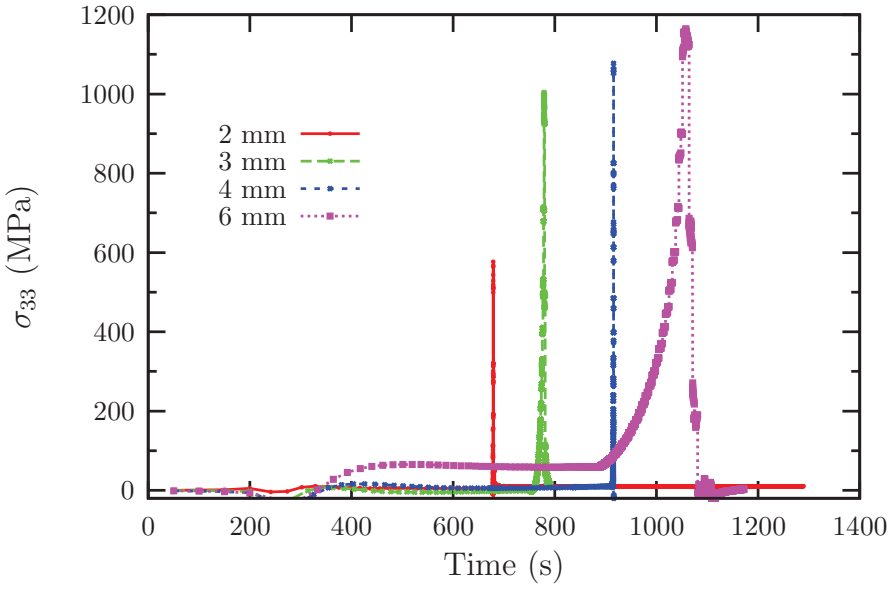


Figure 5.27: Variation of out-of-plane stress (σ_{33}) as a function of loading time for 2-, 3-, 4- and 6 mm-thick Kahn specimens (data taken at 5 mm ahead of the crack tip of midsection).

5.8.5 Variation of stress triaxiality stress with CMOD

Fig. 5.28a shows the variation of stress triaxiality stress as a function of crack mouth opening displacement (CMOD) for 2 mm-thick Kahn specimen for two locations: the first one is at the crack tip (0 mm) and the second one is 5 mm away from crack tip (slant region). The stress triaxiality at crack tip first increases with CMOD, reaches a peak value ($\sim$1.5), and then decreases, when the crack initiates (i.e. CMOD$\approx$0.8 mm) the stress triaxiality drops to zero. In the slanted region (5 mm away from crack tip), stress triaxiality stress is twice lower than that at crack tip, when the crack progresses to 5 mm (i.e. CMOD$\approx$1 mm)), the stress triaxiality stress increases drastically and reaches a much higher peak value, and then drops shortly to zero. Because the node release is not enough smooth (discontinuity), this peak value should not be taken into account. Fig. 5.28b shows the simulation results carried out by Bron *et al.* ([21]) on an AA2024 sheet material using an extension of Rousselier model [91] (Gurson-like model). It can be seen that in the slanted region (5 mm away from crack tip), stress triaxiality increases smoothly to a peak value and this value is lower than that at crack tip.

The simulation results of 4 mm and 6 mm-thick Kahn specimens using nodal release are given in Fig. 5.29a and Fig. 5.29b, respectively. As observed in 2 mm-thick specimen, similar trends are obtained whereas the stress triaxiality value is higher in 6 mm than 4 mm and 2 mm ones.

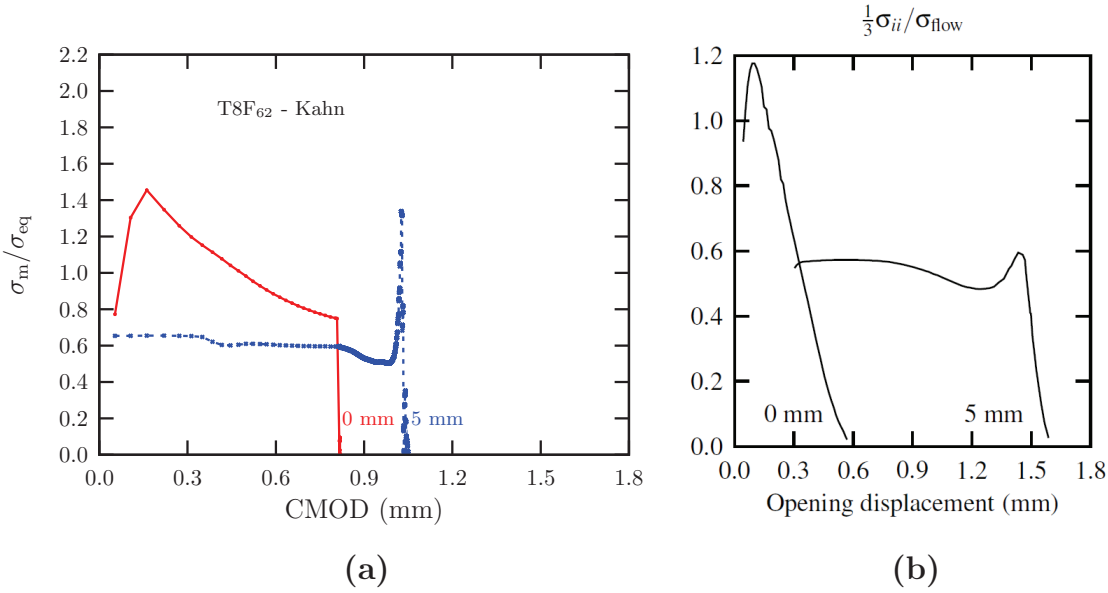


Figure 5.28: Variation of stress triaxiality (σ_m/σ_{flow}) at crack tip (0 mm) and (5 mm away from the crack tip) as a function of the crack mouth opening displacement (CMOD) for 2 mm-thick Kahn specimen (a) and 1.74 mm-thick Kahn specimen (b)([21]) (data taken at midsection of specimen).

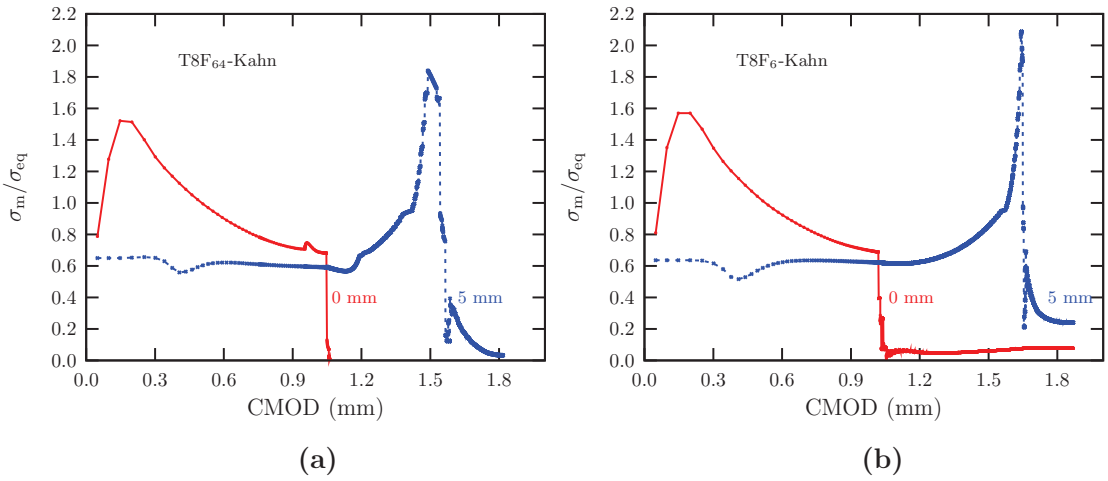


Figure 5.29: Variation of stress triaxiality (σ_m/σ_{flow}) at crack tip (0 mm) and (5 mm away from the crack tip) as a function of the crack mouth opening displacement (CMOD) for 4 mm-thick (a) and 6 mm-thick (b) Kahn specimens (data taken at midsection of specimen).

5.9 Conclusions

This part describes the modeling of ductile tearing behaviour of investigated materials by finite element simulation using cohesive zone models (CZM). The model applied for global mode-I fracture is based on the Needleman traction-separation law. Crack extension with flat crack plane has been simulated on both recrystallized materials ($T3R_2$ and $T8R_2$). Identified cohesive zone parameters on Kahn tests were employed to predict tearing behaviour of M(T) tests. For both L-T and T-L loading of $T8R_2$ materials, M(T) tests are $\sim$14% over-estimated than experimental values. Two reasons were identify to explain this over-estimated results of M(T) tests. The first one is buckling effect of large thin sheets, an anti-buckling device was used during mechanical tests whereas symmetry condition was applied during finite element simulation. The second one is transferability of cohesive zone model from Kahn tests to M(T) test. Simulation results show that the identified cohesive parameters are more sensitive for M(T) than for Kahn tests, very small deviation of load-CMOD curves can result in a strong effect on the prediction of M(T) test. Thickness effect was assessed using different thick Kahn specimens via cohesive zone models, results show that fitted cohesive parameters on thin specimens cannot be used to predict tearing behaviour on thick ones. In slant fracture modeling, mesh of slant fracture surface with flat-to-slant transition was constructed. Modified mixed-mode Scheider cohesive zone model was implanted to model slant fracture. However, due to serious convergence problems during calculations, further work needs in future investigations.

Node release technique was applied to simulate different thick Kahn tests with predefined slant fracture surface, the constraint along thickness direction was compared on specimens having different thicknesses. Out-of-plane stress σ_{33} increases with increasing specimens thickness in both flat and slant regions. Simulation results confirm that the magnitude of σ_{33} is much higher in flat region than in slant region.

5.10 Résumé

Le chapitre 5 présente la modélisation de la déchirure ductile par éléments finis en utilisant le concept de zone cohésive. Cette méthode a été choisie du fait que la croissance diffuse des cavités est inexistante pour les matériaux étudiés. Le modèle utilisé dans le cas de chargement en mode-I est basé sur une loi contrainte-ouverture de Needleman (1987). La propagation de fissure des essais Kahn a été simulée avec succès dans les deux matériaux recristallisés. Les paramètres de zone cohésive identifiés ont été employés pour prédire la déchirure ductile des structures M(T) : la transférabilité éprouvette/structure étant un des objectives de cette étude. La prédiction est surestimée de près de 14% comparativement à l'expérience. Deux raisons ont été identifiées pour expliquer cette surestimation : i) la première est l'effet de flambement par voilement étudiés classiquement pour les structures en tôles minces ; ii) la deuxième raison est la non-transférabilité du modèle de zone cohésive identifié sur l'éprouvette de petite taille Kahn vers la grande plaque M(T). En effet, les résultats de simulation montrent que les paramètres de zone cohésive sont plus sensibles pour les essais M(T) que pour les essais Kahn. L'effet d'épaisseur a également été examiné dans cette partie via le modèle de zone cohésive. Les résultats de simulation montrent que les paramètres identifiés sur une éprouvette mince ne peuvent pas être utilisés pour prédire le comportement de déchirure sur une éprouvette plus épaisse. Pour la modélisation de la rupture en biseau, une loi de mode mixte modifiée sur le modèle Scheider (2001) a été spécialement implantée, une surface de fissure avec transition de plat-à-biseau a été construite. Ces travaux n'ont pu être menés à terme du fait de problèmes de convergences non résolus durant la simulation numérique. Enfin, la technique de relâchement de nuds a été utilisée pour analyser l'effet d'épaisseur avec une surface de fissure en biseau. La contrainte hors-plan σ_{33} a été comparée entre les éprouvettes ayant des épaisseurs différentes dans les deux régions (plate et biseau). La simulation numérique confirme que l'amplitude de la contrainte hors-plan σ_{33} est bien plus importante dans la zone plate que dans

la zone en biseau, ceci permet d'expliquer l'apparition du délaminage lorsque l'épaisseur augmente.

Chapter 6

Conclusions and Prospects

6.1 General conclusions

Aluminium-Copper-Lithium alloys are developed as advanced materials for aerospace constructions primarily because of their high specific strength damage tolerance balance. Since Al-Cu-Li alloys usually exhibit a strongly anisotropic behaviour, it is necessary to take this behaviour into account for structure conception. The current work focuses on the influence of microstructure on the plastic anisotropy and fracture mechanisms of AA2198 Al-Cu-Li alloy in form of sheets. An experimental database including tensile tests and tear tests was established. Plastic anisotropy of sheets was characterized by tests on smooth tensile and notched tensile specimens along different loading directions. Sheet thickness effect on plasticity, ductility and fracture toughness was investigated via mechanical tests and finite element simulations. Fracture mechanisms were investigated using scanning electron microscopy and X-ray tomography techniques. Ductile tearing behaviour was modelled by finite element simulation using a cohesive zone model.

6.2 Main results

The results presented in this work, can be divided into four main parts related to: (I) the microstructure of materials (II) the plastic anisotropic behaviour (III) the ductile tearing behaviour including thickness effect on fracture toughness (IV) the use of cohesive zone model (CZM) and node release technique for modeling of ductile tearing.

(I) The four material ($T3R_2$, $T8R_2$, $T3F_6$ and $T8F_6$) microstructures have been characterized in chapter 2. Metallographic observations indicated that the materials under study present a strongly anisotropic grain structure. Large pan-cake shaped grains were observed in the L–T plane; intermetallic particles are aligned along rolling direction (L). Both 6 mm-thick fibrous materials ($T3F_6$ and $T8F_6$) have much thinner grains and more grain directionality than both 2 mm-thick recrystallized materials ($T3R_2$ and $T8R_2$). TEM investigation results show that inter-granular precipitates are found along almost all grain boundaries or subgrain boundaries areas in T8 condition material ($T8F_6$); hardening T_1 and θ' type precipitates are also formed at this condition. For naturally aged T3 material ($T3F_6$), hardening precipitates T_1 and θ' were not seen; there are no precipitate decorations at grain boundaries or subgrain boundaries. X-ray tomography observations of as-received materials show that the initial void volume fraction is very limited. The volume fraction of intermetallic particles and voids is $\sim 0.34\%$ for recrystallized material (R) and $\sim 0.4\%$ for fibrous material (F).

(II) Plastic anisotropy and fracture mechanisms were investigated in chapter 2. At first, an experimental database including smooth tensile (ST) tests and notched tensile (NT) tests was established. Smooth tensile tests along different loading directions (L, T and D) show that 6 mm-thick fibrous materials ($T3F_6$ and $T8F_6$) present a stronger anisotropic behaviour than 2 mm-thick recrystallized materials ($T3R_2$ and $T8R_2$). This anisotropic behaviour was less pronounced on corresponding notched tensile specimens. In this part, strain rate sensitivity was also investigated via

smooth tensile tests. At room temperature, all four materials exhibit a slightly negative strain rate sensitivity (also called dynamic strain ageing (DSA)). However, this effect becomes positive at high temperature (120°C); Mechanical tests carried out on different thicknesses ST and NT specimens of both fibrous materials show that reducing sheet thickness does not modify material's elastic-plastic behaviour. Thin sheets keep the same level of strength and anisotropy as thick ones. However, reducing sheet thickness decreases significantly material's apparent ductility and maximum nominal stress of notched specimens. The plastic anisotropy of materials can be well represented by the model proposed by Bron and Besson both in terms of strength and Lankford coefficients. The parameters identified on 6 mm-thick fibrous materials can well predict the elastic-plastic behaviour of specimens when the thickness was reduced to 2 mm by machining. Finally, the investigation of strain localization based on Rice's bifurcation analysis shows that failure of smooth tensile specimens is essentially governed by anisotropic plasticity which accounts for the difference observed along L-, T- and D-loadings. This analysis also indicates that this failure mechanism does not control failure of L-loading in the $T3F_6$ material where necking is not observed.

(III) Ductile tearing behaviour was examined in chapter 4 by using three kinds of specimens (Kahn, Arcan and M(T)). All tear test specimens exhibit a slant fracture in the crack propagation region which is typical for thin sheet metals. With Kahn specimens, stable crack extension can be obtained on both recrystallized materials ($T3R_2$ and $T8R_2$). L-T loading tests have a higher toughness than T-L loading. In the case of fibrous materials ($T3F_6$ and $T8F_6$), crack propagation is stable in T3 condition but with a strong crack deviation. No stable crack extension can be obtained in T8 condition ($T8F_6$), strong crack deviation accompanying pop-ins was observed during tests. These tests are not valid for the interpretation of fracture toughness according to ASTM [5].

Thickness effect on fracture toughness were examined on two 6 mm-thick fibrous materials ($T3F_6$ and $T8F_6$) by reducing sheet thickness to 2 mm in the case of Kahn tear specimens. Experimental results show that fracture toughness decreases with decreasing sheet thickness, 2 mm-

thick tests have a lower nominal peak stress and a smaller crack mouth opening displacement. Complementary tests on 3 and 4 mm tests in the case of $T8F_6$ material confirm this evolution of fracture toughness with sample thickness. The results also indicate that thickness has a strong influence on crack turning behaviour. With thinner specimens, a straighter crack extension can be obtained with same type specimen on the same material.

Arcan tear tests were performed on this material ($T8F_6$). In global mode I loading, L-T loading specimens exhibit a more stable crack growth than T-L loadings which fail after a short crack extension. In mixed-mode (I+II) loading specimens, the crack extension are also not stable in both L-T and T-L loadings. Precracked Arcan specimen was tested along T-L direction in which unstable crack extension observed in both mode I and mixed-mode loadings, stable crack extension was obtained in mode I tests. These results suggest that the initial crack tip condition has an important effect on crack extension behaviour.

Large panel M(T) tests carried out on T8 recrystallised material ($T8R_2$) show that L-T loaded panels have a higher toughness than T-L loaded ones. It is consistent with the test results on small sized Kahn specimens. In the case of T8 fibrous material, L-T loading has very similar toughness as T-L loading. Concerning the fracture mechanisms, at macroscopic scale, both Kahn and M(T) specimens exhibit very similar fracture surfaces. The crack begins with a small flat triangular region perpendicular to the loading direction followed by a flat-to-slant transition. Outside of this zone, typical slant fracture is observed. Observations of fracture surface at a microscopic scale indicate that two different fracture mechanisms can be identified on both Kahn samples and M(T) panels. In the flat region, void growth mechanism is dominant due to a higher triaxiality ratio; very large dimples can be seen. In the slant zone, void growth is very limited,

Investigation of arrested Kahn tests via high resolution X-ray tomography techniques including gallium wetting treatment gives more accurate results concerning the fracture mode and damage development. Void growth is limited in the slant regions for all tested materials. For re-

crystallized materials ($T3R_2$ and $T8R_2$), trans-granular fracture is the predominant fracture mode in the crack propagation regions; However, for two fibrous materials ($T3F_6$ and $T8F_6$), inter-granular dominant cracking was observed at the mid-thickness of specimens. The results of tomography investigation give a guide for the choice of ductile tearing modeling models.

(IV) The ductile tearing behaviour has been modelled using finite element simulations, as it is described in chapter 5. Modeling was performed using cohesive zone model (CZM) suggested by analysis results of fracture mechanisms of materials. The model applied for global mode-I fracture is based on the Needleman traction-separation law. Crack extension with flat crack plane has been simulated on two recrystallized materials ($T3R_2$ and $T8R_2$). Identified cohesive parameters on Kahn tests were employed to predict tearing behaviour of M(T) tests. In slant fracture modeling, mesh of slant fracture surface with a flat-to-slant transition was constructed. Modified mixed-mode Scheider cohesive zone model was implanted to model slant fracture. Serious convergence problem was met with the cohesive zone models. The transferability of cohesive zone model from Kahn tests to M(T) test was examined in present work. Simulation results show that the identified cohesive parameters are more sensitive for M(T) than for Kahn tests. Thickness effect was assessed using different thick Kahn specimens via cohesive zone models, results show that fitted cohesive parameters on thin specimens cannot be used to predict tearing behaviour on thick ones. Node release technique was applied to simulate different thick Kahn tests with predefined slant fracture surface, the constraint in thickness direction was compared for specimens having different thicknesses. Stress σ_{33} increases with increasing specimens thickness in both flat and slant regions. Simulation results confirm that the magnitude of σ_{33} is higher in flat region than in slant region.

6.3 Prospects

As observed in the current work, initial crack tip condition has an important effect on the crack growth stability of tearing specimens. For small scale tearing tests, precracked or side-grooved Kahn tear specimens are suggested for the future investigations of ductile tearing behaviour of high strength aluminium alloys (Al-Cu-Li and Al-Zn-Mg).

Concerning the dynamic strain ageing (DSA), it cannot totally explain the premature failure before onset of necking in our case of fibrous material in L-loading ($T3F_6$). The influence of texture anisotropy (between L, T and D) and DSA on the onset of necking could be investigated in further work. It can be assessed by complementary mechanical tests coupled with EBSD (electron backscatter diffraction) characterization of texture.

A better understanding of loading mixity on crack extension behaviour of Arcan tear tests needs further work. New design of Arcan specimen (see Fig. 6.1) proposed by Madi *et al.* [64] could be used in further investigations. At same time, the size effect on ductile tearing behaviour could also be investigated by using mode I loading tests.

The transferability from small sized specimens to large ones needs further investigations. The stress triaxiality is an important parameter in the fracture of ductile metals, the cohesive zone models (CZM) used here and in numerous literatures often do not take it into account. It makes the CZM less transferable than GTN models and other micromechanics based models. Current researches focus on mode-I fracture or pure mode-II fracture, little work has been done for mixed-mode fracture modeling in 3D. Modeling of slant fracture (with flat-to-slant transition) will be one of further research in thin-walled structures. In our work, 3D modeling of mixed-mode (mode I, II and III) fracture was tested, however, due to a serious convergence problem in 3D calculation, further work is needed.

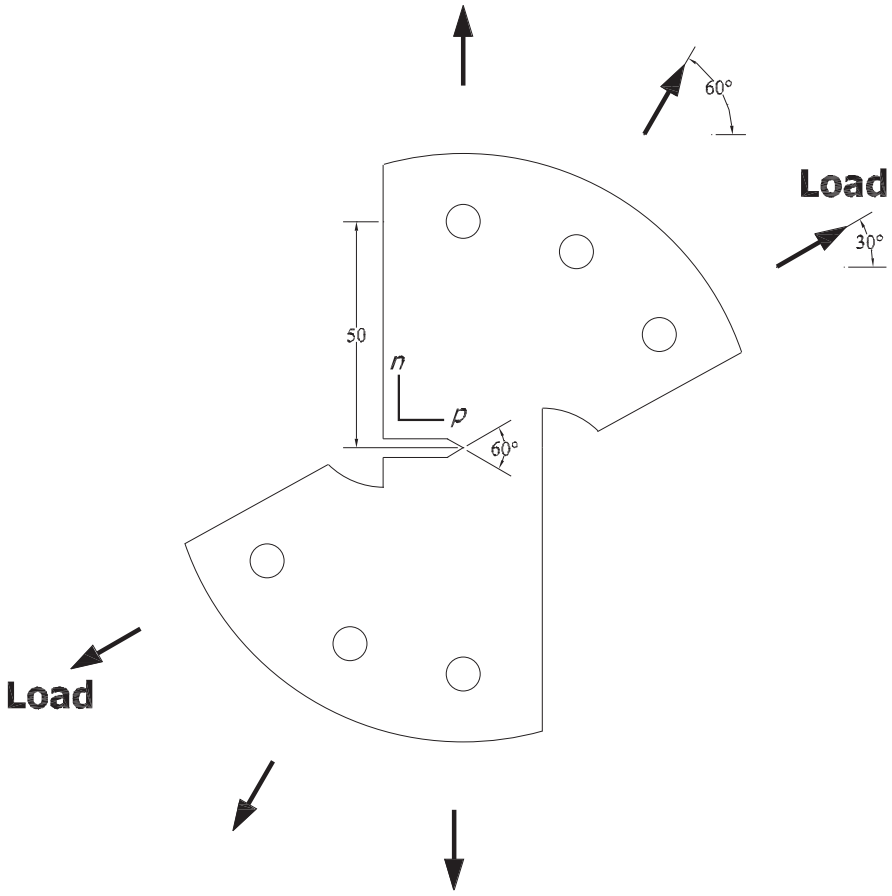


Figure 6.1: New design of Arcan specimen used for mixed-mode loading proposed by Madi *et al.* [64].

Conclusions et perspectives

Conclusions générales

Les alliages d'aluminium-cuivre-lithium ont été développés comme les matériaux avancés aérospatiaux en raison d'un meilleur compromis entre la résistance et la tolérance au dommage. Les alliages Al-Cu-Li présentent souvent une anisotropie importante, du coup il est nécessaire de prendre cette anisotropie en compte pour le dimensionnement de structure. Le travail actuel se concentre sur l'influence de la microstructure sur l'anisotropie plastique et la ténacité de l'alliage 2198 sous la forme de tôles. Une base de données expérimentale y compris des essais de traction et des essais de déchirure a été établie. L'anisotropie plastique de matériaux a été caractérisée par les éprouvettes de traction lisse et les éprouvettes entaillées selon différentes directions de prélèvement. L'effet d'épaisseur sur la plasticité, la ductilité et la ténacité ont été étudiées via des essais mécaniques et des simulations par éléments finis. Les mécanismes de rupture ont été examinés en utilisant le microscope électronique à balayage et la tomographie à rayon X. Le comportement de la déchirure ductile a été modélisé par simulation éléments finis via un modèle de zone cohésive.

Principaux Résultats

Les résultats présentés dans ce travail peuvent se deviser en quatre parties : (I) la microstructure de matériaux, (II) l'anisotropie plastique, (III) le comportement de déchirure ductile et

l'effet d'épaisseur, et (IV) le modèle de zone cohésive et le relâchement de nuds pour la simulation de la déchirure ductile.

(I) Les microstructures des quatre matériaux (T3R2, T8R2, T3F6 et T8F6) ont été caractérisées dans le chapitre 2. Les observations métallographiques indiquent que les matériaux de l'étude présentent des structures granulaires anisotropes. Les grains en forme de crêpe sont observés dans le plan de tôle L-T; les particules intermétalliques sont alignées selon la direction de laminage. Les deux matériaux fibrés (T3F6 et T8F6) ont des grains plus minces et une directivité plus marquée que les deux matériaux recristallisés (T3R2 et T8R2). Les observations MET montrent que les précipités inter-granulaires sont trouvés dans la plupart des joints de grains ou des sous-joints de grains dans les matériaux en état de revenu artificiel T8; les précipités servant au durcissement structurel de type T1 et θ' sont formés aussi dans cette condition de traitement thermique. Pour les matériaux en état revenu naturel T3, les précipités T1 et θ' ne sont pas observés; on observe également une absence de précipitation aux joints de grains contrairement au traitement T8. Les observations effectuées en tomographie à rayon X montrent que la porosité initiale reste limitée. La fraction volumique de particules intermétalliques et de vides est d'environ 0.34% pour les matériaux recristallisés et 0.4% pour les matériaux fibrés.

(II) L'anisotropie plastique et les mécanismes de rupture des éprouvettes de traction ont été examinés en détail dans le chapitre 2. Tout d'abord, une base de données expérimentale comprenant notamment des essais de traction lisse et les essais de traction entaillée a été construite. Les essais de traction sur les éprouvettes lisses selon différentes directions de sollicitation (L, T et D) montrent que les matériaux fibrés d'épaisseur 6 mm présentent une anisotropie plus marquée que les deux matériaux recristallisés d'épaisseur 2 mm. Cette anisotropie est moins importante pour les éprouvettes entaillées. Dans cette partie, l'effet de vitesse de déformation a été également examiné via des essais de traction lisse à différentes vitesses. A la température ambiante, les quatre matériaux (T3R2, T8R2, T3F6 et T8F6) présentent un léger de sensibilité négative à la vitesse (effet PLC). No-

tons qu'à 120°C, la sensibilité à la vitesse redevient positive. Les essais mécaniques effectués sur les éprouvettes de traction lisse et entaillée montrent que la réduction de d'épaisseur ne modifie pas le comportement élasto-plastique des matériaux. Les éprouvettes minces ont le même niveau de résistance et d'anisotropie que les éprouvettes épaisses. Cependant, la réduction de l'épaisseur d'éprouvette diminue de façon significative la ductilité du matériau ainsi que le maximum de contrainte nominale sur les éprouvettes entaillées. L'anisotropie plastique peut être bien représentée numériquement avec le modèle anisotrope proposé par Bron et Besson (2004) au niveau de la contrainte et des coefficients de Lankford. Les paramètres identifiés sur les matériaux fibrés d'épaisseur 6 mm peuvent prédire le comportement élasto-plastique des matériaux d'épaisseur 2 mm. Enfin, l'investigation de la localisation basée sur l'analyse de Rice (1976, 1980) montre que la rupture des éprouvettes de traction lisse est contrôlée essentiellement par la plasticité anisotrope qui tient compte des différences observées selon les directions L, T et D. Cette analyse montre également que l'instabilité liée à la localisation plastique ne permet pas d'expliquer la rupture prématurée (avant striction) du matériau T3F6 sollicité dans la direction L.

(III) Le comportement de la déchirure ductile a été étudié en détail dans le chapitre 4 en utilisant trois différents types d'éprouvettes (Kahn, Arcan et M(T)). Toutes les éprouvettes de déchirure présentent une rupture en biseau dans la région de la propagation de fissure, faciès typique d'une tôle mince. Avec les éprouvettes de petite taille Kahn, la fissure se propage de manière stable dans les deux matériaux recristallisés (T3R2 et T8R2). La configuration L-T est plus tenace que la configuration T-L. Dans le cas de deux matériaux fibrés, la propagation de fissure est stable dans le matériau en état T3 et est accompagnée d'une bifurcation de fissure importante. La propagation de fissure n'est pas du tout stable pour le matériau fibré en état T8, des pop-ins et des bifurcations de fissure ont été observés pendant les essais. Ces essais ne sont pas valides au sens de la norme ASTM [5].

L'effet d'épaisseur sur la ténacité a été étudié dans les deux matériaux fibrés (T3F6 et

T8F6) en réduisant l'épaisseur à 2 mm dans le cas d'éprouvettes Kahn. Les résultats expérimentaux montrent que la ténacité diminue avec la réduction d'épaisseurépaisseur le maximum de la contrainte nominale et l'ouverture d'entaille sont plus petits pour les éprouvettes de 2 mm. Les essais complémentaires effectués sur les éprouvettes d'épaisseur 3 mm et 4 mm ont confirmé la tendance observée sur la ténacité. Les résultats montrent également que l'épaisseur d'éprouvette a une influence non négligeable sur la bifurcation de fissure. La diminution d'épaisseur entrane une propagation de fissure plus stable et plus droite.

Les essais Arcan de chargement en mode mixte sont réalisés sur le matériau fibré en état T8F6. Dans le cas de chargement en mode-I pure, les résultats sont cohérents avec les essais Kahn, la propagation de la fissure est plutôt stable. Dans le cas du chargement en mode-mixte, la propagation de la fissure est instable. Néanmoins, une propagation de fissure stable a été obtenue avec une éprouvette pré-fissurée par fatigue. Ces résultats montrent que la condition du fond d'entaille a un effet important sur la propagation de la fissure.

Les essais sur éprouvette-structure M(T) ont été effectués pour les deux matériaux en état T8. Pour le matériau recristallisé, la configuration L-T est plus tenace que la configuration T-L ce qui est cohérent avec les essais Kahn. Pour le matériau fibré, la configuration L-T a le même niveau de ténacité que la configuration T-L. Concernant le mécanisme de rupture, les éprouvettes M(T) ont un faciès similaire aux éprouvettes Kahn. La propagation de fissure commence avec une petite zone triangulaire perpendiculaire à la direction de sollicitation, suivie par une transition de plat-à-biseau. Au-delà de cette zone, une rupture en biseau est observée. Les observations de la surface de rupture montrent deux mécanismes de rupture différents (similaires pour les éprouvettes Kahn et M(T)). Dans la zone triangulaire, la croissance de cavités est dominante du fait d'un taux de triaxialité élevé : de grands cupules sont observées. En revanche, la croissance de cavité est très limitée dans la zone en biseau ou le taux de triaxialité est plus faible.

Les observations d'essais Kahn interrompu via la tomographie à rayon X haute résolution

nous donnent des résultats plus précis concernant le mécanisme de rupture et le développement de l'endommagement. La croissance de cavité dans la zone de propagation de fissure reste limitée dans tous les matériaux étudiés. Le traitement au gallium à permis de mettre en évidence les joints grains dans les alliages d'aluminium. Pour les deux matériaux recristallisés, la rupture trans-granulaire est prédominante dans la zone de propagation de fissure. Néanmoins, pour les deux matériaux fibrés, la rupture inter-granulaire est observée au milieu d'épaisseur de l'éprouvette. Ces résultats d'analyse peuvent nous aider à choisir le modèle adapté pour décrire l'endommagement ductile de ce type d'alliage.

(IV) La déchirure ductile a été modélisée en utilisant la simulation par éléments finis (décrite au chapitre 5). La modélisation a été effectuée avec un modèle de zone cohésive inspirée par les analyses des mécanismes de rupture qui montrent que le développement d'endommagement est très limité dans ces matériaux. Le modèle utilisé pour la simulation de la rupture en mode I est basé sur la loi de contrainte-ouverture de Needleman (1987). La propagation de fissure d'éprouvettes Kahn a été simulée avec succès avec une surface de rupture plate prédéfinie pour les deux matériaux recristallisés (T3R2 et T8R2). Les paramètres identifiés ont été employés pour prédire la déchirure ductile des plaques fissurées M(T). Pour modéliser la rupture en biseau une loi modifiée de mode-mixte, basée sur le modèle Scheider (2001), a été spécialement implantée, une surface de fissure avec transition de plat-à-biseau a été construite. Ces travaux n'ont pu être menés à terme du fait de problèmes de convergences non résolus durant la simulation numérique. Les résultats de simulation montrent que les paramètres de zone cohésive sont plus sensibles pour les essais M(T) que pour les essais Kahn. L'effet d'épaisseur a été également examiné dans cette partie via le modèle de zone cohésive, les résultats de simulation montrent que les paramètres identifiés sur une éprouvette mince ne peuvent pas être utilisés pour prédire le comportement de la déchirure pour une éprouvette plus épaisse. Enfin, la technique de relâchement des nuds a été utilisée pour analyser l'effet d'épaisseur avec une surface de fissure en biseau. La contrainte hors-plan σ_{33} a été comparée

entre les éprouvettes ayant des épaisseurs différentes. La contrainte σ_{33} augmente avec l'épaisseur d'éprouvette dans la zone plate et dans la zone en biseau. Les résultats de simulation confirment que la contrainte σ_{33} est beaucoup élevée dans la zone plate que dans la zone en biseau, ceci permet d'expliquer l'apparition du délaminage lorsque l'épaisseur augmente.

Perspectives

La présente étude a montré que la condition du fond entaille initiale a un effet non négligeable sur la stabilité de la propagation de fissure. Pour les éprouvettes de déchirure de petite taille (eg. Kahn), les éprouvettes pré-fissurées ou avec des rainures latérales seront recommandées pour l'étude des alliages à haute résistance (Al-Cu-Li et Al-Zn-Mg).

Concernant le vieillissement dynamique, il ne peut pas expliquer complément la rupture prématurée avant la striction dans le cas de matériaux fibré sollicité dans la direction longitudinale (L). L'influence de la texture anisotrope (entre les directions L, T et D) et le vieillissement dynamique doivent être examinés ensemble dans les études ultérieures. Il serait judicieux de réaliser des investigations complémentaires de façon à caractériser les textures par la technique EBSD (Electron Backscatter Diffraction). La transférabilité entre l'éprouvette de petite taille et l'éprouvette de grande taille nécessite de travaux complémentaires. En effet, le taux de triaxialité de contrainte est un paramètre important dans le mécanisme de rupture de matériaux ductiles : le modèle de zone cohésive utilisé ici et de nombreux modèles proposés dans la littérature n'en tiennent pas compte. Il s'avère que les modèles de zone cohésives sont moins transférables que les modèles de type GTN ou les autres modèles micromécaniques.

La recherche actuelle concentre sur la rupture en mode I pure ou mode II pure, peu de travail a été réalisé pour la modélisation de rupture en mode mixte en 3D. La modélisation de la rupture en biseau serait un des grands sujets dans la recherche à venir pour les structures à parois

minces. Dans notre étude, la modélisation de la rupture en mode mixte (I+II+II) a été testée, mais en raison de problème de convergence, il est nécessaire de nouveaux des développements dans la future. L'étude expérimentale en mode mixte n'a que partiellement été abordé, elle nécessite des travaux complémentaires, notamment du point de vue de la conception de l'éprouvette qui s'avère beaucoup trop élancée. Une nouvelle géométrie d'éprouvette Arcan (Fig. 6.1) proposé par Madi et al [64] pourrait être utilisée dans les recherches à l'avenir.

Bibliography

[1] W.R. Andrews and C.F. Shih. Thickness and side-groove effects on J and δ resistance curves for A533–steel at 93°C. In J.D. Landes, J.A. Begley, and G.A. Clarke, editors, *Elastic–Plastic Fracture*, pages 426–450. ASTM STP 668, 1979.

[2] A. Arieli and A. Rosen. Measurements of the strain rate sensitivity coefficient in superplastic Ti-6Al-4V alloy. *Scripta Metall. Mater.*, 10:471–475, 1976.

[3] A. Asserin-Lebert, J. Besson, and A.-F. Gourgues. Fracture of 6056 aluminum sheet materials: Effect of specimen thickness and hardening behavior on strain localization and toughness. *Mater. Sci. Engng A*, 395:186–194, 2005.

[4] ASTM. *Annual book of ASTM Standard 03–01*, chapter E561–98 standard practice for R–curve determination, pages 509–521. 1999.

[5] ASTM. B871–01 Standard test method for tear testing of aluminum alloy products. *Annual Book of ASTM Standards*, 02.02, 2001.

[6] ASTM. E1304–97 Standard test method for plane-strain (chevron-notch) fracture toughness of metallic materials. *ASTM-International*, 2002.

[7] J.P. Bandstra and D.A. Koss. Modeling the ductile fracture process of void coalescence by void-sheet formation. *Mater. Sci. Engng A*, 319–321:490–495, 2001.

[8] Y. Bao. Dependence of fracture ductility on thickness. *Thin-Walled Structures*, 42:1211–1230, 2004.

[9] Y. Bao and T. Wierzbicki. On fracture locus in the equivalent strain and stress triaxiality space. *Int. J. Mech. Sci.*, 46(1):81–98, 2004.

[10] G.I. Barenblatt. The mathematical theory of equilibrium of cracks in brittle fracture. *Adv Appl. Mech.*, 7:55–129, 1962.

[11] F. Barlat, D.J. Lege, and J.C. Brem. A six–component yield function for anisotropic materials. *Int. J. Plasticity*, 7:693–712, 1991.

[12] J. Belotteau. *Comportement et rupture des aciers au C-Mn en présence de vieillissement sous déformation.* PhD thesis, Ecole Centrale Paris, 2009.

[13] J. Belotteau, C. Berdin, S. Forest, A. Parrot, and C. Prioul. Mechanical behavior and crack tip plasticity of a strain aging sensitive steel. *Mater. Sci. Engng A*, 526:156–165, 2009.

[14] J. Besson and R. Foerch. Large scale object–oriented finite element code design. *Comp. Meth. Appl. Mech. Engng*, 142:165–187, 1997.

[15] J. Besson, D. Steglich, and W. Brocks. Modeling of crack growth in round bars and plane strain specimens. *Int. J. Solids Structures*, 38(46–47):8259–8284, 2001.

[16] J. Besson, D. Steglich, and W. Brocks. Modeling of plane strain ductile rupture. *Int. J. Plasticity*, 19(10):1517–1541, 2003.

[17] D. Broek. *Elementary Engineering Fracture Mechanics*. Martinus Nijhoff Publishers, Boston, 1982.

[18] F. Bron. *Déchirure ductile des tôles minces en alliage d'aluminium 2024 pour application aéronautique*. PhD thesis, Ecole des Mines de Paris, 2004.

[19] F. Bron and J. Besson. A yield function for anisotropic materials. Application to aluminium alloys. *Int. J. Plasticity*, 20:937–963, 2004.

[20] F. Bron and J. Besson. Simulation of the ductile tearing for two grades of 2024 aluminum alloy thin sheets. *Engng Fract. Mech.*, 73:1531–1552, 2006.

[21] F. Bron, J. Besson, and A. Pineau. Ductile rupture in thin sheets of two grades of 2024 aluminum alloy. *Mater. Sci. Engng A*, 380:356–364, 2004.

[22] W.A. Cassada, G. J. Shiflet, and E.A. Starke. The effect of plastic deformation on al$_2$culi (t_1) precipitation. *Met. Trans.*, 22.

[23] O. Chabanet, D. Steglich, J. Besson, V. Heitmann, D. Hellman, and W. Brocks. Predicting crack growth resistance of aluminium sheets. *Comput. Mat. Sci.*, 26:1–12, 2003.

[24] J.L. Chaboche. Thermodynamic formulation of constitutive equations and application to the viscoplasticity and viscoelasticity of metals and polymers. *Int. J. Solids Structures*, 34(18):2239–2254, 1997.

[25] J.Q. Chen, Y. Madi, T.F. Morgeneyer, and J. Besson. Plastic flow and ductile rupture of a 2198 Al-Cu-Li aluminium alloy. *Comput. Mat. Sci.*, 50(4):1365–1371, 2011.

[26] A. Cho and B. Bès. Damage tolerance capability of an Al-Cu-Mg-Ag alloy (2139). *Materials Science Forum*, 519-521:603–608, 2006.

[27] C.C. Chu and A. Needleman. Void nucleation effects in biaxially stretched sheets. *J. Engng Mater. Technol.*, 102:249–256, 1980.

[28] D.S. Chung, C.W. Jea, J.H. Yoon, and J.K. Kim. Effect of Mn addition on the mechanical properties in Al-Cu-Li-Mg-Ag-Zr alloys. *Materials Science Forum*, 539-543:481–486, 2007.

[29] M.J. Crill, D.J. Chellman, E.S. Balmuth, M. Phillbrook, K.P. Smith, A. Cho, M. Niedzinski, R. Muzzolini, and J. Feiger. Evaluation of AA2050-T87 Al-Li alloy crack turning behavior. *Materials Science Forum*, 519-521:1323–1328, 2006.

[30] R. Crooks, Z. Wang, V.I. Levit, and R.N. Shenoy. Microtexture,microstructure and plastic anisotropy of AA2195. *Mater. Sci. Engng A*, 257:145–152, 1998.

[31] B. Decreus. *Etude de la précipitation dans les alliages Al-Li-Cu de troisième génération – Relations entre microstructures et propriétés mécaniques*. PhD thesis, Université de Grenoble – Institut Polytechnique de Grenoble, 2010.

[32] B. Decreus, F. Bley, A. Deschamps, and P. Donnadieu. Quantitative characterization of the precipitation in an AA2198 Al-Li-Cu alloy. In *Proc. ICAA11 conference, Aachen, Germany*, volume 1, pages 1040–1046, 2008.

[33] D.S. Dugdale. Yielding of steel sheets containing slits. *J. Mech. Phys. Solids*, 8:100–104, 1960.

[34] D. Dumont, A. Deschamps, and Y. Bréchet. On the relationship between microstructure, strength and toughness in AA7050 aluminium alloy. *Mater. Sci. Engng A*, 356:326–336, 2003.

[35] J. C. Ehrström and T. Warner. Metallurgical Design of Alloys for Aerospace Structures. In *Proc. ICAA7 conference, Charlottesville, Virginia, USA*, volume 331-337, pages 5–16, 2000.

[36] R. Foerch, J. Besson, G. Cailletaud, and P. Pilvin. Polymorphic constitutive equations in finite element codes. *Comp. Meth. Appl. Mech. Engng*, 141:355–372, 1997.

[37] W. M. Garrison and N. R. Moody. Ductile fracture. *J. Phys. Chem. Solids*, 48(11):1035–1074, 1987.

[38] F.W. Gayle, W.T. Tack, F.H. Heubaum, and J.R. Pickens. High toughness, high strength aluminium alloy design and practice. In *Proc. ICAA6 conference, Toyohashi, Japan*, pages 203–208, 1992.

[39] C. Giummarra, R. J. Rioja, G. H. Bray, P. E. Magnusen, and J. P. Moran. Al-Li alloys: Development of Corrosion Resistant, High Toughness Aluminium-Lithium Aerospace Alloys. In *Proc. ICAA11 conference, Aachen, Germany*, volume 1, pages 176–188, 2008.

[40] C. Giummarra, T. Thomas, and R.J. Rioja. New aluminium lithium alloys for aerospace applications. In *Proc. Light Metals Technology conference, Saint-Sauveur-des-Monts, Canada*, pages 1–6, 2007.

[41] S. Graff. *Viscoplastic behavior of zirconium alloys in the temperature range 20°C–400°C : characterization and modeling of strain ageing phenomena*. PhD thesis, Ecole des Mines de Paris, 2006.

[42] A.S. Gullerud, R.H. Dodds, R.W. Hampton, and D.S. Dawicke. Three-dimensional modeling of ductile crack growth in thin sheet metals: computational aspects and validation. *Engng Fract. Mech.*, 63:347–373, 1999.

[43] A.L. Gurson. Continuum theory of ductile rupture by void nucleation and growth: Part I – Yield criteria and flow rules for porous ductile media. *J. Engng Mater. Technol.*, 99:2–15, 1977.

[44] A. Guvenilir, T.M. Breunig, J.H. Kinney, and S.R. Stocks. New direct observations of crack closure processes in Al-Li 2090 T8E41. *Phil. Trans. R. Soc. Lond. A*, 357:2755–2775, 1999.

[45] S.J. Hales and R.A. Hafley. Texture and anisotropy in Al-Li alloy 2195 plate and near-net-shape extrusions. *Mater. Sci. Engng A*, 257:153–164, 1998.

[46] H. Halim, D.S. Wilkinson, and M. Niewczas. The Portevin-Le Chatelier (PLC) effect and shear band formation for an aa5754 alloy. *Acta Mater.*, 55:4151–4160, 2007.

[47] R. Hill. *The mathematical theory of plasticity*. Clarendon Press, Oxford, 1950.

[48] A. Hillerborg, M. Modeer, and P.E. Petersson. Analysis of crack formation and crack growth in concrete by means of fracture mechanics and finite element. *Cement Concrete Res*, pages 773–782, 1976.

[49] B.P. Huang and Z.Q. Zheng. Effect of Li Content on Precipitation in Al-Cu-(Li)-Mg-Ag-Zr Alloys. *Scripta Mater.*, 38:357–362, 1998.

[50] G.R. Irwin. Analysis of stress and strains near the end of a crack traversing a plate. *J. Applied Mech.*, 24:361–364, 1957.

[51] S. Kalyanam, A.J. Beaudoin, R.H. Dodds Jr., and F. Barlat. Delamination cracking in advanced aluminum-lithium alloys–Experimental and computational studies. *Engng Fract. Mech.*, 76:2174–2191, 2009.

[52] J. Kang, D S Wilkinson, M. Jain, J D Embury, A J Beaudoin, S. Kim, R. Mishira, and A K Sachdev. On the sequence of inhomogeneous deformation processes occuring during tensile deformation of strip cast AA5754. *Acta Mater.*, 54:209–218, 2006.

[53] J. Kang, D S Wilminson, J D Embury, M. Jain, and A J Beaudoin. Effect of type B Portevin–Le Chatelier bands on the onset of necking in uniaxial tension of strip cast AA5754 sheets. *Scripta Mater.*, 53:499–503, 2005.

[54] A.P. Karafillis and M.C. Boyce. A general anisotropic yield criterion using bounds and a transformation weighting tensor. *J. Mech. Phys. Solids*, 41:1859–1886, 1993.

[55] K.H. Khor, J.Y. Buffiere, W. Ludwig, and Sinclair I. High resolution X-ray tomography of micromechanisms of fatigue crack closure. *Scripta Mater.*, 55:47–50, 2006.

[56] J.F. Knott. *Fundamentals of Fracture Mechanics*. London Butterworths, 1973.

[57] M. Knüwer, J. Schumacher, H. Ribes, F. Eberl, and B. Bès. 2198 – Advanced Aluminium-Lithium Alloy for A350 Skin Sheet Application. In *Proc. 17th AeroMat Conference & Exposition*, 2006.

[58] J.M. Krafft, A.M. Sullivan, and R.W. Boyle. Effect on Dimensions on Fast Fracture Instability of Notched Sheets. In A.J. Kennedy, editor, *Crack Propagation Symposium*, pages 8–26. College of Aeronautics, Granfield, UK, 1961.

[59] W. Lan, X. Deng, M.A. Sutton, and C.S. Cheng. Study of slant fracture in ductile materials. *Int. J. Frac.*, 141:469–496, 2006.

[60] Ph. Lequeu, K.P. Smith, and A. Daniélou. Aluminum-Copper-Lithium Alloy 2050 Developed for Medium to Thick Plate. *J. Mater. Engng. Performance*, 19(6):841–847, 2009.

[61] G. Lin, A. Cornec, and K.H. Schwalbe. Three-dimensional finite element simulation of crack extension in Aluminium alloy 2024FC. *Fatigue and Fract. Engng Mater. Struct.*, 21:1159–1173, 1998.

[62] W. Ludwig and D. Bellet. Penetration of liquid gallium into the grain boundaries of aluminium: a synchrotron radiation microtomographic investigation. *Mater. Sci. Engng A*, 281:198–203, 2000.

[63] W. Ludwig, S. Bochet, D. Bellet, and J.Y. Buffiere. *X-ray tomography in Materials Science*, chapter 3D observation of grain boundary penetration in Al alloys, pages 155–163. Hermes Science Publications, 2000.

[64] Y. Madi, J. Besson, F. Tankoua, J.Q. Chen, and N. Recho. Mixed-mode ductile fracture of an anisotropic 2024 Al-Cu alloy. In Shibli, IA and Holdsworth, SR, editor, *5th IASME/WSEAS International Conference on Continuum Mechanics*, pages 147–154. World Scientific and Engineering Acad and Soc, 2010.

[65] E. Mahgoub, X. Deng, and M.A. Sutton. Three-dimensional stress and deformation fields around flat and slant cracks under remote Mode I loading conditions. *Engng Fract. Mech.*, 70:2527–2542, 2003.

[66] S. Mahmoud and K. Lease. The effect of specimen thickness on the experimental characterization of critical crack-tip-opening angle in 2024-T351 aluminum alloy. *Engng Fract. Mech.*, 70:443–456, 2003.

[67] E. Maire, J.Y. Buffière, L. Salvo, J.J. Blandin, W. Ludwig, and J.M. Letang. On the application of X-ray microtomography in the field of materials science. *Advanced Engineering Materials*, 3(8):539–546, 2001.

[68] F.A. Mc Clintock. A criterion for ductile fracture by the growth of holes. *J. App. Mech.*, 35:363–371, 1968.

[69] F.A. McClintock and Z.M. Zheng. Ductile fracture in sheets under transverse strain gradients. *Int. J. Frac.*, 64:321–327, 1993.

[70] D. A. Meyn, T.W. Webb, and E.C. Aifantis. Hydrogen-assisted crack studies of 4340 steel by using the optical method of caustics. *Engng Fract. Mech.*, 33:913–925, 1989.

[71] J. Mizera, J.H. Driveri, E. Jezierka, and K.J. Kurzydłowki. Studies of the relationship between the microstructure and anisotropy of the plastic properties of industrial aluminum–lithium alloys. *Mater. Sci. Engng A*, 212:94–101, 1996.

[72] J. Mizera and K.J. Kurzydlowski. On the anisotropy of the Portevin-Le Chatelier plastic instabilities in Al-Li-Cu-Zr alloy. *Scripta Mater.*, 45(7):801–806, 2001.

[73] T. F. Morgeneyer, J. Besson, H. Proudhon, M. J. Starink, and I. Sinclair. Experimental and numerical analysis of toughness anisotropy in AA2139 Al alloy sheet. *Acta Mater.*, 57(13):3902–3915, 2009.

[74] T. F. Morgeneyer, M. J. Starink, and I. Sinclair. Evolution of voids during ductile crack propagation in an aluminium alloy sheet toughness test studied by synchrotron radiation computed tomography. *Acta Mater.*, 56:1671–1679, 2008.

[75] A. Needleman. A continuum model for void nucleation by inclusion debonding. *J. Applied Mech.*, 54:525–531, 1987.

[76] A. Needleman. A Numerical Study of Void Nucleation at Carbides. Technical report, Report of Brown University, 1987.

[77] A. Needleman. An analysis of decohesion along an imperfect interface. *Int. J. Frac.*, 42:21–40, 1990.

[78] A. Needleman. An analysis of tensile decohesion along an interface. *J. Mech. Phys. Solids*, 38:289–324, 1990.

[79] S. Özbilen. Fractography and transmission electron microscopy analysis of an al-li-cu-mg-zr alloy displaying and improved fracture toughness. *J. Mater. Sci.*, 32:4127–4131, 1997.

[80] T. Pardoen, D. Dumont, A. Deschamps, and Y. Bréchet. Grain boundary versus transgranular ductile failure. *J. Mech. Phys. Solids*, 51(4):637–665, 2003.

[81] T. Pardoen, Y. Marchal, and F. Delannay. Thickness dependence of cracking resistance in thin aluminium plates. *J. Mech. Phys. Solids*, 47:2093–2123, 1999.

[82] A. Pirdondi and D. Fersini. Simulation of ductile crack growth in thin panels using the crack tip opening angle. *Engng Fract. Mech.*, 76(1):88–100, 2009.

[83] A. Pirondi and C. Dalle Donne. Characterisation of ductile mixed-mode fracture with the crack-tip displacement vector. *Engng Fract. Mech.*, 68(12):1385–1402, 2001.

[84] I.J. Polmear. *Light Alloys: Metallurgy of the Light Metals (Metallurgy & Materials Science)*. John Wiley & Sons 3 edition, 1995.

[85] H. Proudhon, J.Y. Buffière, and S. Fouvry. Three-dimensional study of a fretting crack using synchrotron X-ray micro-tomography. *Engng Fract. Mech.*, 74:782–793, 2007.

[86] J.R. Rice. The localisation of plastic deformation. In W.T. Koiter, editor, *Proc. 14th Int. Conf. Theoretical and Applied Mechanics, Delft*, pages 207–220. North–Holland, Amsterdam, 1976.

[87] J.R. Rice. The mechanics of earthquake rupture. In Enrico Fermi, editor, *Proc. of the International School of Physics*, pages 555–649. North–Holland, 1980.

[88] J.R. Rice and D.M. Tracey. On the ductile enlargement of voids in triaxial stress fields. *J. Mech. Phys. Solids*, 17:201–217, 1969.

[89] H.A. Richard and K. Benitz. A loading device for the creation of mixed mode in fracture mechanics. *Int. J. Frac.*, 22:R55, 1983.

[90] F. Rivalin, J. Besson, M. Di Fant, and A. Pineau. Ductile tearing of pipeline-steel wide plates — II.: Modeling of in–plane crack propagation. *Engng Fract. Mech.*, 68(3):347–364, 2000.

[91] G. Rousselier. Ductile fracture models and their potential in local approach of fracture. *Nucl. Eng. Design*, 105:97–111, 1987.

[92] S. Roychowdhury and R. Narasimhan. A finite element analysis of quasistatic crack growth in a pressure sensitive constrained ductile layer. *Engng Fract. Mech.*, 66:551–571, 2000.

[93] Y.D.A. Roychowdhury and R.H. Dodds Jr. Ductile tearing in thin aluminum panels: experiments and analyses using large-displacement, 3-D surface cohesive elements. *Engng Fract. Mech.*, 69:983–1002, 2002.

[94] C. Ruggieri, T.L. Panontin, and R.H. Dodds Jr. Numerical modeling of ductile crack growth in 3-d using computational cell elements. *Int. J. Frac.*, 82:67–95, 1996.

[95] I. Scheider. Simulation of cup-cone fracture in round bars using the cohesive zone model. In *First MIT Conference on Computation Fluid and Solid Mechanics*, volume I, pages 460–462. Amsterdam: Elsevier, 2001.

[96] I. Scheider. Residual stress prediction of a complex structure using crack extension analyses. *Engng Fract. Mech.*, 76(1):149–163, 2009.

[97] I. Scheider and W. Brocks. Simulation of cup-cone fracture using the cohesive model. *Engng Fract. Mech.*, 70(14):1943–1961, 2003.

[98] K.H. Schwalbe, I. Scheider, and A. Cornec. In *SIAM CM 09 - The SIAM method for applying cohesive models to the damage behaviour of engineering materials and structures*, pages 1–77, 2009.

[99] R. Shabadi, S. Kumar, H. Roven, and E.S. Dwarakadasa. Effet of specimen condition, orientation and alloy composition on PLC band parameters. *Mater. Sci. Engng A*, 382:203–208, 2004.

[100] Y.Z. Shen, K.H. Oh, and D.N. Lee. The effect of texture on the Portevin-Le Chatelier effect in 2090 Al-Li alloy. *Scripta Mater.*, 51(4):285–289, 2004.

[101] Y. Shinohara, Y. Madi, and J. Besson. A combined phenomenological model for the representation of anisotropic hardening behavior in high strength steel line pipes. *Eur. J. Mech.A*, pages 917–927, 2010.

[102] J.M. Silcock. The structural ageing characteristics of aluminium-copper-lithium alloys. *Journal of the Institute of Metals*, 88:357–364, 1959-1960.

[103] D. Steglich, H. Wafai, and W. Brocks. Anisotropic deformation and damage in aluminium 2198 T8 sheets. *Int. J. Damage Mech.*, page in press.

[104] B. Tanguy, T.T. Luu, G. Perrin, A. Pineau, and J. Besson. Plastic and damage behavior of a high strength X100 pipeline steel: experiments and modelling. *Int. J. of Pressure Vessels and Piping*, 85(5):322–335, 2008.

[105] W.A. Tayon, R.E. Crooks, M.S. Domack, J.A. Wagner, Beaudoin, and R.J. McDonald. Mechanistic study of delamination fracture in Al-Li Alloy C458 (2099). In *AUG 2009 NASA Technical Report Server*, 2009.

[106] X. Teng. Numerical prediction of slant fracture with continuum damage mechanics. *Engng Fract. Mech.*, 75:2020–2041, 2008.

[107] H. Toda, I. Sinclair, J.Y. Buffière, E. Maire, K.H. Khor, P. Gregson, and T. Kobayashi. A 3D measurement procedure for internal local crack driving forces via sychrotron X-ray microtomography. *Acta Metall.*, 52:1305, 2004.

[108] D. Tsivoulas, P. Prangnell, C. Sigli, and B. Bès. Effects of combined Zr and Mn additions on dispersoid formation and recrystallisation bahvior of AA2198 sheet. *Materials Science Forum*, 89-91:568–573, 2006.

[109] V. Tvergaard. Influence of voids on shear band instabilities under plane strain condition. *Int. J. Frac.*, 17(4):389–407, 1981.

[110] V. Tvergaard. On the localization in ductile materials containing spherical voids. *Int. J. Frac.*, 18(4):237–252, 1982.

[111] V. Tvergaard. Effect of fibre debonding in a whisker-reinforced metal. *Mater. Sci. Engng A*, 125:83–151, 1990.

[112] V. Tvergaard. Material failure by void growth to coalescence. *Advances in Applied Mechanics*, 27:83–151, 1990.

[113] V. Tvergaard and J.W. Hutchinson. The relation between crack growth resistance and fracture process parameters in elastic-plastic solids. *J. Mech. Phys. Solids*, 40(6):1377–1397, 1992.

[114] V. Tvergaard and J.W. Hutchinson. The influence of plasticity on mixed mode interface toughness. *J. Mech. Phys. Solids*, 41(6):1119–1135, 1993.

[115] V. Tvergaard and A. Needleman. Analysis of the cup–cone fracture in a round tensile bar. *Acta Metall.*, 32:157–169, 1984.

[116] A.K. Vasudévan and R.D. Doherty. Grain boundary ductile fracture in precipitation hardened aluminum alloys. *Scripta Mater.*, 35:1193–1219, 1987.

[117] K.T. Venkatesara Rao and R.O. Ritchie. Mechanisms influencing the cryogenic fracture-toughness behavior of aluminium-lithium alloys. *Acta Mater.*, 38(11):2309–2326, 1990.

[118] T. Warner. Recently-developed aluminium solutions for aerospace applications. *Materials Sci. Forum*, 519-521:1271–1278, 2006.

[119] V. Weiss and S. Yukawa. Critical appraisal of fracture mechanics. In *Fracture toughness testing and its application*, STP 381, pages 1–22. ASTM, 1964.

[120] R.H. Weitzman and I. Finnie. Measuring fracture toughness – a simplified approach using controlled crack propagation. *J. Mater.*, 7:294–299, 1972.

[121] W. Wen and J.G. Morris. An investigation of serrated yielding in 5000 series aluminum alloys. *Mater. Sci. Engng A*, 354:279–285, 2003.

[122] L. Xia and C.F. Shih. Ductile crack growth – I. A numerical study using computational cells with microstructurally-based length scales. *J. Mech. Phys. Solids*, 43:233–259, 1995.

[123] H. Yuan, G. Lin, and A. Cornec. Verification of a cohesive zone model for ductile fracture. *J. Engng Mater. Technol.*, 118:192–200, 1996.

[124] U. Zerbst, M. Heinimann, C. Dalle Donne, and D. Steglich. Fracture and damage mechanics modelling of thin-walled structures — An overview. *Engng Fract. Mech.*, 76(1):5–43, 2009.

[125] X. Zhang, S. Ma, N. Recho, and J. Li. Bifurcation and propagation of a mixed-mode crack in ductile material. *Engng Fract. Mech.*, 73(13):1925–1939, 2006.

Appendix A

Plan of specimens

The specimens used for the mechanical tests during this work are withdrawn from four different sheets supplied by Alcan CRV. Two 2 mm-thick recrystallized sheets on T3 and T8 conditions, and two 6 mm-thick fibrous sheets on T3 and T8 conditions. For 6 mm fibrous sheets, 2 mm-thick sheets are also prepared by slicing the 6 mm sheets into 2 mm to investigate sheet thickness effect. This section presents the dimension of all testing specimens, smooth tensile specimen ST_{12}, notched tensile specimen NT_1 and NT_2, Kahn tear specimen, Arcan specimen and M(T) panel.

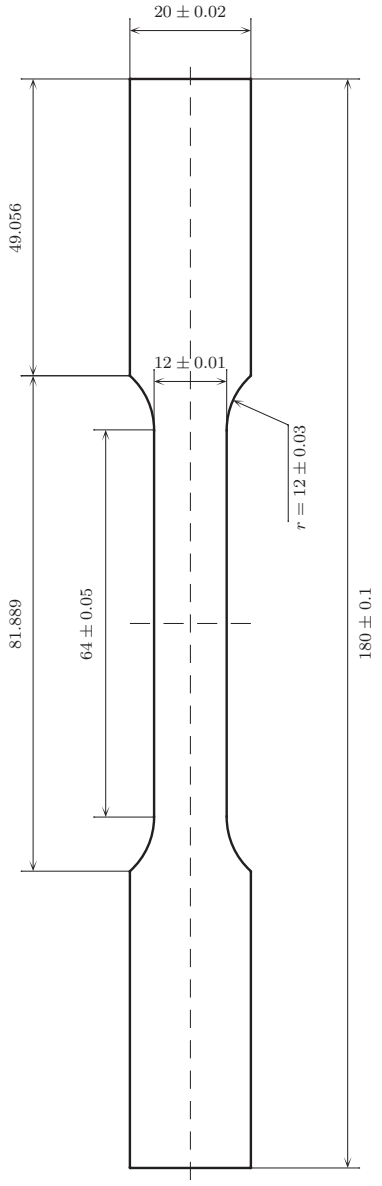


Figure A.1: Smooth tensile specimen ST_{12} (dimension in mm).

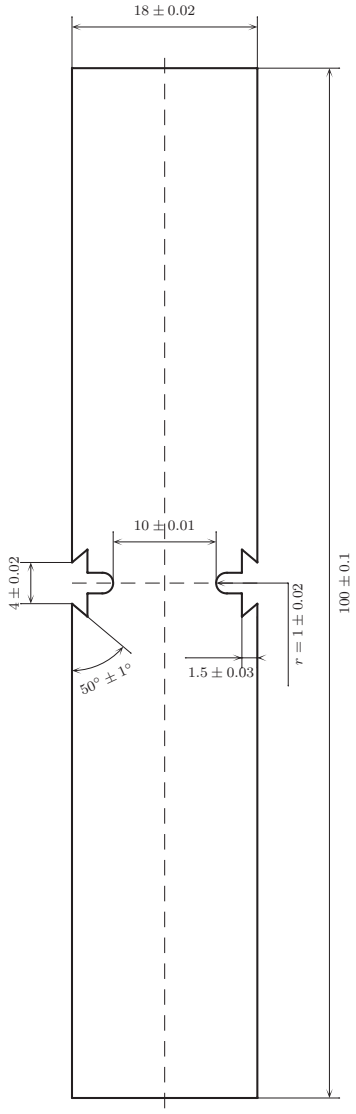


Figure A.2: Notched tensile specimen NT_1 (dimension in mm).

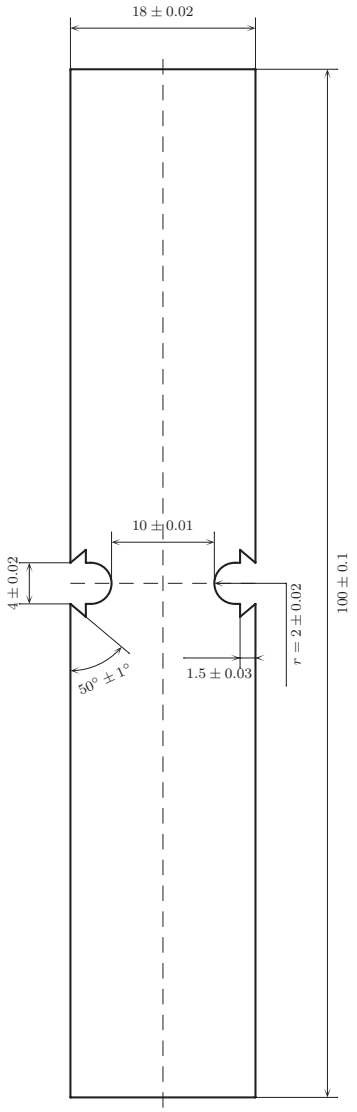


Figure A.3: Notched tensile specimen NT_2 (dimension in mm).

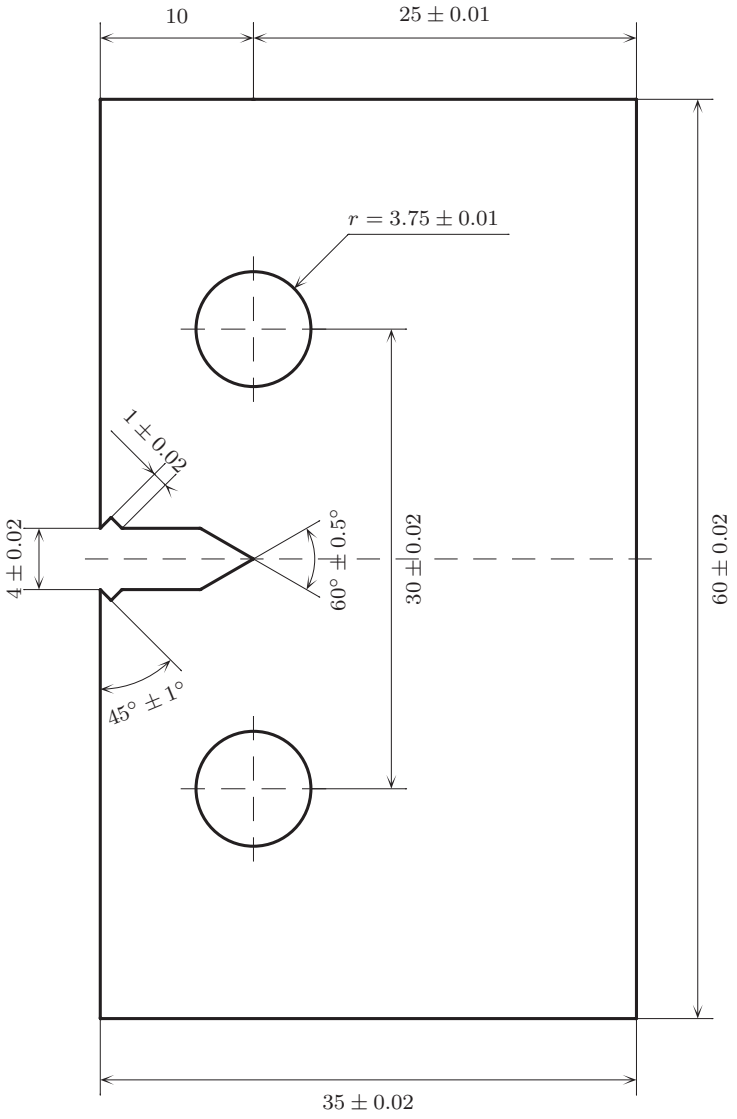


Figure A.4: Kahn tear test specimen (dimension in mm).

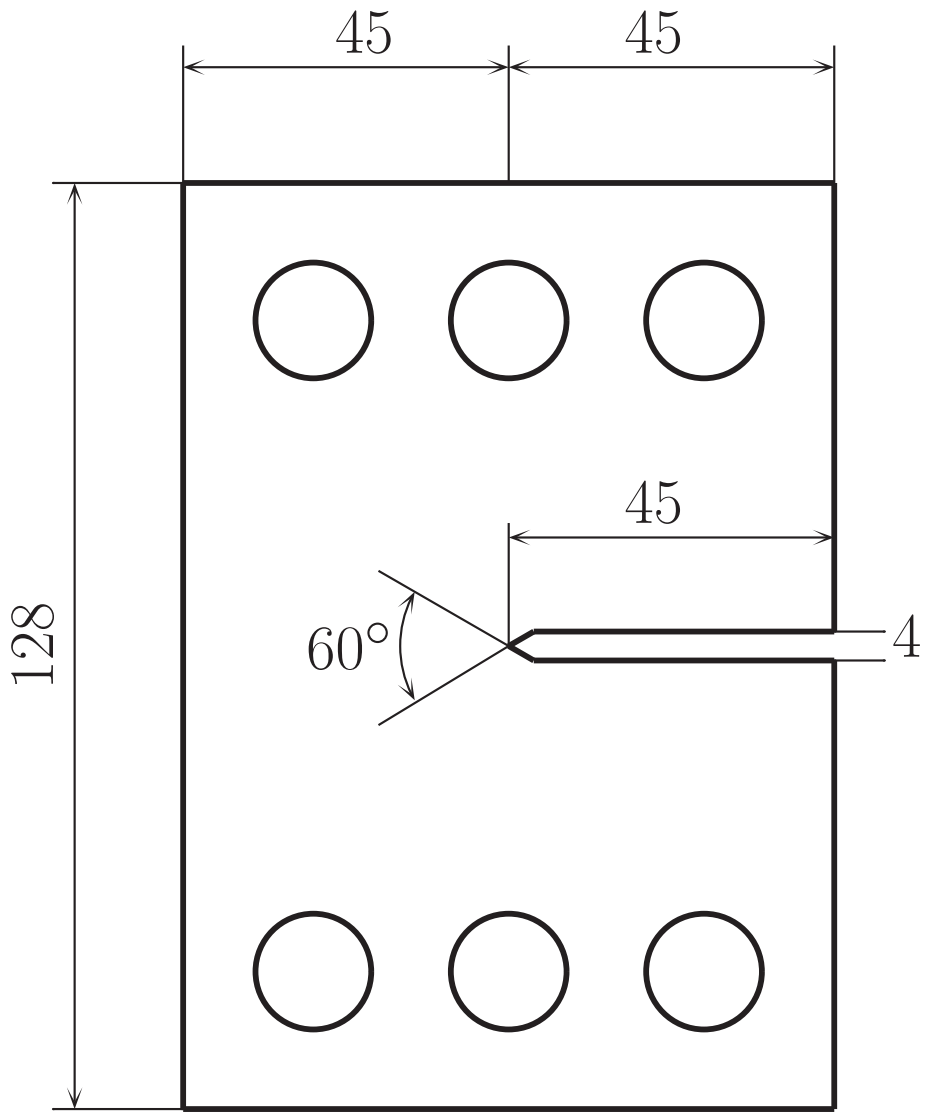


Figure A.5: Arcan tear test specimen (dimension in mm).

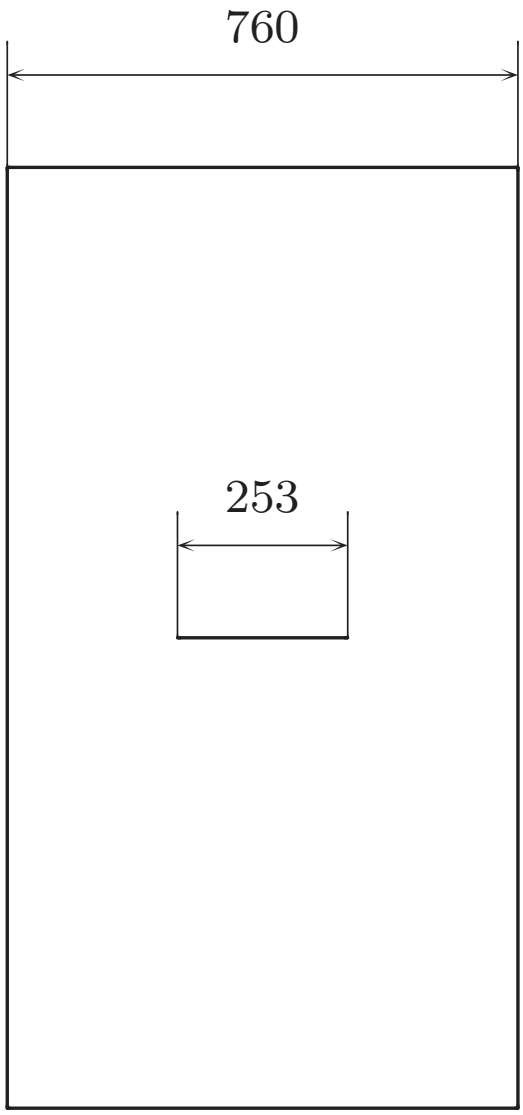


Figure A.6: Center-cracked tension test specimen M(T) (dimension in mm).

Appendix B

Mechanical Tests

In this section, all the mechanical tests carried out during this work are shown in curves.

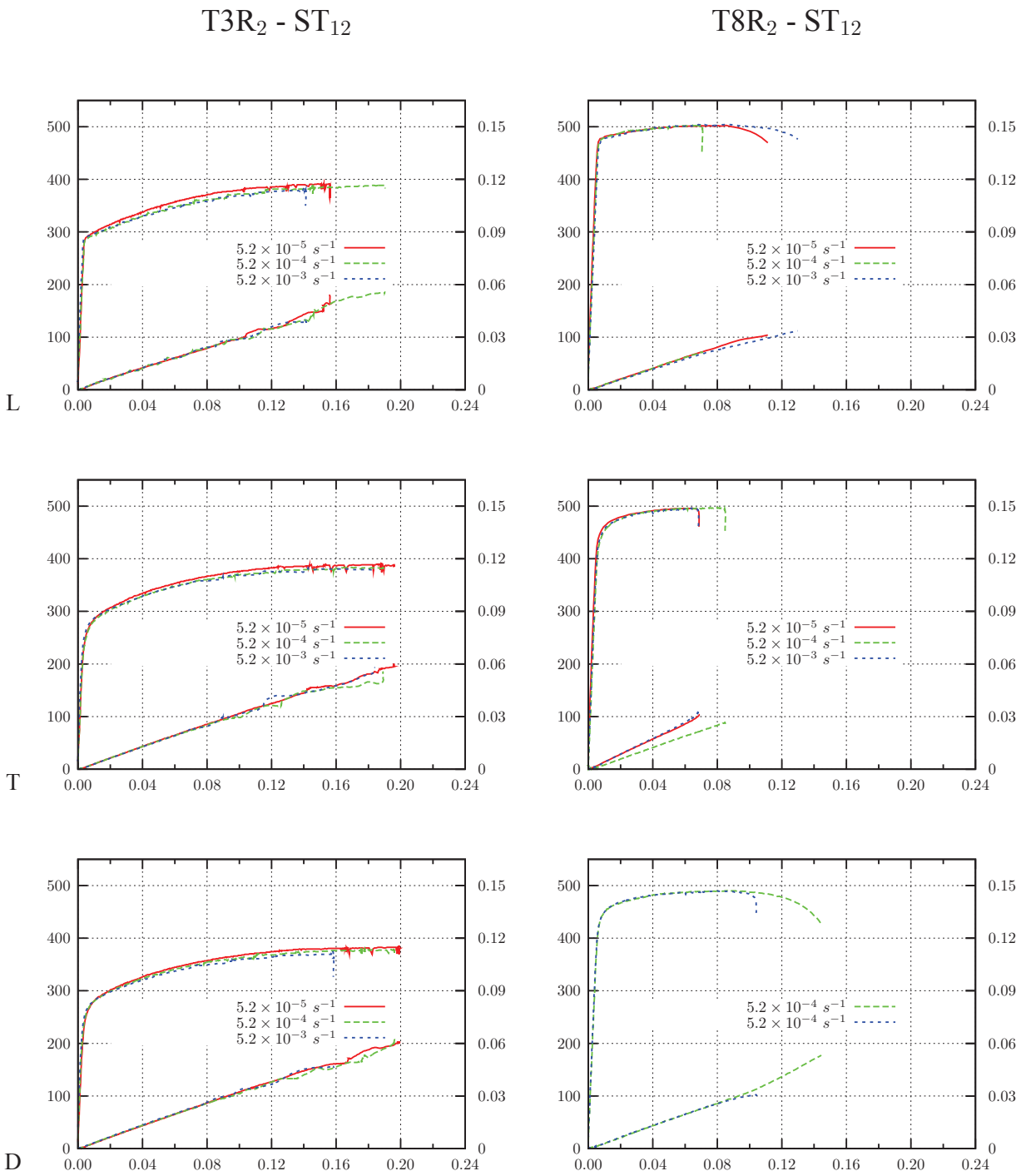


Figure B.1: . Tensile tests on ST_{12} specimens along L, T and D directions for the $T3R_2$ and $T8R_2$ materials at three different strain rates.

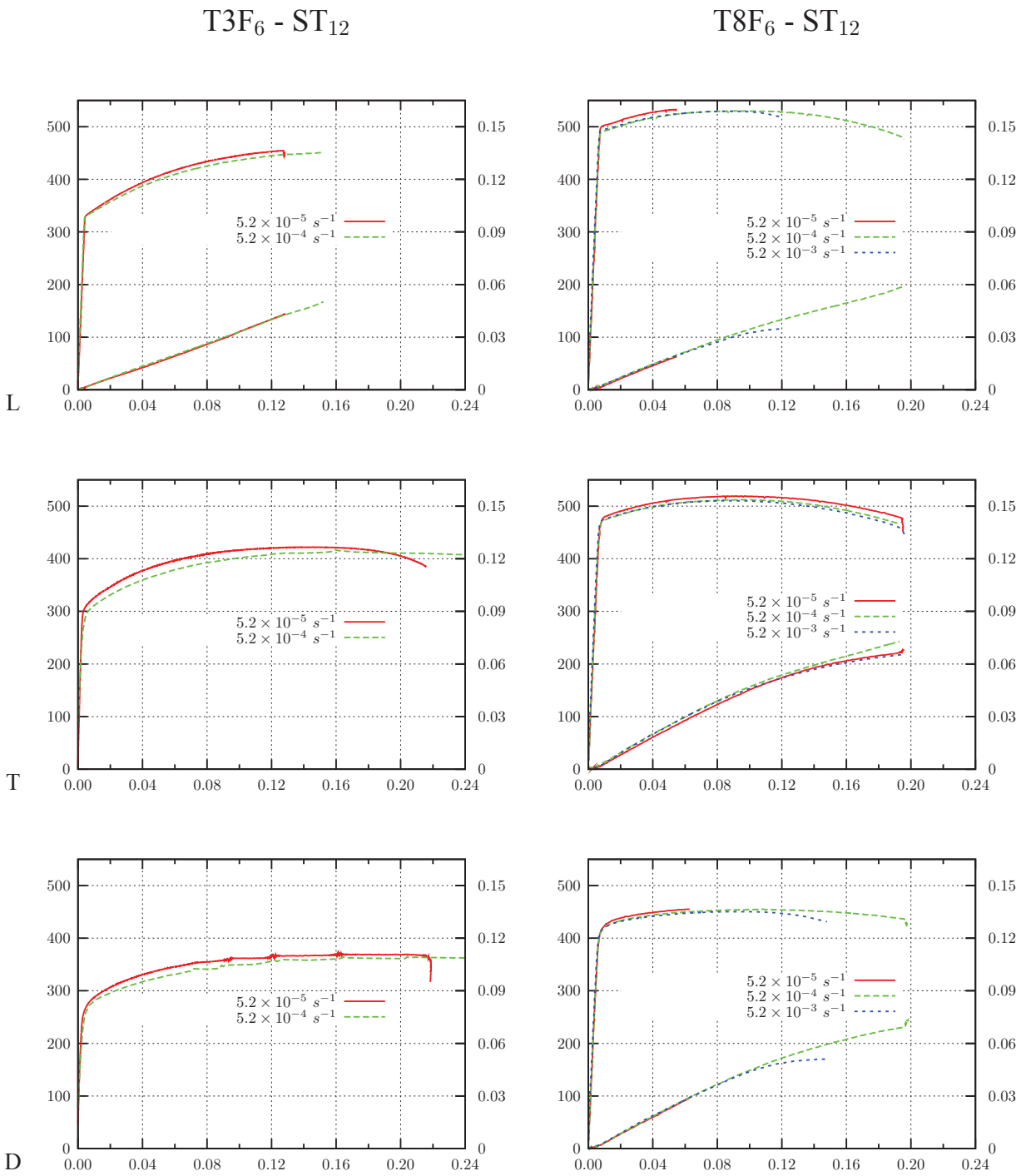


Figure B.2: . Tensile tests on ST_{12} specimens along L, T and D directions for the $T3F_6$ and $T8F_6$ materials at three different strain rates.

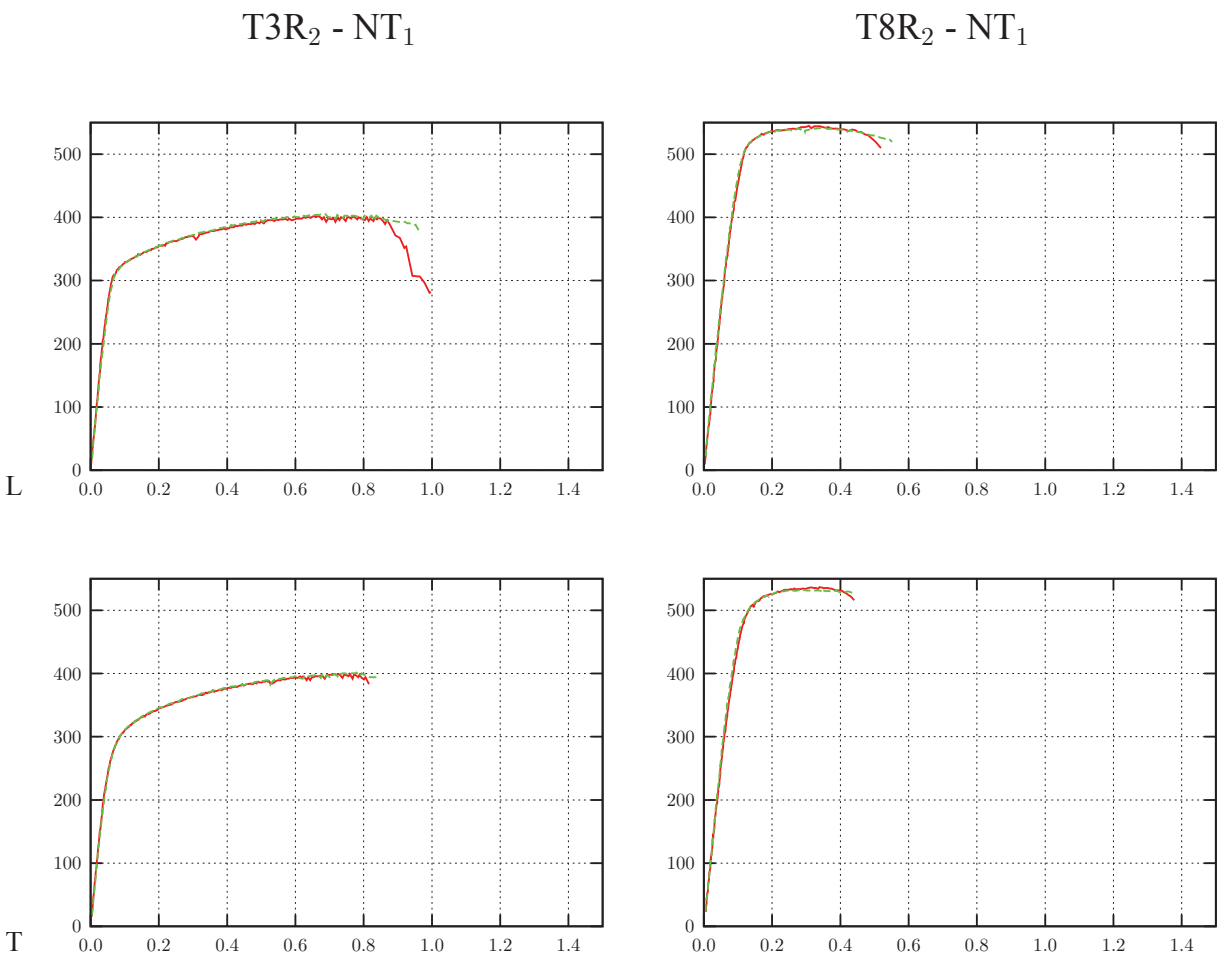


Figure B.3: . Normalized force (F/S_0) as a function of Notch Opening Displacement (NOD) of NT_1 specimens along L and T directions for the $T3R_2$ and $T8R_2$ materials.

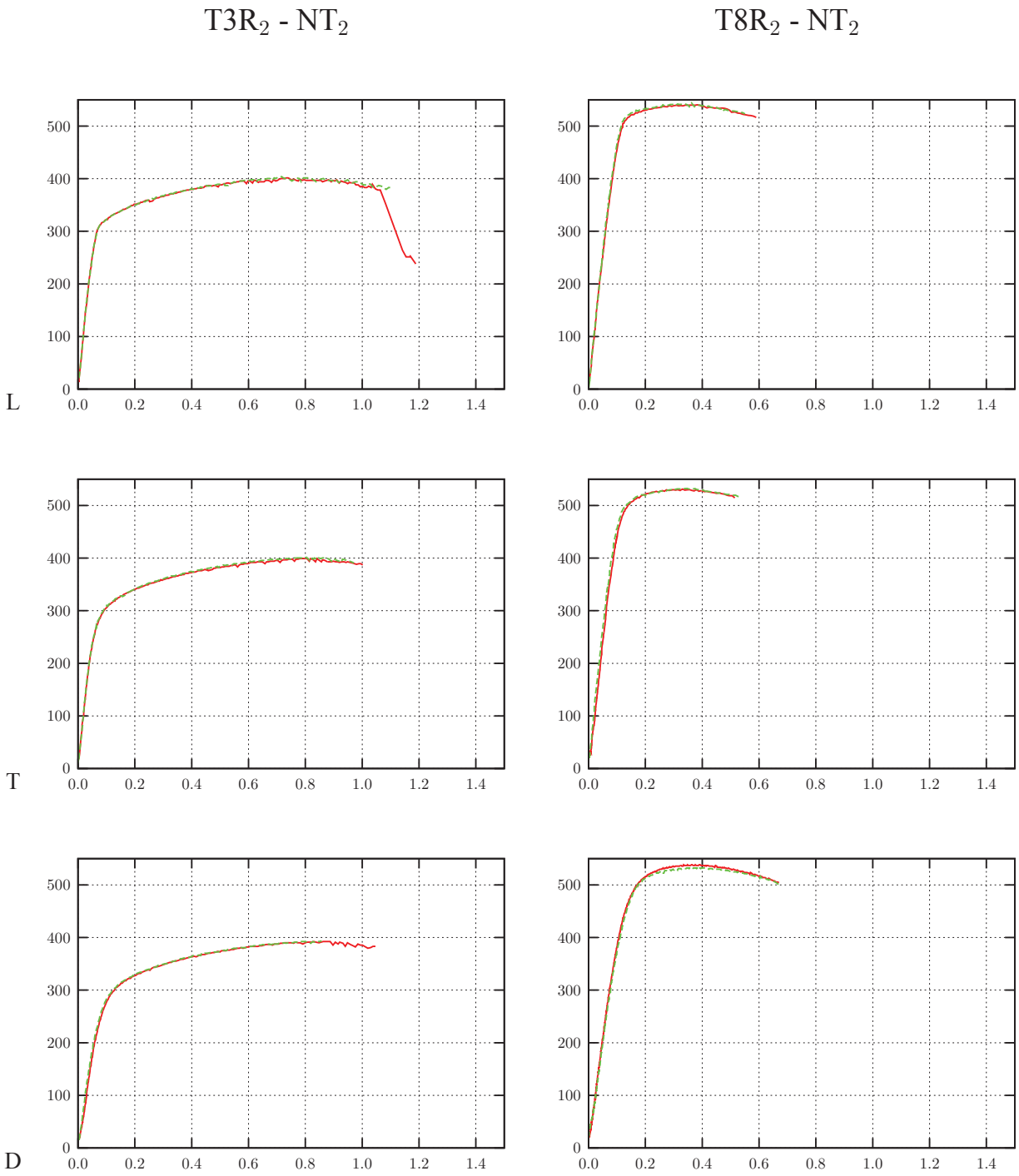


Figure B.4: . Normalized force (F/S_0) as a function of Notch Opening Displacement (NOD) of NT_2 specimens along L, T and D directions for the $T3R_2$ and $T8R_2$ materials.

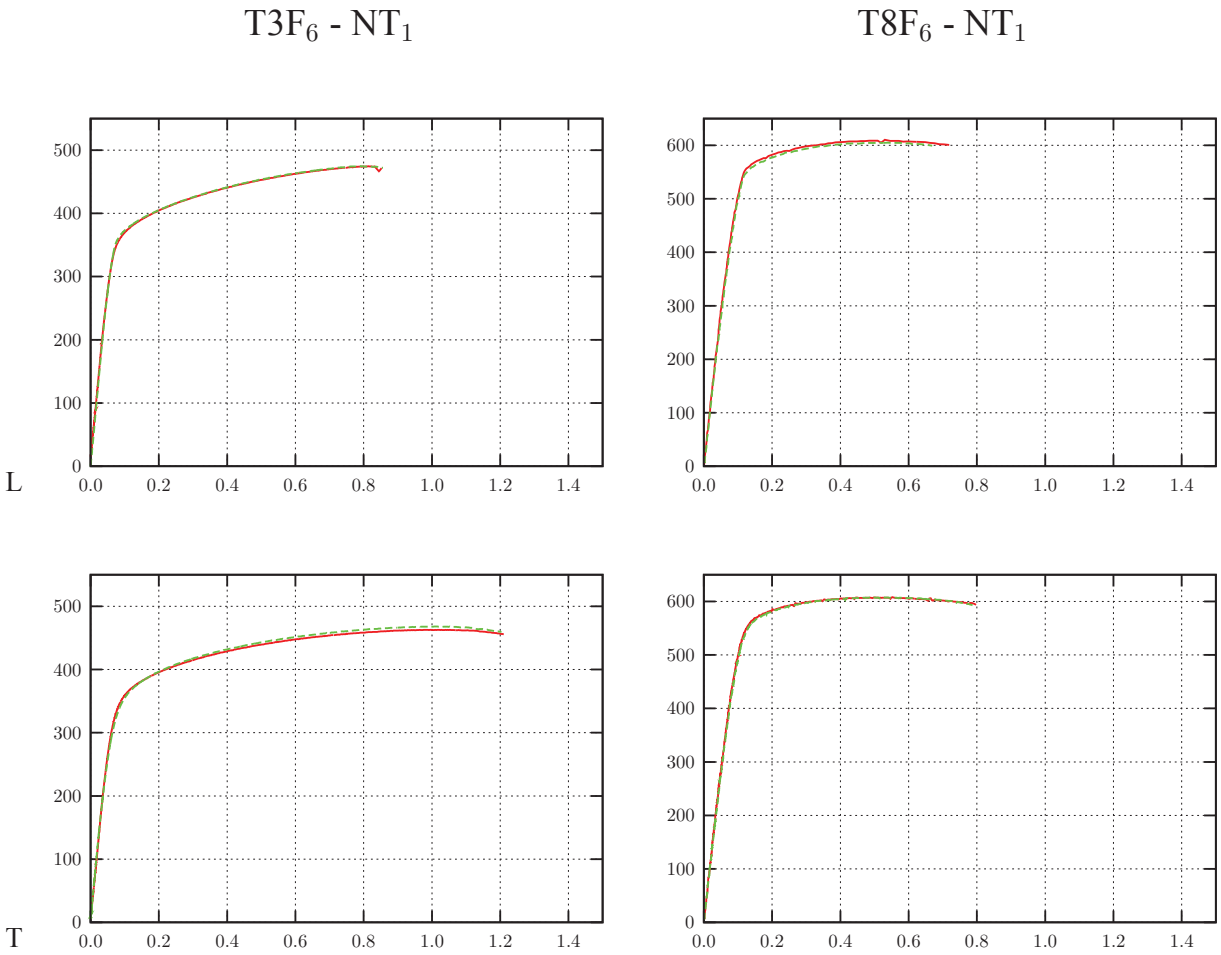


Figure B.5: . Normalized force (F/S_0) as a function of Notch Opening Displacement (NOD) of NT_1 specimens along L and T directions for the $T3F_6$ and $T8F_6$ materials.

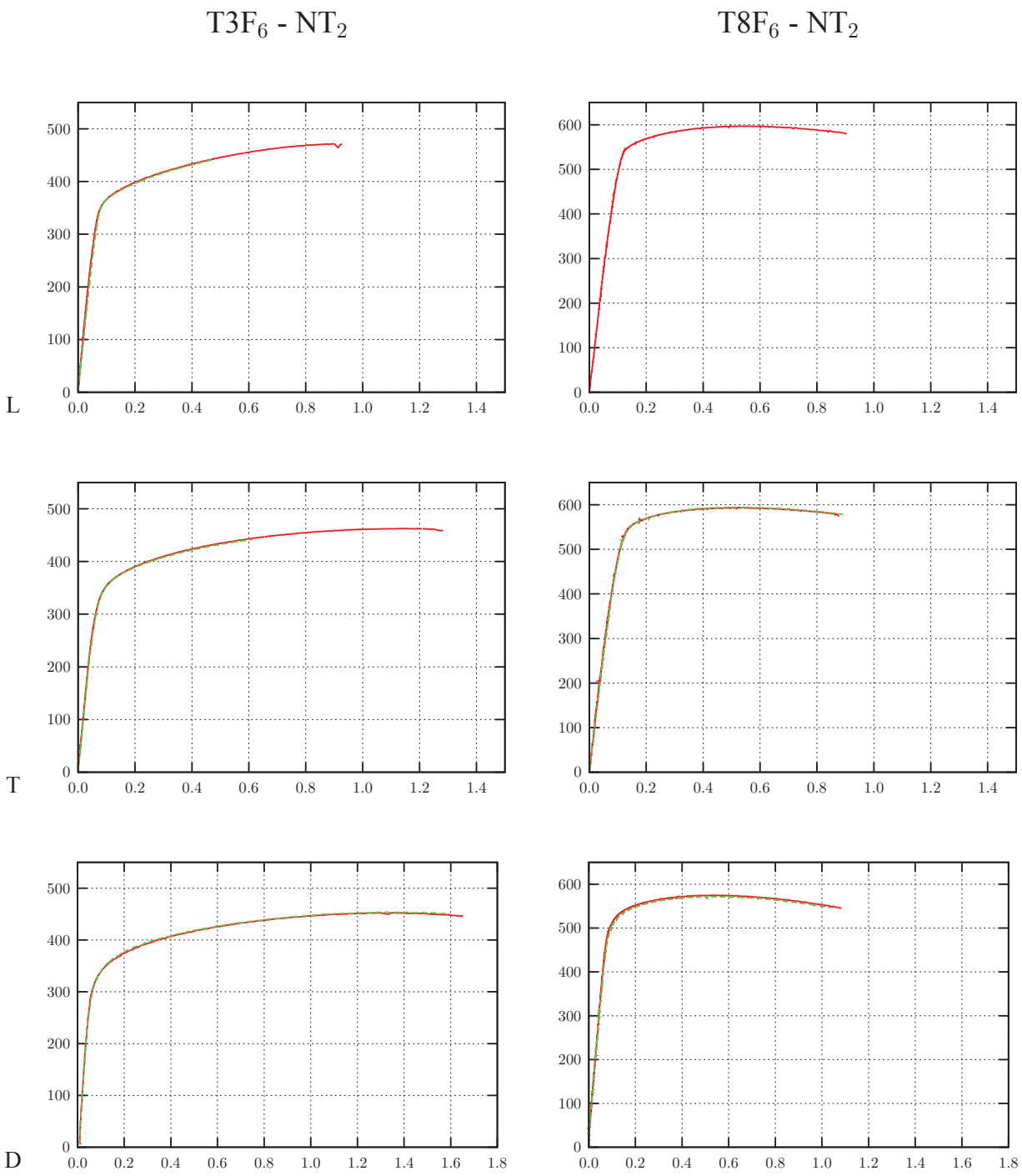


Figure B.6: . Normalized force (F/S_0) as a function of Notch Opening Displacement (NOD) of NT_2 specimens along L, T and D directions for the $T3F_6$ and $T8F_6$ materials.

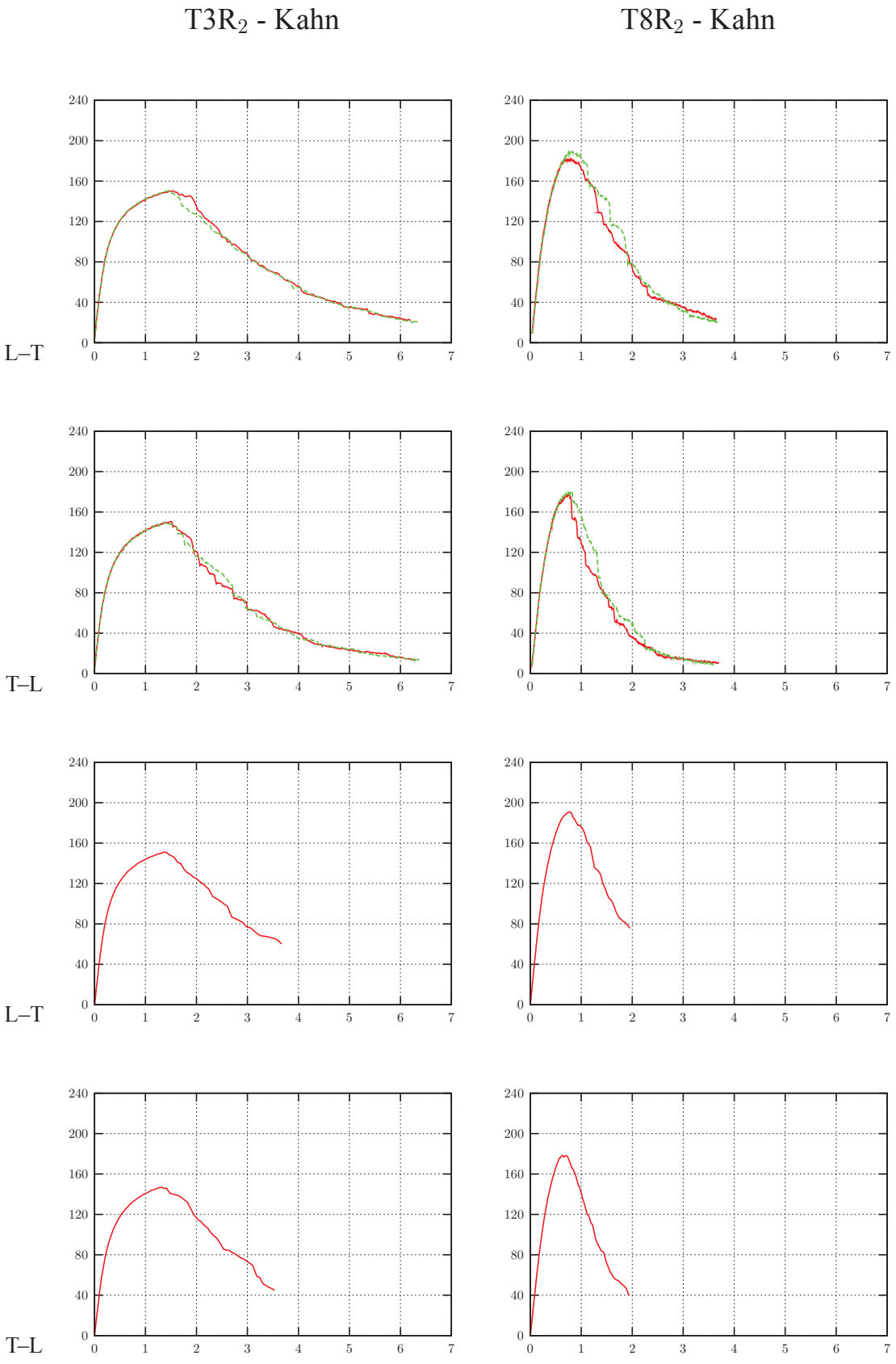


Figure B.7: . Normalized force (F/S_0) as a function of the Crack tip Mouth Opening Displacement (CMOD) of Kahn tear tests along L–T and T–L loadings for the $T3R_2$ and $T8R_2$ materials.

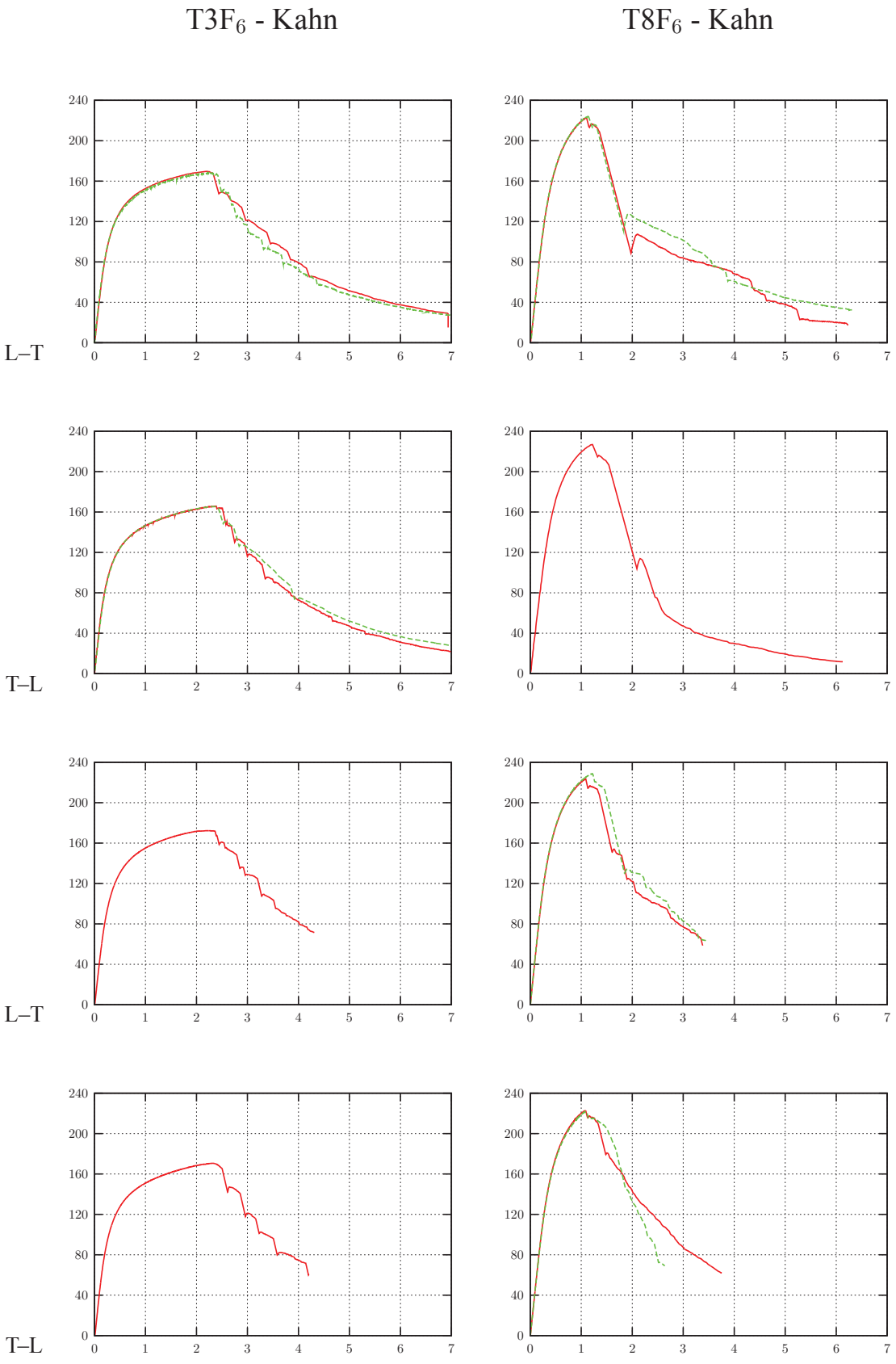


Figure B.8: . Normalized force (F/S_0) as a function of the Crack tip Mouth Opening Displacement (CMOD) of Kahn tear tests along L–T and T–L loadings for the $T3F_6$ and $T8F_6$ materials.

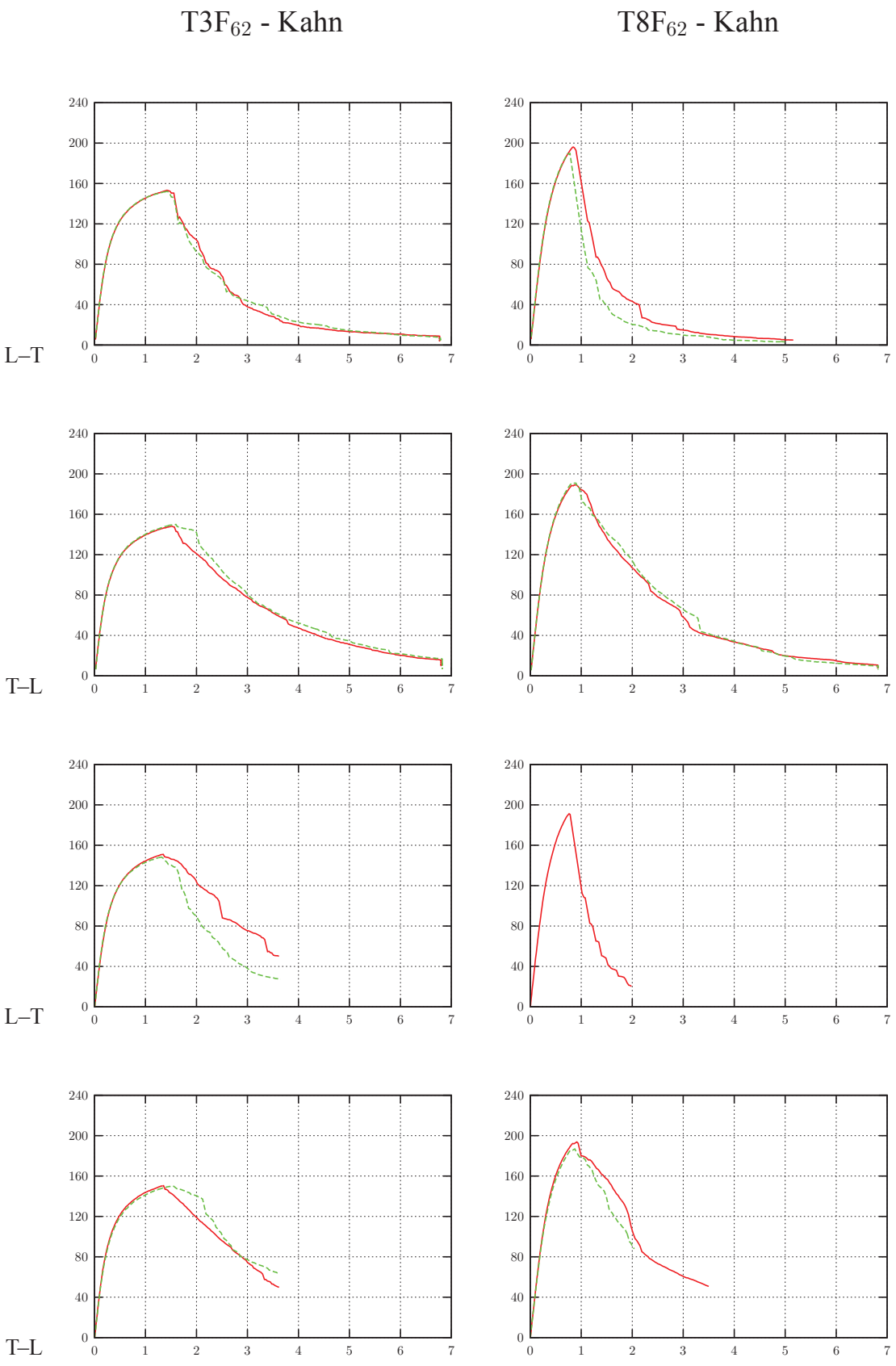


Figure B.9: . Normalized force (F/S_0) as a function of the Crack tip Mouth Opening Displacement (CMOD) of Kahn tear tests along L–T and T–L loadings for $T3F_{62}$ and $T8F_{62}$ materials.

Déchirure Ductile des Tôles en Alliages d'Aluminium-Lithium 2198 pour Application Aéronautqiue

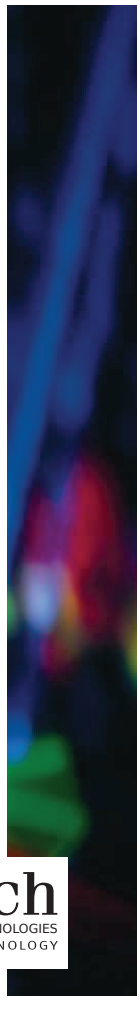
Résumé : L'objectif de cette thèse est de progresser dans la compréhension de l'influence de la microstructure sur l'anisotropie plastique et la ténacité de deux nuances d'alliage Al-Cu-Li 2198 sous forme de tôle. L'épaisseur de tôles est 2 mm et 6 mm. Deux traitements thermiques (T351 et T851) ont été étudiés pour chaque nuance. Différentes techniques de caracterisation multi-échelles telles que la microscopie optique, la microscopie électronique en transmission ou encore la tomographie à rayons X ont été utilisées pour identifier les microstructures des matériaux et les micro-mécanismes d'endommagement. L'anisotropie plastique et l'effet d'épaisseur sur la plasticité ont été étudiés via des essais de traction sur les éprouvettes lisses et entaillées selon différentes directions. Les résultats montrent que le comportement plastique est anisotrope dans le plan de tôle. Le comportement en déchirure ductile a été examiné en utilisant des éprouvettes de petite taille de type Kahn ainsi que des plaques larges de type M(T). L'anisotropie de ténacité a été étudiée sur les éprouvettes chargées selon différentes configurations. La fractographie par microscope électronique à balayage (MEB) et la tomographie synchrotron aux rayons X ont clarifié le rôle des structures granulaires et des traitements thermiques sur les mécanismes de la rupture inter-granulaire et trans-granulaire. La croissance de cavités reste limitée dans la zone de propagation de fissure. Enfin, la simulation de la déchirure ductile par élément finis est basée sur l'approche locale de la rupture en utilisant un modèle de zone cohésive (CZM). Les paramètres cohésifs ont été ajustés sur les éprouvettes Kahn. Les paramètres identifiés ont été employés pour prédire la déchirure ductile des essais M(T). Les résultats montrent que la simulation des essais M(T) est plus sensible aux valeurs des paramètres ajustés que la simulation des essais Kahn. L'effet d'épaisseur a été évalué à l'aide de la technqiue de relâchement des noeuds en analysant la variation de la contrainte et de la déformation dans la direction de l'épaisseur.

Mots clés : alliage d'Al-Li, rupture ductile, endommagement, mécanismes de rupture, anisotropie plastique, effet d'épaisseur, simulation par éléments finis, CZM, tomographie à rayons X

Ductile Tearing of AA2198 Aluminum-Lithium Sheets for Aeronautic Application

Abstract : The purpose of this thesis consists in understanding the influence of microstructure on plastic anisotropy and fracture toughness for two grade 2198 Al-Cu-Li alloys. The sheet thicknesses are 2 mm and 6 mm. Two heat treatment conditions (T351 and T851) were studied for each grade. Multiscale characterization techniques including optical micrography, transmission electron microscopy and X-ray computed tomography have been used to identify materials microstructure and damage micromechanisms. Plastic anisotropy and thickness effect on plasticity have been investigated via tensile tests on smooth flat and notched flat specimens showing an anisotropic plastic behaviour along different loading directions. Ductile tearing behaviour was examined using small sized Kahn specimens and large panels M(T) tests. Fracture toughness anisotropy was investigated on different loading configuration tests. Fractography via scanning electron microscopy (SEM) and synchrotron radiation computed tomography (SRCT) have clarified the intergranular and transgranular mechanisms of fracture with respect to grain structure and heat treatment. Void growth is limited in the crack propagation regions. Finally, the finite element simulation of ductile tearing is based on the local approach to fracture using cohesive zone model (CZM). The cohesive parameters were adjusted on small sized Kahn specimens. Fitted parameters were employed to predict the ductile tearing behaviour of M(T) tests. Simulation results show that the fitted cohesive parameters are more sensitive for M(T) tests than for Kahn tests. The thickness effect was assessed using node release technique by analysing variation of stress and strain along thickness direction.

Keywords : Al-Li alloys, ductile fracture, damage, fracture mechanisms, plastic anisotropy, thickness effect, finite element simulation, CZM, X-ray tomography



MINES ParisTech

ParisTech
INSTITUT DES SCIENCES ET TECHNOLOGIES
PARIS INSTITUTE OF TECHNOLOGY